May 2019

Testing the Late Paleozoic Ice Volume Paradox in the Southernmost Paraná Basin, Brazil

Nicholas David Fedorchuk
University of Wisconsin-Milwaukee

TESTING THE LATE PALEOZOIC ICE VOLUME PARADOX IN THE SOUTHERNMOST

PARANÁ BASIN, BRAZIL

by

Nicholas David Fedorchuk

A Dissertation Submitted in

Partial Fulfillment of the

Requirements for the Degree of

Doctor of Philosophy

in Geosciences

at

The University of Wisconsin-Milwaukee

May 2019

ABSTRACT

TESTING THE LATE PALEOZOIC ICE VOLUME PARADOX IN THE SOUTHERNMOST
PARANÁ BASIN, BRAZIL

by

Nicholas David Fedorchuk

The University of Wisconsin-Milwaukee, 2019
Under the Supervision of Professor John L. Isbell

The late Paleozoic ice age (LPIA; ~372-259 Ma) was the last complete transition from icehouse to greenhouse conditions on a fully vegetated Earth, making it a relevant analog for modern Earth systems. High frequency glacioeustatic fluctuation of ~100-200 m during the late Paleozoic are described by some authors in low paleolatitude basins and attributed to the orbitally-driven, waxing and waning of a massive (~20-35 x 10^6 km^2) hypothetical ice sheet. This massive ice sheet is traditionally interpreted to have covered much of southern Gondwana for >100 m.y. Meanwhile, recent studies of high-paleolatitude glacial deposits imply a much more complex pattern of glaciation with distinct, smaller ice centers that persisted for <10 m.y. Seemingly in support of these more recent studies, climate models indicate that a massive ice sheet would be too stable to produce glacioeustatic fluctuations on a time scale generated by orbital forcing. However, numerous smaller ice sheets of equal spatial coverage would not contain enough water volume to produce glacioeustatic amplitudes like those reported by some authors. To address this ice-volume paradox, the southernmost margin of the Paraná Basin, Brazil was chosen for a detailed sedimentologic, stratigraphic, and geochemical study since it has an unaltered record of Permo-Carboniferous glaciation and since several contradictory hypotheses have been proposed regarding the nature of the glaciation in this region.

Sedimentological and geochemical analyses of glacial deposits on the southernmost margin of the Paraná Basin indicate that the glacier covering this region was warm-based or polythermal and it experienced repeated fluctuations in ice-marginal positions during the Carboniferous. The glacial foreland was as a temperate, transitional, lacustrine to estuarine environment. Paleovalleys on the southern margin of the Paraná Basin were previously viewed as fjords that drained an ice center over northern Namibia, which is also thought to have supplied ice to the eastern Paraná Basin. Contradicting this hypothesis, these paleovalleys were found to be non-glacial in origin. Furthermore, the orientations of subglacial erosional features, paleocurrents, and glaciotectonic deformation structures from the southern Paraná Basin all support an unconfined lobe that advanced radially NNE and NNW out of Uruguay during the late Paleozoic. Therefore, at least two distinct ice centers are believed to have supplied sediment to the eastern and southern margins of the Paraná Basin. Detrital zircon (U-Pb) geochronology was used to assess the provenance of glacial sediments in the eastern Chaco-Paraná Basin (Uruguay) in order to determine the source region of the ice center that flowed N into the southern Paraná Basin. The detrital zircon samples indicate that glaciogenic sediments were derived from SE Uruguay, which was likely connected to the Cargonian highlands of southern Namibia and northern South Africa. This study supports the emerging view of LPIA glaciation, which purports that the glaciation consisted of multiple topographically controlled ice centers. The absence of glaciers on the southernmost Paraná Basin during the early Permian means that glaciation in southern Brazil does not correlate to widespread Permian glaciation in Africa. This is further evidence that late Paleozoic glaciation did not occur everywhere simultaneously. Thus, based on this study, the ice-volume paradox is most likely the result of over-estimates of glacioeustatic fluctuations.

To my parents
Robert and Rosemary Fedorchuk
and my wife
Hanna Yousuf

TABLE OF CONTENTS

LIST OF FIGURES

x

LIST OF TABLES

ACKNOWLEDGEMENTS

Matthew Sanborn, Guilherme Roesler, João Ricetti, Thammy Mottin, Dr. Amanda Carvalho, Dr. Luiz Weinschütz, and Willian Matsumura.

My graduate school friends have always made it a pleasure to come in to the department every day. The entire department is so friendly and encouraging that I have always felt at home here. Thank you to David, Kate, Jane, Megan, Keenan, Liz, Chase, Chad, Gayantha, Levi, Emily, and everyone else. Thank you to my parents for always listening to me and taking an interest in my research. They have encouraged my passion for geology since I was a kid collecting fossils and rocks on the side of the road.

Finally, I cannot say thank you enough to my wife, Hanna Yousuf, who was helping me before I even started graduate school and throughout my entire time here at UWM. Many hours of train and bus rides were taken from South Bend to Milwaukee to visit me. I could never have finished without all the immeasurable ways that she sacrificed her own time, resources, and energy. Thank you!

Chapter 1. Introduction

1.1. The late Paleozoic ice Age

The Earth currently exists in an icehouse condition that is characterized by relatively low atmospheric partial pressure of CO_2 (pCO_2; ~ 400 ppmv today) and glaciation at high to mid-latitudes. However, human activities (i.e. the burning of fossil fuels and deforestation) are currently on pace to increase pCO_2 to levels not seen in 30 million years (~ 2,000 ppmv if all fossil fuels are depleted) (Kump, 2002; Montañez et al., 2011). To understand Earth's response to rising pCO_2, a deep time analog is needed. The late Paleozoic ice age (LPIA), which extended from the Famennian of the Late Devonian until the Wuchiapingian in the Late Permian (~372-259 Ma) serves as the best predictor for future climate change because it represents the last complete transition in Earth's history from an icehouse planet, similar in some ways to today, to a warmer greenhouse planet with relatively high pCO_2 (e.g. Gastaldo et al., 1996, Raymond and Metz, 2004; Montañez and Soreghan, 2006, Isbell et al., 2008, 2012).

The LPIA is also the only such transition to occur on a fully vegetated Earth with a complex biota (e.g. Gastaldo et al., 1996; Montañez and Poulsen, 2013). Despite the usefulness of such an analog, further work is needed to interpret the timing, drivers, and feedbacks of Earth systems during this interval. An area of study within the LPIA that remains particularly problematic is the extent and timing of glaciation. The traditional view is that a massive ice sheet (~20-35 x 10^6 km^2) covered a large part of the southern supercontinent for ~113 million years (e.g. Frakes, 1979; Veevers and Powell, 1987; Frakes et al., 1992; Ziegler et al., 1997; Scotese, 1999; Buggisch et al., 2011). Alternatively, recent studies of temperate to high-latitude

glaciations have suggested that the LPIA was comprised of multiple ice centers and shorter glacial intervals (< 10 m.y.) that are separated by non-glacial periods of equal duration (e.g. Visser, 1997; López Gamundí, 1997; Isbell et al., 2003; 2012; Fielding et al., 2008; Gulbranson et al., 2010). Orbitally-driven glacioeustatic fluctuations as much as 100-200 m have been suggested during the Permo-Carboniferous based on stratigraphic and geochemical evidence at low latitudes (e.g. Wanless and Shephard, 1936; Heckel, 1977, 2008; Ross and Ross, 1985; Soreghan and Giles, 1999; Joachimski et al., 2006; Rygel et al., 2008; Buggisch et al., 2008). However, a paradox exists, whereby models suggest that large continental ice sheets would be too stable to produce massive glacioeustatic fluctuations on orbitally-driven timescales (e.g. Maqueda et al., 1998; Deconto and Pollard, 2003; Horton and Poulsen, 2009; Montañez and Poulsen, 2013) and smaller separate ice sheets of equal geographic coverage would not contain enough water volume to produce such eustatic changes (e.g. Isbell et al., 2003). The difference in ice-volume between these two hypotheses suggests greatly different interpretations of ocean circulation, glacioeustasy, pCO_2, and climate during the critical transition from icehouse to greenhouse conditions (e.g. Poulsen et al., 2007; Horton et al., 2012). Therefore, this discrepancy warrants further work on the nature of near-field, high- to mid-latitude glaciogenic deposits so that the record of far-field eustasy and climate models can be better constrained.

1.2. Significance of the Paraná Basin

Carboniferous and Permian glacial deposits are located in Africa, South America, Australia, Antartica, India, the Arabian Peninsula, and various other small crustal blocks now incorporated into southern Asia (e.g. Veevers and Powell, 1987; Singh, 1993; López Gamundí,

1997; Wopfner and Casshvap, 1997; Visser, 1997; Limarino et al., 2002; Isbell et al., 2003, 2008, 2012; Chakraborty and Ghosh, 2008; Fielding et al., 2008; Martin et al., 2008; Mory et al., 2008; Rocha-Campos et al., 2008; Isbell, 2010). However, in many places the sedimentologic record of the glaciation is incomplete or poorly constrained. The lack of reliable age control in many basins can be attributed to a paucity of ash beds for absolute age dating and imprecise biostratigraphic control of endemic fossil faunas and floras. The Paraná Basin of southern Brazil (Fig. 1.1A) is critical to understanding the late Paleozoic ice-volume paradox because it contains one of the most complete and detailed glacial and post-glacial records from Permo-Carboniferous strata in Gondwana and it contains ash beds that allow for high precision U-Pb dating (e.g. Eyles et al., 1993; Santos et al., 1996; Holz et al., 2008; Rocha-Campos et al., 2008; Mori et al., 2012; Vesely et al., 2015; Cagliari et al., 2016; Griffis et al., 2018). The basin is situated between well dated the late Paleozoic basins with a glacial record in Africa and western South America, thus it provides a critical geographic link in reconstructions of the glacial interval (e.g Stollhofen et al., 2008; Gulbranson et al, 2010). The Paraná Basin is also a hydrocarbon and coal producing basin, which has prompted exploration, including an abundance of drill cores and associated data (França and Potter, 1991; Lopes, 2004; Vesely et al., 2007). Finally, the Paraná Basin was located at mid-paleolatitudes (~55° S; e.g. Rocha-Campos et al., 2008; Torsvik and Cocks, 2013), where it seems likely that glaciation would have been more sensitive to fluctuations in climate compared to a polar setting.

Despite these advantages, there remains little consensus on the timing and character of the glacial interval in the Paraná Basin, which is represented by the Permo-Carboniferous Itararé Group. For example, one hypothesis describes numerous small ice caps extending only short distances into the Paraná Basin from locally elevated areas (Fig. 1.1B; Santos et al., 1996;

3

Rocha-Campos et al., 2008). A competing hypothesis describes a massive ice sheet that originated in Antarctica, extended across Africa, and covered the entire basin (Fig. 1.1C; e.g. Barret, 1991; Veevers et al., 1994; Gesicki et al., 2002; Starck and Papa, 2006). A third hypothesis suggests that two separate ice centers were located over highlands in Africa and extended onto the eastern and southern margins of the basin (Fig. 1.1D; e.g. Frakes and Crowell, 1972; Crowell and Frakes, 1975; Assine et al., 2018). Finally, a fourth hypothesis depicts ice sheets in Africa draining into the southern and eastern Paraná Basin through a series of paleovalleys (Fig. 1.1E; e.g. Tedesco et al., 2016; Fallgatter and Paim, 2017). Additionally, interpretations of the glaciation have ranged from large and small unconfined lobes to small, confined valley glaciers (e.g. Frakes and Crowell, 1972; Rocha-Campos et al., 2008; Tedesco et al., 2016). Interpretations of the glaciers' thermal regimes have ranged from cold-based glaciers with extensive ice-shelves to warm-based temperate glaciers with tidewater termini (e.g. Vesely and Assine, 2002; Trosdtorf et al., 2005). Therefore, this project aims to address some of the questions that persist about the extent, nature, and timing of glaciation in the Paraná Basin and to determine how this information fits into the broader record of high- to mid-latitude glaciation during the LPIA.

To test these hypotheses, focus was placed on the southernmost part of the Paraná Basin, located in the state of Rio Grande do Sul (Fig. 1.2). This area is situated on a paleotopographic high known as the Rio Grande do Sul Shield (RGS) that is comprised of mostly Neoproterozoic igneous and metamorphic terranes (Fig. 1.2). The southern margin of the basin was chosen because it is significantly understudied compared to the better exposed eastern margin of the basin. Work on the southern margin has also previously described, subglacial grooves with different orientations from those on the eastern margin of the basin, which has led to questions

regarding how the glacial deposits were spatially and temporally related to both intra- and extra-basinal deposits (e.g. Gesicki et al., 2002; Rocha-Campos et al., 2008; Rosa et al., 2016; Assine et al., 2018). Furthermore, the southernmost margin of the basin was paleogeographically located between African highlands to the east, the Chaco-Paraná Basin to the south in present Uruguay, and the Paraná Basin to the north, making it an important area for broad-scale reconstructions of the glaciation.

1.3. Project objectives and synopsis

To test the various hypotheses for the extent, nature, and timing of LPIA glaciation in the southernmost Paraná Basin, this project had the following goals:

1. *Conduct a sedimentologic and stratigraphic analysis of glaciogenic deposits in the southern Paraná Basin to determine the presence, size, extent, timing, depositional environments, and thermal regime of the glaciation.*
2. *Constrain the location and size of ice center affecting the study area by determining the provenance of glaciogenic units.*
3. *Compare and contrast the provenance and sedimentology of glaciogenic sediments within the study area to related localities in the Chaco-Paraná Basin, Uruguay to evaluate drainage patterns during the late Paleozoic.*

Chapter 2 of this dissertation focuses on the sedimentary fill of two paleovalleys on the southern margin of the Paraná Basin, named the Marianna Pimentel and Leão Paleovalleys (e.g.

Tedesco et al., 2016). These paleovalleys were a natural starting point for this project because they have been previously described as glacially-carved fjords that were draining a major ice center in Africa onto the RGS (e.g. Tedesco et al., 2016). If true, that would make these paleovalleys a critical link between the glacial record in northern Namibia, the eastern margin of the Paraná basin, and the southern margin of the Paraná Basin. However, in Chapter 2, I argue that based on the sedimentology and stratigraphy of their fill, the paleovalleys were not glacially-carved and do not contain any clear evidence of glaciation. The fill of these paleovalleys is interpreted as entirely post-glacial sediments. Additionally, detrital zircon U-Pb geochronology reveals that the sedimentary fill of the paleovalleys was not derived from Africa and that the valleys appear to have been formed by active tectonism during the Paleozoic. This is significant because it indicates that, unlike the eastern margin of the Paraná Basin, ice did not flow directly E to W from Africa, onto the RGS. It also supports the interpretation that a separate ice center was responsible for glaciation on the southern margin compared to the eastern margin of the basin.

Chapter 3 of this dissertation consists of a detailed description of deformed glaciogenic (Itararé Gp.) strata on the western RGS that were first described by Tomazelli and Soliani Júnior (1997). It is important to analyze these sediments because they contain some clear evidence for glaciation in the form of grooved surfaces, striated clasts, rhythmites with dropstones, and diamictite pellets. In this case, the deformation is determined to be the result of glaciotectonism consistent with an ice-marginal push-moraine complex. The nature of the glaciotectonism provides clues about the thermal regime and motion of the glacier that advanced over this area, the nature of the foreland, as well as the paleoclimate of this region during the Carboniferous. The sediments show evidence of a temperate, terrestrial-to-estuarine, proglacial setting with

6

evidence of seasonal freeze/thaw processes. Deformation structures indicate that the glacier shoved the sediments towards the NW, out of present-day Uruguay. When combined with other published grooved surfaces and subglacaially carved whalebacks in Uruguay (i.e. Assine et al., 2018), this data indicates that ice spread radially across the RGS, supporting unconfined glaciation. Furthermore, the pattern of deformation described in Chapter 3 shows evidence of multiple advance/retreat cycles within a relatively short time span, which supports a dynamic, temperate margin for ice flowing towards the NW in the Carboniferous.

Chapter 4 is a provenance analysis of glacial and post-glacial sediments on the eastern margin of the Chaco-Paraná Basin, Uruguay and the southernmost Paraná Basin, Brazil. It became important for this study to expand into the adjacent Chaco-Paraná Basin (located to the south of the RGS) because the results from Chapters 2 and 3 indicated that an unconfined lobe originated from present-day Uruguay. Therefore, the goal of Chapter 4 is to better understand the location of the ice center that supplied ice N to the Paraná Basin and determine how drainage patterns changed during the shift from glacial to post-glacial conditions. The results presented in Chapter 4 indicate that sediments in the eastern Chaco-Paraná Basin are from igneous and metamorphic sources located in SE Uruguay and likely SW Namibia. This supports the hypothesis that the glaciers entering the southernmost Paraná Basin originated in the Cargonian Highlands of southern Africa. Meanwhile, the glacial sediments on the RGS were primarily derived from erosion and resedimentation of Precambrian/Cambrian metasedimentary rocks located nearby on the RGS. Based on the detrital signatures, changes in drainage were observed between ice-proximal, relatively ice-distal, and post-glacial settings. Ice-proximal and post-glacial sediments were mostly sourced from highly local basement. Meanwhile, relatively ice-distal, glacially-influenced sediments had zircons from a larger drainage area.

7

References

Assine, M.L., de Santa Ana, H., Veroslavsky, G., Vesely, F.F., 2018. Exhumed subglacial landscape in Uruguay; erosional landforms, depositional environments, and paleo-ice flow in the context of the late Paleozoic Gondwanan glaciation. Sedimentary Geology 369, 1-12.

Barrett, P. J., 1991. The Devonian to Jurassic Beacon Supergroup of the Transantarctic Mountains and correlatives in other parts of Antarctica. In: Tingey, R. J. (Ed.), The Geology of Antarctica: Oxford, Oxford University Press, pp. 120-152.

Buggisch, W., Joachimski, M.M., Sevastopulo, G., Morrow, J.R., 2008. Mississippian $\delta^{13}C_{carb}$ and conodont $\delta^{18}O$ records – Their relation to the Late Palaeozoic Glaciation. Palaeogeography, Palaeoclimatology, Palaeoecology, 268, 273-292.

Buggisch, W., Wang, X., Alekseev, A.S., Joachimski, M.M., 2011. Carboniferous-Permian carbon isotope stratigraphy of successions from China (Yangtze platform), USA (Kansas) and Russia (Moscow Basin and Urals). Palaeogeography, Palaeoclimatology, Palaeoecology 301, 18-38.

Cagliari, J., Philipp, R.P., Buso, V.V., Netto, R.G., Hillebrand, P.K., Lopes, R.d.C., Basei, M.A.S, Faccini, U.F., 2016. Age constraints of the glaciation in the Paraná Basin: evidence from new U-Pb dates. Journal of the Geological Society 173, 871-874.

Chakraborty, C., Ghosh, S. K., 2008. Pattern of sedimentation during the Late Paleozoic Gondwanaland glaciation: An example from the Talchir Formation, Satpura Gondwana basin, central India. Journal of Earth System Science 117, 499-519.

Crowell, J.C., Frakes, L.A., 1975. The late Paleozoic glaciation. In: Campbell, K.S.W. (Ed.), Gondwana Geology. Australian National University Press, Canberra, pp. 313-331.

Deconto, R.M., Pollard, D., 2003. Rapid Cenozoic glaciation of Antarctica induced by declining atmospheric CO_2. Nature 421, 245-249.

Eyles, C. H., Eyles, N., Franca, A. B., 1993. Glaciation and tectonics in an active intracratonic basin: the late Palaeozoic Itararé Group, Paraná Basin, Brazil. Sedimentology 40, 1-25.

Fielding, C. R., Frank, T. D., Isbell, J. L., 2008. The late Paleozoic ice age--A review of current understanding and synthesis of global climate patterns. In: Fielding, C. R., Frank, T. D., Isbell, J. L. (Eds.), Resolving the Late Paleozoic Ice Age in Time and Space. Geological Society of America Special Paper 441, pp. 343-354.

Fallgatter, C., Paim, P. S. G., 2017. On the origin of the Itararé Group basal nonconformity and its implications for the Late Paleozoic glaciation in the Paraná Basin, Brazil. Palaeogeography, Palaeoclimatology, Palaeoecology (in press). https://doi.org/10.1016/j.palaeo.2017.02.039

Frakes, L., Crowell, J., 1972. Late Paleozoic glacial geography between the Paraná Basin and the Andean geosyncline. Anais da Academia Brasileira de Ciências 44, 139-145.

Frakes, L.A., 1979. Climates through earth history, Amsterdam, Elsevier, 310 (pp.).

Frakes, L. A., Francis, J. E., Syktus, J. I., 1992. Climate modes of the Phanerozoic, Cambridge, Cambridge University Press, 274 (pp.).

França, A. B., Potter, P. E, 1991. Stratigraphy and Reservoir Potential of Glacial Deposits of the Itararé Group (Carboniferous-Permian), Paraná Basin, Brazil: American Association of Petroleum Geologists Bulletin 75, 62-85.

Gastaldo, R. A., DiMichele, W. A., Pfefferkorn, H. W., 1996. Out of the icehouse into the greenhouse; a late Paleozoic analog for modern global vegetational change. Geological Society of America Today 6, 1-7.

Gesicki, A. L. D., Riccomini, C., Boggianic, P. C., 2002. Ice flow direction during late Paleozoic glaciation in western Paraná Basin, Brazil. Journal of South American Earth Sciences 14, 933-939.

Griffis, N.P., Mundil, R., Montañez, I.P., Isbell, J.L., Fedorchuk, N.D., Vesely, F.F., Iannuzzi, R., Yin, Q.-Z., 2018. A new stratigraphic framework built on U-Pb single zircon TIMS ages with implications for the timing of the penultimate icehouse (Paraná Basin, Brazil). Geological Society of America Bulletin (in press).

Gulbranson, E.L., Montañez, I.P., Schmitz, M.D., Limarino, C.O., Isbell, J.L., Marenssi, S.A., Crowley, J.L., 2010. High-precision U-Pb calibration of Carboniferous glaciation and climate history, Paganzo Group, NW Argentina. Geological Society of America Bulletin 122, 1480-1498.

Heckel, P. H., 1977. Origin of phosphatic black shale facies in Pennsylvanian cyclothems of mid-continent North America. American Association of Petroleum Geologists Bulletin 61, 1045-1068.

Heckel, P. H., 2008. Pennsylvanian cyclothems in Midcontinent North America as far-field effects of waxing and waning of Gondwana ice sheets. Special Paper - Geological Society of America 441, 275-289.

Holz, M., Souza, P. A., Iannuzzi, R., 2008. Sequence stratigraphy and biostratigraphy of the Late Carboniferous to Early Permian glacial succession (Itararé subgroup) at the eastern-southeastern margin of the Paraná Basin, Brazil. In: Fielding, C. R., Frank, T., Isbell, J. L. (Eds.), Resolving the Late Paleozoic Ice Age in Time and Space. Geological Society of America Special Paper 441, pp. 115-129.

Horton, D.E., Poulsen, C.J., 2009. Paradox of late Paleozoic glacioeustasy. Geology 37, 715-718.

Horton, D.E., Poulsen, C.J., Montañez, I.P., DiMichele, W.A., 2012. Eccentricity-paced late Paleozoic climate change. Palaeogeography, Palaeoclimatology, Palaeoecology 331-332, 150-161.

Isbell, J.L., Miller, M.F., Wolfe, K.L., Lenaker, P.A., 2003. Timing of late Paleozoic glaciation in Gondwana: Was glaciation responsible for the development of northern hemisphere cyclothems? In: Chan, M.A., Archer, A.W. (Eds.), Extreme depositional environments: Mega end members in geologic time. Geological Society of America Special Paper 370, 5-24.

Isbell, J. L., Fraiser, M. L., Henry, L. C., 2008. Examining the complexity of environmental change during the late Paleozoic and early Mesozoic. Palaios 23, 267-269.

Isbell, J. L., 2010. Environmental and paleogeographic implications of glaciotectonic deformation of glaciomarine deposits within Permian strata of the Metschel Tillite, southern Victoria Land, Antarctica. In: López-Gamundí, O. R., Buatois, L. A. (Eds.), Late Paleozoic Glacial Events and Postglacial Transgressions in Gondwana. Geological Society of America Special Publication 468, pp. 81-100.

Isbell, J. L., Henry, L. C., Gulbranson, E. L., Limarino, C. O., Fraiser, M. L., Koch, Z. J., Ciccioli, P. L., and Dineen, A. A., 2012. Glacial paradoxes during the late Paleozoic ice age: Evaluating the equilibrium line altitude as a control on glaciation. Gondwana Research 22, 1-19.

Joachimski, M.M., von Bitter, P.H., Buggisch, W., 2006. Constraints on Pennsylvanian glacioeustatic sea-level changes using oxygen isotopes of conodont apatite. Geology 34, 277-280.

Kump, L.R., 2002. Reducing uncertainty about carbon dioxide as a climate driver. Nature 419, 188-190.

Limarino, C. O., Cesari, S. N., Net, L. I., Marenssi, S. A., Gutierrez, R. P., Tripaldi, A., 2002. The Upper Carboniferous postglacial transgression in the Paganzo and Rio Blanco Basins (northwestern Argentina); facies and stratigraphic significance. Journal of South American Earth Sciences 15, 445-460.

Lopes, R. C., 2004. Arquitetura Deposicional e Potencial de Armazenamento de Arenitos Associado às Jazidas de Carvão da Formação Rio Bonito na Região do Rio Jacuí, Rio Grande do Sul. (PhD dissertation). Universidade do Vale do Rio do Sinos, (257 pp.).

López-Gamundí, O. R., 1997. Glacial-postglacial transition in the Late Paleozoic basins of southern South America. In: Martini, I. P. (Ed.), Late glacial and postglacial environmental changes: Quaternary, Carboniferous-Permian, and Proterozoic. Oxford, U.K., Oxford University Press, pp. 147-168.

Maqueda, M.A.M., Willmott, A.J., Bamber, J.L., Darby, M.S., 1998. An investigation of the Small Ice Cap Instability in the Southern Hemisphere with a coupled atmosphere-sea ice-ocean terrestrial ice model. Climate Dynamics 14, 329-352.

Martin, J.R., Redfern, J., Aitken, J.F., 2008. A regional overview of the late Paleozoic glaciation in Oman. Geological Society of America Special Paper 441, 175-186.

Montañez, I., Soreghan, G. S., 2006. Earth's fickle climate; lessons learned from deep-time ice ages. Geotimes 51, 24-27.

Montañez, I. P., Norris, R. D., Algeo, T., Chandler, M. A., Johnson, K. R., Kennedy, M. J., Kent, D. V., Kiehl, J. T., Kump, L. R., Ravelo, A. C., Turekian, K. K., Freeman, K. H., Feary, D. A., Rogers, N. D., Estep, J. T., Gibbs, C. R., Edkin, E. J., 2011. Understanding Earth's deep past; lessons for our climate future, National Academies Press, Washington, DC, (194 pp.).

Montañez, I. P., Poulsen, C. J., 2013. The late Paleozoic ice age: an evolving paradigm. Annual Review of Earth & Planetary Sciences 41, 1-28.

Mory, A.J., Martin, J.R., Redfern, J., 2008. A review of Permian-Carboniferous glacial deposits in Western Australia. In: Fielding, C.R., Frank, T.D., Isbell, J.L. (Eds.), Resolving the late Paleozoic ice age in time and space. Geological Society of America Special Paper 441, pp. 29-40.

Mori, A. L. O., de Souza, P. A., Marques, J. C., Lopes, R. d. C., 2012. A new U–Pb zircon age dating and palynological data from a Lower Permian section of the southernmost Paraná Basin, Brazil: Biochronostratigraphical and geochronological implications for Gondwanan correlations. Gondwana Research 21, 654-669.

Poulsen, C.J., Pollard, D., Montañez, I.P., Rowley, D., 2007. Late Paleozoic tropical climate response to Gondwanan deglaciation. Geology 35, 771-774.

Raymond, A., Metz, C., 2004. Ice and Its Consequences: Glaciation in the Late Ordovician, Late Devonian, Pennsylvanian-Permian, and Cenozoic Compared. Journal of Geology 112, 655-670.

Rocha-Campos, A. C., dos Santos, P. R., Canuto, J. R., 2008. Late Paleozoic glacial deposits of Brazil: Paraná Basin. Geological Society of America Special Papers 441, 97-114.

Rosa, E.L.M., Vesely, F.F., França A.B., 2016. A review of the late Paleozoic ice-related erosional landforms in the Paraná Basin: origin and paleogeographical implications. Brazilian Journal of Geology 46, 147-166.

Ross, C.A., Ross, J.R.P., 1985. Late Paleozoic depositional sequences are synchronous and worldwide. Geology 13, 27-30.

Rygel, M.C., Fielding, C.R., Frank, T.D., Birgenheier, L.P., 2008. The magnitude of late Paleozoic glacioeustatic fluctuations: a synthesis. Journal of Sedimentary Research 78, 500-511.

Santos, P. R. d., Rocha-Campos, A. C., Canuto, J. R., 1996. Patterns of late Palaeozoic deglaciation in the Paraná Basin, Brazil. Palaeogeography, Palaeoclimatology, Palaeoecology 125, 165-184.

Scotese, C. R., Boucot, A. J., McKerrow, W. S., 1999. Gondwana palaeogeography and palaeoclimatology. Journal of African Earth Sciences 28, 99-114.

Singh, T., 1993. Gondwana sediments (Permian) of Arunachal Himalaya: stratigraphic status and depositional environment. In: Findlay, R.H., Unrug, R., Banks, M.R., Veevers, J.J. (Eds.), Gondwana Eight: Assembly, evolution and dispersal. Rotterdam, A.A. Balkema, pp. 333-343.

Soreghan, G.S., Giles, K.A., 1999. Amplitudes of late Pennsylvanian glacioeustasy. Geology 27, 255-258.

Starck, D., Papa, C., 2006. The northwestern Argentina Tarija Basin: stratigraphy, depositional systems, and controlling factors in a glaciated basin. Journal of South American Earth Sciences 22, 169-184.

Stollhofen, H., Werner, M., Stanistreet, I. G., Armstrong, R. A., 2008. Single-zircon U-Pb dating of Carboniferous-Permian tuffs, Namibia, and the intercontinental deglaciation cycle framework. Special Paper - Geological Society of America 441, 83-96.

Tedesco, J., Cagliari, J., Coitinho, J.D.R., da Cunha Lopes, R., Lavina, E.L.C., 2016. Late Paleozoic paleofjord in the southernmost Parana Basin (Brazil); geomorphology and sedimentary fill. Geomorphology 269, 203-214.

Tomazelli, L.J., Soliani Júnior, E., 1997. Sedimentary facies and depositional environments related to Gondwana glaciation in Batovi and Suspiro Regions, Rio Grande do Sul, Brazil. Journal of South American Earth Sciences 10, 295-303.

Torsvik, T. H., Cocks, L. R. M., 2013. Gondwana from top to base in space and time. Gondwana Research 24, 999-1030.

Trosdtorf, I., Rocha-Campos, A., Santos, P.R., Tomio, A., 2005. Origin of Late Paleozoic, multiple, glacially striated surfaces in northern Paraná Basin (Brazil): Some implications for the dynamics of the Paraná glacial lobe. Sedimentary Geology 181, 59-71.

Veevers, J. J., and Powell, C. M., 1987. Late Paleozoic glacial episodes in Gondwanaland reflected in transgressive-regressive depositional sequences in Euramerica. Geological Society of America Bulletin 98, 475-487.

Vesely, F.F., Assine, M.L., 2002. Superfícies estriadas em arenitos do Grupo Itararé produzidas por gelo flutuante, Sudeste do Estado do Paraná. Revista Brasileira de Geociências 32, 587-594.

Vesely, F. F., Rostirolla, S. P., Appi, C. J., Kraft, R. P., 2007. Late Paleozoic glacially related sandstone reservoirs in the Parana´ Basin, Brazil. American Association of Petroleum Geologists Bulletin 91, 151-160.

Vesely, F. F., Trzaskos, B., Kipper, F., Assine, M. L., Souza, P. A., 2015. Sedimentary record of a fluctuating ice margin from the Pennsylvanian of western Gondwana. Paraná Basin, southern Brazil. Sedimentary Geology 326, 45-63.

Visser, J.N.J., 1997. Deglaciation sequences in the Permo-Carboniferous Karoo and Kalahari basins of southern Africa: a tool in the analysis of cyclic glaciomarine basin fills. Sedimentology 44, 507-521.

Wanless, H.R., Shepard, F.P., 1936. Sea level and climatic changes related to late Paleozoic cycles. Geological Society of America Bulletin 47, 1177-1206.

Wopfner, H., Casshvap, S.M., 1997. Transition from freezing to subtropical climates in the Permo-Carboniferous of Afro-Arabia and India. In: Martini, I.P. (Ed.), Late glacial and postglacial environmental changes: Quaternary, Carboniferous-Permian, and Proterozoic. Oxford, U.K., Oxford University Press, pp. 192-212.

Ziegler, A.M., Hulver, M.L., Rowley, D.B., 1997. Permian world topography and climate. In: Martini, I.P. (Ed.), Late glacial and post-glacial environmental changes-Quaternary, Carboniferous-Permian and Proterozoic. Oxford University Press, New York, pp. 111-146.
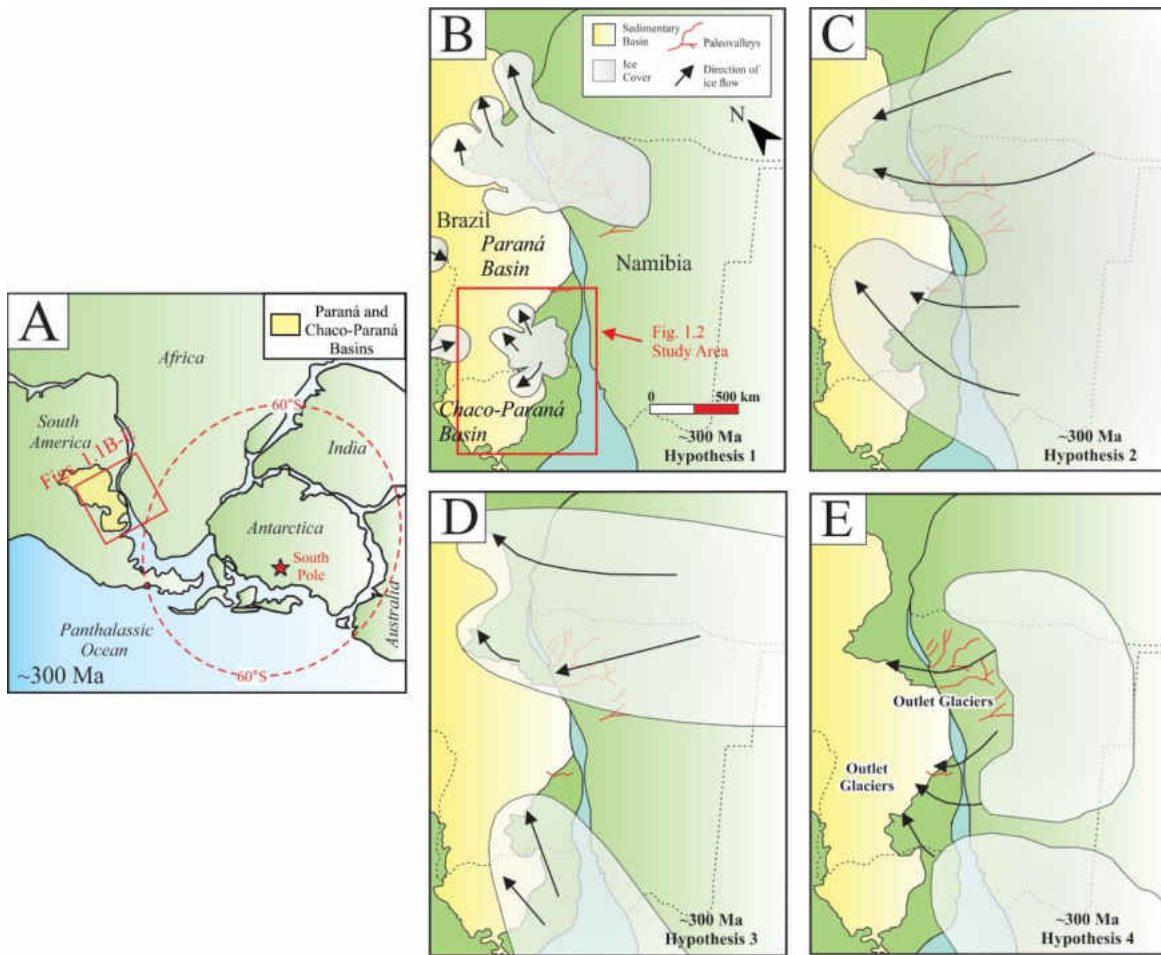
Fig. 1.1. Location of Paraná Basin and hypotheses for size and location of glaciers entering Paraná Basin during late Carboniferous. A. Location of Paraná Basin on Gondwana. B. Hypothesis 1: multiple small ice centers on paleotopographic highs around basin margins (after Rocha-Campos et al., 2008; Santos et al., 1996). C. Hypothesis 2: single massive ice sheet from Africa or Antarctica (after Gesicki et al., 2002). D. Hypothesis 3: two separate, unconfined lobes entering basin, one extending north from Uruguay and another extending west from Namibia (after Frakes and Crowell, 1972; Crowell and Frakes, 1975). E. Hypothesis 4: outlet glaciers entering southern and eastern margin of basin though paleovalleys originating in Africa (after Tedesco et al., 2016; Fallgatter and Paim, 2017).

13
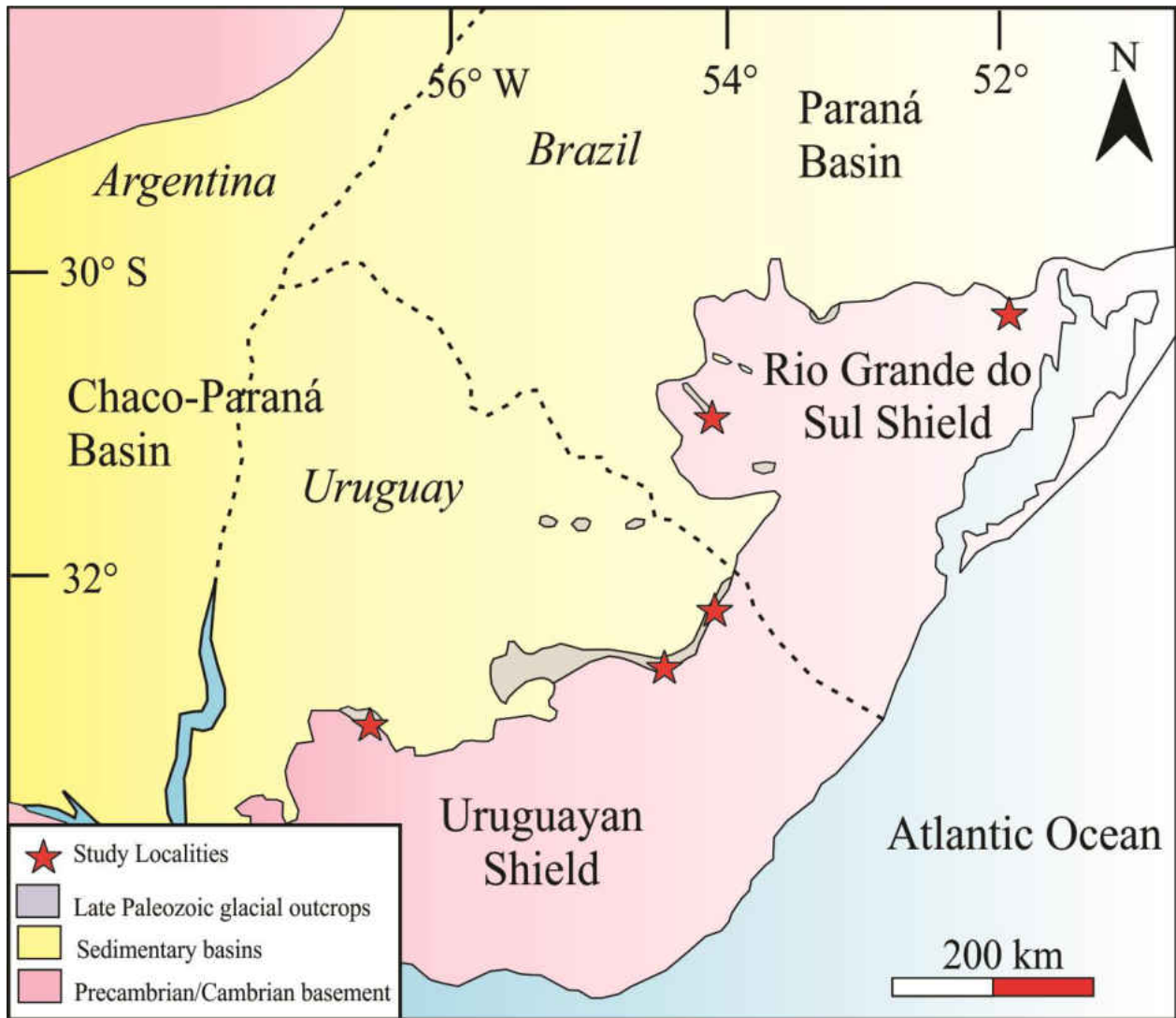
Fig. 1.2. Map of study area and late Paleozoic glacial outcrops (gray). Localities studied in this dissertation indicated by red stars. After Assine et al. (2018).

Chapter 2. Origin of paleovalleys on the Rio Grande do Sul Shield (Brazil): implications for the extent of late Paleozoic glaciation in west-central Gondwana

Abstract

The location, longevity, and geographic extent of late Paleozoic ice centers in west-central Gondwana remain ambiguous. Paleovalleys on the Rio Grande do Sul Shield of southernmost Brazil have previously been interpreted as fjords carved by outlet glaciers that originated in Africa and emptied into the Paraná Basin (Brazil). In this study, the sedimentology, stratigraphy, and provenance of sediments infilling two such paleovalleys (the Mariana Pimentel and Leão paleovalleys) were examined to test the hypothesis that an ice center over present day Namibia drained across southernmost Brazil during the Carboniferous and Permian. Contrary to previous findings, the facies assemblage from within the paleovalleys is inconsistent with a fjord setting and no clear evidence for glaciation was observed. The facies show a transition from a non-glacial lacustrine/estuarine environment to a fluvial-dominated setting, and finally to a restricted marine/estuarine environment. Detrital zircon results present a single population of Neoproterozoic ages (c. 800-550 Ma) from the paleovalley fill that matches the ages of underlying igneous and metamorphic basement (Dom Feliciano Belt) and is incongruent with African sources that contain abundant older (Mesoproterozoic, Paleoproterozoic, and Archean) zircons. Furthermore, results suggest that the formation of the paleovalleys and the deposition of their fill were controlled by the reactivation of Neoproterozoic basement structures during the Carboniferous and Permian. The lack of evidence for glaciation in these paleovalleys highlights the need for detailed studies of supposed late Paleozoic glacial deposits. These results support the hypothesis that well-established glacial sediments on the Rio Grande do Sul Shield (southern

15

margin of the Paraná Basin) may be the product of a separate lobe extending north across Uruguay, rather than a single, massive ice sheet draining west from Africa.

2.1. Introduction

Earth's deep-time climate alternates between long duration (100s of Myr) greenhouse/hothouse and shorter duration (10s Myr to 100 Myr) icehouse conditions. Of the three major Phanerozoic icehouse intervals, the Late Paleozoic Ice Age (LPIA), which extended for ~113 Myr from the Late Devonian (Famennian) until the Late Permian (Wuchiapingian), was the most spatially and temporally extensive (e.g. Isbell et al., 2003, 2012; Fielding et al., 2008b; Montañez and Poulsen, 2013; Frank et al., 2015). The study of this penultimate icehouse event is essential to understanding deep-time climate change and ice ages' influence on Earth systems (e.g. Gastaldo et al., 1996; Montañez and Soreghan, 2006; Horton et al., 2010; Montañez et al., 2011). An important aspect of determining the mechanistic relationship between ice extent and global climate is identifying the timing and extent of ice centers during glacial intervals. However, the nature of ice volume fluctuations during the LPIA in time and space remain enigmatic (Veevers and Powell, 1987; Ziegler et al., 1997; Isbell et al., 2003, 2012; Fielding et al., 2008a, 2008b; Rygel et al., 2008; Buggisch et al., 2011; Chen et al., 2013, 2016; Montañez and Poulsen, 2013; Frank et al., 2015). Recent studies of mid-to-high-latitude glaciogenic deposits suggest that the LPIA consisted of multiple ice centers and shorter (>10 Myr) glacial intervals separated by warm intervals of similar duration (e.g. López-Gamundí, 1997; Visser, 1997; Iannuzzi and Pfefferkorn, 2002; Isbell et al., 2003, 2012; Fielding et al., 2008a, 2008b; Gulbranson et al., 2010; Montañez and Poulsen, 2013). However, to fully understand the

16

complexity of the glaciation, each ice center and its associated depositional basin(s) needs to be thoroughly examined.

The Paraná Basin of southern Brazil, Uruguay, Paraguay, and northeastern Argentina contains a largely complete, mid-latitude (~45-55°S) record of LPIA glaciation (Fig. 2.1A) (e.g. Milani, 1998; Rocha Campos et al., 2008; Torsvik and Cocks, 2013; Vesely et al., 2015). Temperate ice sheets at such paleolatitudes would have been sensitive to climate variability, making this basin a key to reconstructing the stability of ice centers. In particular, the location, extent, dynamics, and timing of glaciation on the southernmost margin of the Paraná Basin remain poorly understood despite numerous studies of Carboniferous-Permian deposits in this region (e.g. Tomazelli and Soliani Júnior, 1982; Ribeiro et al., 1987; Tomazelli and Soliani Júnior, 1997; Holz, 1999; Holz, 2003; Guerra-Sommer et al., 2008a, 2008b, 2008c; Rocha-Campos et al., 2008; Tedesco et al., 2016). This area is underlain by an assemblage of mostly Neoproterozoic igneous and metamorphic terranes known as the Rio Grande do Sul Shield (RGS) (e.g. Gray et al., 2008; Oyhantçabal et al, 2011) that has been interpreted by some authors as the crustal root of a topographic high during the late Paleozoic (Fig. 2.1B) (e.g. Santos et al., 1996; Rocha-Campos et al., 2008). Diamictites, lonestone-bearing rhythmites, striated clasts, faceted clasts, and grooved surfaces have all been described from late Paleozoic units on the RGS, suggesting that at least part of this area was glaciated (e.g. Delaney, 1964; Corrêa da Silva, 1978; Tomazelli and Soliani Júnior, 1982; Santos et al., 1996; Tomazelli and Soliani Júnior, 1997).

There are competing hypotheses for the occurrence and extent of glaciation that influenced the southern portion of the Paraná Basin during the LPIA. These hypotheses range from alpine glaciation, ice caps (<5 x 10^4 km^2), small ice sheets (5 x 10^4 to 1 x 10^6 km^2), to

massive ice sheets (1×10^6 to 35×10^6 km^2) (Fig. 2.2). Such size variations represent vastly different ice volumes and imply that either ice was only locally present, centered locally on the RGS, centered in Africa, or extended to the Paraná Basin from Antarctica (e.g. Frakes and Crowell, 1972; Crowell and Frakes, 1975; Visser, 1993; Santos et al., 1996; Crowell, 1999; Rocha-Campos et al., 2008). How ice entered the basin (as alpine glaciers, outlet glaciers draining through paleovalleys, or as unconfined lobes) and its extent (confined to basin margins vs. extending across the basin) is also in dispute (Fig. 2.2) (e.g. Santos et al., 1996; Gesicki et al., 1998; Riccomini and Velázquez, 1999; Gesicki et al., 2002; Holz et al., 2008; Rocha-Campos et al., 2008; Tedesco et al., 2016; Fallgatter and Paim, 2017). Determining these details is fundamental to understanding the nature of glaciation in the Paraná Basin and its global impact during the LPIA.

The Mariana Pimentel and Leão paleovalleys (Fig. 2.1C), located on the NE of the RGS, are critical for resolving the volume of ice that entered the southern Paraná Basin (e.g. Paim et al., 1983; Visser, 1987; Lopes, 1995; Silveira, 2000; Iannuzzi et al., 2006; Guerra-Sommer et al., 2008b; Iannuzzi et al., 2010; Tedesco et al., 2016; Fallgatter and Paim, 2017). These two paleovalleys, often considered as a single paleovalley system, are interpreted by some authors as glacial fjords (e.g. Tedesco et al., 2016). These paleovalleys are also viewed by some as directly linked to glacial paleovalleys in the Windhoek Highlands that drained ice westward out of Namibia and into eastern South America (e.g. Martin, 1981; Tedesco et al., 2016; Fallgatter and Paim, 2017). Identification of the depositional history and sediment provenance of strata in these paleovalleys will help define the extent of glaciation in the Paraná Basin and test whether the Mariana Pimentel and Leão paleovalleys were fjords with either locally sourced glacial flow,

glacial flow originating from the Windhoek Highlands, or glacial flow from farther afield in Africa/Antarctica.

2.2. Geologic setting

The Paraná Basin is an intracratonic basin located in Brazil, Paraguay, Uruguay, and Argentina that formed following the Brasiliano orogeny (Late Proterozoic – early Paleozoic). Carboniferous and Permian lithostratigraphic units on the southern margin of the Paraná Basin and described from the paleovalleys are the Itararé Gp. and the Guatá Gp., (Fig. 2.3) (e.g. Holz, 1999, 2003). On the RGS, these units rest nonconformably on Precambrian basement.

The Itararé Gp. contains the glaciogenic sediments found throughout the Paraná Basin and is described in the subsurface throughout the Paraná Basin as consisting of three formations. These are (from oldest to youngest) the Lagoa Azul Fm., the Campo Mourão Fm., and the Taciba Fm. (e.g. França and Potter, 1991). However, only the youngest Taciba Fm. occurs in the southernmost part of the basin, which is the focus of this study (e.g. Holz et al., 2010). Palynological studies suggest that the Itararé Gp. was deposited during the Pennsylvanian and, in some areas, extends into the Early Permian (Cisuralian) (e.g. Souza, 2006). Numerous attempts to radiometrically date ash beds in the overlying Rio Bonito Fm. have produced a wide range of ages for the contact between the Itararé Gp. and the Rio Bonito Fm on the RGS (e.g. Matos et al., 2001; Guerra-Somner et al., 2008a, 2008b, 2008c; Mori et al., 2012; Simas et al., 2012; Cagliari et al., 2016). A recent re-analysis by Griffis et al. (2018) of several ash beds contained within coal seams (tonsteins) using chemical abrasion thermal ionizing mass spectrometry (CA-TIMS) U-Pb geochronology more precisely constrains the findings of Cagliari et al. (2016) that suggest

glaciation on the southernmost margin of the basin may have been entirely Carboniferous, with the earliest post-glacial coal beds occurring around the Gzhelian/Asselian boundary at ~298-297 Ma.

The Rio Bonito and the Palermo Fms. of the Guatá Gp. overlie the Itararé Gp. The Rio Bonito Fm. is interpreted to rest unconformably on the Itararé Gp strata in the southern part of the Paraná Basin (Fig. 2.3) (e.g. Holz et al., 2006) and is distinguished as being the fluvio-deltaic coal-forming interval. However, alluvial fan, fluvial, lagoonal, and deltaic sediments are all contained in the Rio Bonito Fm. In some areas, the Palermo Fm. conformably overlies and interfingers with the Rio Bonito Fm., representing the offshore transition/lower shoreface facies that are, in part, time-equivalent to the Rio Bonito Fm. (Fig. 2.3) (e.g. Holz, 2003; Holz et al., 2006). In other areas, an angular unconformity exists between the Rio Bonito and Palermo Fms., which has been used to suggest active tectonism on the RGS during the Early Permian (Holz et al., 2006). The Palermo Fm. consists of laminated and bioturbated sandstones, siltstones, and mudstones (Holz, 1999, 2003). Taken together, the Rio Bonito and the Palermo fms. are part of a 2nd order transgressive systems tract (Holz, 2003; Holz et al., 2006).

2.3. Location: Mariana Pimentel and Leão paleovalleys

The Mariana Pimentel Paleovalley is a narrow, trough-shaped (~0.5-6.5 km wide and >80 km long) feature cut into Neoproterozoic igneous and metamorphic basement of the Dom Feliciano Belt (Fig. 2.1C). The borders of the paleovalley have been noted to correspond closely with faults of the Neoproterozoic Dorsal do Canguçu Shear Zone (Fig. 2.1C) (e.g. Ribeiro, 1987; Guerra-Sommer et al., 2008b). The best-exposed outcrop (Location 1) from the Mariana

Pimentel Paleovalley is a ~50 m thick section located in an abandoned kaolinite quarry called Morro Do Papaléo, located ~7 km NW of the town of Mariana Pimentel (Fig. 2.1C). Location 2 is a ~8 m thick section from a roadside quarry that shows the base of the section and the contact with crystalline basement. It is located ~3 km northwest of Mariana Pimentel. A third outcrop used in this study (Location 3) is a road cut located ~45 km outside of the paleovalley (Fig. 2.1C). This ~7.5 m thick section shows the nonconformity between granite basement and the post-glacial Rio Bonito Fm.

The Mariana Pimentel Paleovalley is connected to a wider and shorter (~15 km wide and ~55 km in length) paleotopographic depression near Minas do Leão, which has been named the Leão Paleovalley (Fig. 2.1C). The Leão Paleovalley is only observed in the subsurface through core descriptions and geophysical logs that show basement relief (Lopes, 1995). This wider paleo-depression extends north into the Paraná Basin. Despite their description as two separate paleovalleys (e.g. Tedesco et al., 2016), some authors refer to them as the Leão-Mariana Pimentel Paleovalley (e.g. Ribeiro et al., 1987; Lopes, 1995) and suggest that they were part of the same ancient drainage system.

Tonsteins from the paleovalleys were originally thought to be coeval to tonstein-bearing coals located across the RGS that are stratigraphically near the base of the Rio Bonito Fm. (e.g. Guerra-Sommer et al., 2008c). However, two tonsteins within and just outside the paleovalleys (Fig. 2.1C) were found to have U-Pb ages of ~285 Ma (Faxinal location; Griffis et al., 2018) and ~289 Ma (Leão-Butia location; Simas et al., 2012), which are respectively 12 and 8 Myr younger than tonsteins from the base of the Rio Bonito (~297 Ma; Quitéria outcrop) (e.g. Griffis et al., 2018). This makes it clear that there are separate coal-forming intervals in the southernmost Paraná Basin. Coals from within the paleovalleys are younger than those located on

paleotopographic highs <10 km outside the paleovalleys (Quitéria outcrop; Fig. 2.1C). Notably, older coals, equivalent to the Quitéria outcrop, are not found within the paleovalley fill (e.g. Griffis et al., 2018).

2.4. Methods

2.4.1. Facies analysis

Stratigraphic sections were measured and outcrops were photographed in the field at Location 1 (Morro do Papaléo), Location 2, and Location 3 (outside of paleovalleys). Observations were made of grain size, lithology, sorting, sedimentary structures, paleocurrent orientations, nature of contacts, sediment body geometries, unit thicknesses, and relationships with adjacent strata. Additionally, 6 cores (LM-09, AB-06, RN-10, IB-94, CA-53, and LA-14) were measured, described, and photographed. Descriptions and measurements of cores AB-06, RN-10, and LM-09 were either supplemented or based on driller logs. Core RN-10 is from outside of the paleovalleys. Cores used in this study are housed at the Companhia de Pesquia de Recursos Minerais (CPRM) facility in Caçapava do Sul and on the campus of Universidade do Vale do Rio do Sinos (UNISINOS), located in São Leopoldo.

2.4.2. Detrital zircon U-Pb geochronology

Two detrital zircon samples were analyzed for this study. One sample (MDP6) was collected from a medium quartz sandstone, previously described as lowermost Rio Bonito Fm.

(e.g. Iannuzzi et al., 2006; Smaniotto et al., 2006) at the Location 1 outcrop. A second sample (MP) was collected at Location 2 from a medium pebbly quartz sandstone previously described as Itararé Gp. (e.g. Iannuzzi et al., 2006; Smaniotto et al., 2006). This sample was collected at the base of the section, ~0.5 m above granite basement. Sediment provenance was assessed using detrital zircon (U-Pb) geochronology to determine if there were local versus extra-basinal sources. Laser ablation inductively coupled plasma mass spectrometry (LA-ICP-MS) analyses were conducted at the University of California, Davis. Kernel density estimate plots were created on the *provenance* package for R and *DensityPlotter* with an adaptive bandwidth (Vermeesch, 2012; Vermeesch et al., 2016). Complete detrital zircon data and a detailed description of laser ablation methods can be found in Appendices A and B.

2.5. Results

2.5.1. Facies analysis and process interpretations

The sedimentary fill of the Mariana Pimentel and Leão paleovalleys can be divided into seven distinct facies which are observed in the cores and outcrops: a sandy conglomerate and breccia facies, a rhythmite facies, a mudrock/fine-grained sandstone facies, a cross-stratified sandstone facies, a diamictite facies, a root-trace-bearing mudrock facies, and a heterolithic bioturbated facies (Table 2.1). These facies are described here as occurring in either the lower, middle, and/or upper section of the paleovalley fill which are later correlated to facies associations. Classification of poorly sorted sediments is based on Hambrey and Glasser (2003). Facies codification is adapted from Benn and Evans (2010) and Farrell et al. (2012).

Sandy conglomerate and breccia facies (Gm/Gp)

The sandy conglomerate and breccia facies (Gm/Gp) consists of sandy conglomerate, breccia, pebbly sandstone, and diamictite beds that occur in the lower and middle portions of the paleovalley fill (Location 2; cores LA-14, CA-53, IB-94, RN-10, and LM-09). This facies often rests directly on igneous and metamorphic basement rocks where it contains a weathering profile that grades upward over 1-2 m from unweathered basement, to basement with chemically altered feldspar phenocrysts, to brecciated basement rocks, to completely disaggregated sandy diamictite or breccia, and ends in conglomerate composed entirely of basement rocks (Fig. 2.4A) (e.g. Location 2; cores LM-09, RN-10, IB-94, and LA-14). Elsewhere in the succession, this facies is 10 cm to 3 m thick and consists of massive (Gm) and planar cross-bedded (Gp) sandy conglomerate. Interbeds of clast-poor to clast-rich, massive and stratified, sandy diamictite, mudstone with root traces and coalified organic matter, and pebbly sandstone are also found in this facies. Clasts are angular to rounded and range from granule to cobble sized. Clasts are composed of granite, gneiss, k-feldspar, and quartz, which closely match the composition of the underlying basement rocks. No exotic clasts were found. The Gm/Gp facies is associated with the mudrock/fine-grained sandstone facies (Fl/Fm) and the rhythmite facies (Flv) in the lower portion of the paleovalley fill. It also occurs associated with the root-trace-bearing mudrock facies (Mrt), the diamictite facies (Dmm/Dms), and the cross-stratified sandstone (St/Sp) facies in the middle portion of the paleovalley fill.

The Gm/Gp facies is interpreted as humid alluvial fan and subaqueous fan delta deposits from both a marginal lacustrine/estuarine and alluvial environment. The clast composition,

angular grains, and weathering profile suggest in-situ weathering of basement with minimal

erosion and transport. The alternation between conglomerate and diamictite beds is consistent

with the surface of a fan that experienced both episodic, turbulent sheet and debris flows during

discharge events (e.g. Bull, 1977; Mack and Rasmussen, 1984; Nemec and Steel, 1984). The

mudstone interbeds with root traces and coalified material are paleosols associated with subaerial

exposure on the fan surface (e.g. Fielding, 1987; Ridgway and Decelles, 1993). The

interpretation of some beds within the Gm/Gp facies as subaqueous fan delta deposits is based on

the interfingering of rhythmite (Flv) or mudrock/fine-grained sandstone (Fl/Fm) beds. The

weathering profiles observed in both cores and in outcrop are indicative of igneous and

metamorphic basement that was exposed at the surface for a long enough period of time to

experience chemical weathering.

Rhythmite facies (Flv)

The rhythmite facies (Flv) occurs as laterally continuous packages up to 50 m thick

(Location 1 and 2; cores CA-53 and AB-06). This facies is located in the lower third of the

paleovalley fill and typically overlies either the conglomerate and breccia (Gm/Gp) facies or

igneous/metamorphic basement (Location 2) (Fig. 2.4B). The Flv facies is also associated with

the mudrock/fine-grained sandstone (Fl/Fm) facies (Fl/Fm). Rhythmites consist of stacked, sharp

to erosional-based (5 mm-10 cm thick) couplets composed of either fine-grained quartz

sandstone or siltstone bases that grade upwards into mudstone caps (Fig. 2.4C). The sandstone

portion of couplets contain climbing ripples (Fig. 2.5A), load and flame structures (Fig. 2.5B),

and rhythmite rip-up clasts (Fig. 2.5C). Extremely rare lonestones (granule and pebble-sized) of

K-feldspar and granite occur in this unit (only 2 pebbles were found in all of the strata examined) (Fig. 2.6A). In cores, discrete zones of brittle faulting (Fig. 2.5D) with calcite vein fill occur, as well as zones of intense ductile deformation with folded rhythmite beds (Fig. 2.6B). Rhythmite beds in core CA-53 also display sheared laminations and contain brecciated zones (Fig. 2.6C). Rhythmite couplets in core AB-06 are thickest near the base of the core and gradually thin upwards where they transition to a carbonaceous mudstone (Fl facies).

The Flv facies is interpreted as the product of dilute, surge-like turbidity currents and/or quasi-continuous hyperpycnal flows in a pro-deltaic lacustrine or estuarine environment. The erosive and sharp contacts between couplets, combined with variable and large couplet thicknesses implies that each couplet was deposited during an individual, surge-like flow rather than as a long-duration suspension settling event. Climbing ripples and rip-up clasts demonstrate that erosive, tractive, underflow currents deposited the lower part of the couplet while normal grading suggest that hydraulic sorting and settling from suspension occurred following dissipation of the current. Load and flame structures indicate that an insufficient amount of time had passed between flow events to allow for compaction and water loss of previously deposited couplets. The features discussed above are typical of either surge-like turbidity currents (e.g. Talling et al., 2012) or quasi-steady hyperpycnal flows produced by increased river discharge during episodic flooding events (e.g. Dadson et al., 2005; Girardclos et al., 2007; Crookshanks and Gilbert; 2008; Talling, 2014). Outsized clasts are often interpreted as iceberg rafted debris. However, such clasts can also occur as out runner clasts in sediment gravity flows, from vegetational rafting, rock falls off narrow valley walls, anchor ice, and/or due to sea/lake ice rafting (e.g. Ferguson, 1970; Postma et al., 1988; Woodborne et al., 1989; Gilbert, 1990; Dionne, 1993; Bennett et al., 1996; Doublet and Garcia, 2004; Garden et al., 2011; Kempema et al., 2001;

Kempema and Ettema, 2011; Carto and Eyles, 2012) Folded rhythmite beds are likely the product of synsedimentary slumping caused by either over-steepening of prograding depositional surfaces (e.g., delta front), over pressurization and fluid expulsion in rapidly deposited sediments, or active tectonism (e.g. Posamentier and Martinsen, 2011). However, discrete faulted zones with vein fill suggest that deformation also occurred following lithification.

Mudrock/fine-grained sandstone facies (Fl/Fm)

The mudrock/fine-grained sandstone facies (Fl/Fm) is ~3 cm to ~10 m thick (Locations 1 and 3; cores LA-14, CA-53, and AB-06) (Figs. 2.7A,B,C). It is laterally continuous across outcrops and consists of massive (Fm) to finely laminated (Fl) mudstone, siltstone, and very-fine to fine-grained quartz sandstone. The facies is bounded below by either a sharp or gradational contact. In core AB-06, the Fl/Fm facies consist of black carbonaceous mudstone. At Location 1 (Morro do Papaléo), terrestrial vegetation (ferns, lycophytes, glossopterid and cordaitalean plants) typical of the earliest Permian or latest Carboniferous occur in discrete siltstone beds along with the microplankton *Leiosphaeridia,* which is found in estuarine environments (Figs. 2.7B,C) (i.e. Guy-Ohlson, 1996; Iannuzzi et al., 2006; Smaniotto et al., 2006). This facies is found in the lower third of the paleovalley fill in association with the rhythmite facies (Flv) and the sandy conglomerate and breccia facies (Gm/Gp). Outside of the paleovalley (Location 3), it is observed overlying the diamicite (Dmm/Dms) and root-trace-bearing mudrock facies (Mrt).

This facies is interpreted as deposits of stable, low-energy conditions in a lacustrine or estuarine setting. The fine-grained sediments and laminations suggest that settling from suspension into a standing body of water was the dominant form of deposition. Furthermore, the

presence of well-preserved intact plant fossils, including some stems found in living position (Iannuzzi et al., 2006), and carbonaceous mudstones also implies a low energy environment near terrestrial vegetation. The presence of one estuarine microplankton element found at Location 1 may suggest a distal connection with a marine environment (i.e. Iannuzzi et al., 2006; Smaniotto et al., 2006).

Cross-stratified sandstone facies (St/Sp)

The cross-stratified sandstone facies (St/Sp) is the most common facies observed at Location 1 and is present in every core described (Fig. 2.8). This facies consists of stacked, erosional-based, lenticular sand bodies (up to 7 m thick and 15 m wide) that incise into each other as well as underlying mudstone, coal, and diamicitite beds (Fig. 2.8A). The sandstones contain scattered pebbles at the base of individual beds as well as medium to coarse-grained sets of trough (St) and planar cross stratification (Sp) (Figs. 2.8B,C). Interbeds of very-fine to fine-grained cross-laminated/asymmetric current rippled sandstone are present (Fig. 2.8D). Paleocurrent orientations (cross-stratification; n = 22) from two horizons at Location 1 return mean paleoflow directions of 290±12° and 223±10° (1σ). Stratigraphically, this facies is located in the middle section of the paleovalley fill and is associated with the root-trace-bearing mudrock facies (Mrt), the sandy conglomerate and breccia facies (Gm/Gp), and the diamictite facies (Dmm/Dms).

This facies is interpreted as channel bodies within a fluvial system based on the occurrence of cross-stratified beds with normal grading, beds with erosional bases, pebble lags, asymmetric current ripples, and the incised chanelform sand body geometries seen in outcrop.

Cross-stratified beds are diagnostic of bedload dominated flows and sand body geometries indicate channelization. Paleoflow orientations at Location 1 are indicative of transport towards the center and down the axis of the paleovalley. The close association with the root-trace-bearing mudrock facies (Mrt), which contains clay-rich paleosols, coal beds, and in-situ plant fossils, is evidence for a terrestrial environment. Stacked sand bodies that are floored by an unconformity and incise into each other occur in the basal portion of this facies. This suggests that the channels migrated in a setting with low accommodation space and may be part of a lowstand systems tract (e.g. Martinsen et al., 1999).

Diamictite facies (Dmm/Dms)

The diamictite facies (Dmm/Dms) beds are up to 3 m thick and consist of stacked, en echelon-like, lenses and wedge-shaped bodies composed of massive (Dmm) to crudely stratified (Dms), clast-poor to clast-rich, muddy, matrix-supported diamictite (Locations 1 and 3; Cores LA-14, RN-10, and AB-06). On outcrops, individual diamictite bodies have sharp to erosional bases. Dmm/Dms beds thin and pinch out over a few tens of meters and, at Location 3, the diamictite onlaps igneous basement rocks (Fig. 2.9). Clasts are angular to subangular and consist of quartz, feldspar, and highly weathered granite granules and pebbles. Meter-scale lenses of clast-supported conglomerate sometimes occur within the diamictites, as do thin coal lenses (Fig. 2.10A). Mudstones with root traces and coal beds (Mrt) frequently overlie the diamictite beds (Figs. 2.10B,C). Mudstone, siltstone, and coal rip-up clasts up to 30 cm in length are also common in the Dmm/Dms facies (Fig. 2.10D). The internal fabric, including the A axes of clasts, is sub-horizontal and parallel to bedding. Siltstone rafts with soft sediment deformation are also

observed in Dmm/Dms beds (Fig. 2.10E). This facies is located in the middle section of the paleovalley fill as well as outside the paleovalleys and occurs in association with the cross-stratified sandstone facies (Sp/St), the sandy conglomerate and breccia facies (Gm/Gp), and the root-trace-bearing mudrock facies (Mrt).

The Dmm/Dms facies is interpreted as high density debris flows deposited on alluvial fans and fan deltas. This determination is based on the occurrence of stratified and bedded diamictites, coal and siltstone rip-up clasts, soft-sediment deformation, the internal bedding-parallel fabric, and erosive or sharp lower contacts. Matrix-supported beds with a strong bedding-parallel fabric suggest that a high density fluid is responsible for sediment transport (e.g. Enos, 1977). Stacked, en echelon beds observed in the Dms facies at Location 3 support successive high density flows or surges that piled into and overrode previous flows or surges. The isolated lenses of clast-support with normal grading are zones of low viscosity fluidized flow within the overall high viscosity debris flow. Thin coal lenses, coal rip-up clasts, the association with root-trace-bearing mudrock facies, and root traces that occur on the top of diamictite beds is evidence for deposition in a humid subaerial environment.

Root-trace-bearing mudrock facies (Mrt)

The root-trace-bearing mudrock facies (Mrt) (Location 1 and 3; all cores) consists of laterally continuous, 5 cm to 5 m thick, root-trace-bearing, massive or (less commonly) laminated mudstone and siltstone beds (Figs. 2.10C and 2.11A, B). This facies also contains poorly-developed, low-grade coal beds up to 2 meters thick with intercalated mudstone and siltstone laminations (Fig. 2.10C). Rocks of this facies rest on sharp or gradational lower

contacts and are occasionally cut by overlying diamictite beds or channel-form, cross-stratified sandstone bodies. Clay-lined root traces, mud cracks, intact and disaggregated plant remains, slickensides, and wedge shaped peds, are all common throughout this facies (Fig. 2.11A, B). Mudrock in this facies occurs in the middle section of the paleovalley fill in association with the cross-stratified sandstone facies (St/Sp), the sandy conglomerate and breccia facies (Gm/Gp), and the diamictite facies (Dmm/Dms).

This facies is interpreted as overbank floodplain deposits from within a fluvial-dominated valley and incipient paleosols that formed on top of fan deltas. The association with erosional sand bodies from the cross-stratified sandstone (St/Sp) facies suggests proximity to fluvial channels that experienced base level fluctuations. Furthermore, the wedge-shaped peds, mud cracks, slickensides, and clay-lined root traces are typical of vertisols that formed on crevasse splays/floodplain sediments and experienced shrinking and swelling from episodic wetting and drying (e.g. Gustavson, 1991). Massive mudstone and siltstone beds were likely deposited during flooding and were subsequently bioturbated by vegetation, giving them a homogenous appearance. Coal beds and fossil plant fragments also indicate of a flooded, anoxic terrestrial setting such as a floodplain that allowed for intervals of peat accumulation. The discontinuous and poorly developed nature of the coals, along with the presence of clastic laminations and interbeds, are consistent with coals that formed over relatively short intervals of time due to repeated flooding.

Heterolithic bioturbated facies (mSb)

31

Heterolithic bioturbated facies (mSb) packages are up to 20 m thick and consist of laterally continuous beds (<3 m thick) of mudstone, siltstone, and very-fine to medium-grained quartz sandstone (Cores LA-14, IB-94, and RN-10). Beds typically display bioturbation levels from 2-3 on the Droser and Bottjer (1986) ichnofabric index. The beds have sharp or gradational lower contacts and sharp or gradational upper contacts. Beds contain both horizontal and vertical traces of *Gyrolithes* and *Teichichnus. Teichichnus* traces are retrusive with concave-up spreite (Fig. 2.11D). The facies also contains medium-grained, micro-hummocky cross-stratified sandstone, rhythmites with alternating fine-grained sandstone and crinkled or wavy carbonaceous muddy laminae (Fig. 2.11C), and discrete mudstone beds containing coalified organic debris and disaggregated fossil plant fragments. Sulfur occurs in beds throughout this facies. Deposits of the mSb facies occur in the upper third of the paleovalley fill.

This facies represents restricted marine or estuarine deposits that accumulated above storm wave base with episodic influxes of coarse-grained sediment and plant/organic matter. The occurrence of sulfur-rich beds with *Teichichnus* and *Gyrolithes* suggest a restricted, marine influenced depositional environment. Discrete beds containing abundant plant fragments, micro-hummocky cross-stratification, and alternating mud and sand laminae are evidence for episodic high energy storm beds or possible tidal influence within an overall low-energy environment. *Teichichnus* traces with retrusive spreite also suggest that organisms moved upward through the substrate to adjust to an episodic influx of coarser sediment.

2.5.2. Stratigraphy

A longitudinal section of the paleovalley system was created using a combination of core and outcrop measurements (Fig. 2.12). The lowermost coal bed in each core or outcrop was used as a datum since these are interpreted to indicate an increase in accommodation (clastic starved conditions) following the development of a regional unconformity (e.g. SB-3; Holz, 2003; Holz et al., 2006; changed to SB-4 in Holz et al., 2010). Individual facies show a high degree of vertical and horizontal variability within the paleovalleys and cannot be traced across the entire length of the longitudinal profile. Furthermore, abrupt changes in basement relief and sediment thickness are indicated from the core data and supported by resistivity measurements collected by Tedesco et al. (2016). These sharp variations in basement topography correspond closely to the location of faults mapped by the Brazilian Geologic Survey (CPRM) (Fig. 2.12). The sandy conglomerate and breccia facies, rhythmite facies, and mudrock/fine-grained sandstone facies occur in the lower portion of the paleovalley system fill within the paleotopographic lows (Fig. 2.12). The cross-stratified sandstone facies, sandy conglomerate and breccia facies, diamictite facies, and root-trace-bearing mudrock facies coexist in the middle section of the paleovalley system fill and are thicker to the southeast, away from the Paraná Basin (Fig. 2.12). The heterolithic bioturbated facies occurs in the upper portion of the fill and is thickest in the northwestern portion of the Leão Paleovalley near the margin of the Paraná Basin and thins towards the southeast (Fig. 2.12).

2.5.3. Detrital zircon (U-Pb) geochronology results

Detrital zircon samples were collected from a medium, pebbly, quartz-rich sandstone bed (Gm/Gp facies) ~0.5 m above basement in the basal section of the paleovalley fill (sample MP,

Location 2) and a medium, quartz-rich sandstone bed (St/Sp facies) in the middle section of the paleovalley fill (sample MDP6, Location 1) (Fig. 2.13). Sample MP was from a unit previously interpreted as the Itararé Gp., and sample MDP6 was from a unit previously interpreted as the Rio Bonito Fm. (e.g. Iannuzzi et al., 2006; Smaniotto et al., 2006; Tedesco et al., 2016). Both samples were found to contain a single (unimodal) population of Neoproterozoic grains (c. 800-550 Ma) (Fig. 2.14). U-Pb data for these samples can be found in Appendix B. Kernel density estimate (KDE) plots show strongly overlapping peaks at ~595 Ma (MDP6) and ~605 Ma (MP) (Fig. 2.14). A comparison of the two samples using a Komogorov-Smirnoff (K-S) test yielded a P-value of 0.191, indicating that there is a >95% probability zircon populations from the two samples are not significantly different (i.e. P-value > 0.05).

2.6. Discussion

Three distinct facies associations were observed that correspond to the lower, middle, and upper section of the paleovalley fill. These are a lacustrine/estuarine facies association in the basal portion of the paleovalleys, a fluvial-dominated facies association in the middle section, and a restricted marine/estuarine facies association in the upper portion. None of these contained any evidence of glacially-influenced deposition. Additionally, detrital zircon geochronology results demonstrate that the Mariana Pimentel and Leão Paleovalleys were internally drained and do not contain extra-basinal sediments that were derived from an ice center over Africa.

2.6.1. Lacustrine/estuarine facies association

The bottom portion of the paleovalley fill is significant to this study because it has been previously interpreted as the glaciogenic Itararé Gp. based on the presence of rhythmites and poorly sorted sediments. This implies that the sediments were deposited in a temperate, glacial fjord (e.g. Iannuzzi et al., 2006; Tedesco et al., 2016). However, these sediments are interpreted here as having been deposited in several isolated, non-glacial lacustrine basins or a single estuarine system with internal sub-basins connected to the Paraná Basin (Fig. 2.15A). This corresponds to a facies association of the sandy conglomerate and breccia facies (Gm/Gp), the mudrock/fine-grained sandstone facies (Fl/Fm), and the rhythmite facies (Flv). These sediments would be temporally equivalent to the Triunfo and Paraguaçu Mbrs., which are defined as the basal-to-middle portion of the Rio Bonito Fm. (Fig. 2.3).

The Gm/Gp facies is consistent with alternating sheet flow and mass transport from an alluvial fan/fan delta system on the steep margins of a lacustrine/estuarine basin. The in-situ weathering of crystalline basement, which grades into conglomerate and breccia, combined with the immature sediment composition, angular (non-striated) clasts, and poor sorting, suggest that sediment was shed directly off the subaerially exposed paleovalley walls and was not glacially transported. The cross section indicates that the alluvial fan sediments are thickest near or on top of fault-bounded, raised basement blocks (Fig. 2.12). The weathering profile in the Gm/Gp facies implies that bedrock was exposed to chemical weathering for an extended duration of time. This is not what would be expected in a fjord environment where glacial erosion would rapidly remove weathered bedrock, producing a scoured bedrock surface beneath sediment fill (e.g. Syvitski et al., 1987). Furthermore, interbeds from these alluvial fan sediments, which contain root traces and coalified organic matter, imply that the alluvial fans/fan deltas existed in a humid, vegetated setting rather than in a glacially influenced fjord.

Rhythmites (Flv facies) and fine-grained, laminated rocks (Fl/Fm facies) are found within fault-bounded, sub-basins (high accommodation zones; Fig. 2.12) that may have started as separate, small lacustrine basins. The mixture of terrestrial flora and rare estuarine microplankton elements described by Iannuzzi et al. (2006) and Smaniotto et al. (2006) from fine-grained rocks near the top of the lacustrine/estuarine facies association (base of Location 1) indicate a possible marine inundation of these basins. This is likely due to the transgression of the "Paraguaçu Sea" (Fig. 2.3). Although a transition from a lacustrine to estuarine setting is hypothesized, there is no marker bed or facies change that clearly marks this change across the paleovalley(s). However, in core AB-06, there is gradual shift from thick rhythmites (Flv facies) to thinner rhythmites and carbonaceous mudstone of Fl facies. This may represent a gradual progression from more proximal to distal hyperpycnal flows associated with a marine transgression.

The Flv facies is interpreted as turbidites or hyperpycnites in which flows were triggered by floods, failure along a prograding delta front, or sediment shed during intermittent tectonic activity. In tidewater fjords, buoyant meltwater typically forms an overflow plume as it rises to the surface over denser saltwater (e.g. Cowan and Powell, 1990; Powell, 1990; Mugford and Dowdeswell, 2011). The rhythmites observed in the Mariana Pimentel and Leão Paleovalleys appear to be the product of underflows rather than rain-out from overflow plumes. Although hyperpycnal flows and turbidites are also important depositional processes in fjords due to the high sedimentation rates and steep slopes (e.g. Syvitski et al., 1987; Ó Cofaigh and Dowdeswell, 2001; Powell, 2003), they also occur in almost any depositional environment where a riverine-introduced, dense sediment-water admixture is transported as underflows down a slope and, therefore, are not diagnostic of glacial meltwater sedimentation (e.g. Zavala and Arcuri, 2016). This highlights the important distinction that not all rhythmites in the Paraná Basin are

glaciogenic, and some may be temporally equivalent to the post-glacial Rio Bonito Fm. In general, rhythmic sediments across the Paraná Basin could be the product of annual or seasonal lake processes (i.e. true varves), surge-like turbidites, or tidal activity among other cyclical processes (e.g. Ó Cofaigh and Dowdeswell, 2001; Zolitschka et al., 2015; Schimmelmann et al., 2016; Zavala and Arcuri, 2016).

Another line of evidence that was previously used to support a glaciogenic interpretation of the Mariana Pimentel and Leão Paleovalleys is the presence of rare dropstones contained within the rhythmite facies. However, as discussed earlier, dropstones commonly occur in non-glacial environments due to processes such as rock falls off of narrow valley walls, or rafting by lake ice, vegetation, or riverine/lacustrine anchor ice (e.g. Ferguson, 1970; Woodborne et al., 1989; Gilbert, 1990; Dionne, 1993; Bennett et al., 1996; Kempema et al., 2001; Doublet and Garcia, 2004; Garden et al., 2011; Kempema and Ettema, 2011). Thus, the presence of exceedingly rare (only 2 observed in >800 m of core, none in outcrop) and isolated dropstones is not in and of itself indicative of a glacially-influenced environment. The outsized clasts observed in this study have lithologies consistent with the underlying basement. Furthermore, there are no associated clast clusters (iceberg dump structures), diamictite pellets, or ice-keel marks, which are commonly found in the ice rain-out facies of temperate fjords (e.g. Dowdeswell et al., 1993; Powell, 2003). Granule and pebble sized clasts that occur along discrete bedding planes and associated with other coarse sediment are interpreted here as small debris flows rather than as dropstones (e.g. Postma et al., 1988).

Finally, when tidewater glaciers retreat from a fjord they tend to calve rapidly across deep sub-basins and stabilize on shallow and narrow "pinning points", often located on bedrock sills (e.g. Molnia, 1983; Syvitski et al., 1987; Cowan et al., 2010). Here, the rate of calving is

reduced and they are able to maintain temporary ice-balance equilibrium. The sills and proximal

parts of adjacent basins typically have evidence of subglacial abrasion, trapped icebergs (keel

marks), morainal bank build-up, and grounding line fan sedimentation (e.g. Syvitski et al., 1987;

Cowan et al., 2010; Ottensen and Dowdeswell, 2009). Sediments deposited in the deep sub-

basins, located in front of the sills, will show abundant evidence of ice-rafted debris, turbidity

currents, and plume rain-out (e.g. Syvitski et al., 1987; Powell, 2003). Contradicting this model,

cores (LM-09, IB-94, LA-14) located on bedrock highs within the Mariana Pimentel and Leão

Paleovalleys show a weathering profile in igneous and metamorphic basement that grades into

the sandy conglomerate and breccia facies (humid alluvial fan deposits) and root-trace-bearing

mudrock facies (coal-bearing floodplain deposits). No grooves or striations were observed on

basement surfaces and no striated, faceted, or exotic clasts were observed as would be expected

in ice proximal basins. As previously described, cores from within the deep sub-basins (AB-06,

CA-53) do not show any evidence of plume rain-out (overflows) or abundant ice-rafted debris, as

would be expected <10 km in front of pinning points (e.g. Powell, 2003).

2.6.2. Fluvial-dominated facies association

The middle portion of the paleovalley fill is interpreted here as lowstand fluvial-

dominated sediments of the Rio Bonito Fm. (equivalent to the Sideropolis Mbr.) (Figs. 2.3 and

2.15B). Tonsteins from this facies association are used to place the paleovalley system within a

broader stratigraphic context. The fluvial-dominated facies association contains the cross-

stratified sandstone facies (St/Sp), the sandy conglomerate and breccia facies (Gm/Gp), the

diamictite facies (Dmm/Dms), and the root-trace-bearing mudrock facies (Mrt). The St/Sp facies

is interpreted as fluvial channels and the Mrt facies represents overbank floodplain and peat deposits. The poorly-developed, discontinuous nature of the coal seams in the Mariana Pimentel paleovalley is consistent with episodic flooding along a lowstand fluvial system rather than a more prolonged interval of standing water. The Dmm/Dms facies has the characteristics of muddy debris flows that are derived from the valley slopes. The fact that the Dmm/Dms facies also occurs at Location 3, outside of the paleovalleys where it onlaps granite basement, suggests paleotopographic relief outside of the paleovalleys as well.

A drop in base level within the lacustrine/estuarine system, occurring at the base of the St/Sp facies, allowed the fluvial-dominated facies association to extend out into the Paraná Basin. We correlate this drop in base level in the study area to SB-3 (Fig. 2.3; e.g. Holz, 1999, 2003; Holz et al., 2006) rather than SB-2 (contact between Itararé Gp. and Rio Bonito Fm.) because tonsteins within the paleovalleys have been radiometrically dated by Simas et al. (2012) and Griffis et al. (2018) to ~8 and 12 Myr younger than the coals from the base of the Rio Bonito Fm. (located outside of the paleovalleys) and because there is no evidence for glaciation within the basal fill of the paleovalleys. It should be noted that Holz et al. (2006) related SB-3 to tectonism on other areas of the RGS. The fact that younger coals exist within the paleovalleys below the paleotopographic level of older coals (such as those at Quitéria; Fig 2.1C) located outside of the paleovalley supports the interpretation that base level fell, and incision occurred after the older coals were deposited.

2.6.3. Restricted marine/estuarine facies association

The top portion of the paleovalley fill is interpreted as a restricted marine/estuarine environment (Fig. 2.15C). It is comprised of the heterolithic bioturbated facies (mSb). This facies association is thickest near the northwestern (basinward) portion of the Leão Paleovalley and pinches out near the connection with the Mariana Pimentel Paleovalley. This bioturbated facies association represents a marine transgression of the "Palermo Sea" (Fig. 2.3) into the Leão Paleovalley. The mSb facies has the characteristics of a low-energy restricted marine or estuarine environment in which sediment settled from suspension. This setting experienced episodic input of coarse sediment from either tidal action or storms. Coals seams located near the connection of the Mariana Pimentel and the Leão Paleovalley contain sulfur, suggesting an interaction between the fluvial-dominated setting and the estuarine environment in this location.

2.6.4. Detrital zircon geochronology

The unimodal zircon population ranging from c. 800-550 Ma in both the basal lacustrine/estuarine facies association and the overlying fluvial-dominated facies association suggests that the sediment source area remained unchanged throughout deposition within the paleovalleys. This age range is consistent with magmatic events that occurred during the Neoproterozoic Pan-African/Brasiliano tectonic cycle. In particular, the ages are nearly identical to the igneous and metamorphic basement of the Pelotas Batholith (part of the Dom Feliciano Belt; ~820-580 Ma) that the paleovalleys directly overlie, indicating a local source (e.g. Babinski et al., 1997; Silva et al., 1999; Cordani et al., 2000; Leite et al., 2000; Gastal et al., 2005; Philipp and Machado, 2005; Saalmann et al., 2011). Possible igneous and metamorphic sources from the underlying Pelotas Batholith include: the Capão do Leão Granite, the Encruzilhada do Sul

Intrusive Suite, the Arroio Moinho Granite, the Pinheiro Machado Suite, the Cordilheira Metagranite, the Quitéria Metagranite, and the Piratini gneiss (e.g. Gastal et al., 2005). All of these sources have ages that closely overlap the zircon populations identified from the paleovalley fill (e.g. Silva et al., 1999; Gastal et al., 2005).

These results can be contrasted to detrital zircon samples analyzed by Foster et al. (2015) from Neoproterozoic sedimentary and metasedimentary rocks across the Damara Belt in central Namibia (Fig. 2.14). The Damara Belt is interpreted to have been adjacent to the RGS during the Carboniferous and Permian so that any glaciers emanating out of Africa would have drained across this area (Fig. 2.1B) (e.g. de Wit et al., 2008). Conspicuously absent in the detrital zircon samples from the paleovalleys is the presence of late Mesoproterozoic to early Neoproterozoic (~1200-900 Ma) ages that are prevalent in all of the Damara Belt samples (Fig. 2.14) (Foster et al., 2015). There is no source of equivalent Mesoproterozoic to early Neoproterozoic grains in southern Brazil, making this age range a useful indicator of African provenance. Paleoproterozoic and Neo-Archean ages are also present in Damara Belt samples but absent from the paleovalleys (Foster et al., 2015). Furthermore, Itararé Gp. and Rio Bonito Fm. detrital zircon samples collected on the eastern margin of the Paraná Basin show strong Mesoproterozoic, Paleoproterozoic, and Neo-Archean peaks that have been interpreted to represent African sources (Fig. 2.14) (e.g. Canile et al., 2016). This demonstrates that, unlike the eastern margin of the Paraná Basin, the paleovalleys examined here on the RGS were internally drained with no direct connection to Africa. Hypothetically, even if glacial sediments were deposited in this region and were subsequently eroded and resedimented during post-glacial times, we would still expect African zircons to be present in the fluvial sandstones but they were not detected.

2.6.5. Origin of the Mariana Pimentel and Leão paleovalleys

Multiple lines of evidence support the interpretation that the Mariana Pimentel and Leão Paleovalley system was formed by the reactivation of older basement structures during the Carboniferous and early Permian. This includes: (1) abrupt changes in sediment thickness, vertical and lateral facies changes, as well as the discontinuous nature of individual facies within the paleovalleys that correspond closely to the location of mapped faults (Fig. 2.12), (2) the position of the paleovalleys within a bend and offset in the major NE-SW trending Neoproterozoic Dorsal do Canguçu Shear Zone (Fig. 2.1C) (e.g. Fernandes and Koester, 1999; Philipp and Machado 2005; Passarelli et al., 2011), (3) discrete zones of faulting and slumping within rhythmites and fine-grained sediments from the basal portion of the paleovalleys (Figs.2. 5 and 2.6), (4) coarse-grained, immature sediments such as conglomerates, breccias, and diamictites with coal clasts (alluvial fan sediments) that onlap basement and are thickest near mapped faults (Fig. 2.12), (5) the drop in base level between the basal lacustrine/estuarine facies association and the overlying fluvial-dominated facies association, corresponding to a tectonically-related regional sequence boundary (Fig. 2.3; SB-3) (Holz et al., 2006) to which an angular unconformity on some areas of the RGS is associated, and finally (6), apatite fission track analysis of the Pelotas Batholith conducted by Oliveira et al. (2016) is suggestive of basement uplift and reactivation of faults on the NE part of the RGS during the Permian.

The reactivation of faults across the Paraná Basin, including the RGS, during the Carboniferous and Permian has been described by multiple authors and attributed by some to accretion on the southern margin of Gondwana (Gondwanides or San Rafael Orogeny) (e.g. Holz et al., 2006; Trzaskos et al., 2006; Kleiman and Japas; 2009; Oliveira et al., 2016). Furthermore,

the correlation between the Mariana Pimentel and Leão Paleovalleys and basement structures has been discussed in previous studies. Holz (2003) and Tedesco et al. (2016) both noted that the borders of the paleovalleys correspond closely to known faults. Ribeiro (1987) and Guerra-Sommer et al. (2008b) indicate that the thickest coal deposits in the paleovalleys occur within downthrown basement blocks controlled by a NE trending fault system.

The position of the Mariana Pimentel Paleovalley within the DCSZ and the facies assemblage of the paleovalley are both consistent with the evolution of a small tectonically controlled basin or basins. The thickest sedimentary fill within the paleovalley (core AB-06) corresponds to a major bend and offset in the master faults of the DCSZ (Fig. 2.12). Releasing bends in such systems form a zone of separation between parallel strike-slip master faults, which can nucleate small pull-apart basins. Such basins are common along reactivated older faults in rigid intracratonic settings. Basin fill is often comprised of lacustrine facies and pro-deltaic facies that form on down-dropped grabens (towards the fault with the most slip) and alluvial fan/fan delta sedimentation on basin margins (e.g. Hempton and Dunne, 1984; Waldron, 2003; Sarp, 2015). Rhythmic, underflow sediments of non-glacial origin are common within these basins (e.g. van der Lingen and Pettinga, 1980; Hempton and Dunne, 1984). It is common for separate lacustrine sub-basins to evolve into a fluvial valley (e.g. Hempton and Dunne, 1984; Waldron, 2004; Kwon et al., 2011). There are also examples of these features being inundated by marine waters, creating estuaries (e.g. Ysufoğflu, 2013). A tectonic origin for the Mariana Pimentel and Leão paleovalley system during the Carboniferous and early Permian, would explain why the coal seams within the paleovalleys are younger than transgressive coals found across the RGS uplands (e.g. Griffis et al., 2018).

The unusually wide shape and shallow depth of the Mariana Pimentel paleovalley was characterized in detail by Tedesco et al. (2016). It was interpreted as an eroded (truncated) U-shape, which is more characteristic of a glacially carved valley, rather than a V-shaped fluvial valley. However, modern fluvial systems often flow down the axes of pull-apart basins such as the Anatolian Fault system in Turkey, and these basins often have depth/width ratios similar to glacially carved valleys (e.g. Hempton and Dunne, 1984; Gürbüz, 2010). Furthermore, the dimensions of the Mariana Pimentel Paleovalley do not correspond well with the Namibian paleovalleys (e.g. Martin, 1981) to which they are supposedly related. The Namibian paleovalleys, which contain glacial features, range in width from ~7-13 km as compared to the Mariana Pimentel Paleovalley that range from ~0.5-6.5 km wide.

2.6.6. Implications for the extent of glaciation in west-central Gondwana

A non-glacial interpretation of the paleovalleys and the lack of African-sourced zircons contradict the hypothesis that outlet glaciers flowed directly onto the RGS from the Windhoek Highlands (Namibia) through a series of glacially-carved fjords (Fig. 2.2D). Additionally, the lack of African provenance for sediments on the RGS, combined with previously described grooved surfaces on the western RGS showing ice flow towards the N-NW (i.e. Tomazelli and Soliani Júnior, 1982; Tomazelli and Soliani Júnior, 1997), do not support the hypothesis that large, unconfined lobes from Africa or Antarctica extended E to W across the RGS (Fig. 2.2B).

Importantly, this study does not negate the clear evidence for glaciation on the western RGS (e.g. Tomazelli and Soliani Júnior, 1982; Tomazelli and Soliani Júnior, 1997). Additionally, it does not contradict the hypothesis that outlet glaciers from Africa may have

flowed through bedrock lows onto the eastern margin of the basin (e.g. Fallgatter and Paim, 2017). Rather, combined with ice flow directions from other studies (i.e. Tomazelli and Soliani Júnior, 1982; Tomazelli and Soliani Júnior, 1997; Amato, 2017), these results are in agreement with the hypothesis proposed by Crowell and Frakes (1975) that a separate, unconfined ice lobe extended N-NW out of Uruguay across the western RGS (Fig. 2.2C). This "Uruguayan Lobe" may have originated in southern Africa, or it may have nucleated on the Rio de la Plata Craton (Uruguay and Argentina). Although an ice advance out of Uruguay may have predated the formation of the paleovalleys on the eastern half of the RGS, evidence for such an event is currently unsubstantiated.

The other possibility, that glaciation on the RGS existed as stand-alone, small ice caps or alpine glaciers (e.g. Santos et al., 1996) can also not be ruled out based on the evidence presented here (Fig. 2.2A). Regardless, it seems probable that glaciogenic sediments on the RGS have a separate provenance from the same lithostratigraphic unit (Taciba Fm.) on the eastern margin of the Paraná Basin. Along these same lines, the lack of an African detrital zircon signature within the paleovalleys makes it more difficult to link glaciation on the RGS (southernmost Paraná Basin) to extra-basinal deposits such as the Dwyka Gp. in the Greater Karoo Basin.

Separate ice centers on the southern and eastern margins of the Paraná Basin would have contained substantially less ice volume compared to a single, massive ice sheet. For comparison, a massive hypothetical ice sheet covering the entire RGS and the eastern margin of the basin, centered over western Africa, and measuring ~1,250,000 km^2 would be capable of producing ~4.6 m of global sea-level change. Two separate ice centers, of equal combined area, would produce ~3.9 m of global sea-level change (c.f. Crowley and Baum, 1991; Isbell et al., 2003). However, neither scenario would add significantly to some estimates of ~100-120 m of sea-level

fluctuations during the Carboniferous and Permian (e.g. Rygel et al., 2008; Chen et al., 2016). If sea-level oscillations of such magnitudes occurred, contemporaneous with deposition in the Mariana Pimentel and Leão paleovalleys, the required ice center(s) must have existed elsewhere.

2.7. Conclusions

(1) The facies assemblage from the Mariana Pimentel and Leão Paleovalley system does not support the previously hypothesized origin as a glacially-influenced depositional environment. The basal portion of the paleovalleys contains a transition from a non-glacial lacustrine or estuarine environment into a fluvial-dominated incised valley. The top portion of the paleovalley system fill consists of a restricted marine/estuarine facies association.

(2) Detrital zircon geochronology results show a unimodal population of ages ranging from ~800-550 Ma. This is consistent with a local (non-African), Dom Feliciano Belt provenance for the sedimentary fill of the paleovalleys.

(3) The facies assemblage, stratigraphy, and position of the paleovalleys within a Neoproterozoic shear zone suggest a tectonic control on the initial formation of the paleovalleys and the deposition of their fill. The Mariana Pimentel Paleovalley has many characteristics of a small pull-apart basin.

(4) This study suggests that outlet glaciers from Namibia did not travel onto the RGS through a network of paleovalleys. It is also inconsistent with the hypothesis that a single, massive, unconfined ice sheet in Africa (or Antarctica) was responsible for deposition on both the eastern margin of the Paraná Basin and on the RGS (southern margin). The most likely source of glaciation on the RGS was a lobe, separate from the eastern margin of the Paraná

Basin, which extended N-NW out of Uruguay onto the western RGS. Another possible explanation is that glaciation on the RGS was restricted to a small ice cap or alpine glaciers.

(5) These findings are supportive of the general hypothesis that Carboniferous-Permian glaciation in west-central Gondwana was comprised of smaller, separate ice centers with less ice-volume than some previous estimates for this region.

References

Amato, J.A., 2017. Using AMS to help interpret glaciogenic deposits of the late Paleozoic ice age in the Paraná Basin, Brazil (Masters Thesis). University of Wisconsin-Milwaukee, Milwaukee, WI.

Babinski, M., Chemale Jr., F., Van Schmus, W.R., Hartmann, L.A., Silva, da L.C., 1997. U–Pb and Sm–Nd geochronology of the Neoproterozoic granitic-gneissic Dom Feliciano Belt, southern Brazil. Journal of South American Sciences 10, 263-274.

Benn, D.I., Evans, D.J.A., 2010. Glaciers and glaciation. Hodder Education, London (802 pp.).

Bennett, M.R., Doyle, P., Mather, A.E., 1996. Dropstones: their origin and significance. Palaeogeography, Palaeoclimatology, Palaeoecology 121, 331-339.

Buggisch, W., Wang, X., Alekseev, A.S., Joachimski, M.M., 2011. Carboniferous-Permian carbon isotope stratigraphy of successions from China (Yangtze platform), USA (Kansas) and Russia (Moscow Basin and Urals). Palaeogeography, Palaeoclimatology, Palaeoecology 301, 18-38.

Bull, W.B., 1977. The alluvial-fan environment. Progress in Physical Geography 1, 222-270.

Cagliari, J., Philipp, R.P., Buso, V.V., Netto, R.G., Hillebrand, P.K., Lopes, R.d.C., Basei, M.A.S, Faccini, U.F., 2016. Age constraints of the glaciation in the Paraná Basin: evidence from new U-Pb dates. Journal of the Geological Society 173, 871-874.

Canile, F.M., Babinski, M., Rocha-Campos, A.C., 2016. Evolution of the Carboniferous-Early Cretaceous units of the Paraná Basin from provenance studies based on U-Pb, Hf and O isotopes from detrital zircons. Gondwana Research 40, 142-169.

Carto, S., Eyles, N., 2012. Sedimentology of the Neoproterozoic (c. 580 Ma) Squantum 'Tillite', Boston Basin USA: mass flow deposition in a deep-water arc basin lacking direct glacial influence. Sedimentary Geology 269, 1-14.

Chen, B., Joachimski, M.M., Shen, S., Lambert, L.L., Lai, X., Wang, X., Chen, J., Yuan, D., 2013. Permian ice volume and palaeoclimate history: oxygen isotope proxies revisited. Gondwana Research 24, 77-89.

Chen, B., Joachimski, M.M., Wang, X., Shen, S., Qi, Y., Qie, W., 2016. Ice volume and paleoclimate history of the late Paleozoic ice age from conodont apatite oxygen isotopes from Naqing (Guizhou, China). Palaeogeography, Palaeoclimatology, Palaeoecology 448, 151-161.

Cordani, U.G., Sato, K., Teixeira, W., Tassianri, C.C.G., Basei, M.A.S., 2000. Crustal evolution of the South American Platform. In: Cordani, U.G., Milani, E.J., Thomaz Filho, A., Campos, D.A. (Eds.), Tecontic Evolution of South America. International Geological Congress 31, Rio de Janeiro, pp. 19-40.

Cowan, E.A., Powell, R.D., 1990. Suspended sediment transport and deposition of cyclically interlaminated sediment in a temperate glacial fjord, Alaska, U.S.A. In: Dowdeswell, J.A., Scourse, J.D. (Eds.), Glacimarine Environments: Processes and Sediments. Geological Society Special Publication 53, pp. 75-89.

Cowan, E.A., Seramur, K.C., Powell, R.D., Willems, B.A., Gulick, S.P.S., Jaeger, J.M., 2010. Fjords as temporary sediment traps: history of glacial erosion and deposition in Muir Inlet, Glacier Bay National Park, southeastern Alaska. Geological Society of America Bulletin 122, 1067-1080.

Crookshanks, S., Gilbert, R., 2008. Continuous, diurnally fluctuating turbidity currents in Kluane Lake, Yukon Territory. Canadian Journal of Earth Science 45, 1123–1138.

Crowell, J.C., Frakes, L.A., 1975. The late Paleozoic glaciation. In: Campbell, K.S.W. (Ed.), Gondwana Geology. Australian National University Press, Canberra, pp. 313-331.

Crowell, J.C., 1999. Pre-Mesozoic ice ages: their bearing on understanding the climate system. Geological Society of America Memoir 192, Boulder (106 pp.).

Corrêa da Silva, Z.C., 1978. Observações sobre o Grupo Tubarão no Rio Grande do Sul, com especial destaque á estratigrafia da Formação Itararé. Pesquisas—UFRGS 9, pp. 27-44.

Dadson, S., Hovius, N., Pegg, S., Dade, W.B., Horng, M.J., Chen, H., 2005. Hyperpycnal river flows from an active mountain belt. Journal of Geophysical Research 110, 4-16.

Delaney, P.I.V., 1964. Itararé outliers in Rio Grande do Sul, Brazil. Boletim Paranaense Geografia 10/15, 161-173.

de Wit, M.J., Stankiewicz, J., Reeves, C., 2008. Restoring Pan-African—Brasiliano connections: more Gondwana control, less trans-Atlantic corruption. In: Pankhurst, R.J., Trouw, R.A.J., Brito Neves, B.B., de Wit, M.J. (Eds.), West Gondwana: Pre-Cenozoic Correlations Across the South Atlantic Region. Geological Society of London Special Publications 294, pp. 399-412.

Dionne, J.C., 1993. Sediment load of shore ice and ice rafting potential, Upper St. Lawrence Estuary, Quebec, Canada. Journal of Coastal Research 9, 628-646.

Doublet, S., Garcia, J.P., 2004. The significance of dropstones in tropical lacustrine setting, eastern Cameros Basin (Late Jurassic–Early Cretaceous, Spain). Sedimentary Geology 163, 293–309.

Dowdeswell, J.A., Villinger, H., Whittington, R.J., Marienfeld, P., 1993. Iceberg scouring in Scoresby Sund and on the East Greenland continental shelf. Marine Geology 111, 37-53.

Drosner, M.L., Bottjer, D.J., 1986. A semiquantitative field classification of ichnofabric. Journal of Sedimentary Petrology 56, 558-559.

Enos, P., 1977. Flow regimes in debris flow. Sedimentology 24, 133-142.

Fallgatter, C., Paim, P.S.G., 2017. On the origin of the Itararé Group basal nonconformity and its implications for the late Paleozoic glaciation in the Paraná Basin, Brazil. Palaeogeography, Palaeoclimatology, Palaeoecology (in press).

Farrell, K.M., Harris, W.B., Mallinson, D.J., Culver, S.J., Riggs, S.R., Pierson, J., Self-Trail, J.M., Lautier, J.C., 2012. Standardizing texture and facies codes for a process-based classification of clastic sediment and rock. Journal of Sedimentary Research 82, 364-378.

Ferguson, L., 1970. "Armored snowballs" and the introduction of coarse terrigenous material into sea-ice. Journal of Sedimentary Petrology 40, 1057-1060.

Fernandes, L.A.D., Koester, E., 1999. The Neoproterozoic Dorsal de Canguçú strike-slip shear zone: its nature and role in the tectonic evolution of southern Brazil. Journal of African Earth Sciences 29, 3-24.

Fielding, C.R., 1987. Coal depositional models for deltaic and alluvial plain sequences. Geology 15, 661-664.

Fielding, C.R., Frank, T.D., Birgenheier, L.P., Rygel, M.C., Jones, A.T., Roberts, J., 2008a. Stratigraphic record and facies associations of the late Paleozoic ice age in eastern Australia (New South Wales and Queensland). In: Fielding, C. R., Frank, T. D., Isbell, J. L. (Eds.), Resolving the Late Paleozoic Ice Age in Time and Space. Geological Society of America Special Publication 441, pp. 41-57.

Fielding, C. R., Frank, T. D., Isbell, J. L., 2008b. The late Paleozoic ice age-A review of current understanding and synthesis of global climate patterns. In: Fielding, C. R., Frank, T. D., Isbell, J. L. (Eds.), Resolving the Late Paleozoic Ice Age in Time and Space. Geological Society of America Special Publication 441, pp. 343-354.

Frakes, L.A., Crowell, J.C., 1972. Late Paleozoic glacial geography between the Paraná Basin and the Andean Geosyncline. Anais. Academia Brasileira de Ciencias 44, pp. 139- 145.

França, A. B., Potter, P. E, 1991. Stratigraphy and Reservoir Potential of Glacial Deposits of the Itararé Group (Carboniferous-Permian), Paraná Basin, Brazil. American Association of Petroleum Geologists Bulletin 75, 62-85.

Frank, T.D., Shultis, A.I., Fielding, C.R., 2015. Acme and demise of the late Paleozoic ice age: a view from the southeastern margin of Gondwana. Palaeogeography, Palaeoclimatology, Palaeoecology 418, 176-192.

Foster, D.A., Goscombe, B.D., Newstead, B., Mapani, B., Mueller, P.A., Gregory, L.C., Muvangua, E., 2015. U-Pb age and Lu-Hf isotopic data of detrital zircons from the Congo and Kalahari before Gondwana. Gondwana Research 28, 179-190.

Garden, C.J., Craw, D., Waters, J.M., Smith, A., 2011. Rafting rocks reveal marine biological dispersal: A case study using clasts from beach-cast macroalgal holdfasts. Estuarine, Coastal and Shelf Science 95, 388-394.

Gastal, M.C.P., Lafon, J.M., Hartmann, L.A., Koester, E., 2005. Sm–Nd isotopic compositions as a proxy for magmatic processes during the Neoproterozoic of the southern Brazilian shield. Journal of South American Earth Sciences 18, 255-276.

Gastaldo, R. A., DiMichele, W. A., Pfefferkorn, H. W., 1996. Out of the icehouse into the greenhouse; a late Paleozoic analog for modern global vegetational change. Geological Society of America Today 6, 1-7.

Gesicki, A. L. D., Riccomini, C., Boggianic, P. C., Coimbra, A. M., 1998. The Aquidauana Formation (Paraná Basin) in the context of the late Paleozoic glaciation in western Gondwana. Journal of African Earth Sciences 27, 81-82.

Gesicki, A. L. D., Riccomini, C., Boggianic, P. C., 2002. Ice flow direction during late Paleozoic glaciation in western Paraná Basin, Brazil. Journal of South American Earth Sciences 14, 933-939.

Gilbert, R., 1990. Rafting in glacimarine environments. In: Dowdeswell, J.A., Scourse, J.D. (Eds), Glacimarine Environments: Processes and Sediments. Geological Society of London Special Publications 53, pp. 105-120.

Girardclos, S., Schmidt, O.T., Sturm, M., Ariztegui, D., Pugin, A., Anselmetti, F.S., 2007. The 1996 AD delta collapse and large turbidite in Lake Brienz. Marine Geology 241, 137-154.

Gray, D.R., Foster, D.A., Meert, J.G., Goscombe, B.D., Armstrong, R., Trouw, R.A.J., Passchier, C.W., 2008. A Damara orogeny perspective on the assembly of southwestern Gondwana. In: Pankhurst, R.J., Trouw, R.A.J., Brito Neves, B.B., De Wit, M.J. (Eds), West Gondwana: Pre-Cenozoic Correlations Across the South Atlantic Region. Geological Society of London Special Publications 294, pp. 257-278.

Griffis, N.P., Mundil, R., Montañez, I.P., Isbell, J.L., Fedorchuk, N.D., Vesely, F.F., Iannuzzi, R., Yin, Q.-Z., 2018. A new stratigraphic framework built on U-Pb single zircon TIMS ages with implications for the timing of the penultimate icehouse (Paraná Basin, Brazil). Geologcial Society of America Bulletin (in press).

Guerra-Sommer, M., Cazzulo-Klepzig, M., Menegat, R., Mendonça, J.G., 2008a. U-Pb dating of tonstein layers from a coal succession of the southern Paraná Basin (Brazil): a new geochronological approach. Gondwana Research 14, 474-482.

Guerra-Sommer, M., Cazzulo-Klepzig, M., Menegat, R., Formoso, M. L. L., Basei, M. A. S., Barboza, E. G., Simas, M. W., 2008b. Geochronological data from the Faxinal coal succession, southern Paraná Basin, Brazil: A preliminary approach combining radiometric U-Pb dating and palynostratigraphy. Journal of South American Earth Sciences 25, 246-256.

Guerra-Sommer, M., Cazzulo-Klepzig, M., Santos, J.O.S., Hartmann, L.A., Ketzer, J.M.M., Formoso, M.L.L., 2008c. Radiometric age determination of tonsteins and stratigraphic constraints for the lower Permian coal succession in southern Paraná Basin, Brazil. International Journal of Coal Geology 74, 13-27.

Gulbranson, E.L., Montañez, I.P., Schmitz, M.D., Limarino, C.O., Isbell, J.L., Marenssi, S.A., Crowley, J.L., 2010. High-precision U-Pb calibration of Carboniferous glaciation and climate history, Paganzo Group, NW Argentina. Geological Society of America Bulletin 122, 1480-1498.

Gürbüz, A., 2010. Geometric characteristics of pull-apart basins. Lithosphere 2, 199-206.

Gustavson, T.C., 1991. Buried vertisols in lacustrine facies of the Pliocene Fort Hancock Formation, Hueco Bolson, West Texas and Chihuahua, Mexico. Geological Society of America Bulletin 103, 448-460.

Guy-Ohlson, D., 1996. Chapter 7B. Prasinophycean algae. In: Jansonius, J., McGregor, D. C. (Eds.), Palynology: principles and applications. American Association of Stratigraphic Palynologists Foundation, 1, pp. 181-189.

Hambrey, M. J., Glasser, N. F., 2003. Glacial sediments: processes, environments and facies. In: Middleton, G.V. (Ed.), Encyclopedia of Sediments and Sedimentary Rocks. Kluwer, Dordrecht, pp. 316-331.

Hempton, M.R., Dunne, L.A., 1984. Sedimentation in pull-apart basins: active examples in eastern Turkey. The Journal of Geology 92, 513-530.

Holz, M., 1999. Early Permian sequence stratigraphy and the palaeophysiographic evolution of the Paraná Basin in southernmost Brazil. Journal of African Earth Sciences 29, 51-61.

Holz, M., 2003. Sequence stratigraphy of a lagoonal estuarine system—an example from the lower Permian Rio Bonito Formation, Paraná Basin, Brazil. Sedimentary Geology 162, 305-331.

Holz, M., Küchle, J., Philipp, R.P., Bischoff, A.P., Arima, N., 2006. Hierarchy of tectonic control on stratigraphic signatures: base-level changes during the Early Permian in the Paraná Basin, southernmost Brazil. Journal of South American Earth Sciences 22, 185-204.

Holz, M., Souza, P. A., Iannuzzi, R., 2008. Sequence stratigraphy and biostratigraphy of the Late Carboniferous to Early Permian glacial succession (Itararé subgroup) at the eastern-southeastern margin of the Paraná Basin, Brazil. In: Fielding, C. R., Frank, T., Isbell, J. L. (Eds.), Resolving the Late Paleozoic Ice Age in Time and Space. Geological Society of America Special Paper 441, pp. 115-129.

Holz, M., França, A.B., Souza, P.A., Iannuzzi, R., Rohn, R., 2010. A stratigraphic chart of the Late Carboniferous/Permian succession of the eastern border of the Paraná Basin, Brazil, South America. Journal of South American Earth Sciences 29, 381-399.

Horton, D.E., Poulsen, C.J., Pollard, D., 2010. Influence of high-latitude vegetation feedbacks on late Palaeozoic glacial cycles. Nature Geoscience 3, 572-577.

Iannuzzi, R., Pfefferkorn, H.W., 2002. A pre-glacial, warm-temperate floral belt in Gondwana (Late Visean, Early Carboniferous). Palaios 17, 571-590.

Iannuzzi, R., Scherer, C.M.S., Souza, P.A., Holz, M., Caravaca, G., Adami-Rodrigues, K., Tybusch, G.P., Souza, J.M., Smaniotto, L.P., Fischer, T.V., Silveira, A.S., Lykawka, R., Boardman, D.R., Barboza, E.G., 2006. Afloramento Morro do Papaléo, Mariana Pimentel, R.S., Registro ímparda sucessão pós-glacial do Paleozóico da Bacia do Paraná. In: Winge, M., Schobbenhaus, C., Souza, C.R.G., Fernandes, A.C.S., Queiroz, E.T., Berbert-Born, M.L.C., Campos, D.A. (Eds.), Sítios Geológicos e Paleontológicos do Brasil 2, pp. 1-13.

Iannuzzi, R., Souza, P.A., Holz, M., 2010. Stratigraphic and paleofloristic record of the Lower Permian postglacial succession in the southern Brazilian Paraná Basin. Geological Society of America Special Papers 468, 113-132.

Isbell, J.L., Miller, M.F., Wolfe, K.L., Lenaker, P.A., 2003. Timing of late Paleozoic glaciation in Gondwana: Was glaciation responsible for the development of northern hemisphere cyclothems? In: Chan, M.A., Archer, A.W. (Eds.), Extreme depositional environments: Mega end members in geologic time. Geological Society of America Special Paper 370, 5-24.

Isbell, J. L., Henry, L. C., Gulbranson, E. L., Limarino, C. O., Fraiser, M. L., Koch, Z. J., Ciccioli, P. L., Dineen, A. A., 2012. Glacial paradoxes during the late Paleozoic ice age: Evaluating the equilibrium line altitude as a control on glaciation. Gondwana Research 22, 1-19.

Kempema, E.W., Reimnitz, E., Barnes, P.W., 2001. Anchor-ice formation and ice rafting in southwestern Lake Michigan, U.S.A. Journal of Sedimentary Research 71, 346-354.

Kempema, E.W., Ettema, R., 2011. Anchor ice rafting: observations from the Laramie River. River Research and Applications 27, 1126-1135.

Kleiman, L.A., Japas, M.S., 2009. The Choiyoi volcanic province at 34°S–36°S (San Rafael, Mendoza, Argentina): implications for the late Paleozoic evolution of the southwestern margin of Gondwana. Tectonophysics 473, 283-299.

Kwon, C.W., Jeong, J.O., Sohn, Y.K., 2011. Sedimentary records of rift to pull-apart tectonics in the Miocene Eoil Basin, SE Korea. Sedimentary Geology 236, 256-271.

Leite, J.A.D., Hartmann, L.A., Fernandes, L.A.D., McNaughton, N.J., Soliani Jr., Ê, Koester, E., Santos, J.O.S., Vasconcellos, M.A.Z., 2000. Zircon U–Pb SHRIMP dating of gneissic basement of the Dom Feliciano Belt, southernmost Brazil. Journal of South American Earth Sciences 13, 739-750.

Lopes, R.d.C., 1995. Acabouço Aloestratigráfico para o Intervalo "Rio Bonito-Palermo" (Eopermiano da bacia do Paraná), entre Butiá e São Sepé, Rio Grande do Sul (Masters Thesis). Universidade do Vale do Rio do Sinos, São Leopoldo (254 pp.).

López-Gamundí, O. R., 1997. Glacial-postglacial transition in the Late Paleozoic basins of southern South America. In: Martini, I. P. (Ed.), Late Glacial and Postglacial Environmental Changes: Quaternary, Carboniferous-Permian, and Proterozoic. Oxford University Press, Oxford, pp. 147-168.

Mack, G.H., Rasmussen, K.A., 1984. Alluvial-fan sedimentation of the Cutler Formation (Permo-Pennsylvanian) near Gateway, Colorado. Geological Society of America Bulletin 95, 109-116.

Mann, P., Hempton, M.R., Bradley, D.C., Burke, K., 1983. Development of pull-apart basins. The Journal of Geology 91, 529-554.

Martin, H., 1981. The late Palaeozoic Dwyka Group of the South Kalahari Basin in Namibia and Botswana and the subglacial valleys of the Kaokoveld in Namibia. In: Hambrey, M.J., Harland, W.B. (Eds.), Earth's Pre-Pleistocene Glacial Record. Cambridge University Press, Cambridge, pp. 61-66.

Martinsen, O. J., Ryseth, A., Helland-Hansen, W., Flesche, H., Torkildsen, G., Idil, S., 1999. Stratigraphic base level and fluvial architecture: Ericson Sandstone (Campanian), Rock Springs Uplift, SW Wyoming, USA. Sedimentology 46, 235-259.

Matos, S.L.F., Yamamoto, J.K., Riccomini, C., Hachiro, J., Tassinari, C.C.G., 2001. Absolute dating of Permian ash-fall in the Rio Bonito Formation, Paraná Basin, Brazil. Gondwana Research 4, 421-426.

Milani, E.J., Faccini, U.F., Scherer, C.M., Araújo, L.M., Cupertino, J.A., 1998. Sequences and Stratigraphic Hierarchy of the Paraná Basin (Ordovician to Cretaceous), Southern Brazil. Boletim IG USP. 29, 125-173.

Montañez, I., Soreghan, G. S., 2006. Earth's fickle climate; lessons learned from deep-time ice ages. Geotimes 51, 24-27.

Montañez, I. P., Norris, R. D., Algeo, T., Chandler, M. A., Johnson, K. R., Kennedy, M. J., Kent, D. V., Kiehl, J. T., Kump, L. R., Ravelo, A. C., Turekian, K. K., Freeman, K. H., Feary, D. A., Rogers, N. D., Estep, J. T., Gibbs, C. R., Edkin, E. J., 2011. Understanding Earth's deep past; lessons for our climate future. National Academies Press, Washington, DC (194 pp.).

Montañez, I. P., Poulsen, C. J., 2013. The late Paleozoic ice age: an evolving paradigm: Annual Review of Earth & Planetary Sciences 41, 1-28.

Molnia, B.F., 1983. Subarctic glacial-marine sedimentation: a model. In: Molnia, B.F. (Ed.), Glacial-Marine Sedimentation. Plenum Press, New York, pp. 95-114.

Mori, A. L. O., de Souza, P. A., Marques, J. C., Lopes, R. d. C., 2012. A new U–Pb zircon age dating and palynological data from a Lower Permian section of the southernmost Paraná Basin, Brazil: Biochronostratigraphical and geochronological implications for Gondwanan correlations. Gondwana Research 21, 654-669.

Mugford, R.I., Dowdeswell, J.A., 2011. Modeling glacial meltwater plume dynamics and sedimentation in high-latitude fjords. Journal of Geophysical Research 116, F01023.

Nemec, W., Steel, R.J., 1984. Alluvial and coastal conglomerates: their significant features and some comments on gravelly mass-flow deposits. In: Koster, R.H., Steel, R.J. (Eds.), Sedimentology of Gravels and Conglomerates. Canadian Society of Petroleum Geologists Memoirs 10, 1-31.

Ó Cofaigh, C., Dowdeswell, J.A., 2001. Laminated sediments in glacimarine environments: diagnostic criteria for their interpretation. Quaternary Science Reviews 20, 1411-1436.

Oliveira, C.H.E., Jelinek, A.R., Chemale Jr., F., Bernet, M., 2016. Evidence of post-Gondwana breakup in southern Brazilian Shield: insights from apatite and zircon fission track thermochronology. Tectonophysics 666, 173-187.

Ottensen, D., Dowdeswell, J.A., 2009. An inter-ice-stream glaciated margin: Submarine landforms and a geomorphic model based on marine-geophysical data from Svalbard. Geological Society of America Bulletin 121, 1647-1665.

Oyhantçabal, P., Siegesmund, S., Wemmer, K., 2011. The Río de la Plata Craton: a review of units, boundaries, ages and isotopic signature. International Journal of Earth Science 100, 201-220.

Paim, P.S.G., Piccoli, A.E.M., Sarturi, J.A.D., Munaro, P., Holz, M., Granitoff, W., 1983. Evolução paleogeográfica do Supergrupo Tubarãona área de Mariana Pimentel-Faxinal, Guaíba, RS. Simpósio Sul Brasileiro de Geologia 1, pp. 121-134.

Passarelli, C.R., Basei, M.A.S., Wemmer, K., Siga Jr., O., Oyhantçabal, P., 2011. Major shear zones of southern Brazil and Uruguay: escape tectonics in the eastern border or Rio de La Plata and Paranapanema cratons during western Gondwana amalgamation. International Journal of Earth Science 100, 391-414.

Philipp, R.P., Machado, R., 2005. The late Neoproterozoic granitoid magmatism of the Pelotas Batholith, southern Brazil. Journal of South American Earth Sciences 19, 461-478.

Posamentier, H.W., Martinsen, O.J., 2011. The character and genesis of submarine mass-transport deposits; insights from outcrop and 3D seismic data. In: Shipp, R.G., Weimer, P., Posamentier, H.W. (Eds.), Mass-transport Deposits in Deepwater Settings. Society for Sedimentary Geology Special Publication 96, pp. 7-38.

Postma, G., Nemec, W., Kleinspehn, K.L., 1988. Large floating clasts in turbidites: a mechanism for their emplacement. Sedimentary Geology 58, 47-61.

Powell, R.D., 1990. Glacimarine processes at grounding-line fans and their growth to ice-contact deltas. In: Dowdeswell, J.A., Scourse, J.D. (Eds.), Glacimarine Environments: Processes and Sediments. Geological Society Special Publication 53, pp. 53-73.

Powell, R.D., 2003. Subaquatic landsystems: fjords. In: Evans, D.A.J. (Ed.), Glacial Landsystems. Arnold, London, pp. 313-347.

Ribeiro, N.V.B., Freitas, J.T., Souza, R., 1987. Correlação estratigráfica entre três bacias carboníferas do paleovale Leão/Mariana Pimentel. III Simpósio Sul Brasileiro de Geologia, Curitiba, Actas, pp. 335-350.

Riccomini, C., Velázquez, V.F., 1999. Superfície estriada por geleira Neopaleozoica no Paraguai oriental. Revista Basileira de Geociências 29, 233-236.

Ridgway, K.D., Decelles, P.G., 1993. Stream-dominated alluvial fan and lacustrine depositional systems in Cenozoic strike-slip basins, Denali fault system, Yukon Territory, Canada. Sedimentology 40, 645-666.

Rocha-Campos, A. C., dos Santos, P. R., and Canuto, J. R., 2008. Late Paleozoic glacial deposits of Brazil: Paraná Basin. In: Fielding, C.R., Frank, T.D., Isbell, J.L. (Eds.), Resolving the Late Paleozoic Ice Age in Time and Space. Geological Society of America Special Papers 441, pp. 97-114.

Rosa, E.L.M., Vesely, F.F., França A.B., 2016. A review of the late Paleozoic ice-related erosional landforms in the Paraná Basin: origin and paleogeographical implications. Brazilian Journal of Geology 46, 147-166.

Rygel, M.C., Fielding, C.R., Frank, T.D., Birgenheier, L.P., 2008. The magnitude of late Paleozoic glacioeustatic fluctuations: a synthesis. Journal of Sedimentary Research, 500-511.

Saalmann, K., Gerdes, A., Lahaye, Y., Hartmann, L.A., Remus, M.V.D., Läufer, A., 2011. Multiple accretion at the eastern margin of the Rio de la Plata craton: the prolonged Brasiliano orogeny in southernmost Brazil. International Journal of Earth Science 100, 355-378.

Santos, P. R. d., Rocha-Campos, A. C., Canuto, J. R., 1996. Patterns of late Palaeozoic deglaciation in the Paraná Basin, Brazil. Palaeogeography, Palaeoclimatology, Palaeoecology 125, 165-184.

Sarp, G., 2015. Tectonic controls on the North Anatolian Fault System (NAFS) on the geomorphic evolution of the alluvial fans and fan catchments in Erzincan pull-apart basin; Turkey. Journal of Asian Earth Sciences 98, 116-125.

Schimmelmann, A., Lange, C.B., Schieber, J., Francus, P., Ojala, A.E.K., Zolitschka, B., 2016. Varves in marine sediments: a review. Earth-Science Reviews 159, 215-246.

Silva, da L.C., Hartmann, L.A., McNaughton, N.J., Fletcher, L.R., 1999. SHRIMP U/Pb zircon dating of Neoproterozoic granitic magmatism and collision in the Pelotas Batholith, southernmost Brazil. International Geological Review 41, 531-551.

Silveira, A.S., 2000. Estratigrafia de seqüências e evolução paleoambiental da sucessão Permiana (Sakmariano-Eokazaniano) da Bacia do Paraná, entre Rio Pardo e Mariana Pimentel (RS) (Masters Thesis). Universidade do Vale do Rio do Sinos, São Leopoldo (140 pp.).

Simas, M.W., Guerra-Sommer, M., Cazzulo-Klepzig, M., Menegat, R., Santos, J.O.S., Ferreira, J.A.F., Degani-Schmidt, I., 2012. Geochronological correlation of the main coal interval in Brazilian Lower Permian: radiometric dating of tonstein and calibration of biostratigraphic framework. Journal of South American Earth Sciences 39, 1-15.

Smaniotto, L.P., Fischer, T.V. , Souza, P.A., Iannuzzi, R., 2006. Palinologia do Morro do Papaléo, Mariana Pimentel (Permiano Inferior, Bacia do Paraná), Rio Grande do Sul, Brazil. Revista Brasileira de Paleontologia 9, 311-322.

Souza, P.A., 2006. Late Carboniferous palynostratigraphy of the Itararé Subgroup, northeastern Paraná Basin, Brazil. Review of Palaeobotany and Palynology 138, 9-29.

Syvitski, J.P.M., Burrell, D.C., Skei, J., 1987. Fjords: processes and products. Springer-Verlag, New York (379 pp.).

Talling, P.J., Masson, D.G., Sumner, E.J., Malgesini, G., 2012. Subaqueous sediment density flows: depositional processes and deposit types. Sedimentology 59, 1937-2003.

Talling, P.J., 2014. On the triggers, resulting flow types and frequencies of subaqueous sediment density flows in different settings. Marine Geology 352, 155–182.

Tedesco, J., Cagliari, J., Coitinho, J.R., Lopes, R.C.L, Lavina, E.L.C., 2016. Late Paleozoic paleofjord in the southernmost Parana Basin (Brasil): Geomorphology and sedimentary fill. Geomorphology 269, 203-214.

Tomazelli, L.J., Soliani Júnior, E., 1982. Evidências de atividade glacial no Paleozóico Superior do Rio Grande do Sul, Brasil. Anais II Congresso Brasileiro de Geologia, Salvador 4, pp. 1378-1389.

Tomazelli, L.J., Soliani Júnior, E., 1997. Sedimentary facies and depositional environments related to Gondwana glaciation in Batovi and Suspiro Regions, Rio Grande do Sul, Brazil. Journal of South American Earth Sciences 10, 295-303.

Torsvik, T. H., Cocks, L. R. M., 2013. Gondwana from top to base in space and time. Gondwana Research 24, 999-1030.

Trzaskos, B., Vesely, F.F., Rostirolla, S.P., 2006. Recurrence of tectonic events overprint in the Carboniferous Vila Velha Sandstones of the Itararé Group, Paraná Basin, South Brazil. Boletim Paranaense de Geociências 58, 89-104.

van der Lingen, G.J., Pettinga, J.R., 1980. The Makara Basin: a Miocene slope-basin along the New Zealand sector of the Australian-Pacific obliquely convergent plate boundary. In Balance, P.F., Reading, H.G. (Eds.), Sedimentation in Oblique-slip Mobile Zones. Blackwell Scientific Publications, Oxford, pp. 191-215.

Veevers, J.J., Powell, C.McA., 1987. Late Paleozoic glacial episodes in Gondwanaland reflected in transgressive-regressive depositional sequences in Euramerica. Geological Society of America Bulletin 98, 475-487.

Vesely, F. F., Trzaskos, B., Kipper, F., Assine, M. L., Souza, P. A., 2015. Sedimentary record of a fluctuating ice margin from the Pennsylvanian of western Gondwana: Paraná Basin, southern Brazil. Sedimentary Geology 326, 45-63.

Vermeesch, P., 2012. On the visualization of detrital age distributions. Chemical Geology 312-313, 190-194.

Vermeesch, P., Resentini, A., Garzanti, E., 2016. An R package for statistical provenance analysis. Sedimentary Geology 336, 14-25.

Visser, J.N.J., 1987. The palaeogeography of part of southwestern Gondwana during the Permo-Carboniferous glacaiation. Palaeogeography, Palaeoclimatology, Palaeoecology 61, 205-219.

Visser, J.N.J., 1993. A reconstruction of the late Palaeozoic ice sheet on southwestern Gondwana. In: Findlay, R.H., Unrug, R., Banks, M.R., Veevers, J.J. (Eds.), Gondwana 8 Assembly, Evolution and Dispersal. AA Balkema, Rotterdam, pp. 449-458.

Visser, J.N.J., 1997. Deglaciation sequences in the Permo-Carboniferous Karoo and Kalahari basins of southern Africa: a tool in the analysis of cyclic glaciomarine basin fills. Sedimentology 44, 507-521.

Waldron, J.W.F., 2004. Anatomy and evolution of a pull-apart basin, Stellarton, Nova Scotia. Geological Society of America Bulletin 116, 109-127.

Woodborne, M.W., Rogers, J., Jarman, N., 1989. The geological significance of kelp-rafted rock along the West Coast of South Africa. Geo-Marine Letters 9, 109-118.

Ysufoğflu, H., 2013. An intramontane pull-apart basin in tectonic escape deformation: Elbistan Basin, eastern Taurides, Turkey. Journal of Geodynamics 65, 308-329.

Zavala, C., ArcuriM., 2016. Intrabasinal and extrabasinal turbidites: origin and distinctive characteristics. Sedimentary Geology 337, 36-54.

Ziegler, A.M., Hulver, M.L., Rowley, D.B., 1997. Permian world topography and climate. In: Martini, I.P. (Ed.), Late glacial and post-glacial environmental changes-Quaternary, Carboniferous-Permian and Proterozoic. Oxford University Press, New York, pp. 111-146.

Zolitschka, B., Francus, P., Ojala, A.E.K., Schimmelmann, A., 2015. Varves in lake sediments – a review. Quaternary Science Reviews 117, 1-41.
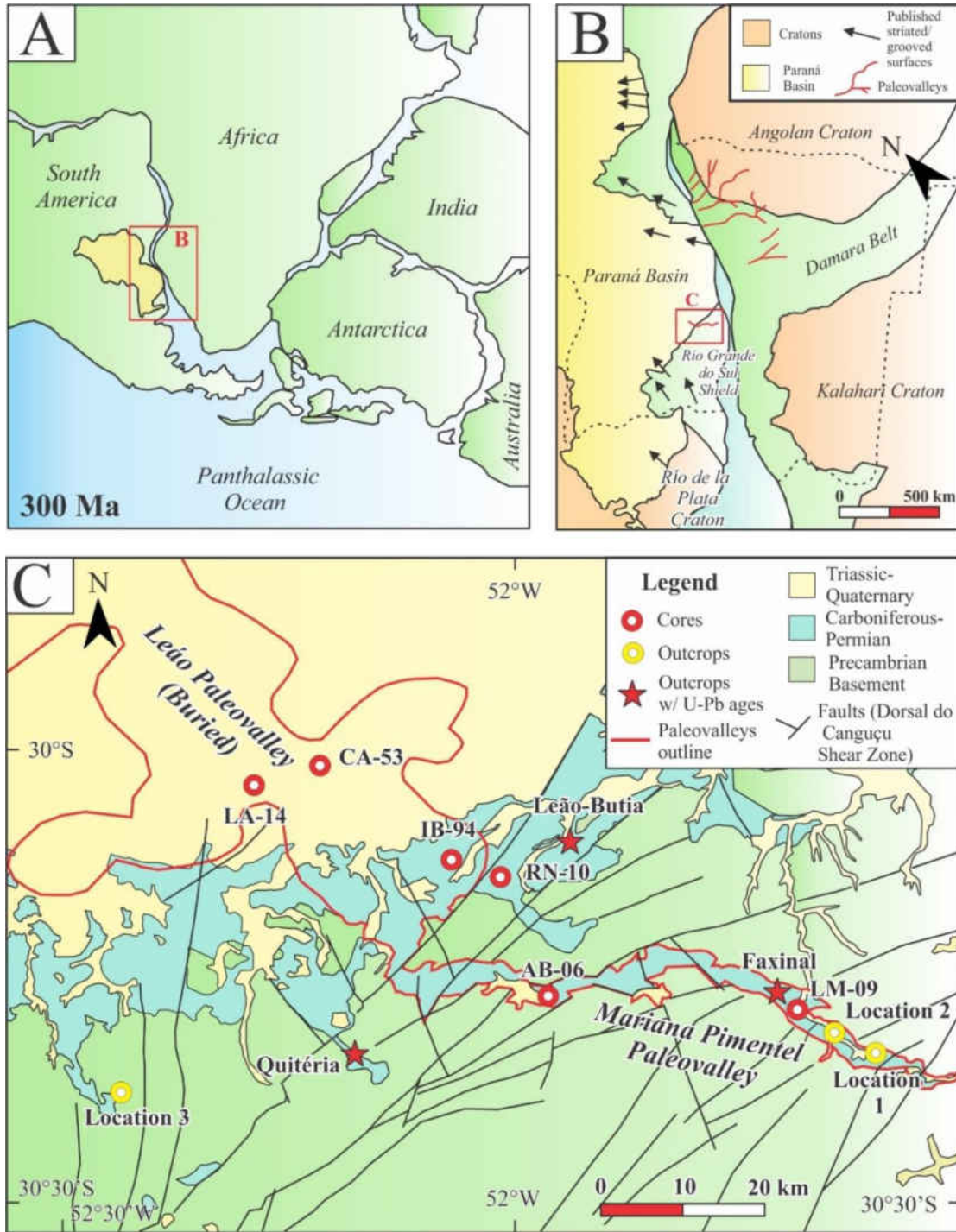
Fig. 2.1. Paleogeography and study location. A. Gondwana paleogeography and Paraná Basin (yellow) during Pennsylvanian (after PLATES/UTIG; Fallgatter and Paim, 2017). B. Southern and eastern margin of Paraná Basin relative to western Africa. Paleovalleys indicated by red lines. Published striated/grooved surface locations with interpreted ice flow directions represented by black arrows (after Rosa et al., 2016; Fallgatter and Paim, 2017). C Study location with Mariana Pimentel and Leão paleovalleys outlined in red. Outcrops indicated by orange/white circles and cores indicated by red/white circles (after Lopes, 1995; Tedesco et al., 2016). Location 1 at 30°18'27.78''S, 51°38'35.22''W, Location 2 at 30°19'40.91''S, 51°35'47.15''W, Location 3 at 30°22'66''S, 52°25'33.13''W.
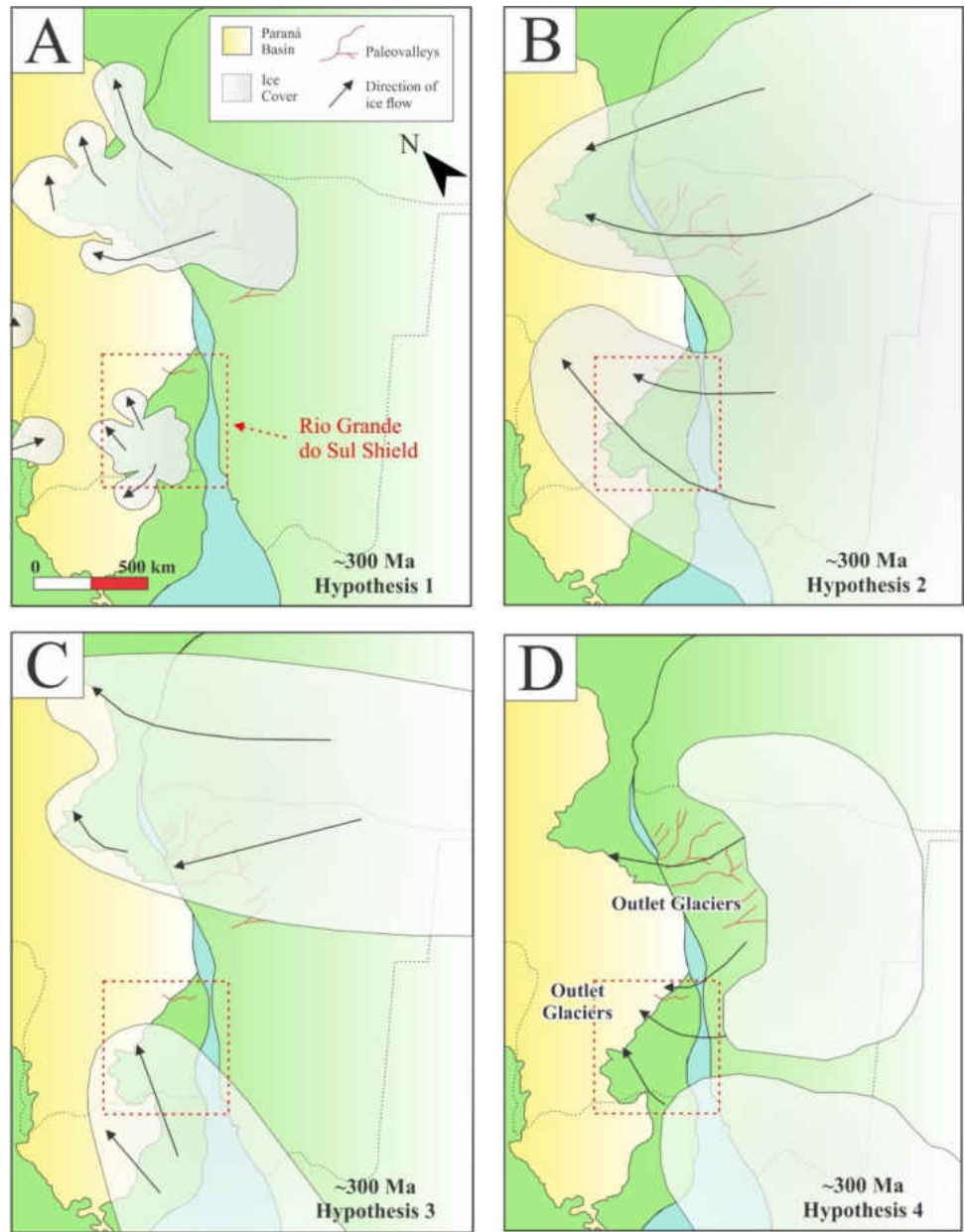
Fig. 2.2. Hypotheses for size and location of glaciers entering Paraná Basin during late Carboniferous. Rio Grande do Sul Shield in red box. A. Hypothesis 1: multiple small ice centers on paleotopographic highs around basin margins (after Rocha-Campos et al., 2008; Santos et al., 1996). B. Hypothesis 2: single massive ice sheet from Africa or Antarctica (after Visser, 1993). C. Hypothesis 3: two separate, unconfined lobes entering basin, one extending north from Uruguay and another extending west from Namibia (after Frakes and Crowell, 1972; Crowell and Frakes, 1975). D. Hypothesis 4: outlet glaciers entering southern and eastern margin of basin though paleovalleys originating in Africa (after Tedesco et al., 2016; Fallgatter and Paim, 2017).

60

Fig. 2.3. Third-order sequence stratigraphic framework for southern and eastern Paraná Basin (after Holz et al., 2006). SB = sequence boundary, LST = lowstand systems tract, TST = transgressive systems tract, HST = highstand systems tract.

Lithofacies name	Symbol	Lithologies	Key features and sedimentary structures	Bed thickness	Interpretation
Sandy conglomerate and breccia facies	Gm (massive) Gp (planar cross beds)	Sandy conglomerate and breccia, interbeds of clast-poor to clast-rich sandy diamictite, pebbly sandstone, and mudstone	Mostly clast supported with rare matrix support, clast composition consistent with local basement material, interbeds contain coalified material and root traces	~10 cm to 3 m thick, interbeds range from ~4 cm to 0.5 m thick	Alluvial fans or subaqueous fan deltas in marginal lacustrine or estuarine setting
Rhythmite facies	Flv	Fine to very fine sandstone, siltstone, and mudstone	Normally graded sand or silt rhythmites with mudstone caps, climbing ripples, flame structures, rip-up clasts, very rare outsized clasts, zones of brittle and ductile deformation	~5 mm to 10 cm thick couplets, up to ~50 m thick packages of rhythmites	Distal turbidity currents or hyperpycnal flows in lacustrine or estuarine setting
Mudrock/fine-grained sandstone facies	Fl (laminated) Fm (massive)	Mudstone, siltstone, very fine to fine sandstone	Plant fossils, organic debris, laminated or massive	~3 cm to 10 m thick massive beds, ~1 m to 10 m thick packages of finely laminated sediment	Stable, low energy conditions, sediment settling out of suspension, in lacustrine or estuarine setting
Cross-stratified sandstone facies	St (trough cross beds) Sp (planar cross beds)	Very fine to very coarse quartz sandstone, sometimes pebbly	Planar and trough cross beds, normally graded, sometimes contains granule to pebble sized clasts, interbeds contain current ripples	~4 cm to 7 m thick, interbeds range from 1 cm to 0.5 m thick	High-energy, flowing water within fluvial system
Diamictite facies	Dmm (massive) Dms (stratified)	Clast-poor to clast-rich, muddy, stratified and massive diamictite	Granite, quartz, potassium feldspar clasts, coalified material and root traces common	~10 cm to 3 m thick	High density debris flows

Root-trace-bearing mudrock facies	Mrt	Siltstone, mudstone, and coal	Typically massive, sometimes finely laminated, abundant root traces, thin coal beds, peds, organic debris and intact plant fossils	~5 cm to 5 m thick	Paleosols, overbank floodplain deposits
Heterolithic bioturbated facies	mSb	Heterolithic, very-fine to medium quartz sandstone, siltstone, and mudstone	Sulfur-rich, vertical and horizontal bioturbation, plant material common, may contain micro-hummocky cross stratification	~10 cm to 3 m thick beds, ~20 m thick amalgamated packages	Restricted shallow marine or estuarine setting with periodic sediment/organic influx (likely tidally influenced)

Table 2.1. Lithofacies codes, descriptions, and paleoenvironmental interpretations. Facies codes from Benn and Evans (2010) and Farrell et al. (2012).
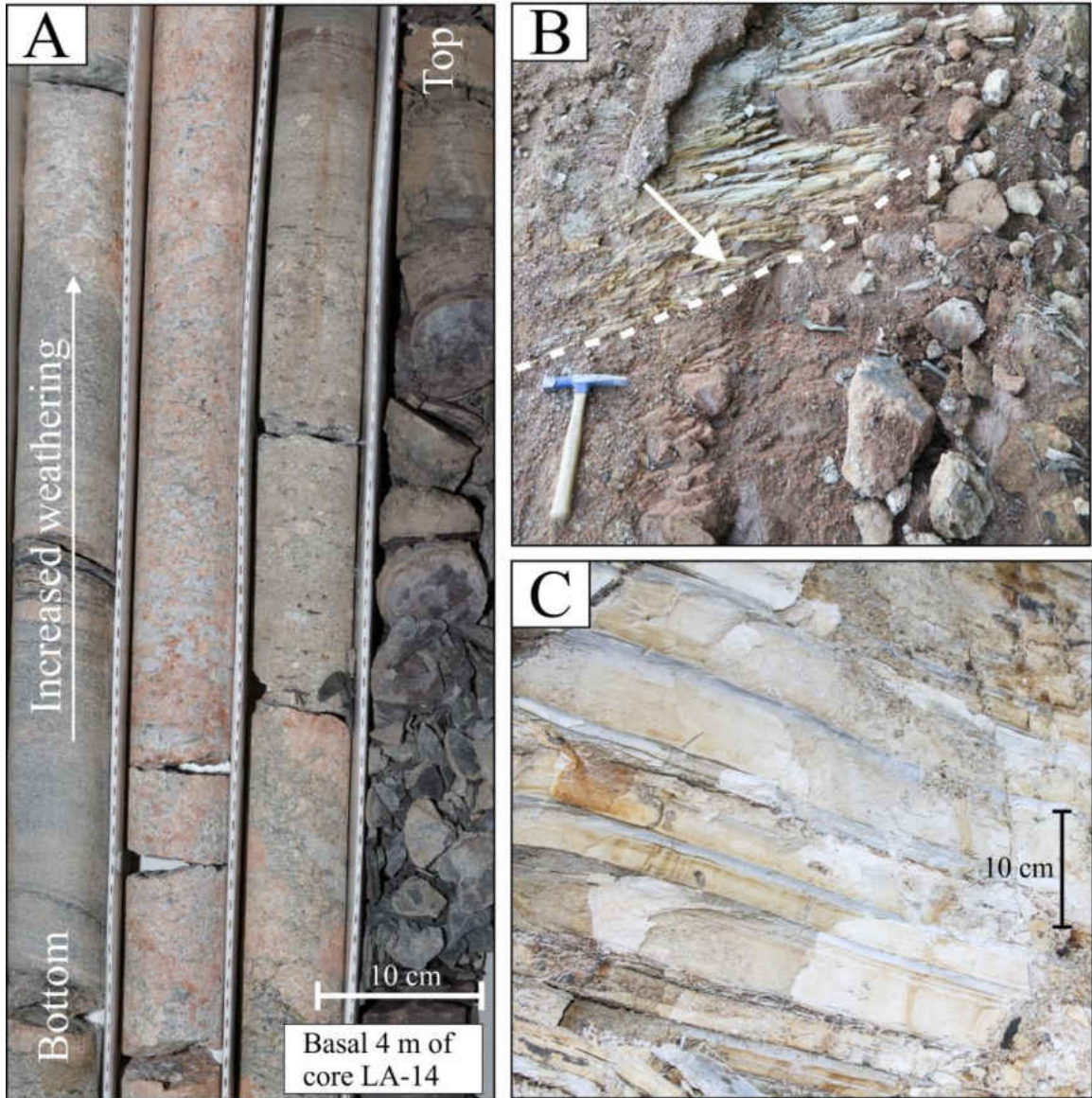
Fig. 2.4. Sandy conglomerate and breccia facies (Gm/Gp) in core LA-14 and rhythmite facies (Flv) at Location 2. A. Typical weathering profile of Gm/Gp facies in core directly above crystalline basement. B. Rhythmites (tilted) overlying weathered granite basement (also tilted) at Location 2. Contact between basement and rhythmites indicated by white dashed line and white arrow. Rock hammer (28 cm) used for scale. C. ~10 cm rhythmite couplets from the Flv facies in outcrop.

Fig. 2.5. Key features of rhythmite facies (Flv) in cores AB-06 and CA-53. A. Ripples (black arrows) in sandy, bottom portion of couplets, indicating traction between flows and underlying substrate. B. Load and flame structures (black arrows) suggesting rapid loading of unlithified substrate. C. Rip-up clasts of deformed rhythmites in sandstone interbed of Flv facies (black arrow), suggesting traction between flows and underlying substrate. D. Discrete zone of brittle faulting in basal portion of core CA-53, possible evidence for tectonism or failure along delta front.

65
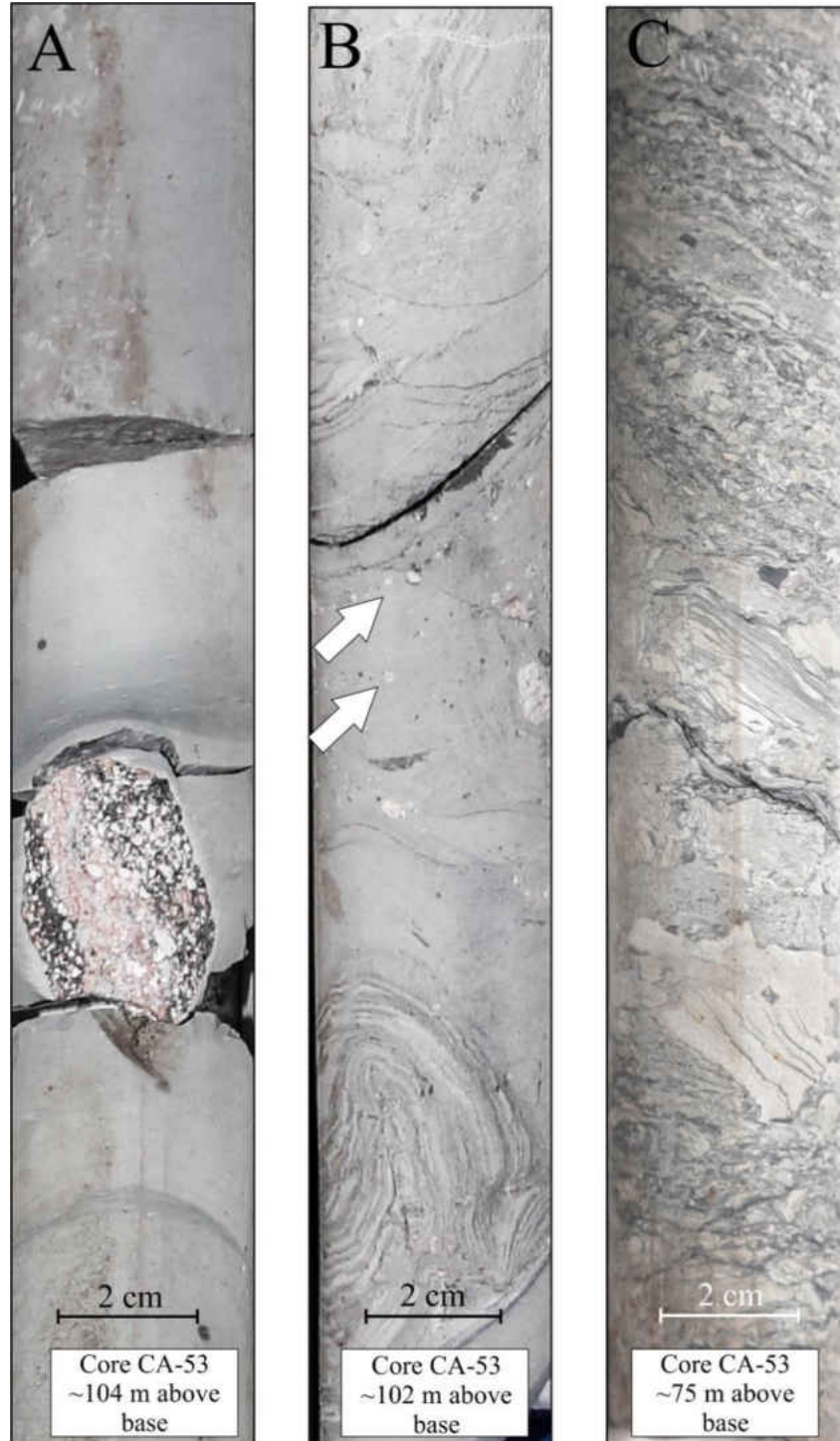
Fig. 2.6. Key features of rhythmite facies (Flv) in cores AB-06 and CA-53. A. Very rare example of lonestone. B. Folded and faulted rhythmites from syndepositional brittle (faulting) and ductile deformation (slumping). White arrows indicate small granule and pebble sized clasts occurring along bedding planes. C. Brecciated and sheared rhythmites, possible evidence for tectonism or failure along delta front.
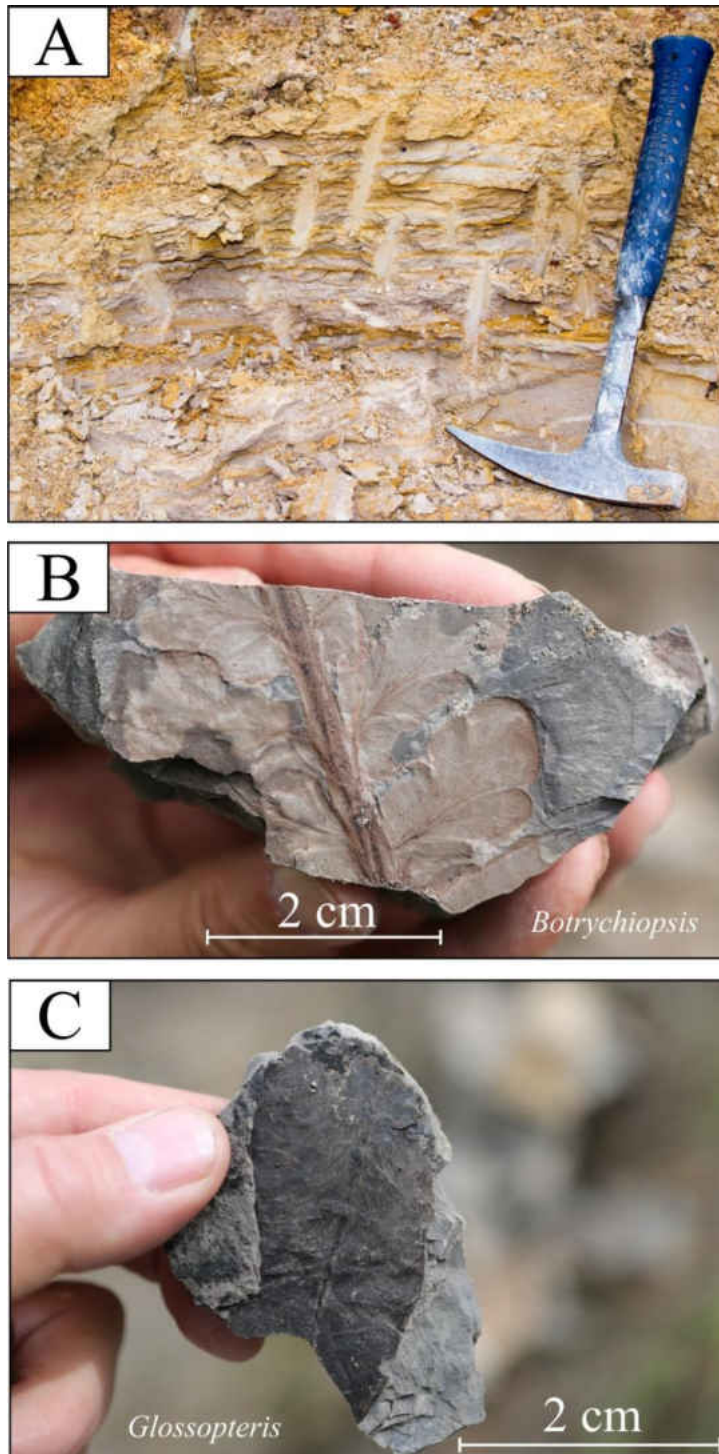
Fig. 2.7. Mudrock/fine-grained sandstone facies (Fl/Fm) in outcrop. A. Laminated siltstone (Fl facies) beds at Location 3. Rock hammer (28 cm) for scale. B. Botrychiopsis fossil from top of the Fl facies at Location 1. C. Glossopteris fossil from top of Fl facies at Location 1.
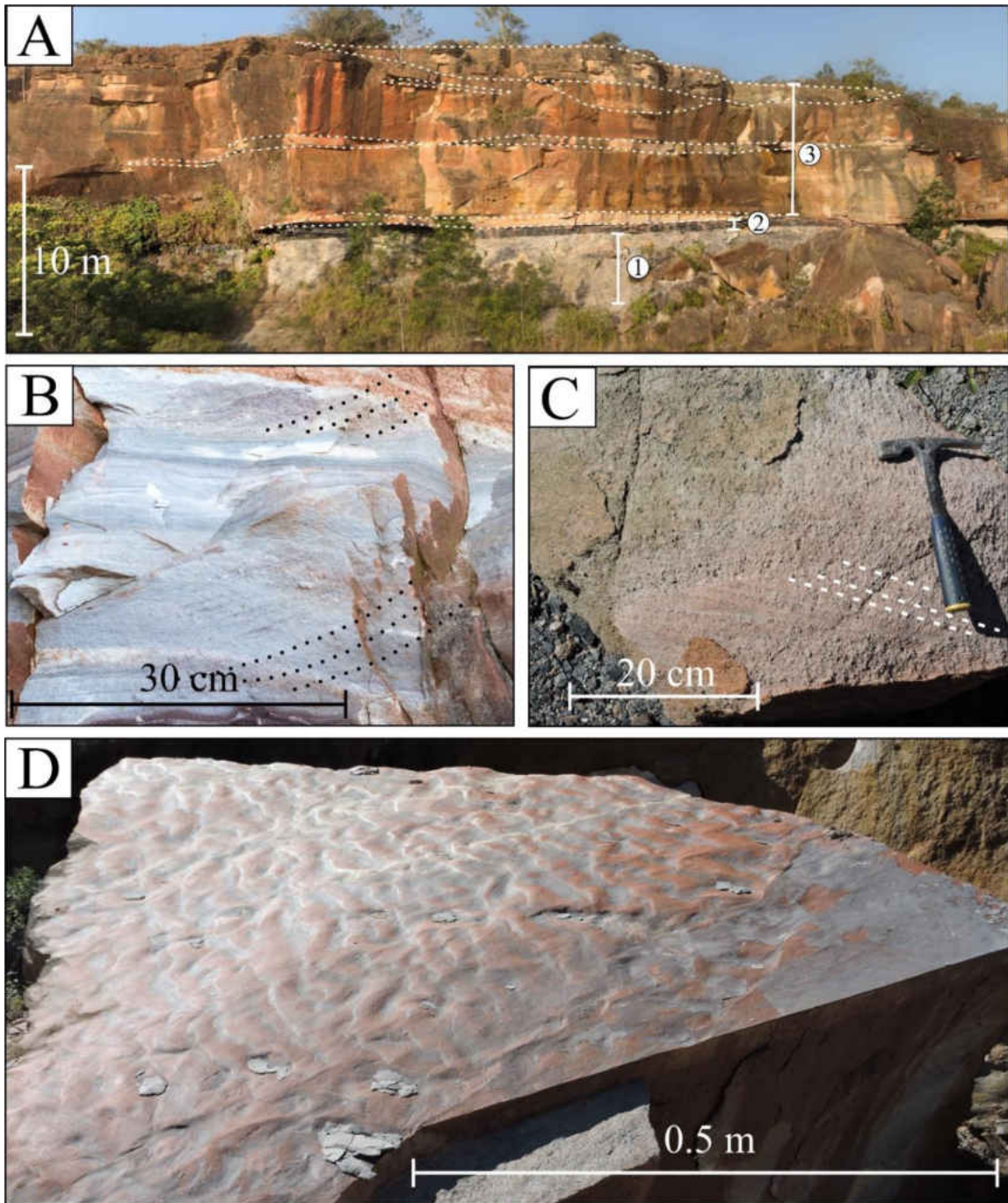
Fig. 2.8. A. Photomosaic of Location 1 (Morro do Papaléo). (1) Diamictite (Dmm/Dms) facies. (2) Root-trace-bearing mudrock facies (Mrt). (3) Cross-stratified sandstone facies (St/Sp). Channel body geometries within St/Sp facies outlined by dashed white lines. B. Trough cross beds from St facies at Location 1 indicated by black dashed lines. C. Planar cross beds from Sp facies at Location 1 indicated by white dashed lines. D. Rippled bedding surface at Location 1.

68
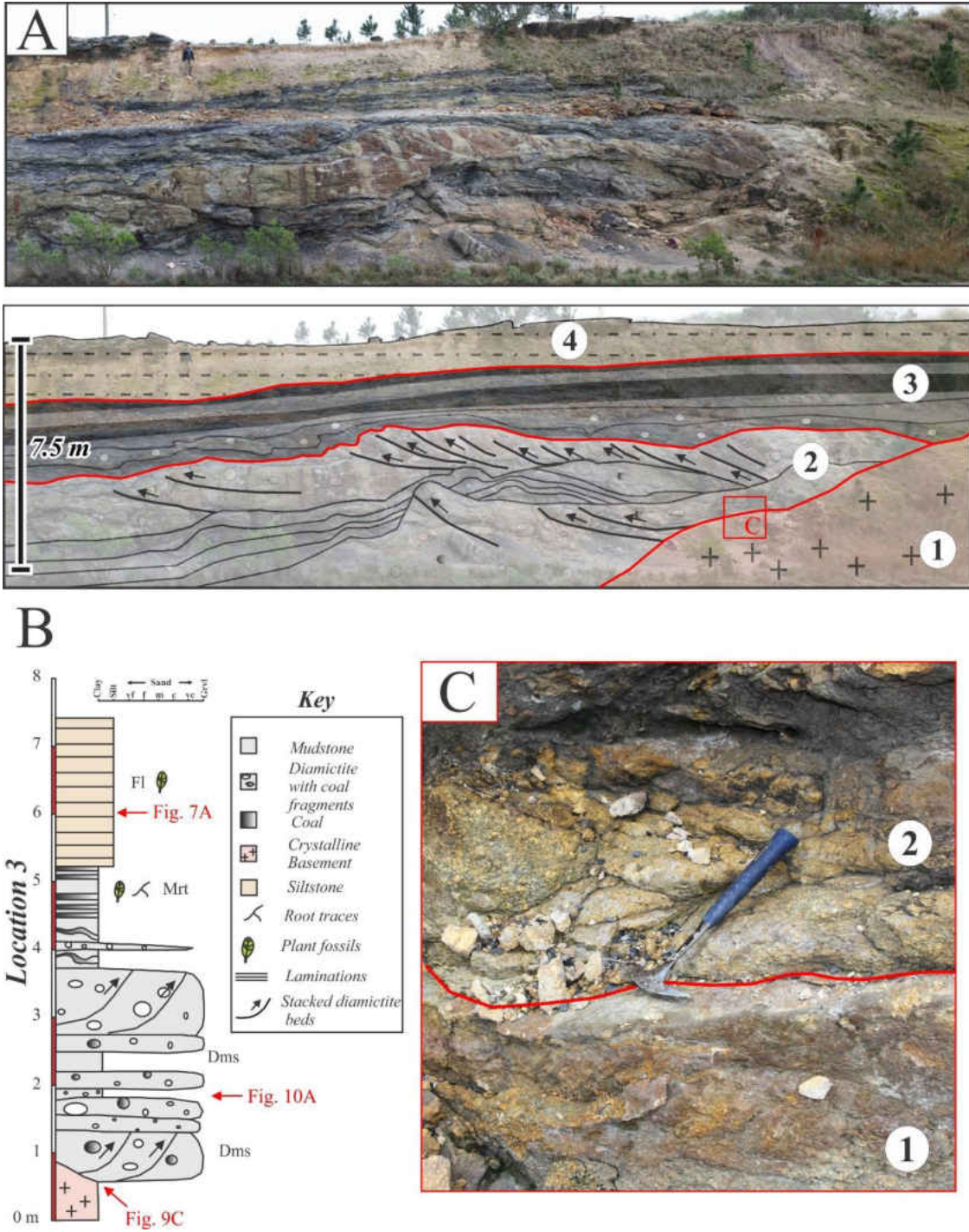
Fig. 2.9. A. Photomosaic of Location 3. Red solid lines are contacts between facies and black lines with arrows are stacked diamictite beds. (1) Granite basement. (2) Diamictite (Dms) facies. (3) Root-trace-bearing mudstone (Mrt) facies. (4) Mudrock/fine-grained sandstone (Fl) facies. B. Stratigraphic column of Location 3. C. Location 3 contact between unpolished/unstriated granite basement (1) and onlapping Dms facies (2) indicated by red solid line. Rock hammer (28 cm) for scale.

69
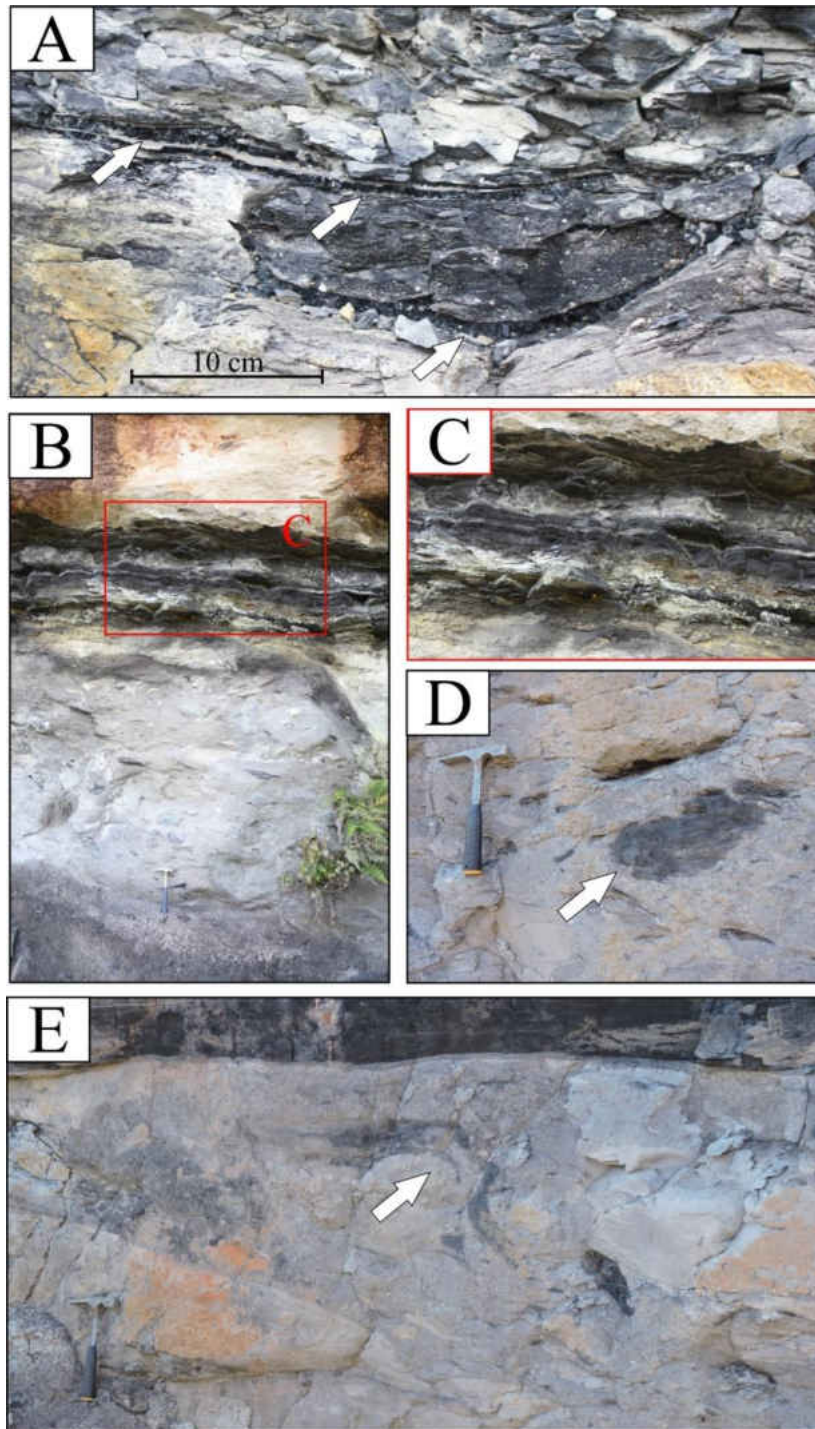
Fig. 2.10. A. Thin coal lenses in the diamictite (Dms) facies at Location 3. B. Outcrop at Location 1 with root-trace-bearing mudrock facies overlying the diamictite facies (Dmm). Rock hammer (28 cm) for scale. C. Root-trace-bearing mudrock facies. D. Carbonaceous siltstone rip-up clast in Dmm facies at Location 1. Rock hammer (28 cm) for scale. E. Soft-sediment deformation of siltstone raft in Dmm facies at Location 1. Rock hammer (28 cm) for scale.
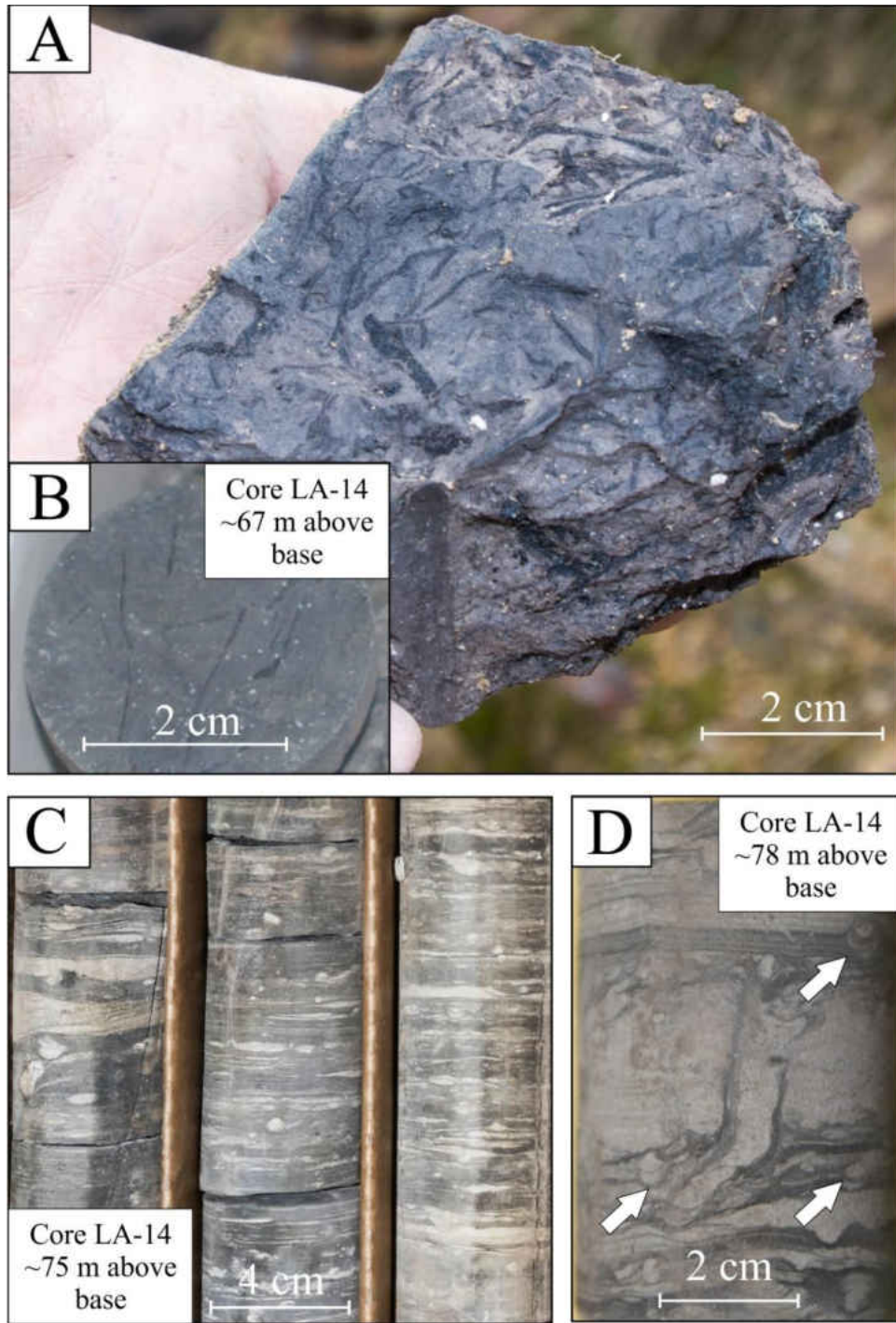
Fig. 2.11. Root-trace-bearing mudstone (Mrt) facies and heterolithic bioturbated (mSb) facies. A. Root traces within Mrt facies at Location 3. B. Root traces within Mrt facies in core LA-14. C. Heterolithic bioturbated beds in core IB-94. D. Bioturbation with concave-up spreite (white arrows) in core LA-14.
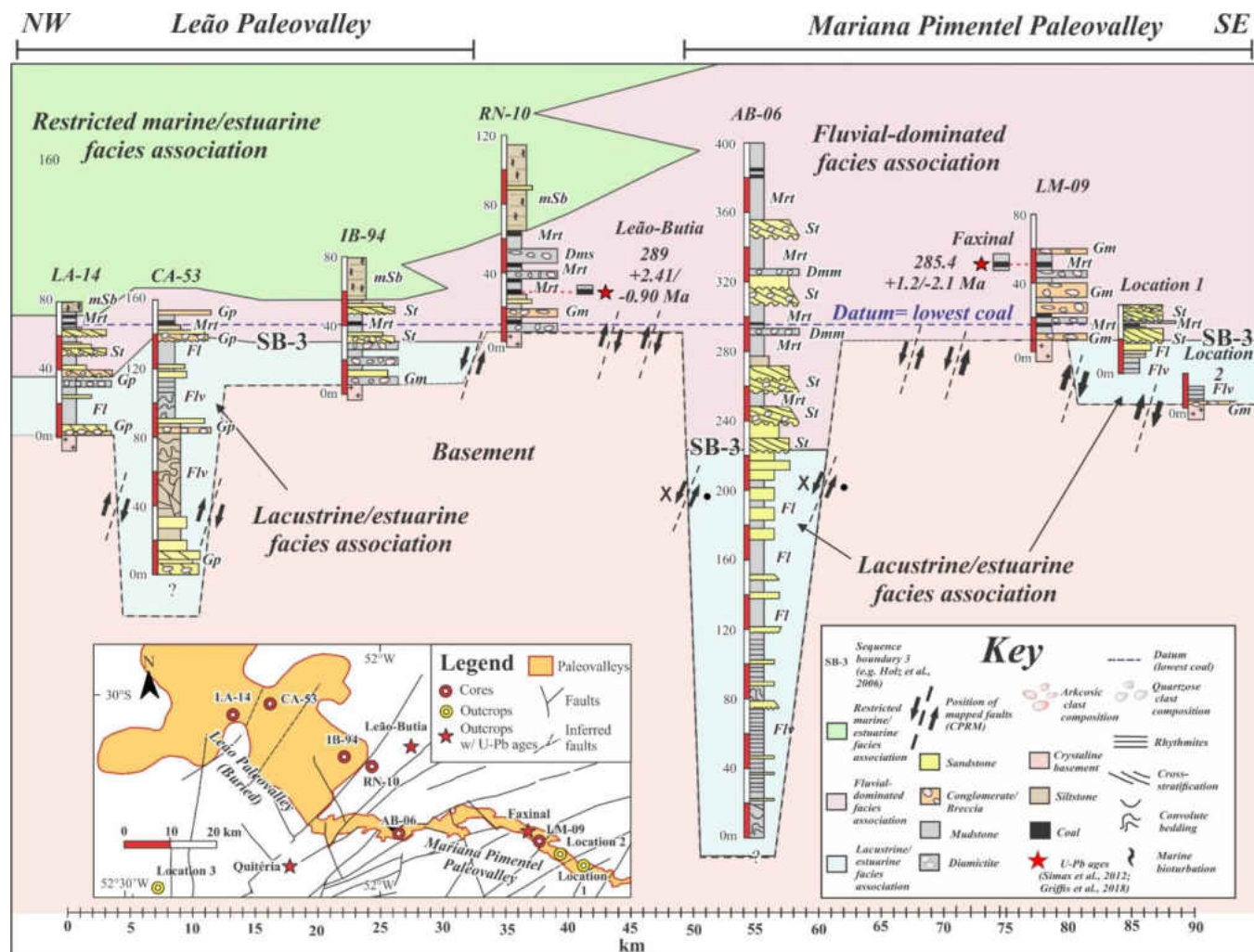
Fig. 2.12. Cross section of Mariana Pimentel and Leão paleovalleys. Vertical exaggeration is 140x and datum (dashed blue line) is based on lowermost coal beds. U-Pb ages (red stars) are from Simas et al. (2012) and Griffis et al. (2017).
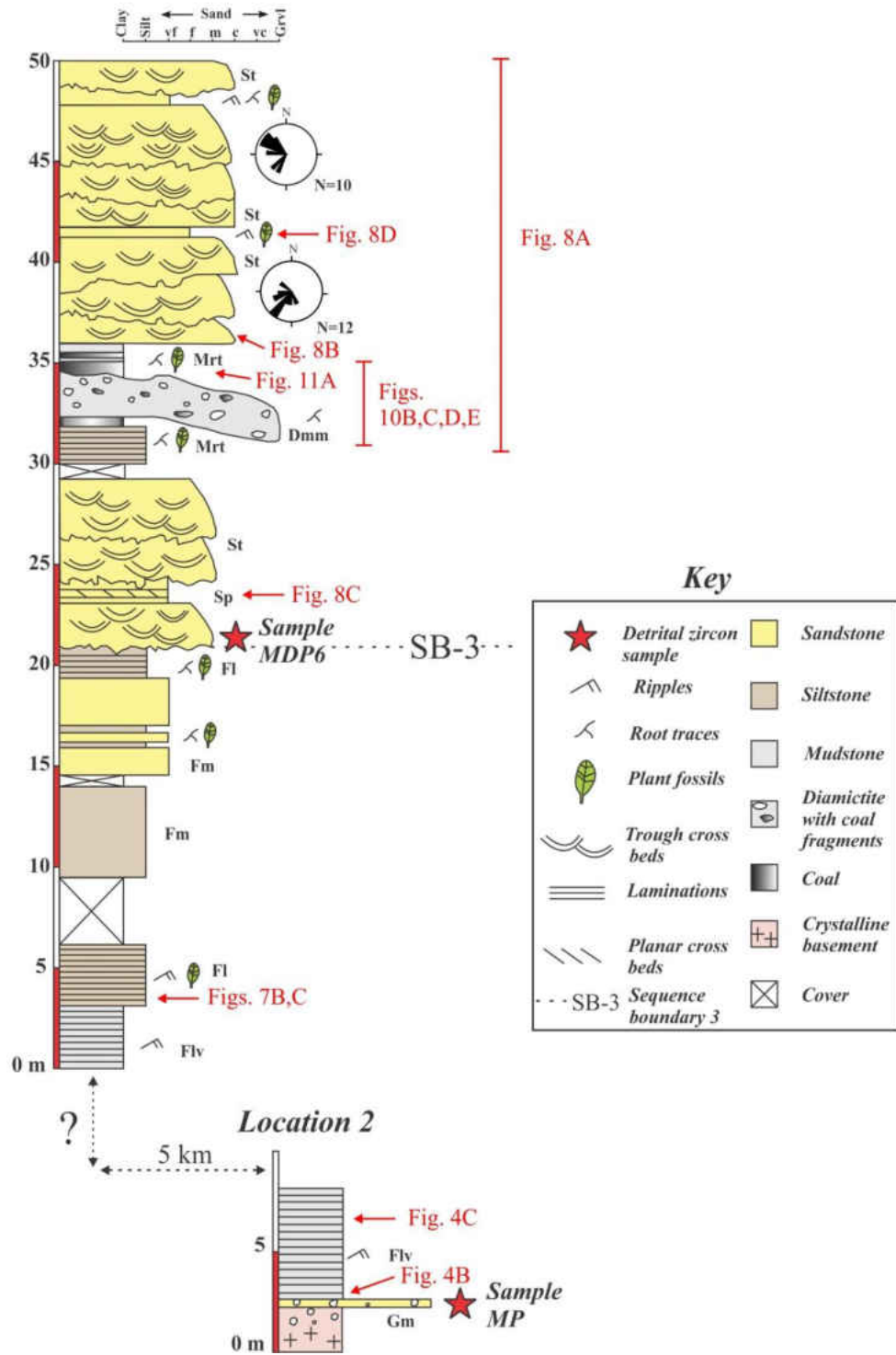
Fig. 2.13. Stratigraphic columns from Location 1 (Morro do Papaléo) and Location 2 with detrital zircon sample locations indicated by red stars (column after Iannuzzi et al. (2006); Smaniotto et al. (2006)).
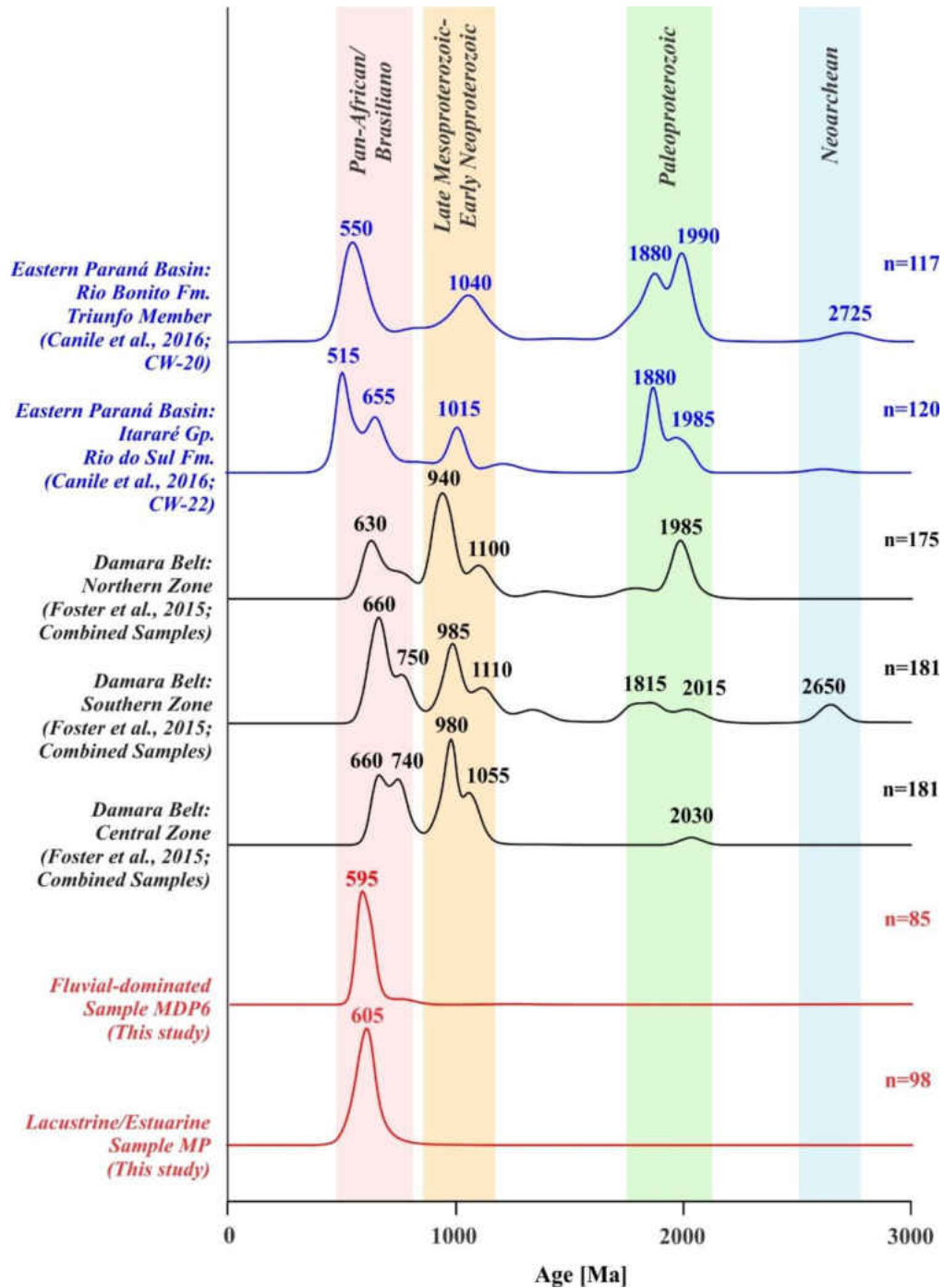
Fig. 2.14. Detrital zircon results from Mariana Pimentel Paleovalley. Kernel density estimates for samples MP and MDP6 (red; this study) compared to the Damara belt in Namibia (black; Foster et al., 2015) and the eastern margin of the Paraná Basin (blue; Canile et al., 2016).

Evolution of Mariana Pimentel
and Leão paleovalleys
(Asselian-Artinskian)
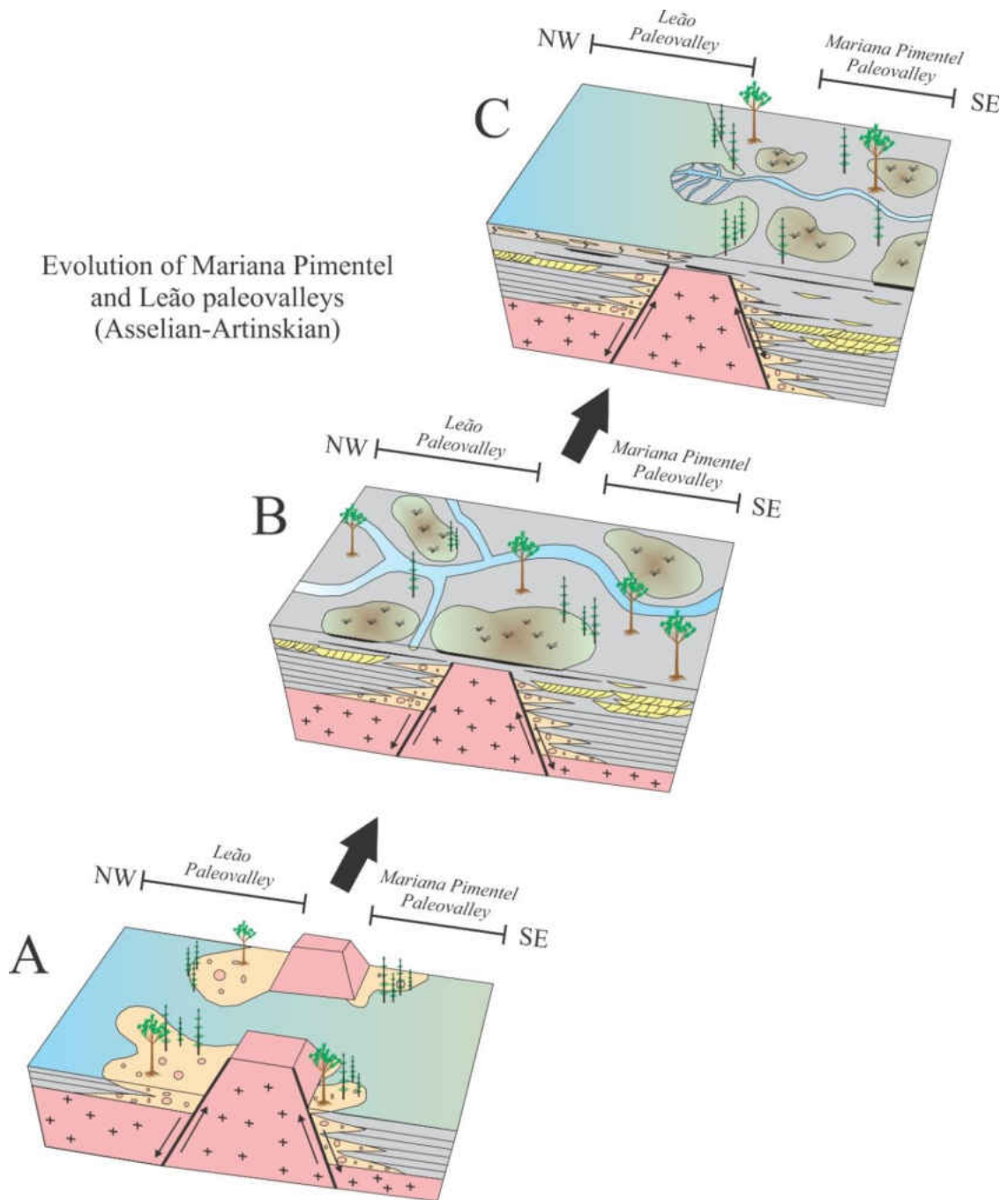
Fig. 2.15. Block diagrams showing evolution of Mariana Pimentel and Leão paleovalleys during early Permian. A. Lacustrine/Estuarine facies association. B. Fluvial-dominated facies association. C. Restricted marine/estuarine facies association.

Chapter 3. Carboniferous glaciotectonized sediments in the southernmost Paraná Basin, Brazil: Ice marginal dynamics and paleoclimate indicators

Abstract

Carboniferous glaciogenic strata (Itararé Gp.) in the southernmost Paraná Basin, Brazil exhibit soft-sediment deformation features previously interpreted as glaciotectonism. These sediments were studied in detail to confirm that they were deformed by ice and to assess the nature of the glaciation, depositional environments, and paleoclimate in this region during the Carboniferous. Five outcrops were described along a railroad transect that contains a conglomerate and diamictite facies with striated and faceted clasts, a medium sandstone facies, a fine grained silt/clay rhythmite and mudstone facies with dropstones and diamictite pellets, a sandy clinoform facies, and a folded sandstone with interbedded mudstone facies. The depositional environment for these sediments is interpreted as an outwash fan and fan delta from an ice-proximal, transitional terrestrial-to-estuarine setting. Rb/K values from the rhythmites reflect a transition from a freshwater to brackish environment and the Chemical Index of Alteration (CIA) of the rhythmites ranges from 65-73, reflecting a relative increase in the degree of chemical weathering through time. Deformation features include widespread folding, thrust faults, hydrofractures, décollement surfaces, and piggyback fold-thrust complexes. The deformation is interpreted as evidence of a push-moraine complex formed by at least two complete ice advance/retreat cycles. The occurrence of décollement surfaces, plastically deformed proglacial sediments, and hydrofractures indicate a dynamic, warm-based or polythermal glacier. Abundant outwash sediments, seasonal rhythmite laminae, and the shift to average CIA values all support a temperate paleoclimate. Deformation structures indicate a NW direction of ice shove that is in agreement with the regional-scale hypothesis that a NNW flowing lobe extended out of Uruguay during the Carboniferous and terminated in the

southernmost Paraná Basin. This study demonstrates that late Paleozoic glaciation in this region was more dynamic than previously understood, with high frequency fluctuations in ice marginal positions.

3.1. Introduction

The preservation of pre-Cenozoic glaciotectonized sediments is rare and this is particularly true of glacially-deformed sediments deposited in terrestrial settings. However, when recognized, these features provide information that is useful for reconstructing the motion of ancient glaciers and determining the paleoclimate under which they existed (e.g. Visser and Loock, 1982; Rocha-Campos et al., 2000; Le Heron et al., 2005; Isbell, 2010; Busfield and Le Heron, 2013; Blignault and Theron, 2015; Vesely et al., 2015). Both subglacial and proglacial deformation structures contain clues about the thermal conditions of ancient glaciers (i.e. cold based vs. warm based vs. polythermal), the hydrology, the rheology of the sediments, and the direction of ice flow (e.g. Alley, 1989, 1991; Hart and Boulton, 1991; van der Wateren, 1995, 2002; van der Wateren et al., 2000; Phillips et al., 2002, 2007, 2008; van der Meer et al., 2003; Evans and Hiemstra, 2005; Evans et al., 2006; Lee and Phillips, 2008; Menzies et al., 2010). Furthermore, proglacial deformation structures are directly linked to glaciers' ice-marginal processes as well as the nature of the foreland into which they advanced (e.g. Hart and Boulton, 1991; van der Wateren, 1995, 2002; Bennett, 2001; Benediktsson et al., 2015; Phillips, 2018). Thus, combining observations of glaciotectonism with descriptions of primary sedimentology is especially helpful when interpreting deep-time glaciations.

Despite this, identifying glaciotectonism in pre-Cenozoic sediments can be difficult as some non-glacial mass transport processes (i.e. slumps and slides) can produce similar deformation related to shearing, folding, and thrusting (e.g. Visser et al., 1984). Slides and slumps can also create grooved surfaces that are commonly misidentified as subglacial in origin (e.g. Posamentier and Walker, 2006). Further complicating such interpretations, slumps and slides of glaciogenic sediments are common in glacially-influenced environments due to the high sedimentation rates and steep slopes of depositional surfaces (e.g. Hart and Roberts, 1994). Many diamictites, once considered subglacial tillites and used to estimate the extent of deep-time glaciations, are now reinterpreted as sediments that were redeposited in deep-water basins via mass transport processes or ice-rafting (e.g. Eyles, 1990; Eyles and Eyles, 2000; Isbell et al., 2012a; Mottin et al., 2018; Vesely et al., 2018). For these reasons, a number of questions must be addressed before evaluating deformed strata. This includes determining whether the paleoenvironment was marine or terrestrial and identifying whether the sediments were deformed by entirely non-glacial processes, processes indirectly related to glaciation, or by the direct movement of a grounded glacier. Specifically, this means distinguishing whether deformation was the product of slumps, slides, overriding ice, iceberg keels, and/or thrusting and ploughing in front of a glacier.

Late Paleozoic glacial deposits are both geographically and temporally widespread, providing an ideal test for recognizing, describing, and interpreting glaciotectonism in deep time. The late Paleozoic ice age (LPIA; Famennian - Wuchiapingian) was the last major icehouse of the Phanerozoic and the only pre-Cenozoic glaciation with a complex terrestrial biota (e.g. Isbell et al., 2003, 2012b; Fielding et al., 2008; Montañez and Poulsen, 2013; Frank et al., 2015). This has made the LPIA an important time interval for studying the feedbacks between glacial extent,

climate, and other Earth systems. Insight into these complex relationships requires a detailed understanding of the extent, location, and nature (i.e. thermal regime, confined vs. unconfined) of glaciers during the LPIA.

Tomazelli and Soliani Júnior (1997) identified compressively-deformed, late Paleozoic glacial strata on the southernmost margin of the Paraná Basin (Brazil), which they interpreted as proglacial, terrestrial deposits that were deformed by a combination of glaciotectonism and/or mass-transport processes. LPIA glaciation remains poorly understood in this region of west-central Gondwana as there are multiple competing hypotheses regarding the paleoenvironment (marine vs. terrestrial), the extent and location of ice centers (multiple smaller ice centers vs. a single massive ice sheet), and the paleoclimate (temperate, warm based glaciation vs. polar, cold based glaciation) (e.g. Frakes and Crowell, 1972; Crowell and Frakes, 1975; Visser, 1993; Santos et al., 1996; Tomazelli and Soliani Júnior, 1997; Crowell, 1999; Rocha-Campos et al., 2008; Tedesco et al., 2016; Fedorchuk et al., 2018).

Therefore, the aims of this study are to: (1) better characterize the architecture and sedimentology of these deformed glacial deposits, (2) distinguish the processes involved in their deposition and determine whether the deformation fits the criteria for glaciotectonism, and (3) decipher what this tells us about the nature of glaciation and the paleoclimate of west-central Gondwana during the Carboniferous. These objectives were accomplished by describing multiple stratigraphic sections through the outcrops in question, measuring the orientation of meso- to macro-scale deformation structures and paleocurrent indicators, evaluating thin section evidence, and examining the geochemistry of the sediments.

3.2. Geologic setting and location

The Paraná Basin is an intracratonic basin that covers much of southern Brazil and extends into Uruguay, Paraguay, and Argentina (Fig. 3.1A). Basin fill was deposited from the Ordovician to the Cretaceous, containing a detailed record of glaciation during the Carboniferous and early Permian. Paraná Basin glacial sediments from the Carboniferous and Permian are part of the Itararé Gp. In subsurface descriptions (basin-wide), the Itararé Gp. is divided into three formations (oldest to youngest): the Lagoa Azul, the Campo Mourão, and the Taciba (e.g. França and Potter, 1991).

In the study area (southernmost margin of the Paraná Basin), Taciba Fm. glacial sediments rest unconformably on top of Proterozoic igneous and metamorphic terranes known as the Rio Grande do Sul Shield (RGS) as well as the sedimentary rocks of the Neoproterozoic to early Cambrian Camaquã Basin (Fig. 3.1B). The RGS was part of a paleotopographic high during the late Paleozoic and the glacial sediments in this region are highly discontinuous, occurring in isolated patches on the western half of the Shield (Fig. 3.1B). This is likely due to erosion and differential uplift during post-glacial times or preservation in paleotopographic depressions (e.g. Mau, 1960; Martin, 1961; Santos et al., 1996; Tomazelli and Soliani Júnior, 1997). Meanwhile, the eastern half of the RGS contains no preserved direct evidence of glaciation (Fedorchuk et al., 2018). While the onset of glaciation in the Paraná Basin is poorly constrained, U-Pb ages collected from postglacial tonsteins suggest that the ice center on the southernmost margin of the Paraná Basin had receded from the RGS by the end of the Carboniferous. This is based on the fact that the oldest post-glacial sediments (Rio Bonito Fm.), which unconformably overlie the Itararé Gp. in this area, were dated at ~298 Ma, close to the

Gzhelian/Asselian boundary (e.g. Cagliari et al., 2016; Griffis et al., 2018). Biostratigraphically, the upper Itararé Gp. and Rio Bonito Fm. interval on the RGS corresponds to the range of the *Vittatina costabilis* Interval Zone (VcIZ), which contains the first occurrence of glossopterids (Souza and Marques-Toigo, 2005; Iannuzzi et al., 2010). The appearance of *Vittatina* and bissacate grains has been used to define the Carboniferous-Permian boundary by palynologists throughout Gondwana (Stephenson, 2008). Although *Vittatina* is found in the post-glacial Rio Bonito Fm., it remains unclear whether a latest Caboniferous (Itararé Gp.) *Vittatina*-type association occurs on the RGS.

The outcrops described in this study are ~85 km N of the Brazil-Uruguay border and were first described by Tomazelli and Soliani Júnior (1997). They occur along a ~2.5 km stretch of railroad tracks located ~3 km NW of Ibaré, part of the Lavras do Sul municipality, Rio Grande do Sul State (Brazil) (Fig. 3.1C). The railroad cut is oriented NW-SE and there are five separate locations along the cut, listed here in numerical order (Figs. 3.1 and 3.2). Location 1 is the southernmost outcrop and Location 5 is the northernmost outcrop. Locations 1, 2, and 3 are laterally equivalent, as beds can be traced horizontally between these sections. Similarly, Locations 4 and 5 are laterally equivalent (Fig. 3.2). There is a 1.5 km covered section between Locations 1-3 and Locations 4-5. Locations 1-3 are ~10 m higher in elevation compared to Locations 4 and 5 (Fig. 3.2) with beds exhibiting no overall dip (excluding discrete deformed zones). All the railroad track localities occur within the the Ibaré lineament, a major NW-SE trending Proterozoic transcurrent shear zone that separates two terranes of the RGS.

3.3. Previous work

Glacial sediments on the RGS have been recognized for some time (e.g. Mau, 1960; Martin, 1961; Delaney, 1964; Corrêa da Silva, 1978; Santos et al., 1996; Tomazelli and Soliani Júnior, 1997). Tomazelli and Soliani Júnior (1997) described a grooved surface only ~8 km from the study area that was formed by ice overriding soft sediment. Such grooved surfaces have been described across the western half of the RGS with N-S and NE-SW orientations (e.g. Tomazelli and Soliani Júnior, 1982, 1997). Although some of these grooved surfaces lack evidence of relative motion, other outcrops contain clasts that were ploughed towards the north. Hence, most studies of late Paleozoic glaciation on the RGS have concluded that an unconfined lobe flowed towards the NNW out of Uruguay during the Carboniferous (e.g. Frakes and Crowell, 1972, Crowell and Frakes, 1975; Amato, 2017; Assine et al., 2018; Griffis et al., 2019; Vesely et al., 2018). This interpretation is supported by recently collected magnetic fabrics from some of the grooved surfaces that lack ploughed clasts that also show a N direction of ice flow (Amato, 2017). However, it has also been suggested that some grooved surfaces on the southern RGS might indicate ice flowing to the S or SE, implying an ice center on the RGS that radiated outward in all directions (e.g. Santos et al., 1996; Rocha-Campos et al., 2008). Other authors have interpreted (confined) outlet glaciers, restricted to a network of paleovalleys, on the RGS that were draining westward from an ice center over Africa (e.g. Mau, 1960; Tedesco et al., 2016). In contrast to this, a recent review of the sedimentary fill of these paleovalleys on the eastern RGS was found to lack clear evidence for glaciation (Fedorchuk et al., 2018). Finally, others have depicted a long-lived, unconfined ice sheet, originating in Africa, that extended

across the entire Paraná Basin (e.g. Gesicki et al., 1998; Riccomini and Velázquez, 1999; Gesicki et al., 2002; Starck and Papa, 2006).

Additionally, while almost all recent work has interpreted temperate, warm-based glaciation in the Paraná Basin based on the paleolatitude (~45-55°S; Torsvik and Cocks, 2013) and facies assemblage (e.g. Santos et al., 1996; Trosdtorf et al., 2005; Vesely et al., 2015), some authors have described ice shelves from the adjacent Greater Karoo Basin in South Africa (e.g. Visser, 1989). This could imply colder conditions on the nearby and less studied RGS (southernmost margin of basin) since modern ice-shelves only exist under an isotherm of less than -5°C (e.g. Cook et al., 2005). Finally, several studies have suggested that the thin patchy rhythmite facies deposited on the RGS is terrestrial in nature (deposited in ice-marginal lakes) (e.g. Tomazelli and Soliani Júnior, 1997). However, the presence of *Tasmanites* in some of these rhythmite beds has been used to suggest a marine or marine-influenced environment (e.g. Santos et al., 1996).

3.4. Methods

Outcrops along the railroad tracks were photographed and studied using standard sedimentology field techniques. Stratigraphic sections were measured at each of the five locations and observations were noted of the following: grain size, sorting, sedimentary structures, lithology, facies, paleocurrent orientations, fold axes orientations, thrust sheet orientations, nature of contacts, sediment body geometries, relationships with adjacent strata, and unit thicknesses. Twelve samples (<0.5 kg) were collected across all five locations for thin

section analysis of microfabrics. Facies analysis was conducted based on sedimentary structures, lithologies, and key features observed in both macro and micro scales.

Fourteen samples were collected at an interval of every 10 cm from rhythmites at Location 3 for geochemical analyses using X-ray fluorescence (XRF) and laser ablation inductively coupled plasma mass spectrometry (LA-ICP-MS). Samples were taken from 10-20 cm in the outcrop to avoid recently weathered surfaces. Both XRF and LA-ICP-MS data was collected at Michigan State University according to the procedures of Rooney et al. (2012, 2013). Fused disk samples were analyzed on a Bruker S4 Pioneer (4 kW wavelength dispersive X-ray fluorescence spectrometer) for major element oxides. Trace element data was collected from these samples by LA-ICP-MS using a Thermo Scientific ICAP Q quadrupole inductively coupled plasma mass spectrometer connected to a Photon Machines Analyte G2 193 nm excimer laser. Complete XRF and LA-ICP-MS data can be found in Appendix C.

3.4.1. Rb/K paleosalinity proxy

Rb/K ratios were measured from rhythmites at Location 3. These values were used as a paleosalinity proxy (e.g. Campbell and Williams, 1965; Scheffler et al., 2003; Scheffler et al., 2006; Ocakoğlu et al., 2016; Ye et al., 2016). This proxy is based on the fact that Rb^+ (1.48 Å) has a similar ionic radius to K^+ (1.33 Å) and, therefore, can be substituted for the K^+ in illite (Ye et al., 2016). Since Rb is significantly more abundant in seawater (~0.12 ppm) compared to freshwater (~0.0013 ppm), Rb/K ratios are typically higher in marine clays compared to lacustrine clays (e.g. Campbell and Williams, 1965; Taylor and McLennan, 1985). Rb/K ratios $<4{\cdot}10^{-3}$ are interpreted as freshwater and Rb/K ratios $>6{\cdot}10^{-3}$ are interpreted as marine, in which

ratios in between these values are interpreted as representing brackish conditions (e.g. Campbell and Williams, 1965; Scheffler et al., 2003; Scheffler et al., 2006). It should be noted that Rb/K ratios are also affected by chemical weathering, in which Rb/K values tend to increase slightly in response to higher illite and kaolinite content (e.g. Harriss and Adams, 1966; Nesbitt et al., 1980; Scheffler et al., 2006). This is due to the larger Rb^+ ion being preferentially retained on clay minerals (Nesbitt et al., 1980). In this study, Rb/K values were used to help constrain the depositional setting of the study area by determining if the rhythmites were deposited under freshwater, brackish, or marine conditions.

3.4.2. Chemical index of alteration (CIA)

Rhythmites at Location 3 were also evaluated using the chemical index of alteration (CIA) as a proxy for the degree of chemical weathering (e.g. Nesbitt and Young, 1982; 1996). The CIA is defined as $\{(Al_2O_3)/(Al_2O_3 + K_2O + Na_2O + CaO)\} \cdot 100$, in which a value of 50 represents unweathered feldspar and 100 represents kaolinite. Typical mudstone values are ~70-75 (e.g. Nesbitt and Young, 1982). Chemical weathering of labile minerals causes the leaching of Ca^{2+}, K^+, and Na^+, which leads to the formation of more stable minerals such as illite, kaolinite, hematite, and goethite (Nesbitt and Young, 1982; Nesbitt et al., 1996). Conversely, physical weathering processes such as glacial erosion can break down grains into smaller sizes without altering the chemical composition and mineralogy of the sediments. Therefore, the CIA can often distinguish between dry and cool glacial intervals in which the degree of chemical weathering on a landscape is relatively low (compared to physical weathering), versus wet and humid interglacial or post-glacial periods when chemical weathering is relatively high (e.g. Bahlburg

and Dobrzinski, 2011). This information was used in conjunction with the sedimentological evidence to help assess the paleoclimate of the RGS during the late Paleozoic.

3.5. Facies analysis and process interpretations

Five lithofacies (Facies A-E) were observed at Locations 1-5 (Table 3.1). These include a conglomerate and diamictite facies (A), a sandy clinoform facies (B), a medium sandstone facies (C), a folded sandstone with interbedded mudstone facies (D), and a rhythmite and mudstone with outsized clasts facies (E). Classification of poorly sorted sediments was based on the criteria of Hambrey and Glasser (2003).

Conglomerate and diamictite facies (Facies A)

The conglomerate and diamictite facies (Facies A) outcrops on the southern end of the study area (Locations 1, 2, and 3). Facies A is comprised of grain-supported, sandy conglomerate and gravelly sandstone interbedded with matrix-supported, clast-rich sandy diamictite. Clasts range from granule-to-cobble sized, are sub-rounded to well-rounded, and have diverse compositions that include abundant alkali-feldspar granite, diorite, schist, phyllite, gneiss, quartzite, and sandstone. Some clasts exhibit faint striations and facets, which is consistent with subglacial abrasion during part of their transport history (Fig. 3.3A). Conglomerate beds are erosionally based and exhibit crude bedding and cross stratification in some areas (Fig. 3.3B). Similarly, interbedded gravelly sandstones contain ripples that indicate flow towards the NW (mean azimuth of all cross stratification in Facies A and C=312±10.2°, Fig. 3.2). Conglomerate

and diamictite beds range from 4 cm-1 m thick, are laterally extensive, and do not contain channelized geometries. At Locations 2 and 3, this facies shows evidence of deformation in the form of a décollement surface and two forward propagating fold-thrust complexes (i.e. piggyback thrusting) that are 1-3 m high and ~50 m apart (Fig. 3.4A-C). The dip of the thrust planes increases to the SSE of each complex, away from the frontal fault. Fold axes are oriented NE-SW and all thrust sheets dip towards the SSE (Fig. 3.2). At localities 2 and 3, Facies A is overlain by the dipping fine sandstone beds of Facies B and the rhythmites of Facies E. One critical observation is that the basal rhythmites (Facies E), which overlie Facies A at Locations 2 and 3, are undeformed and do not drape over the fold-thrust complexes. Rather, the horizontally-laminated and undeformed rhythmites, which occur between the complexes, onlap onto the limbs of the anticlinal fold-thrust complexes before eventually overtopping them (Fig. 3.4A).

Facies A is interpreted as a combination of coarse grained outwash and cohesive debris flows from a proglacial outwash fan. The fact that undeformed, basal rhythmites (Facies E) onlap onto folded and faulted conglomerate and diamictite beds (Facies A) demonstrates that deformation of this facies occurred after deposition but prior to deposition of the overlying rhythmites and mudstone with outsized clasts (Facies E). Since striations and facets are still preserved on some clasts, it is likely that deposition occurred in a glacially-influenced setting. A terrestrial environment would suggest that the conglomerate and gravelly sandstone beds were deposited by unconfined braided streams on the fan surface while a subaqueous environment implies that the sediments were deposited as part of a fan delta or as jet-efflux deposits at the exit of submerged sub/englacial tunnels. These interpretations are based on the grain-supported beds with cross stratification and sub-rounded to well-rounded clasts that indicate transport by bedload dominated flows. The lack of evidence for well-established, channelized flow supports

the interpretation of a poorly confined system with abundant sediment supply. The interbedded, matrix-supported diamictite beds are viewed as cohesive debris flows on the fan surface that were comprised of resedimented outwash. These debris flows may have been triggered during intervals of intense meltwater discharge or the sliding of debris off the glacier.

Sandy clinoform facies (Facies B)

The sandy clinoform facies (Facies B) consists of thin (~1-4 cm thick), undeformed, siltstone to fine sandstone beds with sharp contacts that are dipping ~25° to the NW (Fig. 3.5). Facies B is observed at Location 2 where it overlies Facies A. Flat-lying medium-grained sandstone, diamictite, and conglomerate beds (Facies A and C) at Location 1 grade laterally into the thin, siltstone and fine sandstone beds (Facies B) at Location 2, which dip steeply for ~10 m before flattening out and grading laterally into silt/clay rhythmites (Facies E). The entire package of dipping clinoforms is only ~2-3 m in height.

Facies B is interpreted as a small Gilbert-type delta prograding into a shallow body of water. The relatively flat lying conglomerate, diamictite, and sandstone beds at Location 1 are interpreted as the topsets, the steeply dipping siltstone and fine sandstone beds are interpreted as foresets, and the siltstone beds that flatten out and grade laterally into rhythmites are interpreted as the bottomsets. The fine sandstone clinoforms exhibit a rising delta-brink trajectory (Fig. 3.5). This stacking pattern suggests a slow and steady rise in base level (e.g. Winsemann et al., 2018). Sandstone beds that grade into silt/clay rhythmites are indicative of a delta building into a standing body of water where settling from suspension is the dominant form of sedimentation. When streams enter a still standing body of freshwater (of similar density to the effluent stream)

the water mixes and sediments quickly drop from suspension, creating steep depositional surfaces (~25° in this case) such as the dipping sandstone beds observed here (e.g. Bhattacharya, 2006).

Medium sandstone facies (Facies C)

The medium sandstone facies (Facies C) occurs at Locations 1, 4, and 5. This facies consists of undeformed, erosionally based, fine- to medium-grained sandstone and gravelly sandstone with mostly structureless beds, although rare cross-stratified beds occur. Facies C is laterally extensive, lacks evidence of channelization, and is interbedded with conglomerate and diamictite beds at Location 1. At Locations 4 and 5, Facies C occurs at the base of the section. Sandstone beds range in thickness from 4 cm to 0.5 m thick. Facies C is interpreted as sandy outwash related to Facies A from an outwash fan setting. This interpretation is based on the rare cross-stratified beds that indicate tractive flows, lack of established channels, and the fact that Facies C is interbedded with conglomerate and diamictite beds at Location 1.

Folded sandstone with interbedded mudstone facies (Facies D)

The folded sandstone with interbedded mudstone facies (Facies D) is observed at Locations 4 and 5 where it overlies Facies C. Facies D is comprised of ~1-20 cm thick fine- to medium-grained sandstone beds with intercalated mudstone beds of similar thickness. Some beds exhibit grading from sand to mud. This facies fines upwards, as beds near the base of Facies D are almost entirely composed of sandstone, while mudstone beds increase vertically in both

abundance and thickness. Facies D beds are highly deformed and exhibit both intense folding and faulting (Figs. 3.6 and 3.7). Folds increase vertically in tightness and asymmetry above a décollement surface, below which lies the undeformed sandstone beds of Facies C (Fig. 3.7A). Folds directly above the décollement surface begin as concentric and upright and become similar, overturned, and recumbent towards the top of the facies. Small parasitic folds occur in some folded beds towards the top of the facies (Figs. 3.7B and 3.7C). All the folds at Locations 4 and 5 have axes oriented NE-SW, indicating a NW-SE direction of shortening (Fig. 3.2). Folded sandstone and mudstone beds are dissected by listric thrust faults at Location 4 that originate from the underlying décollement surface and cut through the entire deformed section (Figs 3.6 and 3.7). Thrust planes are all observed dipping to the SE, indicating a NW direction of movement (mean vector of thrusting=301±24°, Fig. 3.2).

Folded beds follow the same pattern of deformation throughout the entire interval, without breaks in deformation. Furthermore, some thrust faults appear concurrent with folding as drag folds are found along fault planes. This indicates a period of time when brittle and plastic deformation occurred simultaneously (Fig. 3.6). Meanwhile, smaller normal and reverse faults clearly cross-cut the folded beds without any evidence of plastic deformation, suggesting a later stage of purely brittle faulting (Figs. 3.7D and 3.7E). At Location 5, several ~1-2 m wide medium sandstone blocks (apparently detached) can be seen within the folded sandstone and mudstone beds, which drape around them (Figs. 3.8A and 3.8B).

Facies D is interpreted as prodeltaic sediments from an outwash fan delta. Sandstone beds represent relatively higher energy conditions and may have been produced by tractive hyperpycnal flows that occurred during intervals of increased discharge. Grading between sandstone and mudstone beds suggests that the mudstone interbeds may represent suspended

sediment from waning hyperpycnal flows or low energy background settling from suspension into a standing body of water. The fining upwards trend within Facies D is interpreted as the delta back-stepping in response to increasing accommodation or decreasing sediment supply.

Deformation of Facies D is interpreted to have occurred after deposition but prior to lithification, likely with most folding and large-scale thrust faulting resulting from a sustained event that shoved the sediments to the NW. This interpretation is based on the fact that the facies lacks breaks in deformation that would indicate discrete slumping events. The vertical deformation profile (increasing intensity of folding vertically) is interpreted as the product of the variable rheology of the sediments, which is related to the fining upwards trend in grain size. An alternate interpretation is that vertical change in fold morphology represents the strain profile of an overriding mass. This hypothesis is not favored because there is no truncation of folds or typical deforming bed profile (no sheared or homogenized layer) that would indicate an overriding mass such as a glacier or large slide block. Small-scale, brittle, normal and reverse faults could be the result of dewatering or collapse after the cessation of compression. The (apparently) detached sandstone blocks may represent small slide blocks that were transported down the depositional surface of the fan delta or, alternatively, they may be sediments that were squeezed and extruded between folds and are not actually detached when viewed three-dimensionally.

Rhythmites and mudstone with outsized clasts facies (Facies E)

Thin (mm-scale) silt/clay rhythmite couplets and massive mudstone with outsized clasts (Facies E) occur at Locations 2, 3, and 5. At Locations 2 and 3, the rhythmites overlie the folded

and faulted conglomerate and diamictite beds of Facies A (Fig. 3.4). At these two locations, the rhythmites are undeformed but occur between the fold-thrust complexes comprised of conglomerate and diamictite, suggesting that the rhythmites were deposited after the deformation of the underlying facies. These rhythmites also onlap onto the limbs of the folded and faulted conglomerate and diamictite beds rather than draping over them (Fig. 3.4). There were not any observed slump features off the relatively steep sides of the fold-thrust complexes. At Location 5, the rhythmites grade vertically to massive mudstone with outsized clasts and do not have this same onlapping stratal relationship as Locations 2 and 3. Here, the rhythmites conformably overlie the folded mudstone and sandstone beds of Facies D and contain brittle faults and dewatering features near their base.

The rhythmites themselves lack grading and consist of alternating light brown silt and dark brown clay laminae that occur as silt/clay couplets (Fig. 3.9A). There are planar, sharp contacts between both individual laminae and between laminae couplets (Fig. 3.9B). The light brown silt laminae are typically thicker (~0.1-6 mm) than the dark brown/black clay laminae (~0.1-3 mm) and the combined couplets are ~0.25-6.0 mm in thickness (Fig. 3.9C). The average thickness of the couplets is ~1.14±1.04 mm (1σ) (Fig. 3.9C). Some silt laminae contain very thin (~0.1 mm) interlaminae of clay (Fig. 3.9D). Clay laminae often contain a layer of fine sand grains on the top and/or bottom of the laminae (Fig. 3.9D and 3.9E). Such fine-grained sand layers only occur on the outer edges of the clay laminae or within the clay laminae and are not found within the center of the clay or silt laminae (Fig. 3.9D and 3.9E). Outsized clasts are common and are dispersed throughout Facies E (Fig. 3.10). These outsized clasts range from granule-to-cobble-sized, are mostly composed of granite, and can be observed piercing through underlying laminae (Figs. 3.10A-C). Outsized clasts that pierce laminae suggest that the clasts

were rafted and then dropped on to the substrate from above. Also common, and scattered throughout the rhythmites, are rounded, spherical to prolate, diamictite pellets (Figs. 3.10D-F). These pellets are typically 2-3 mm in diameter and have a clay and silt matrix with fine sand-sized quartz grains scattered evenly around a central clast or clast cluster. Some pellets show evidence of internal clast rotation around the central core (Fig 3.10D). Rhythmites from location 5 are deformed within a 1-2 m thick interval above Facies D, with small (cm-scale) normal and reverse faults, brecciated zones, and fractures that cross-cut through the rhythmites (Fig. 3.11). Fractures are filled with sediment, creating small clastic dikes and sills that preferentially follow the weak boundaries between silt and clay laminae (Figs. 3.11A and 3.11B). Clastic dikes and sills are filled with brecciated rhythmite clasts, lithic fragments, and quartz sand grains.

Facies E is interpreted as meltwater-fed, lacustrine and/or estuarine sediments. The rhythmites were likely deposited by settling from suspension into a standing body of water rather than as density underflows. This conclusion is based on the lack of ripples, rip-up clasts, or erosive contacts that would indicate flows in contact with the substrate. Rhythmite couplets could potentially represent diurnal, annual, decadal, centennial, or even millennial-scale cycles related to a diverse set of biological, tidal, meteorological, or climatic variables (e.g. Church and Gilbert, 1975; Ó Cofaigh and Dowdeswell, 2001; Franco and Hinnov, 2012; Zavala and Arcuri, 2016; Zolitschka et al., 2015). However, diurnal cycles typically form thin, normally graded rhythmites with sharp basal contacts, representing a gradual change in discharge throughout the day or a waning surge-like flow (e.g. Ashley, 1975; Phillips and Auton, 2000). Conversely, like the rhythmites seen here, seasonal cycles typically produce distinct sand, silt, or clay laminae with planar sharp contacts between them, resulting from marked differences in sedimentation during summer and winter months (e.g. Ashley, 1975; Phillips and Auton, 2000; Zolitschka et

al., 2015). The rhythmite couplet thicknesses described here are consistent with those of varves

in modern proglacial environments (e.g. Ashley, 1975; Leonard, 1997; Loso, 2009; Zolitschka et

al., 2015). Furthermore, an interpretation of seasonal or annual cycles (i.e. true varves) is favored

for these particular rhythmites based on the fine sand layers that occur on either side of the clay

laminae (Figs. 3.9D and 3.9E). These fine sand layers are interpreted as either ice-rafted grains,

wind-blown grains scattered on a frozen water body, or the product of rapid snow melt discharge

and, thereby, suggest seasonal freeze-thaw cycles. In this scenario, the clay layers were deposited

when the lakes froze during winter, meltwater discharge declined, and sedimentation rates were

low. The fine sand grains (the largest grains) only occur on either side of the clay laminae or

within the outer edges of the clay laminae. Therefore, these may represent early and late ice

formation/break-up or snow melt that scattered the sand grains via ice rafting or sudden

meltwater discharge during intervals of overall low sedimentation rates (e.g. Zolitschka et al.,

2015). Meanwhile, the silt layers may represent summer sedimentation, when relatively coarser

(silt) grains are transported into the environment due to overall higher meltwater discharge.

The prevalence of large (up to cobble-sized) and abundant granite dropstones, piercing

through silt/clay rhythmites, supports the interpretation that ice-rafting was common in the

depositional environment. Furthermore, diamictite pellets are often cited as evidence of ancient

glacially influenced sedimentation (e.g. Ovenshine, 1970; Chumakov et al., 2011; Hoffman et

al., 2011; Menzies and Meer, 2017). These pellets are often deposited by ice rafting in bodies of

water that are in direct contact with the ice margin (e.g. Goldschmidt et al., 1992). Cowan et al.

(2012) suggest two possible mechanisms for the formation of diamicite pellets within a glacier's

deforming bed. One is a mechanical model that involves fracturing and brecciation of subglacial

till under low pore-water, high shear, conditions. Fractured till clasts are rotated and rounded

when the glacier thickens and basal melting occurs, which increases pore-water pressure. A thermal model for pellet formation suggests that basal freezing occurs preferentially in large pore spaces where unconsolidated till is frozen and a pellet is formed. Basal melting and thawing under distributed shear stress causes rotation and consolidation of the pellets which are entrained upward into a debris rich zone (Cowan et al., 2012). Both models suggest that diamictite pellets are evidence of a subglacial deforming bed under freezing-thawing conditions, which may be representative of both stagnant and fast moving ice. Therefore, diamictite pellets have been considered by some authors as evidence for ancient ice streams (Piotrowski et al., 2006; Cowan et al., 2012). Despite this, Gilbert (1990) points out that diamictite pellets can form under sea or lake ice without direct glacial influence and be rafted seasonally when the ice breaks up.

Deformed rhythmites at Location 5 are consistent with hydrofracturing and microfaulting of partially cohesive sediments. The rhythmites must have been deposited for long enough to be compacted and partially lithified to deform in a brittle fashion. An alternate possibility is that the rhythmites were frozen when hydrofractured. The hydrofracturing of subglacial or proglacial sediments is commonly produced as glaciers advance over their own deposits, creating high pore-water pressures under a confining layer, such as the silt and clay rhythmites observed here (e.g. Phillips and Auton, 2000; Phillips et al., 2007; Roberts et al., 2009; Phillips et al., 2013; Ravier et al., 2015). The pressure gradient from underneath a glacier, radiating outwards to its margins, will drive meltwater to the ice margin (e.g. Boulton et al., 1999). Once the pore-water pressure exceeds the minimum cohesive stress of the confining proglacial sediments then hydrofracturing occurs (e.g. Phillips and Auton, 2000).

3.6. Geochemistry of rhythmites

Rhythmite (Facies E) samples were acquired from Location 3 for geochemical analysis (see Appendix C). Fourteen samples (s1-s14) were collected at a sampling interval of 10 cm, starting at the base of Facies E and moving upwards. Rb/K ratios were used as a proxy for the paleosalinity. These ratios show a gradual increase in values vertically that range from $3.30 \cdot 10^{-3}$ to $4.95 \cdot 10^{-3}$ (Fig. 3.12). The three basal samples (s1-s3) contain Rb/K values of $<4.00 \cdot 10^{-3}$, which is considered typical of a freshwater depositional environment (e.g. Campbell and Williams, 1965). The rest of the values (s4-s14) have Rb/K values between $4.00 \cdot 10^{-3}$ and $6.00 \cdot 10^{-3}$ that are considered more indicative of a brackish environment (e.g. Campbell and Williams, 1965; Fig. 3.12). However, the increase in Rb/K values could also reflect an increase in chemical weathering. Chemical index of alteration values (CIA) were also calculated from these same samples (s1-s14) as a proxy for the degree of chemical weathering. CIA data shows a similar trend to Rb/K values, with a gradual increase vertically through the section (Fig. 3.12). The values range from 65.4 at the base of the sampling interval to 73.7 near the top (Fig. 3.12). The two basal CIA values (s1-s2) are below average shale values (i.e. 70-75, Nesbitt and Young, 1982), while the rest (s3-s14) are within the range of average shale. Therefore, the Rb/K and CIA data may reflect a shift from freshwater to brackish conditions, a gradual transition from an environment dominated by physical weathering to a more average chemical weathering of the landscape, or some combination of these two trends.

3.7. Horizontal variability of facies and deformation

Trends in grain size and deformation were observed horizontally across the five outcrops (~2.5 km). In general, there is a fining of sediments towards the NW (Fig. 3.2). Location 1 (southernmost outcrop) contains coarse grained beds of diamictite, conglomerate, and medium sandstone (Facies A and C). At Locations 2 and 3, coarse-grained conglomerates, diamictites, and sandstones are overlain by rhythmites of Facies E. Locations 4 and 5 have beds of medium-grained sandstone (Facies C) at the base of the outcrops below a décollement surface. Interbedded mudstone and sandstone beds (Facies D) overlie the décollement surface. At Location 5, the interbedded mudstone and sandstone beds are overlain by ~4 m of the silt/clay rhythmites of Facies E (Fig. 3.2).

Deformation at Locations 2 and 3 consists of fold-thrust complexes (~50 m apart and 1-3 m in height) that originate from an underlying décollement surface (Fig. 3.4). Location 4 has short wavelength (<1 m) folds that are relatively small compared to the anticlinal fold-thrust complexes at Locations 2 and 3 (Figs. 3.6 and 3.7). Location 4 is also dissected by thrust faults originating from the underlying décollement surface, while Location 5 does not contain thrust faults. Deformation at Location 5 consists entirely of short (<1 m) wavelength folds, dissected by normal and reverse faults, within a vertical deformation profile.

3.8. Discussion

The outcrops described in this study are interpreted as part of an outwash fan and fan delta system from a transitional terrestrial-to-estuarine, ice-proximal setting. These sediments

were likely deformed by a polythermal or warm-based glacier frozen to the foreland, which exhibited episodic stagnation and advances. The pattern of deformation is consistent with a multi-crested push-moraine complex formed during at least two glacial advances and retreat cycles. Highly pressurized groundwater, abundant outwash, and possible seasonal freeze/thaw cyclicity is suggestive of a temperate paleoclimate.

3.8.1. Interpretation of depositional environment

The sediments described are interpreted to have been deposited in an ice-proximal depositional environment. Evidence for this includes striated and faceted clasts that are indicative of subglacial abrasion, rhythmites with outsized clasts that pierce laminae (i.e. dropstones), and diamictite pellets. Diamictite pellets and dropstones are often cited as evidence of ice rafting and are common in glacially-influenced settings. Additionally, CIA values of ~65 from the basal rhythmites are below that of average shale (~70-75) and are consistent with both modern and ancient glacial deposits where physical weathering is dominant over chemical weathering (e.g. Nesbitt and Young, 1982). The interpretation of a glacially-influenced environment is also in agreement with Tomazelli and Soliani Júnior (1997) who described grooved surfaces interpreted as subglacial within the same facies described here ~8 km from the study area.

Diamictites, conglomerates, and sandstones from Facies A and C are interpreted as outwash fan deposits since they show evidence of bedload dominated transport in the form of cross-stratification and ripples. They also contain poorly sorted sediments that alternate between grain and matrix support beds, suggesting alternations between high viscosity debris flows and

flowing water. Paleocurrent orientations from Facies A and C indicate flow towards the NW (mean azimuth=312±10.2°), down the axis of the Ibaré Lineament. The interbedded mudstones and sandstones of Facies D are interpreted as outwash fan delta sediments deposited into a standing body of water. Fine-grained silt/clay rhythmites (Facies E) are interpreted as glacially-influenced lacustrine and/or estuarine sediments that were deposited primarily by settling from suspension and ice-rafting. The sand/silt clinoforms of Facies B are interpreted to be a small gilbert-type delta that is time equivalent to the rhythmites of Facies E. This is based on the fact that the dipping sand/silt beds can be traced laterally into the rhythmites of Facies E.

Although a solely estuarine setting cannot be ruled out, a transitional lacustrine to estuarine environment is favored for the rhythmites and mudstone of Facies E. The undeformed, horizontally-bedded, basal rhythmites onlap (rather than drape over) thrusted and folded beds of underlying sediments at Locations 2 and 3, which suggests that the anticlinal fold-thrust complexes of Facies A existed as positive topographic features with standing water between them. There do not appear to be any slump features off the relatively steep sides of these deformation features as would be expected if the sediments were deposited from above on an inclined surface. Furthermore, the steeply dipping sandy clinoforms of Facies B are only ~2-3 m high, laterally grading into rhythmites within a synclinal fold, indicating that they were prograding into a shallow body of water. The rising delta-brink geometry of the gilbert-type delta suggests a gradual rise in accommodation within these small sub-basins (e.g. Winsemann et al., 2018). It is common for small proglacial lakes to form between push/thrust ridges on an outwash plain or directly at the ice margin during ice retreat or stagnation. Analogous shallow, interconnected glacio-fluvial-lacustrine sediments can be found in both modern and Pleistocene deformational moraines (e.g. Ashley, 2002; Roberts et al., 2009; Benediktsson et al., 2015).

Based on the hypothesis that the rhythmite couplets are annual varves with an average thickness of ~1.14 mm, the rhythmite packages (~1.5-3 m thick) observed in this study would represent ~1,315-2,631 years of sedimentation. This rough estimate is within the range of varve chronologies collected from modern proglacial lakes (e.g. Ashley, 1975; Leonard, 1997; Loso, 2009; Larsen et al., 2011). Additionally, the Rb/K values of the basal rhythmites at Location 2 (s1-s3) are <4.00 · 10^{-3}, which is typical of sediments deposited in a freshwater environment. Both the CIA and Rb/K values increase vertically through the section. Increasing CIA values are possibly related to climate amelioration and increased chemical weathering of the landscape during glacial retreat. Meanwhile, the increase in Rb/K values may reflect a marine inundation of the area following ice retreat. Similar glacio-lacustrine to estuarine transitions have been interpreted from paleovalleys on the eastern margin of the Paraná Basin based on changes in ichnology (e.g. Netto et al., 2009). However, an alternative interpretation to be considered is that the basal freshwater Rb/K values may be reflective of a surge in meltwater into a pre-existing estuarine environment due to the rapid retreat of the glacier. This interpretation is not favored here because the stratal relationships described above support small standing bodies of water between deformed ridges.

3.8.2. Glaciotectonic versus mass transport related deformation

Distinguishing glaciotectonic folding and thrusting from mass transport deformation is difficult and must be considered before addressing deformation processes. Therefore, the following criteria were considered for identification of glaciotectonized sediments: (1) truncation of underlying strata throughout the entire zone of deformation, (2) compressional features found

100

throughout the entire deposit, (3) décollement surfaces that ramp up and over truncated proglacial beds near the frontal thrust, (4) thrust complexes where older thrust sheets rest on top of younger thrust sheets (piggyback thrusting), (5) when older thrust sheets are near vertical due to rotation due to transport on younger thrust sheets during continued thrusting, (6) decreasing deformation in the direction of transport (Croot, 1987; Aber et al., 1989; Hart and Boulton, 1991; Isbell, 2010).

Conversely, the following criteria can be used to identify deformation related to slumps and slides: (1) truncation of underlying strata from rotational extension in areas adjacent to the slump-slide scarp, (2) deposits where the head of the slump/slide dips away from the headwall scarp, (3) at the toe of the slump/slide, the deposits typically rest on slopes that dip in the direction of sliding, (4) deposits are composed of one to several sheets and younger sheets rest on the backs of older sheets, (5) the occurrence of slump fold noses, (6) an increase in the degree of deformation in the direction of transport because compression occurs at the toe of the slump-slide, and (7) deformation concentrated near a basal shear zone (e.g. Isbell, 2010; Ogata et al., 2012).

The deformation described in this study fits with the criteria for glaciotectonism rather than slumps for several reasons. First, there is clear sedimentologic evidence of a fluctuating glacial margin in the form of striated/faceted clasts, rhythmites with dropstones, diamictite pellets and subglacial grooves. Within the deformed intervals, fairly unidirectional folds and thrusts, without breaks in deformation, suggest that the sediments were deformed by sustained events rather than multiple discrete events, which negates the interpretation of multiple smaller slumps. Assuming the entire succession deformed as a single large slump, there is no supporting evidence of detachment from the laterally equivalent undeformed beds (at Location 1).

101

Moreover, there is no evidence of a headwall scarp to trigger a large slump or evidence for a deep-water environment where large-scale slumps are common. Rather, evidence supporting a glaciotectonic origin to the deformation described includes: compressional features found throughout the entire succession, décollement surfaces that ramp over proglacial facies, examples of piggyback thrusting in which older thrust sheets becoming increasingly steeper on the backs of large folds and thrusted beds, and decreasing deformation in the direction of sediment transport at Locations 2-5.

3.8.3. A late Paleozoic push-moraine complex

Push-moraines are defined broadly by Bennet and Glasser (2009) as "the product of constructional deformation of ice, sediment and/or rock to produce a ridge or ridges, transverse or oblique to the direction of ice flow in front of, at, or beneath an ice margin". This definition of push-moraines is applied herein. However, it should be noted that features matching this description are also described by some authors as composite ridges, thrust-block moraines, thrust-block ridges, or thrust moraines (e.g. Benn and Evans, 1998). These features can be either terrestrial or marine (e.g. Boulton, 1986). Over the past few decades, push-moraines have become better characterized and they have been increasingly used to reconstruct Pleistocene ice dynamics (e.g. Bennet, 2001). However, few examples of push-moraines exist from deep-time glacial deposits (e.g. Le Heron et al., 2005; Isbell, 2010; Vesely et al., 2015) and it is even less common to find pre-Cenozoic terrestrial examples preserved.

Comparisons are frequently been made between push-moraines and "thin-skinned" orogenic belts in which both thrusting and folding occur throughout a relatively thin zone of deformation that is subjected to lateral stresses above a detachment surface (e.g. Croot, 1987).

There are some generally recognized conditions that favor the formation of push-moraines. This includes: (1) the coupling (freezing) of a glacier's snout to the foreland wedge due to the cessation of pressure melting, (2) the build-up of an outwash fan during ice-front stagnation, which a subsequently advancing glacier can push into and deform, (3) a reverse bedrock slope, which can also provide the required resistance to an advancing ice mass, and (4) the development of a décollement surface along a weak layer in the substrate, due to either high pressure groundwater and/or the presence of permafrost (e.g. Bennet, 2001; van der Wateren, 1995).

The deformed strata described in this study fit the criteria of Bennet and Glasser (2009) for identification as a late Paleozoic, multi-crested push-moraine. The deformation is considered "constructive" since a stagnant ice front had to first build-up a wedge comprised of braided stream and lacustrine sediments before subsequently coupling to and advancing into these sediments without eroding them. Additionally, the two fold-thrust complexes at Locations 2 and 3 have axes roughly transverse (NE-SW orientation indicated by fold axes) to the SE dipping thrust planes, which indicate a NW (mean vector=301±24°) direction of shove. These deformational features certainly would have existed as elongated ridges since there is evidence of ponded rhythmites onlapping them. The variability in deformation along the railroad transect is consistent with observations of recent push moraines and is most likely attributed to the rheology of the proglacial sediment wedge (e.g. Hart and Watts, 1997). The coarser grained sediments (Locations 2 and 3) behave in a brittle fashion with faults and long wavelength folds while the finer grained sediments (Locations 4 and 5) tend to deform in a plastic manner with short wavelength folds.

At least two glacier advance and retreat cycles are recorded in the outcrops from this study (Fig. 3.13). However, it should be noted that the 1.5 km covered section may contain a

more complex pattern of ice advance and retreat. Nevertheless, the following sequence of events

is interpreted based on the observable deformation (Fig. 3.13): (1) outwash fan and fan delta

sediments (Facies C and D) were deposited (observed at Locations 4 and 5), (2) a glacier,

coupled to its foreland, advanced NW to the edge of the fan delta and intensely folded and

faulted the sediments (Facies C and D, observed at Locations 4 and 5), (3) the glacier rapidly

retreated to the SE, depositing rhythmites and mudstone (Facies E) on top of the folded deltaic

sediments (Facies D) at Locations 4 and 5 and proglacial outwash fan sediments (Facies A and

C) at Locations 2, and 3, (4) the glacier re-advanced to the NW, creating fold-thrust complexes

comprised of outwash fan sediments (Facies A) at Locations 2 and 3, and causing pressurized

groundwater to hydrofracture through the partially-consolidated, impermeable rhythmites (Facies

E) previously deposited at Locations 4 and 5, and (5) the glacier again retreated to the SE,

depositing undeformed outwash fan beds (Facies and A and C) at Location 1 and thin ponded

rhythmites (Facies E) between the fold-thrust complexes at Locations 2 and 3. At the same time,

the small gilbert-type delta (Facies B) built out into the shallow, ponded water between the fold-

thrust complex ridges at Location 2. As the glacier continued to retreat, a marine transgression

flooded the study area, creating brackish conditions consistent with the observed shift in Rb/K

values.

3.8.4. Regional implications for glacier dynamics and paleoclimate

The NW direction of ice movement observed in the glaciotectonic complex is in

agreement with the regional-scale interpretation, based on the orientations of grooved surfaces,

that an unconfined ice lobe advanced NNW out of Uruguay during the Carboniferous and

radiated across the western half of the RGS (Figs. 3.14A-C; e.g. Frakes and Crowell, 1972;

Crowell and Frakes, 1975; Assine et al., 2018). This implies that separate ice centers were responsible for glaciation on the southern and eastern margins of the Paraná Basin. The NW direction of ice shove recorded in this study is slightly different from previously described N-S oriented grooved surfaces on the RGS (Fig. 3.14A). This implies that the "Uruguayan Lobe" either spread out radially across the RGS or was channelized into zones of pre-existing bedrock weakness such as that associated with the Ibaré Lineament as it flowed into the Paraná Basin.

The possible presence of fast-flowing channelized ice is supported by previously described, streamlined "whaleback" structures carved into igneous basement in Uruguay (e.g. Assine et al., 2018). These structures are located ~185 km SE of the outcrops described here and also have a NW orientation (Fig. 3.14). Whalebacks are commonly formed under rapidly flowing, thick ice (e.g. Stokes and Clark, 1999; Margold et al., 2015; Assine et al., 2018). Fast flowing ice that advanced out of the Chaco-Paraná Basin in Uruguay excludes the interpretation of a small ice cap on the RGS that expanded outwards in all directions as depicted by some authors (e.g. Santos et al., 1996; Rocha-Campos et al., 2008). The whalebacks also suggest that glaciation did not consist of outlet glaciers flowing E to W out of Namibia through a series of paleovalleys onto the eastern RGS (e.g. Tedesco et al., 2016). Rather, such a NW flowing glacier may have originated farther afield in the Cargonian Highlands of Africa, terminating on the RGS.

The sediments and the pattern of deformation described here are supportive of an ice margin that experienced episodic stagnation and re-advances. The ice must have been stagnant for long enough to build-up proglacial outwash fan deposits. However, not enough time elapsed for the sediments to lithify before the glacier subsequently advanced into its own deposits and deformed them (e.g. Bennet and Glasser, 2009). The fact that at least two advance and retreat

cycles are recorded along the railroad track outcrops is possible evidence for surging behavior. Surging is thought to occur when subglacial water pressure builds up enough for a glacier to detach from its bed and rapidly advance (e.g. Weertman, 1969). Boulton et al. (1999) attributed the surging behavior recorded in a modern push-moraine to the sub-polar thermal regime of the glacier, in which the thinner outer zone of the glacier is frozen and the thicker inner zone produces a build-up of meltwater that eventually overcomes bed friction. Once the pressurized meltwater is released during a surge, the glacier recouples to its bed and the process begins again.

Several pieces of evidence support a temperate paleoclimate and a warm based or polythermal glacier. The presence of a deforming bed is implied by the nearby grooved surfaces described by Tomazelli and Soliani Júnior (1997) and the ice rafted diamictite pellets with rotational features found throughout Facies E that may have formed subglacially (e.g. Cowan et al., 2012). High porewater pressures are required to lower the effective stress of the sediments and facilitate the movement of a glacier through its bed (e.g. Boulton, 1996; Fischer et al., 2001; Evans et al., 2006; Busfield and Le Heron, 2013). High porewater pressures are also implied by the plastically deformed proglacial sediments, décollement surfaces, and hydrofractures in rhythmites. In particular, the propagation of décollement surfaces is often driven by overpressurized groundwater within a permeable bed that allows for separation between layers of different composition (e.g. Boulton et al., 1999; Bennet, 2001; Waller et al, 2012). In the case of the hydrofractures, the cohesive stress of the confining, overlying rhythmite beds must have been overcome by the upwards-directed pressure of the underlying groundwater (Phillips and Auton, 2000). Push moraines comprised of glaciofluvial and glaciolacustrine sediments, such as the one

observed here, are common products of both temperate and polythermal glaciers (e.g. Hambrey and Glasser, 2012).

Based on a paleolatitude of ~45-55° S (e.g. Torsvik and Cocks, 2013) a temperate paleoclimate is expected for this region. At least some of the rhythmic, fine-grained sediments described here are interpreted as the product of annual freeze-thaw cycles. The seasonality expressed in the freeze-thaw cycles is possibly direct sedimentological evidence for such a temperate paleoclimate. Moreover, the abundance of coarse-grained outwash deposits that contain evidence of flowing water suggests significant meltwater discharge at the ice front. These features are not observed in polar environments, where surficial meltwater production is rare to minimal (e.g. Menzies and van der Meer, 2018). Other evidence for a temperate paleoclimate is the CIA values of the rhythmites. The majority of the CIA values are within the range of average shale (70-75), suggesting a shift to relatively average chemical weathering of the landscape, which would be unusual in a frigid, polar setting (e.g. Nesbitt and Young, 1982). While no direct evidence for permafrost was observed in these sediments, some authors have argued that permafrost conditions are often necessary for the formation of a push moraine (e.g. Boulton and Caban, 1995; Boulton et al., 1999). This is because permafrost allows the transmission of stress to be concentrated into a relatively thin package of sediments for up to kilometers when a glacier is frozen to the foreland. The permafrost table also facilitates the build-up of high porewater pressures by inhibiting proglacial drainage and, therefore, contributes to surging behavior and the deformation observed in some push moraines. However, it should be noted that the exact role of permafrost in push-moraine formation is still unresolved and some researchers do not consider permafrost to be a requirement (e.g. Aber, 1988; van der Wateren, 1995). Further biostratigraphic work is needed to determine how these glacial deposits on the

RGS correlate to the VcIZ-bearing intervals. The dominance of pollen species with conifer and pteridosperm affinities (e.g. mono- and bissaccate pollen) in the post-glacial Rio Bonito Fm. supports the presence of temperate forests on the RGS, which could hypothetically coexist on the RGS with partial ice cover (e.g. Iannuzzi et al., 2010).

Nevertheless, the combined evidence challenges conventional interpretations of the LPIA that argued for a long-lived, massive, and stable ice center covering much of Gondwana during the Carboniferous and Permian. This study suggests that a dynamic, warm-based or polythermal ice margin terminated in the southernmost Paraná Basin during the late Carboniferous. This ice margin may represent the end of a thick, fast-flowing lobe extending NNW out of Uruguay. The evidence for a temperate paleoenvironment implies that it is unlikely that an extensive ice shelf covered the entire southern Paraná Basin and that a single, massive ice sheet covered the entire basin during the late Carboniferous.

3.9. Conclusions

(1) Deformed Carboniferous (Itararé Gp.) sediments near Ibaré, Rio Grande do Sul State, Brazil are interpreted to have a glaciogenic origin. This conclusion is based on the presence of striated and faceted clasts, rhythmites with abundant dropstones, and diamictite pellets.

(2) The depositional environment for these sediments is interpreted to have been an ice-proximal outwash fan and fan delta in a transitional, terrestrial-to-estuarine setting. Cross-stratified sandstone and conglomerate beds indicate the presence of flowing water. Stratal relationships are indicative of small, ponded bodies of water on the surface of the

outwash fan that were situated between positive, paleotopographic deformation features. Rb/K values reflect a shift from freshwater to estuarine conditions.

(3) The pattern of soft-sediment deformation observed in this study is typical of a glacier coupled to its foreland. Key features supporting this interpretation include: compressional features through the entire succession, décollement surfaces that ramp over proglacial facies, examples of piggyback thrusting in which younger thrust sheets become increasingly steeper on the backs of folded and thrusted beds, and decreasing deformation in the direction of movement.

(4) The glacially-deformed sediments described in this study fit the Bennet and Glasser (2009) definition of a late Paleozoic push moraine because they contain evidence for constructive deformation and transverse ridges oriented perpendicular to the direction of ice shove.

(5) Hydrofractured rhythmites, décollement surfaces, and the plastic deformation of sediments are supporting evidence for pressurized groundwater under a warm-based or polythermal glacier.

(6) Rhythmites with dropstones and possible seasonal laminae are interpreted as evidence for a temperate paleoclimate. This is supported by average CIA values and outwash-dominated proglacial sediments with abundant sedimentologic evidence for meltwater production.

(7) Measurements of fold axes and thrust planes support a NW (~301±24°) direction of ice shove, which is consistent with other regional interpretations of a NNW moving ice lobe that extended out of Uruguay. The ice dynamics interpreted from the pattern of

deformation and sedimentation reflect an ice margin that fluctuated between stagnation and rapid advances.

References

Aber, J.S., 1988. Ice-shoved hills of Saskatchewan compared with Mississippi delta mudlumps—implications for glaciotectonic models. In: Croot D.G. (Ed.), Glaciotectonics Forms and Processes. A.A. Balkema, Rotterdam, pp. 1-9.

Aber, J.S., Croot, D.G., Fenton, M.M., 1989. Glaciotectonic landforms and structures. Kluwer Academic Publishers, Dordrecht (200 pp.).

Alley, R.B., 1989. Water pressure coupling of sliding and bed deformation: I. Water system. Journal of Glaciology 35, 108-118.

Alley, R.B., 1991. Deforming-bed origin for southern Laurentide till sheets? Journal of Glaciology 37, 67-76.

Amato, J.A., 2017. Using AMS to Help Interpret Glaciogenic Deposits of the Late Paleozoic Ice Age in the Paraná Basin, Brazil (Masters Thesis). University of Wisconsin-Milwaukee, Milwaukee.

Ashley, G.M., 1975. Rhythmic sedimentation in glacial Lake Hitchcock, Massachusetts-Connecticut. Published by: Society of economic paleontologists and mineralogists, Tulsa, Oklahoma (USA).

Ashley, G.M., 2002. 11 - Glaciolacustrine environments. In: Menzies J. (Ed.), Modern and Past Glacial Environments. Butterworth-Heinemann, Oxford, pp. 335-359.

Assine, M.L., de Santa Ana, H., Veroslavsky, G., Vesely, F.F., 2018. Exhumed subglacial landscape in Uruguay; erosional landforms, depositional environments, and paleo-ice flow in the context of the late Paleozoic Gondwanan glaciation. Sedimentary Geology 369, 1-12.

Bahlburg, H., Dobrzinski, N., 2011. A review of the Chemical Index of Alteration (CIA) and its application to the study of Neoproterozoic glacial deposits and climate transitions. Memoir, 36. Geological Society, London, pp. 81-92.

Benediktsson, I.O., Schomacker, A., Johnson, M.D., Geiger, A.J., Ingolfsson, O., Guethmundsdottir, E.R., 2015. Architecture and structural evolution of an early Little Ice Age terminal moraine at the surge-type glacier Mulajokull, Iceland. Journal of Geophysical Research: Earth Surface 120, 1895-1910.

Benn, D.I., Evans, D.J.A., 1998. Glaciers and Glaciation. Arnold, London (734 pp.).

Bennet, M.R., 2001. The morphology, structural evolution and significance of push-moraines. Earth Science Reviews 53, 197-236.

Bennet, M.R., Glasser, N.F., 2009. Glacial Geology: Ice Sheets and Landforms. Wiley-Blackwell, Chichester (385 pp.).

Bhattacharya, J.P., 2006. Deltas. Society for Sedimentary Geology, Special Publication 84, 237-292.

Blignault, H.J., Theron, J.N., 2015. The facies association tillite, boulder beds, boulder pavements, liquefaction structures and deformed drainage channels in the Permo-

Carboniferous Dwyka Group, Elandsvlei area, South Africa. South African Journal of Geology 118.2, 157-172.

Boulton, G.S., 1986. Push-moraines and glacier-contact fans in marine and terrestrial environments. Sedimentology 33, 677-698.

Boulton, G.S., 2017. Theory of glacial erosion, transport and deposition as a consequence of subglacial sediment deformation. Journal of Glaciology 42, 43-62.

Boulton, G.S., Caban, P., 1995. Groundwater flow beneath ice sheets: Part II — Its impact on glacier tectonic structures and moraine formation. Quaternary Science Reviews 14, 563-587.

Boulton, G.S., van der Meer, J.J.M., Beets, D.J., Hart, J.K., Ruegg, G.H.J., 1999. The sedimentary and structural evolution of a recent push moraine complex: Holmstrømbreen, Spitsbergen. Quaternary Science Reviews 18, 339-371.

Boulton, G.S., van der Meer, J.J.M., Beets, D.J., Ruegg, G.H.J., 1999. The sedimentary and structural evolution of a recent push moraine complex; Holmstrombreen, Spitsbergen. Quaternary Science Reviews 18, 339-371.

Busfield, M.E., Le Heron, D.P., 2013. Glacitectonic deformation in the Chuos Formation of northern Namibia: implications for Neoproterozoic ice dynamics. Proceedings of the Geologists' Association 124, 778-789.

Cagliari, J., Philipp, R.P., Buso, V.V., Netto, R.G., Klaus Hillebrand, P., da Cunha Lopes, R., Stipp Basei, M.A., Faccini, U.F., 2016. Age constraints of the glaciation in the Paraná Basin: evidence from new U–Pb dates. Journal of the Geological Society 173, 871-874.

Campbell, F.A., Williams, G.D., 1965. Chemical composition of shales of Manville Group (Lower Cretaceous) of central Alberta, Canada. Bulletin of the American Association of Petroleum Geologists 49, 81-87.

Chumakov, N.M., Pokrovsky, B.G., Melezhik, V.A., 2011. The glaciogenic Bol'shoy Patom Formation, Lena River, central Siberia. Memoir 36. Geological Society of London, pp. 309-316.

Church, M., Gilbert, R., 1975. Proglacial fluvial and lacustrine environments. Published by: Society of economic paleontologists and mineralogists, Tulsa, Oklahoma (USA).

Cook, A.J., Fox, A.J., Vaughan, D.G., Ferrigno, J.G., 2005. Retreating Glacier Fronts on the Antarctic Peninsula over the Past Half-Century. Science 308, 541-544.

Corrêa da Silva, Z.C., 1978. Observações sobre o Grupo Tubarão no Rio Grande do Sul, com especial destaque á estratigrafia da Formação Itararé. Pesquisas—UFRGS, 9, 27-44.

Cowan, E.A., Christoffersen, P., Powell, R.D., 2012. Sedimentological signature of a deformable bed preserved beneath an ice stream in a late Pleistocene glacial sequence, Ross Sea, Antarctica. Journal of Sedimentary Research 82, 270-282.

Croot, D.G., 1987. Glacio-tectonic structures: a mesoscale model of thin-skinned thrust sheets? Journal of Structural Geology 9, 797-808.

Crowell, J.C., 1999. Pre-Mesozoic ice ages: Their bearing on understanding the climate system. Geological Society of America, Memoir 192, The Geological Society of America, Boulder (106 pp.).

Crowell, J.C., Frakes, L.A., 1975. The late Paleozoic glaciation. In: Cambell, K.S.W. (Ed.), Gondwana Geology. Australian National University Press, Canberra, pp. 313-331.

Delaney, P.I.V., 1964. Itararé outliers in Rio Grande do Sul, Brazil. Bol. Paran. Geogr. 10, 161-173.

Eyles, N., 1990. Marine debris flows; late Precambrian "tillites" of the Avalnoian-Cadomian orogenic belt. Palaeogeography, Palaeoclimatology, Palaeoecology 79, 73-98.

Eyles, C.H., Eyles, N., 2000. Subaqueous mass flow origin for Lower Permian diamictites and associated facies of the Grant Group, Barbwire Terrace, Canning Basin, Western Australia. Sedimentology 47, 343 – 356.

Evans, D.J.A., Hiemstra, J.F., 2005. Till deposition by glacier submarginal, incremental thickening. Earth Surface Processes and Landforms 30, 1633-1662.

Evans, D.J.A., Phillips, E.R., Hiemstra, J.F., Auton, C.A., 2006. Subglacial till: formation, sedimentary characteristics and classification. Earth Science Reviews 78, 115-176.

Fedorchuk, N.D., Isbell, J.L., Griffis, N.P., Montañez, I.P., Vesely, F.F., Iannuzzi, R., Mundil, R., Yin, Q.-Z., Pauls, K.N., Rosa, E.L.M., 2019. Origin of paleovalleys on the Rio Grande do Sul Shield (Brazil): Implications for the extent of late Paleozoic glaciation in west-central Gondwana. Palaeogeography, Palaeoclimatology, Palaeoecology. In Press. http://dx.doi.org/10.1016/j.palaeo.2018.04.013

Fielding, C.R., Frank, T.D., Isbell, J.L., 2008. The late Paleozoic ice age – a review of current understanding and synthesis of glaobal climate patterns. In: Fielding, C.R., Frank, T.D., Isbell, J.L. (Eds.), Resolving the Late Paleozoic Ice Age in Time and Space. Geological Society of America Special Paper 441, pp. 343-354.

Fischer, U.H., Porter, P.R., Schuler, T., Evans, A.J., Gudmundsson, G.H., 2002. Hydraulic and mechanical properties of glacial sediments beneath Unteraargletscher, Switzerland: implications for glacier basal motion. Hydrological Processes 15, 3525-3540.

Frakes, L., Crowell, J., 1972. Late Paleozoic glacial geography between the Paraná Basin and the Andean geosyncline. Anais da Academia Brasileira de Ciências 44, 139-145.

Franca, A.B., Potter, P.E., 1991. Stratigraphy and reservoir potential of glacial deposits of the Itarare Group (Carboniferous-Permian), Parana Basin, Brazil. American Association of Petroleum Geologists Bulletin 75, 62-85.

Franco, D.R., Hinnov, L.A., 2012. Anisotropy of magnetic susceptibility and sedimentary cycle data from Permo-Carboniferous rhythmites (Paraná Basin, Brazil): a multiple proxy record of astronomical and millennial scale palaeoclimate change in a glacial setting. Geological Society, London, Special Publications 373, 355-374.

Frank, T.D., Shultis, A.I., Fielding, C.R., 2015. Acme and demise of the late Paleozoic ice age: a view from the southeastern margin of Gondwana. Palaeogeography. Palaeoclimatology., Palaeoecology 418, 176-192.

Gesicki, A.L.D., Riccomini, C., Boggiani, P.C., 2002. Ice flow direction during late Paleozoic glaciation in western Paraná Basin, Brazil. Journal of South American Earth Sciences 14, 933-939.

Gesicki, A.L.D., Riccomini, C., Boggiani, P.C., Coimbra, A.M., 1998. The Aquidauana Formation (Parana Basin) in the context of late Palaeozoic glaciation in western Gondwana. Journal of African Earth Sciences 27, 81-82.

Gilbert, R.,1990. Rafting in glacimarine environments. In: Dowdeswell, J.A., Scourse, J.D. (Eds.), Glacimarine Environments: processes and sediments. Geological Society, London, Special Publication 53, pp. 105-120.

Goldschmidt, P.M., Pfirman, S.L., Wollenburg, I., Henrich, R., 1992. Origin of sediment pellets from the Arctic seafloor: sea ice or icebergs? Deep Sea Research Part A. Oceanographic Research Papers 39, S539-S565.

Griffis, N.P., Montañez, I.P., Fedorchuk, N., Isbell, J., Mundil, R., Vesely, F., Weinshultz, L., Iannuzzi, R., Gulbranson, E., Taboada, A., Pagani, A., Sanborn, M.E., Huyskens, M., Wimpenny, J., Linol, B., Yin, Q.-Z., 2019. Isotopes to ice: Constraining provenance of glacial deposits and ice centers in west-central Gondwana. Palaeogeography, Palaeoclimatology, Palaeoecology. In Press. http://dx.doi.org/10.1016/j.palaeo.2018.04.020

Griffis, N.P., Mundil, R., Montañez, I.P., Isbell, J., Fedorchuk, N., Vesely, F., Iannuzzi, R., Yin, Q.-Z., 2018. A new stratigraphic framework built on U-Pb single-zircon TIMS ages and implications for the timing of the penultimate icehouse (Paraná Basin, Brazil). Geological Society of America Bulletin 130, 848-858.

Hambrey, M. J., Glasser, N. F., 2003. Glacial sediments: processes, environments and facies. In: Middleton, G.V. (Ed.), Encyclopedia of Sediments and Sedimentary Rocks. Kluwer, Dordrecht, pp. 316-331.

Hambrey, M.J., Glasser, N.F., 2012. Discriminating glacier thermal and dynamic regimes in the sedimentary record. Sedimentary Geology 251-252, 1-33.

Harriss, R.C., Adams, J.A.S., 1966. Geochemical and mineralogical studies on the weathering of granitic rocks. American Journal of Science 264, 146-173.

Hart, J.K., Boulton, G.S., 1991. The interrelation of glaciotectonic and glaciodepositional processes within the glacial environment. Quaternary Science Reviews 10, 335-350.

Hart, J.K., Roberts, D.H., 1994. Criteria to distinguish between subglacial glaciotectonic and glaciomarine sedimentation, I. Deformation styles and sedimentology. Sedimentary Geology 91, 191-213.

Hart, J.K., Watts, R.J., 1998. A comparison of the styles of deformation associated with two recent push moraines, South Van Keulenfjorden, Svalbard. Earth Surface Processes and Landforms 22, 1089-1107.

Hoffman, P.F., Halverson, G.P., 2011. Neoproterozoic glacial record in the Mackenzie Mountains, northern Canadian Cordillera. Memoir, 36. Geological Society, London, pp. 397-412.

Iannuzzi, R., Souza, P.A., Holz, M., 2010. Stratigraphic and paleofloristic record of the Lower Permian post-glacial succession in the southern Brazilian. In: López-Gamundí, O.R., Buatois, L.A. (Eds.), Late Paleozoic Glacial Events and Postglacial Transgressions in Gondwana. Geological Society of America Special Paper 468, 113-132.

Isbell, J.L., 2010. Environmental and paleogeographic implications of glaciotectonic deformation of glaciomarine deposits within Permian strata of the Metschel Tillite, southern Victoria Land, Antarctica. In: López-Gamundí, O.R., Buatois, L.A. (Eds.), Late Paleozoic Glacial Events and Postglacial Transgressions in Gondwana. Geological Society of America Special Paper 486, 81-100.

Isbell, J.L., Miller, M.F., Wolfe, K.L., Lenaker, P.A., 2003. Timing of late Paleozoic glaciation in Gondwana: Was glaciation responsible for the development of northern hemisphere cyclothems? In: Chan, M.A., Archer, A.W. (Eds.), Extreme depositional environments: Mega end members in geologic time. Geological Society of America Special Paper 370, 5-24.

Isbell, J.L., Henry, L.C., Fraiser, M.L., 2012a. Sedimentology and palaeoecology of lonestone-bearing mixed clastic rocks and cold-water carbonates of the Lower Permian Basal Beds at Fossil Cliffs, Maria Island, Tasmania (Australia): Insight into the initial decline of the late Palaeozoic ice age. In: Gąsiewicz, A., Słowakiewicz, M. (Eds.), Palaeozoic Climate Cycles: Their Evolutionary and Sedimentological Impact. Geological Society, London, Special Publication 376, 307-341.

Isbell, J.L., Henry, L.C., Gulbranson, E.L., Limarino, C.O., Fraiser, M.L., Koch, Z.J., Ciccioli, P.L., Dineen, A.A., 2012b. Glacial paradoxes during the late Paleozoic ice age: evaluating the equilibrium line altitude as a control on glaciation. Gondwana Research 22, 1-19.

Larsen, D.J., Miller, G.H., Geirsdóttir, Á., Thordarson, T., 2011. A 3000-year varved record of glacier activity and climate change from the proglacial lake Hvítárvatn, Iceland. Quaternary Science Reviews 30, 2715-2731.

Lawver, L.A., Dalziel, I.W.D., Norton, I.O., Gahagan, L.M., 2011. The Plates 2011 Atlas of Plate Reconstructions (500 Ma to Present Day). Plates Progress Report No. 345-0811, University of Texas Technical Report No. 198 (189 pp.).

Lee, J.R., Phillips, E.R., 2008. Progressive soft sediment deformation within a subglacial shear zone – a hybrid mosaic-pervasive deformation model for Middle Pleistocene glaciotectonised sediments from Eastern England. Quaternary Science Reviews 27, 1350-1362.

Le Heron, D.P., Sutcliffe, O.E., Whittington, R.J., Craig, J., 2005. The origins of glacially related soft-sediment deformation structures in Upper Ordovician glaciogenic rocks: implications for ice-sheet dynamics. Palaeogeography., Palaeoclimatology, Palaeoecology 218, 75-103.

Leonard, E.M., 1997. The relationship between glacial activity and sediment production: evidence from a 4450-year varve record of neoglacial sedimentation in Hector Lake, Alberta, Canada. Journal of Paleolimnology 17, 319-330.

Loso, M.G., 2009. Summer temperatures during the Medieval Warm Period and Little Ice Age inferred from varved proglacial lake sediments in southern Alaska. Journal of Paleolimnology 41, 117-128.

Margold, M., Stokes, C.R., Clark, C.D., 2015. Ice streams in the Laurentide Ice Sheet: Identification, characteristics and comparison to modern ice sheets. Earth-Science Reviews 143, 117-146.

Martin, H., 1981. The late Palaeozoic Dwyka Group of the South Kalahari Basin in Namibia and Botswana and the subglacial valleys of the Kaokoveld in Namibia. In: Hambrey, M.J., Harland, W.B. (Eds.), Pre-Pleistocene Glacial Record. Cambridge University Press, Cambridge, pp. 61-66.

Mau, H., 1960. Vale pré-glacial ao norte de Lavras do Sul. Boletim da Sociedade Brasileira de Geologia 9, 79-82.

Menzies, J., van der Meer, J.J.M., Domack, E., Wellner, J.S., 2010. Micromorphology: as a tool in the detection, analyses and interpretation of (glacial) sediments and man-made materials. Proceedings of Geologists' Association 121, 281-292.

Menzies, J., van der Meer, J.J.M., 2018. Chapter 21 - Micromorphology and Microsedimentology of Glacial Sediments. In: Menzies, J., van der Meer, J.J.M. (Eds.), Past Glacial Environments (Second Edition). Elsevier, Amsterdam, pp. 753-806.

Montañez, I.P., Poulsen, C.J., 2013. The late Paleozoic ice age: an evolving paradigm. Annual Review of Earth Planetary Sciences 41, 1-28.

Mottin, T.E., Vesely, F.F., de Lima Rodrigues, M.C.N., Kipper, F., de Souza, P.A., 2018. The paths and timing of late Paleozoic ice revisited; new stratigraphic and paleo-ice flow interpretations from a glacial succession in the upper Itarare Group (Parana Basin, Brazil). Palaeogeography, Palaeoclimatology, Palaeoecology 490, 488-504.

Nesbitt, H.W., Markovics, G., Price, R.C., 1980. Chemical processes affecting alkalis and alkaline earths during continental weathering. Geochimica et Cosmoschimica Acta 44, 1659-1666.

Nesbitt, H.W., Young, G.M., 1982. Early Proterozoic climates and plate motions inferred from major element chemistry of lutites. Nature 299, 715.

Nesbitt, H.W., Young, G.M., McLennan, S.M., Keays, R.R., 1996. Effects of Chemical Weathering and Sorting on the Petrogenesis of Siliciclastic Sediments, with Implications for Provenance Studies. The Journal of Geology 104, 525-542.

Netto, R.G., Balistieri, P., Lavina, E.L.C., Silveira, D.M., 2009. Ichnological signatures of shallow freshwater lakes in the glacial Itarare Group (Mafra Formation, Upper Carboniferous-Lower Permian of Parana Basin, S Brazil). Palaeogeography, Palaeoclimatology, Palaeoecology 272, 240-255.

Ó Cofaigh, C., Dowdeswell, J.A., 2001. Laminated sediments in glacimarine environments: diagnostic criteria for their interpretation. Quaternary Science Reviews 20, 1411-1436.

Ocakoğlu, F., Dönmez, E.O., Akbulut, A., Tunoğlu, C., Kır, O., Açıkalın, S., Erayık, C., Yılmaz, İ.Ö., Leroy, S.A.G., 2015. A 2800-year multi-proxy sedimentary record of climate change from Lake Çubuk (Göynük, Bolu, NW Anatolia). The Holocene 26, 205-221.

Ogata, K., Mutti, E., Pini, G.A., Tinterri, R., 2012. Mass transport-related stratal disruption within sedimentary mélanges: examples from the northern Apennines (Italy) and south-central Pyrenees (Spain). Tectonophysics 568-569, 185-199.

Ovenshine, A.T., 1970. Observations of Iceberg Rafting in Glacier Bay, Alaska, and the Identification of Ancient Ice-Rafted Deposits. Geological Society of Association Bulletin 81, 891-894.

Phillips, E.R., 2018. 13 – Glacitectonics. In: Menzies, J., van der Meer, J.J.M. (Eds.), Past Glacial Environments. Elsevier, Amsterdam, pp. 467-502.

Phillips, E.R., Auton, C.A., 2000. Micromorphological evidence for polyphase deformation of glaciolacustrine sediments for Strathspey, Scotland. Geological Society, Special Publication 176, 279-292.

Phillips, E.R., Evans, D.J.A., Auton, C.A., 2002. Polyphase deformation of an oscillating ice margin following the Loch Lomond Readvance, central Scotland, UK. Sedimentary Geology 149, 157-182.

Phillips, E., Everest, J., Reeves, H., 2012. Micromorphological evidence for subglacial multiphase sedimentation and deformation during overpressurized fluid flow associated with hydrofracturing. Boreas 42, 395-427.

Phillips, E.R., Lee, J.R., Burke, H., 2008. Progressive proglacial to subglacial deformation and syntectonic sedimentation at the margins of the Mid-Pleistocene British Ice Sheet: evidence from north Norfolk, UK. Quaternary Science Reviews 27, 1848-1871.

Phillips, E.R., Merrit, J., Auton, C., Golledge, N., 2007. Microstructures in subglacial and proglacial sediments: understanding faults, folds and fabrics, and the influence of water on the style of deformation. Quaternary Science Reviews 26, 1499-1528.

Piotrowski, J.A., Larsen, N.K., Menzies, J., Wysota, W., 2006. Formation of subglacial till under transient bed conditions; deposition, deformation, and basal decoupling under a Weichselian ice sheet lobe, central Poland. Sedimentology 53, 83-106.

Posamentier, H.W., Walker, R.G., 2006. Deep-water turbidites and submarine fans. Society for Sedimentary Geology, Special Publication 84, 399-520.

Ravier, E., Buoncristiani, J.F., Menzies, J., Guiraud, M., Portier, E., 2015. Clastic injection dynamics during ice front oscillations: A case example from Sólheimajökull (Iceland). Sedimentary Geology 323, 92-109.

Riccomini, C., Velázquez, V.F., 1999. Superfície estriada por geleira Neopaleozoica no Paraguai oriental. Revista Basileira de Geociências 29, 233-236.

Roberts, D.H., Yde, J.C., Knudsen, N.T., Long, A.J., Lloyd, J.M., 2009. Ice marginal dynamics during surge activity, Kuannersuit Glacier, Disko Island, West Greenland. Quaternary Science Reviews 28, 209-222.

Rocha-Campos, A.C., Canuto, J.R., Santos, P.R., 2000. Late Paleozoic glaciotectonic structures in northern Paraná Basin, Brazil. Sedimentary Geology 130, 131-143.

Rocha-Campos, A.C., Santos, P.R., Canuto, J.R., 2008. Late Paleozoic glacial deposits of Brazil: Paraná Basin. In: Fielding, C.R., Frank, T.D., Isbell, J.L.(Eds.). Resolving the Late Paleozoic Ice Age in Time and Space. Geological Society of America Special Paper 441, 97-114.

Rooney, T.O., Hart, W.K., Hall, C.M., Ayalew, D., Ghiorso, M.S., Hidalgo, P.J., Yirgu, G., 2012. Peralkaline magma evolution and the tephra record in the Ethiopian Rift. Contributions to Mineralogy and Petrology 164, 407-426.

Rooney, T.O., Mohr, P., Dosso, L., Hall, C.M., 2013. Geochemical evidence of matle reservoir evolution during progressive rifting. Geochimica et Cosmoschimica Acta 102, 65-88.

Rosa E.L.M., Vesely, F.F., França, A.B., 2016. A review on late Paleozoic ice-related erosional landforms in the Paraná Basin: origin and paleogeographical implications. Brazilian Journal of Geology 46, 147-166.

Rotnicki, K., 1976. The theoretical basis for and a model of the origin of glaciotectonic deformations. Quaestiones geographicae 3, 103-139.

Santos, P.R., Rocha-Campos, A.C., Canuto, J.R., 1996. Patterns of late Palaeozoic deglaciation in the Paraná Basin, Brazil. Palaeogeography, Palaeoclimatology, Palaeoecology 125, 165-184.

Scheffler, K., Buehmann, D., Schwark, L., 2006. Analysis of late Palaeozoic glacial to postglacial sedimentary successions in South Africa by geochemical proxies; response to climate evolution and sedimentary environment. Palaeogeography, Palaeoclimatology, Palaeoecology 240, 184-203.

Scheffler, K., Hoernes, S., Schwark, L., 2003. Global changes during Carboniferous-Permian glaciation of Gondwana; linking polar and equatorial climate evolution by geochemical proxies. Geology (Boulder) 31, 605-608.

Souza, P.A., 2006. Late Carboniferous palynostratigraphy of the Itarare Subgroup, northeastern Parana Basin, Brazil. Review of Palaeobotany and Palynology 138, 9-29.

Souza, P.A. Marques-Toigo, M., 2005. Progress on the palynostratigraphy of the Paraná strata in Rio Grande do Sul State, Paraná Basin, Brazil. Anais da Academia Brasileira de Ciências, 77, 353-365.

Starck, D., Papa, C., 2006. The northwestern Argentina Tarija Basin: stratigraphy, depositional systems, and controlling factors in a glaciated basin. Journal of South American Earth Sciences 22, 169-184.

Stephenson, M.H., 2008. A review of the palynostratigraphy of Gondwanan Late Carboniferous to Early Permian glacigene successions. In: Fielding, C.R., Frank, T.D., Isbell, J.L.(Eds.).

Resolving the Late Paleozoic Ice Age in Time and Space. Geological Society of America Special Paper, 441, 115-129.

Stokes, C.R., Clark, C.D., 2017. Geomorphological criteria for identifying Pleistocene ice streams. Annals of Glaciology 28, 67-74.

Taylor, S.R., McClennan, S.M., 1985. The continental crust; its composition and evolution; an examination of the geochemical record preserved in sedimentary rocks. Blackwell Scientific Publication, Oxford (312 pp.).

Tedesco, J., Cagliari, J., Coitinho, J.D.R., da Cunha Lopes, R., Lavina, E.L.C., 2016. Late Paleozoic paleofjord in the southernmost Parana Basin (Brazil); geomorphology and sedimentary fill. Geomorphology 269, 203-214.

Tomazelli, L.J., Soliani Júnior, E., 1982. Evidências de atividade glacial no Paleozóico Superior do Rio Grande do Sul, Brasil. Anais II Congresso Brasileiro de Geologia, Salvador 4, 1378-1389.

Tomazelli, L.J., and Soliani Júnior, E., 1997. Sedimentary facies and depositional environments related to Gondwana glaciation in Batovi and Suspiro Regions, Rio Grande do Sul, Brazil. Journal of South American Earth Sciences 10, 295-303.

Torsvik, T.H., Cocks, L.R.M., 2013. Gondwana from top to base in space and time. Gondwana Research 24, 999-1030.

Trosdtorf, I., Rocha-Campos, A., Santos, P.R., Tomio, A., 2005. Origin of Late Paleozoic, multiple, glacially striated surfaces in northern Paraná Basin (Brazil): Some implications for the dynamics of the Paraná glacial lobe. Sedimentary Geology 181, 59-71.

van der Meer, J.J.M., Menzies, J., Rose, J., 2003. Subglacial till: the deforming glacier bed. Quaternary Science Reviews 22, 1659-1685.

van der Wateren, D.F.M., 1985. A model of glacial tectonics, applied to the ice-pushed ridges in the central Netherlands. Bulletin of the Geological Society of Denmark 34, 55-74.

van der Wateren, F.M., 1995. Structural geology and sedimentology of push moraines; processes of soft sediment deformation in a glacial environment and the distribution of glaciotectonic styles. Mededelingen Rijks Geologische Dienst 54, 167.

van der Wateren, F.M., 2002. 14-Processes of glaciotectonism. In: Menzies, J. (Ed.), Modern and Past Glacial Environments. Butterworth and Heinemann, Oxford, pp. 417-443.

van der Wateren, F.M., Kluiving, S.J., Bartek, L.R., 2000. Kinematic indicators of subglacial shearing. In: Maltman, A.J., Hubbard, B., Hambrey, M.J. (Eds.), Deformation of Glacial Materials. Geological Society, London, Special Publication 176, 259-278.

Vesely, F.F., Rodrigues, M.C.N.L., Rosa, E.L.M., Amato, J.A., Trzaskos, B., Isbell, J.L., Fedorchuk, N.D., 2018. Recurrent emplacement of non-glacial diamictite during the late Paleozoic ice age. Geology (Boulder) 46, 615-618.

Vesely, F.F., Trzaskos, B., Kipper, F., Assine, M.L., Souza, P.A., 2015. Sedimentary record of a fluctuating ice margin from the Pennsylvanian of western Gondwana: Paraná Basin, southern Brazil. Sedimentary Geology 326, 45-63.

Visser, J.N.J., 1989. The Permo-Carboniferous Dwyka Formation of Southern Africa: Deposition by a predominantly subpolar marine ice sheet. Palaeogeography, Palaeoclimatology, Palaeoecology 70, 377-391.

Visser, J.N.J., 1993. A reconstruction of the late Palaeozoic ice sheet on southwestern Gondwana. In: Findlay, R.H., Unrug, R., Banks, M.R., Veevers, J.J. (Eds.), Gondwana 8 Assembly, Evolution and Dispersal. A.A. Balkema, Rotterdam, pp. 449-458.

Visser, J.N.J., Colliston, W.P., Terblanche, J.C., 1984. The origin of soft-sediment deformation structures in Permo-Carboniferous glacial and proglacial beds, South Africa. Journal of Sedimentary Petrology 54, 1183-1196.

Visser, J.N.J., Loock, J.C., 1982. An investigation of the basal Dwyka Tillite in the southern part of the Karoo Basin, South Africa. Transactions of Geological Society of South Africa 85, 179-187.

Waller, R.I., Murton, J.B., Kristensen, L., 2012. Glacier–permafrost interactions: Processes, products and glaciological implications. Sedimentary Geology 255-256, 1-28.

Winsemann, J., Lang, J., Polom, U, Loewer, M., Igel, J., Pollok, L., Brandes, C., 2018. Ice-marginal forced regressive deltas in glacial lake basins: geomorphology, facies variability and large-scale depositional architecture. Boreas 47, 973-1002.

Weertman, J., 1969. Water lubrication mechanism of glacier surges. Canadian Journal of Earth Sciences 6, 929-942.

Ye, C., Yang, Y., Fang, X., Zhang, W., 2016. Late Eocene clay boron-derived paleosalinity in the Qaidam Basin and its implications for regional tectonics and climate. Sedimentary Geology 346, 49-59.

Zavala, C., Arcuri, M., 2016. Intrabasinal and extrabasinal turbidites: Origin and distinctive characteristics. Sedimentary Geology 337, 36-54.

Zolitschka, B., Francus, P., Ojala, A.E.K., Schimmelmann, A., 2015. Varves in lake sediments – a review. Quaternary Science Reviews 117, 1-41.
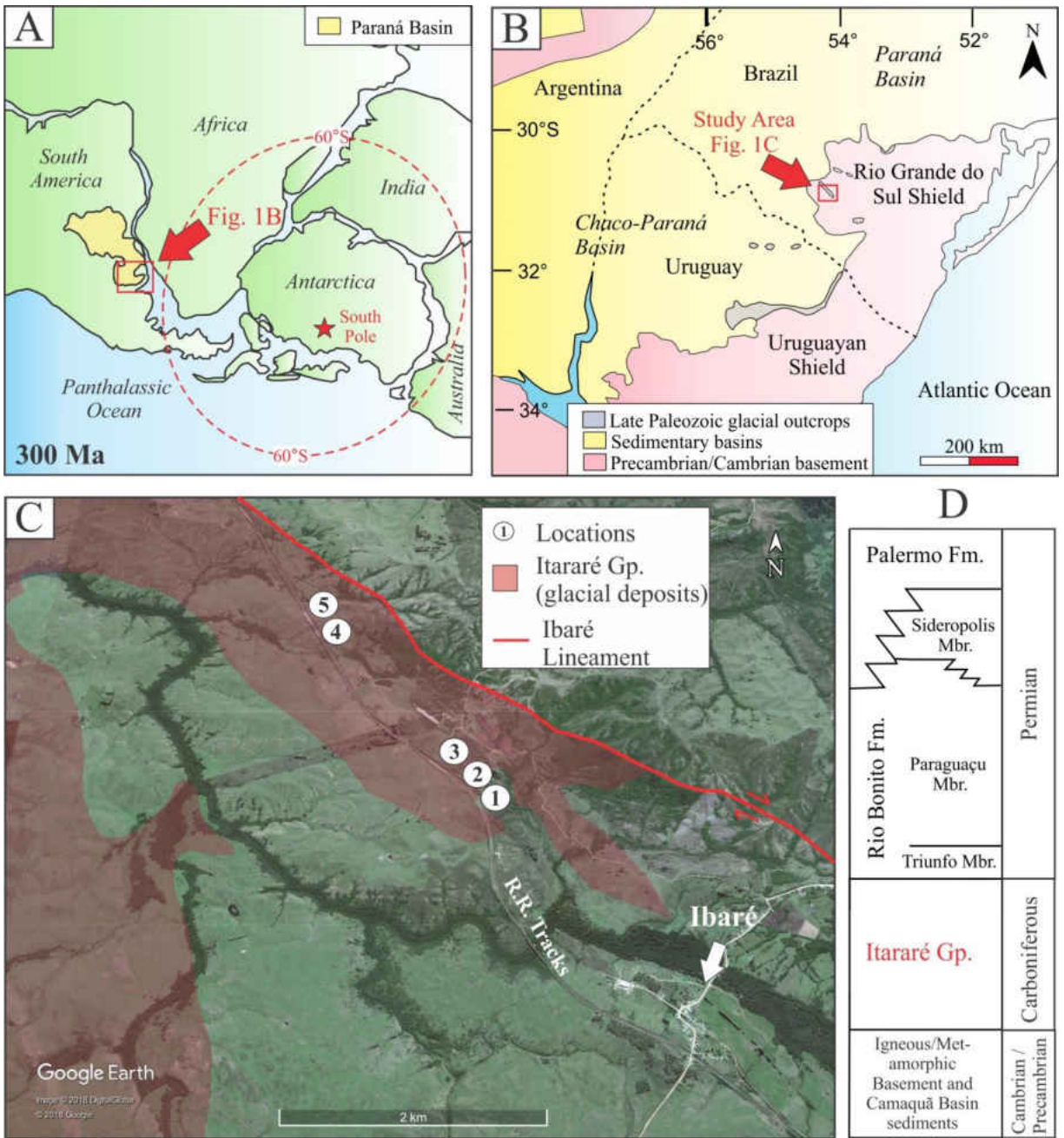
Fig. 3.1. Paleogeography, location, and stratigraphy of study area. (A) Gondwanan paleogeography with location of Paraná Basin in yellow and Rio Grande do Sul Shield located within red square. After Lawver et al. (2011) and Torsvik and Cocks (2013). (B) Map of Rio Grande do Sul Shield and late Paleozoic glacial outcrops (gray) with study area (Fig. 3.1C) located within red square. After Assine et al. (2018). (C) Geologic map of the study area located 3 km NW of Ibaré, Rio Grande do Sul State. Study locations 1-5 numbered along railroad tracks. Image from GoogleEarth (2018) and location of Itararé Gp./Ibaré Lineament from Companhia de Pesquia de Recursos Minerais (Brazilian Geological Survey). (D) Stratigraphic position of glacial strata on the Rio Grande do Sul Shield, Itararé Gp. in red. Modified from Holz et al. (2006).
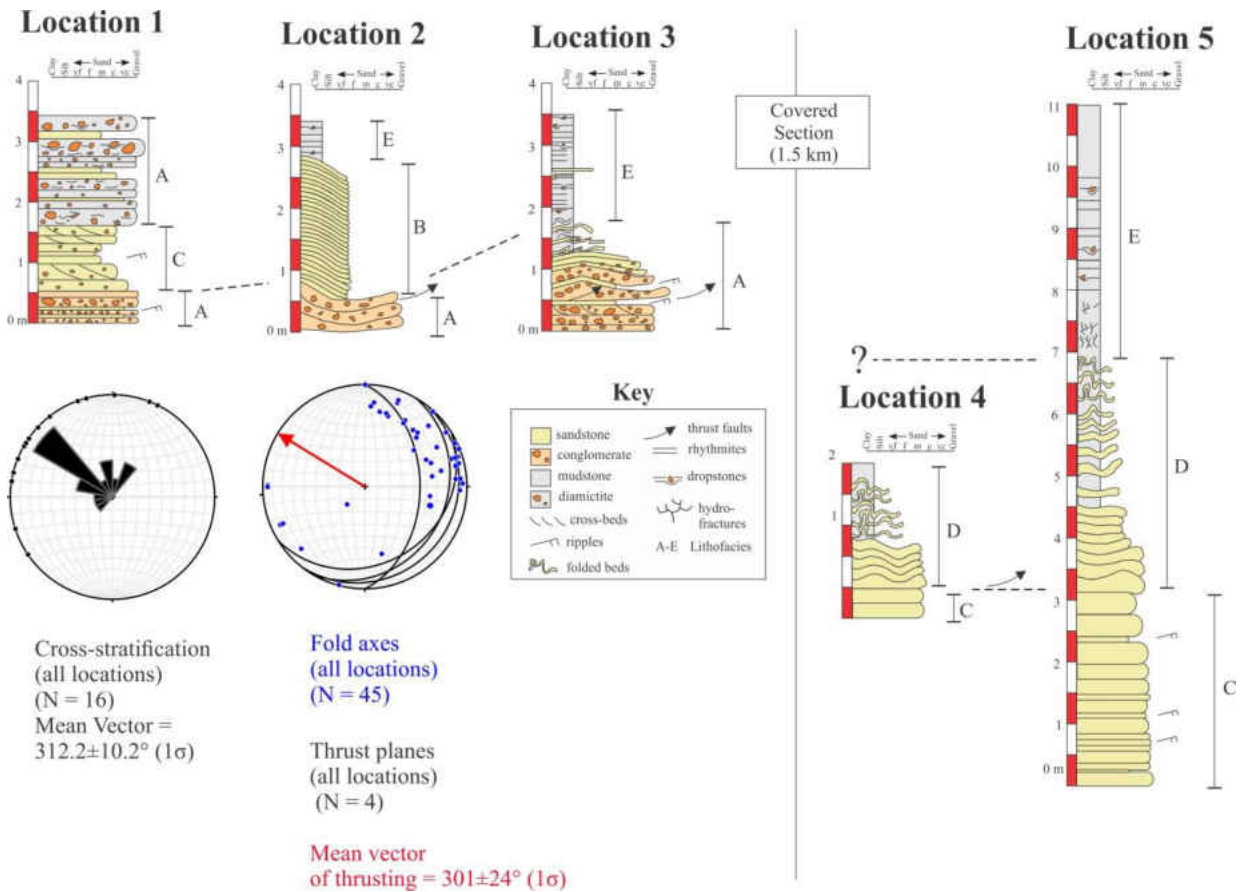
Fig. 3.2 Measured stratigraphic sections from Locations 1-5. Paleocurrent data, fold axes, and thrust planes data combined from all locations.

122

Lithofacies name	Symbol	Lithologies	Key features and sedimentary structures	Bed thickness	Interpretation
Conglomerate and diamictite facies	A	Sandy conglomerate and clast-rich sandy diamictite, interbeds of gravelly sandstone	Rare crude cross-bedding and ripples, diverse clast composition, clasts have striations and facets, deformation of this facies includes large (1-3 m high) folds-thrust complexes	~4 cm to 1 m	Coarse grained outwash and debris flows from outwash fan, deformed by ice pushing into sediment wedge
Sandy clinoform facies	B	Siltstone to fine sandstone	Undeformed thin siltstone and sandstone beds dip ~25° before laterally grading into silt/clay rhythmites	~1-4 cm	Foresets from small gilbert-type delta prograding into a shallow meltwater-fed lake that ponded between positive deformation features
Medium sandstone facies	C	Fine- to medium-grained sandstone and gravelly sandstone	Undeformed, mostly structureless, contains rare ripples and cross-beds	~4 cm to 0.5 m	Sandy outwash fan deposits (distal to Facies A)
Folded sandstone with interbedded mudstone facies	D	Fine- to medium-grained sandstone with interbedded mudstone	Some normal grading between sandstone and mudstone beds, deformation includes intense folding , thrust faults, normal faults, reverse faults, fractures	~1-20 cm	Fan delta deposits formed by combination of settling from suspension and hyperpycnal flows, deformed by ice pushing into sediment wedge
Rhythmites and mudstone with outsized clasts facies	E	Massive mudstone and clay/silt rhythmites with mm-scale laminae	Contains outsized clasts that pierce through laminae ranging from granule to cobble sized, mm-sized diamictite pellets, hydrofractures filled with brecciated rhythmite fragments	Individual rhythmite laminae are ~0.1-6 mm thick and occur in packages up to ~3 m thick, massive mudstone is ~1 m thick	Settling from suspension into meltwater-fed lakes or estuary, rhythmites interpreted as annual varves, outsized clasts and diamictite pellets are interpreted as ice-rafted dropstones, hydrofractures produced by pressurized proglacial porewater trapped under confining rhythmites

Table 3.1. Lithofacies codes, descriptions, and paleoenvironmental interpretations.
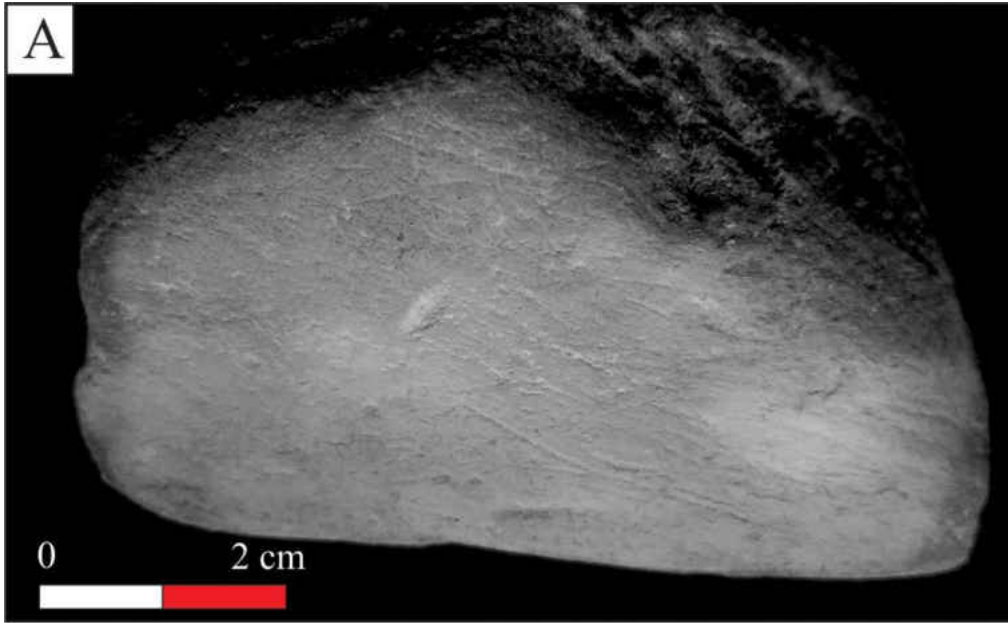
Fig. 3.3. Key features from Facies A. (A) Striated clast from Facies A at Location 3. (B) Crudely bedded sandy conglomerate from Facies A at Location 1.
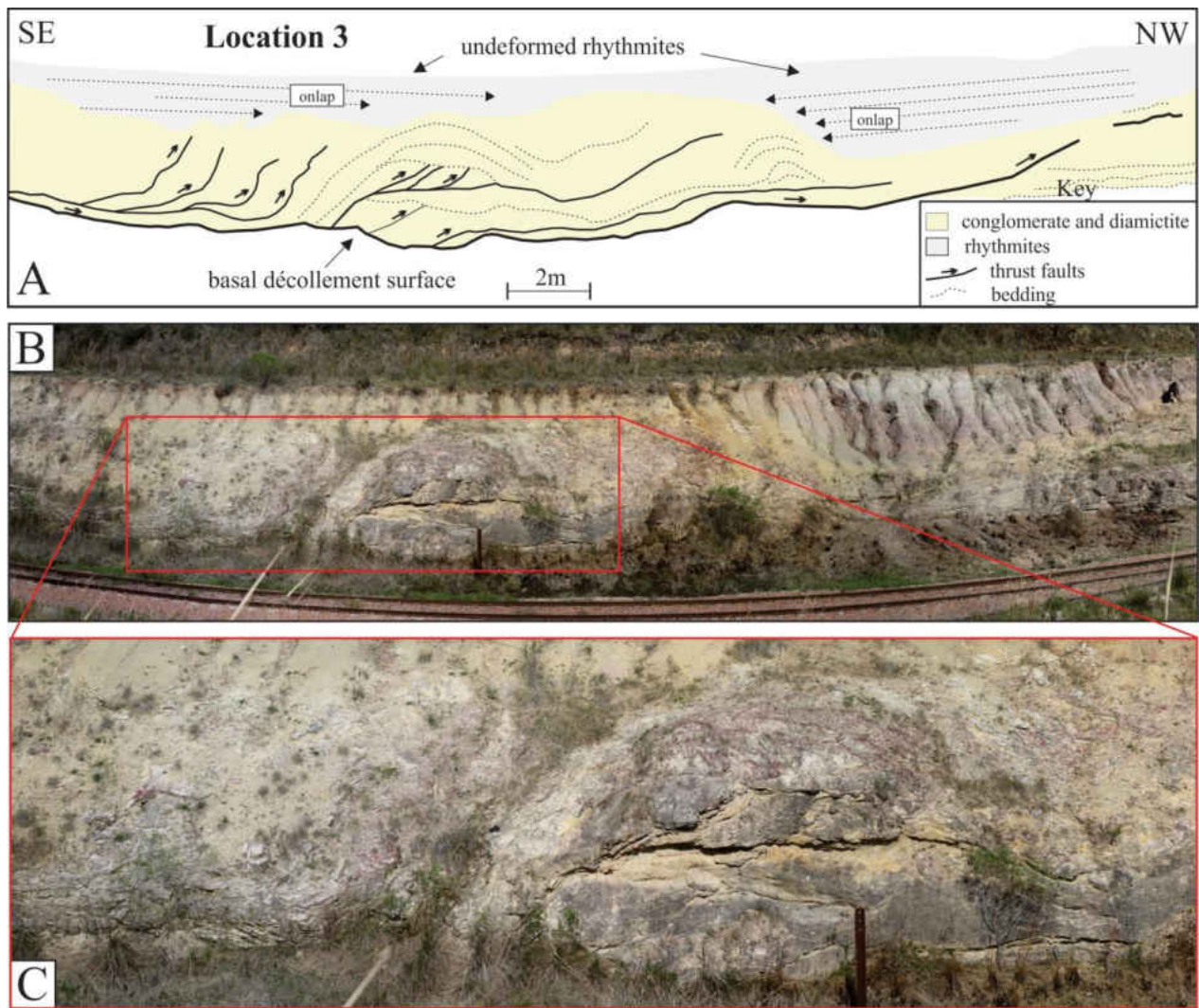
Fig. 3.4. (A-C) Example of piggyback fold-thrust complex at Location 3 indicating motion towards the NW.

Fig. 3.5. (A-B) Sandy clinoforms (white dashed lines) of Facies B at Location 2.
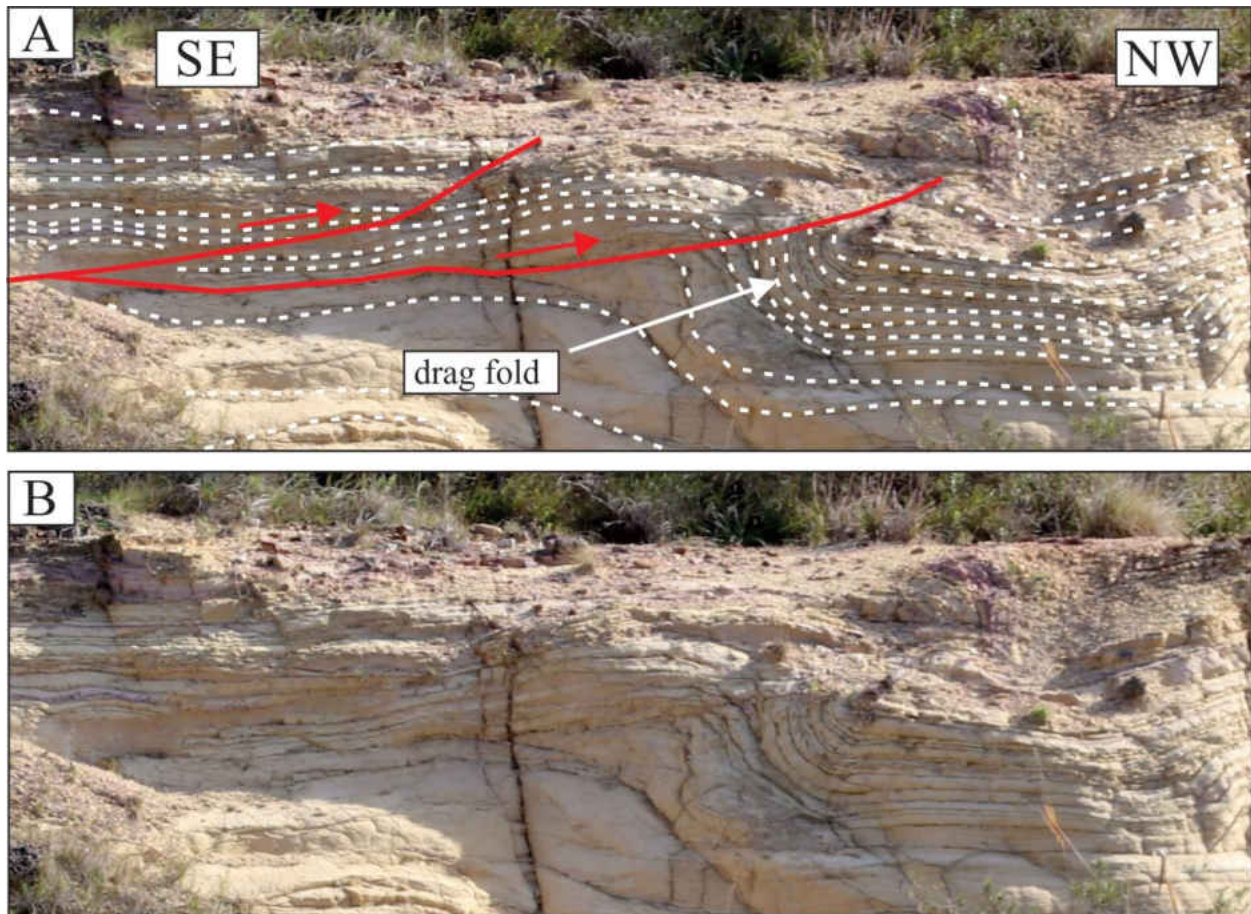
Fig. 3.6. (A-B) Drag fold (white arrow) and thrust faults (red solid lines) in folded sandstone with interbedded mudstone facies (Facies D, bedding=white dashed lines) at Location 4.

127
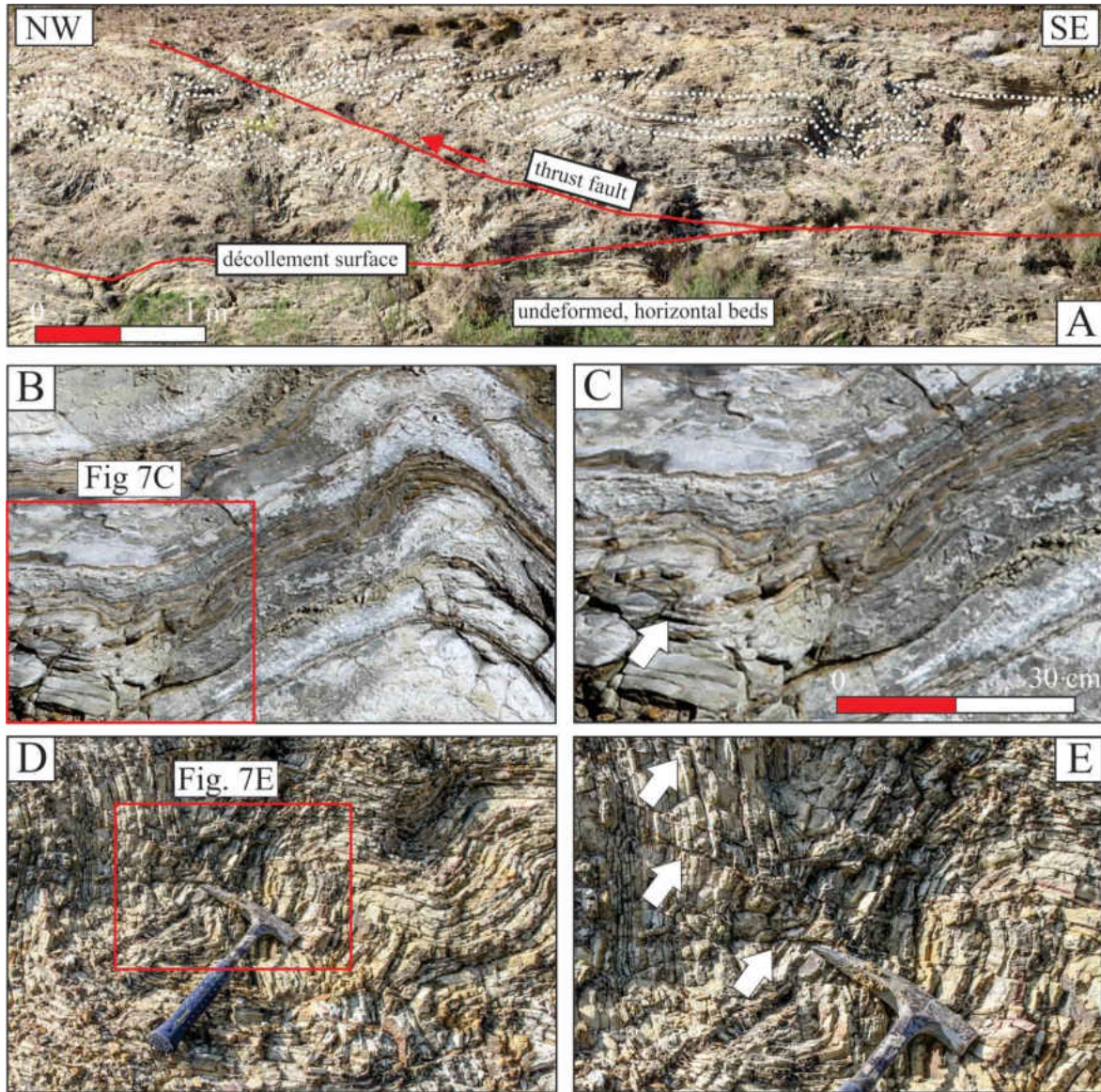
Fig. 3.7. Key features of folded sandstone with interbedded mudstone facies (Facies D) at Locations 4 and 5. (A) Folded beds (white dashed lines) overlying a décollement surface (red solid lines) and dissected by thrust fault (red solid line) at Location 4. (B-C) Small parasitic folds (white arrow) superimposed on larger fold at Location 5. (D-E) Intensely folded beds with later stage brittle faulting and fractures (white arrows) at Location 5. Rock hammer (28 cm) for scale.
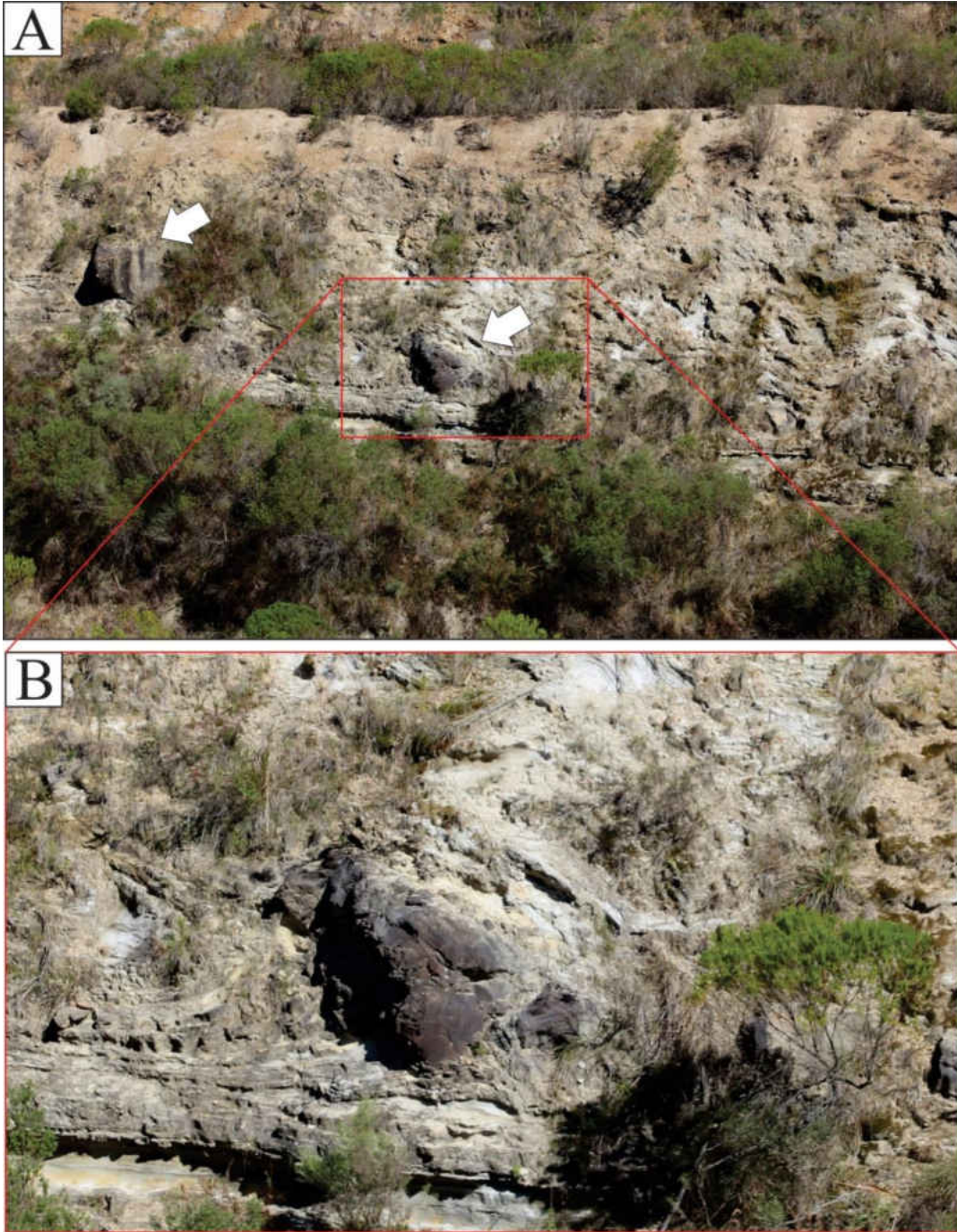
Fig. 3.8. (A-B) Possible slide blocks or extruded sediment between folds (white arrows) within the folded sandstone with interbedded mudstone facies (Facies D) at Location 5.
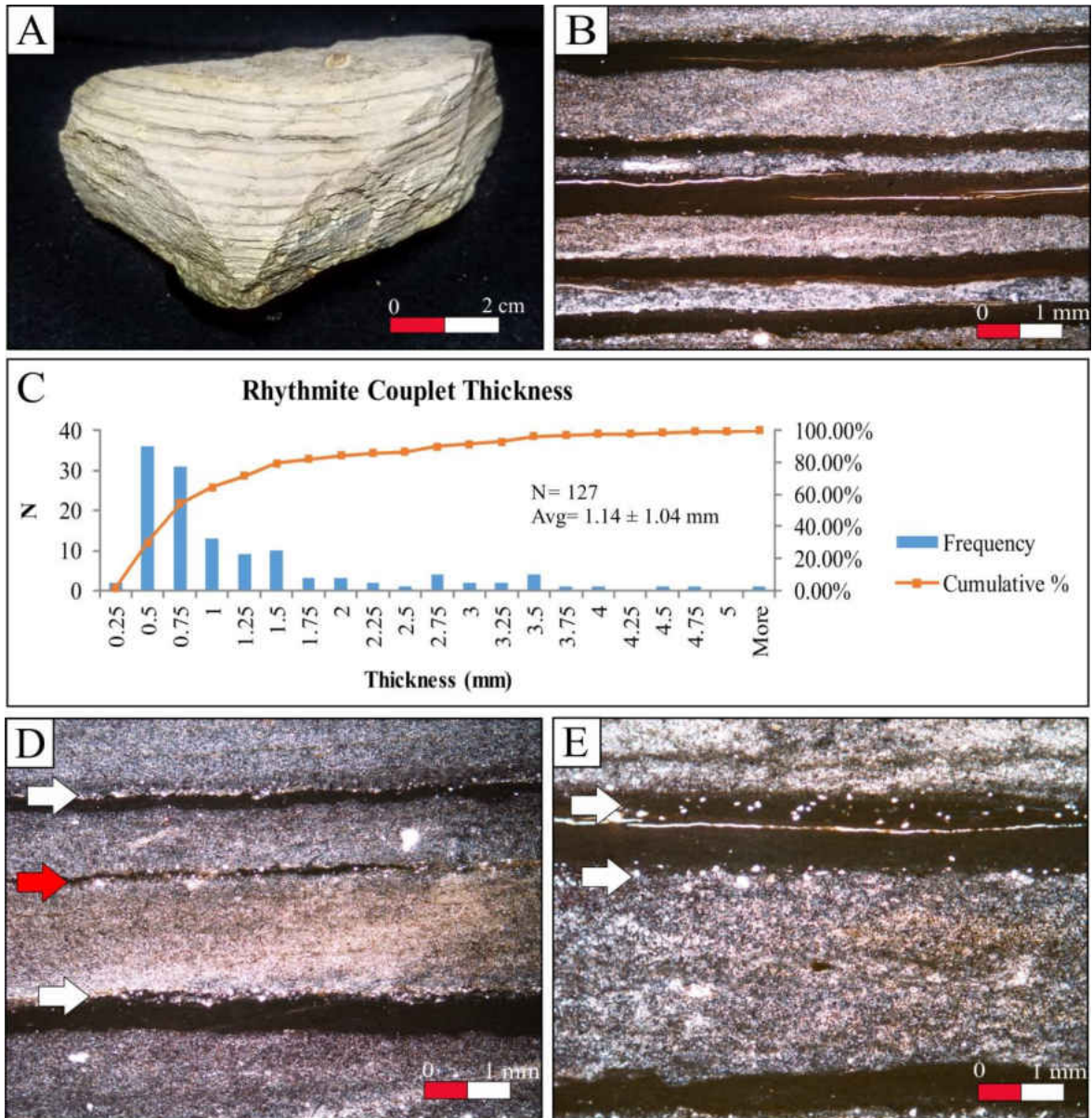
Fig. 3.9. Key features of rhythmites and mudstone with outsized clasts facies (Facies E) at Location 3 and 5. (A) Hand sample of rhythmites from Location 3. (B) Thin section viewed under crossed polars of alternating silt/clay rhythmite laminae with sharp contacts from Location 3. (C) Histogram and cumulative frequency distribution plot of rhythmite couple thicknesses (standard deviation of average thickness is 1σ). Measurements collected from four thin section samples collected at Locations 3 and 5. (D) Thin section viewed under crossed polars of clay interlamina (red arrow) and fine-sand-sized layers (white arrows) always located within clay laminae or on borders of clay laminae. (E) Thin section viewed under crossed polars of fine sand layers (white arrows).
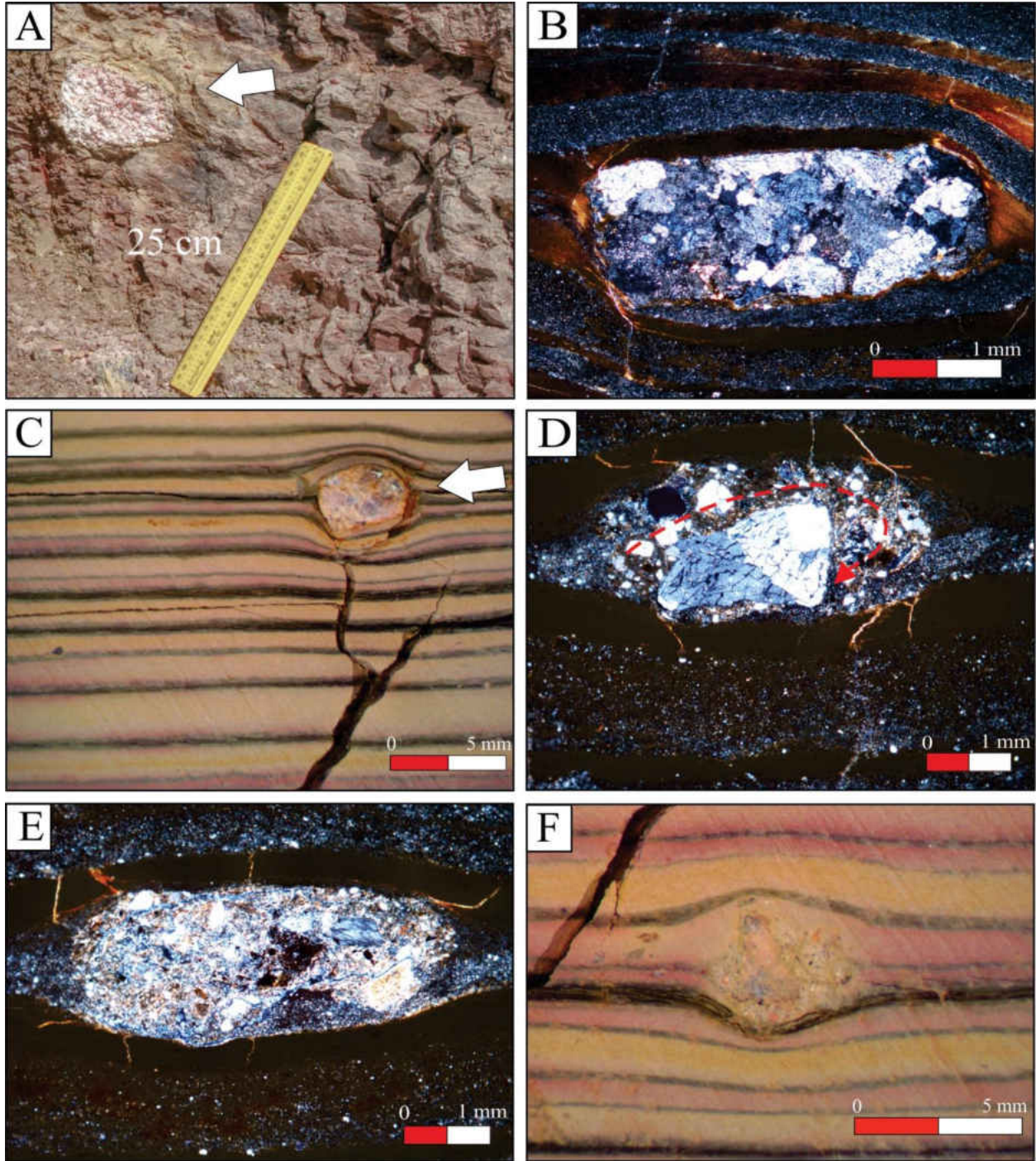
Fig. 3.10. Dropstones and diamictite pellets viewed under crossed polars and located within the rhythmites and mudstone with outsized clasts facies (Facies E) from Location 3. (A) Large (cobble-sized), granite outsized clast (white arrow) that pierces through rhythmite laminae (i.e. dropstone). (B) Thin section (viewed under crossed polars) of granule-sized granite outsized clast that pierces through rhythmite laminae (i.e. dropstone). (C) Pebble-sized, granite outsized clast (white arrow) that pierces through rhythmite laminae (i.e. dropstone). (D) Thin section of diamictite pellet viewed under crossed polars with grains rotated around a central clast (red dashed arrow). (E) Thin section viewed under crossed polars of diamictite pellet. (F) Diamictite/till pellet viewed under reflected light.

131
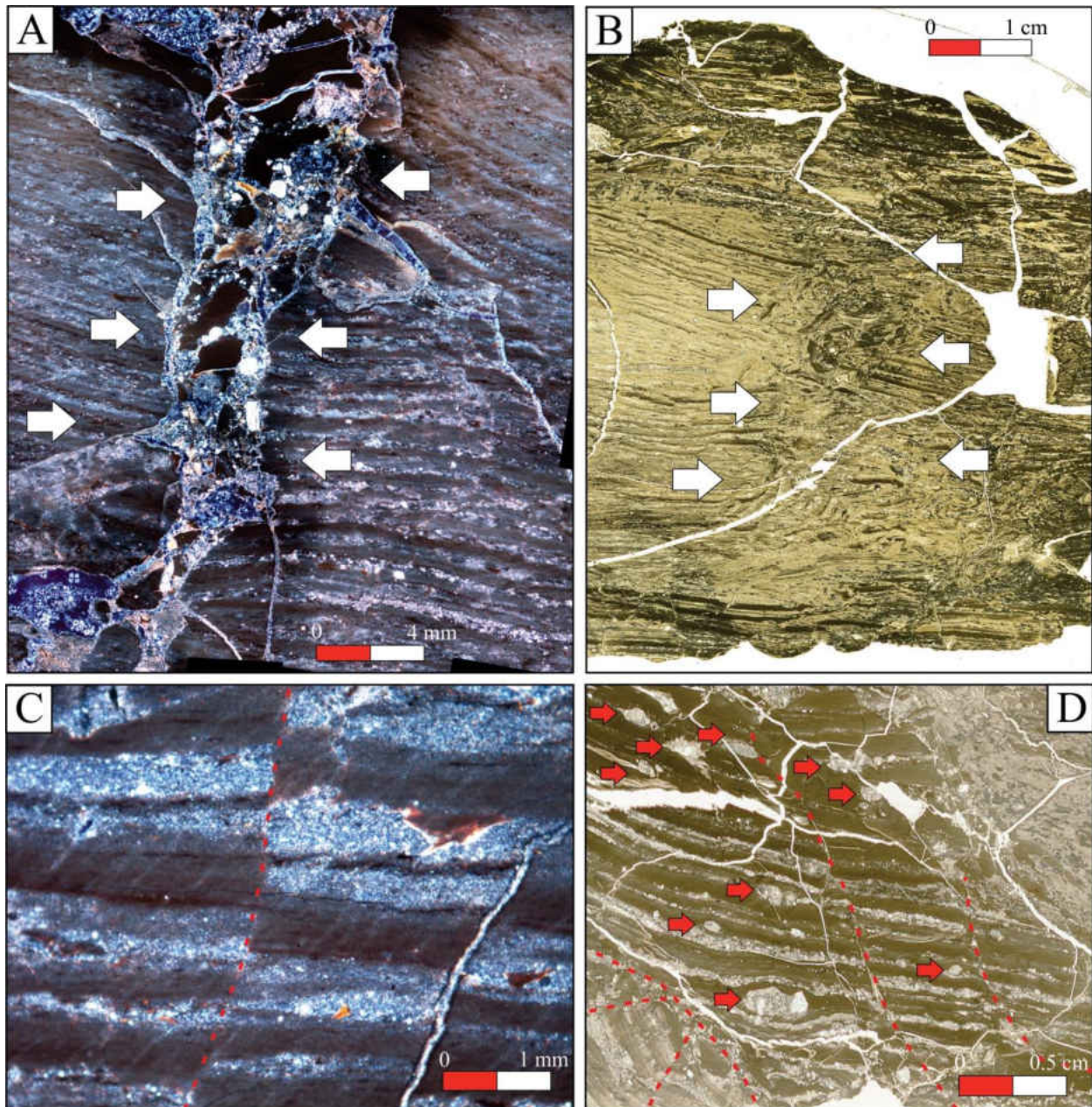
Fig. 3.11. Deformation features within rhythmites and mudstone with outsized clast facies (Facies E) at Location 5. (A) Thin section photomosaic of clastic dike (hydrofracture) through rhythmites viewed under crossed polars. Boundaries indicated by white arrows. (B) Clastic dike (hydrofracture) through rhythmites viewed under plain polarized light. Boundaries indicated by white arrows. (C) Thin section under crossed polars of small (mm-scale) reverse fault (red dashed line) in rhythmites. (D) Thin section of (mm-scale) normal faults (red dashed lines) and diamictite pellets (red arrows) in rhythmites viewed under plain polarized light.
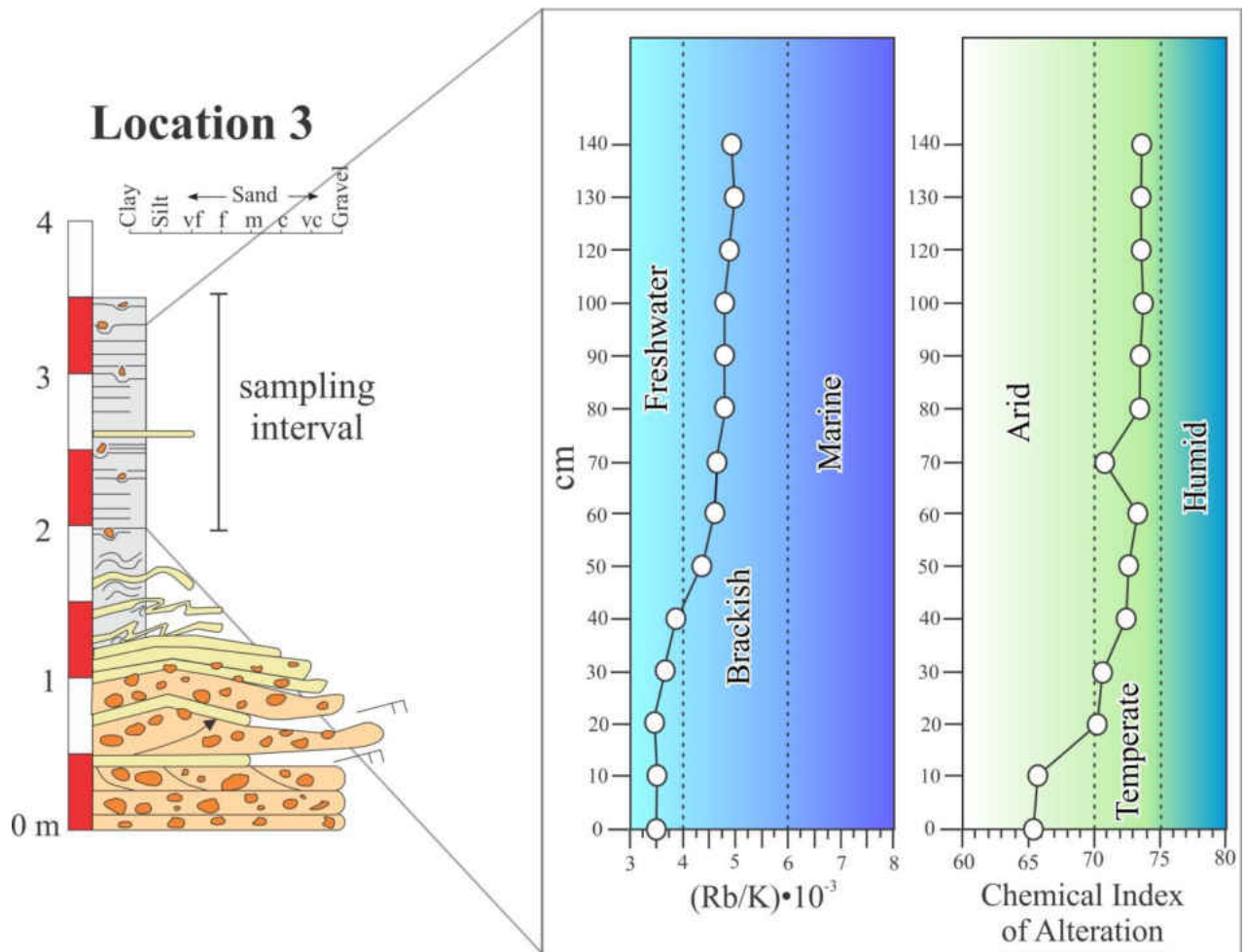
Fig. 3.12. Geochemical (Rb/K and Chemical Index of Alteration) data collected from rhythmites at Location 3. The increase in Rb/K values could be related to an influx of freshwater, increased chemical weathering, or a combination of the two.
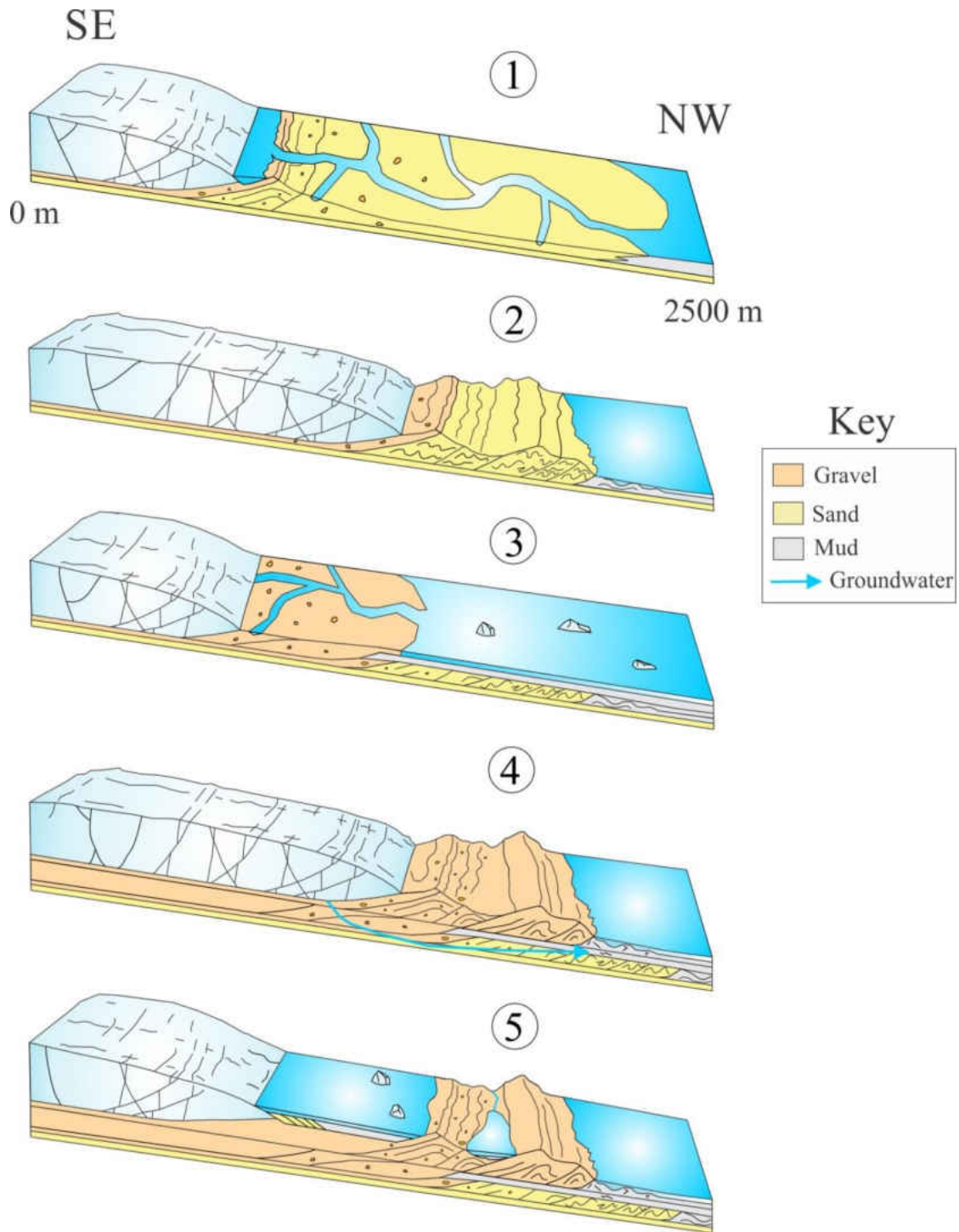
Fig. 3.13. Interpretation of two advance/retreat cycles responsible for deposition and deformation observed at Locations 1-5. After Roberts et al. (2009).
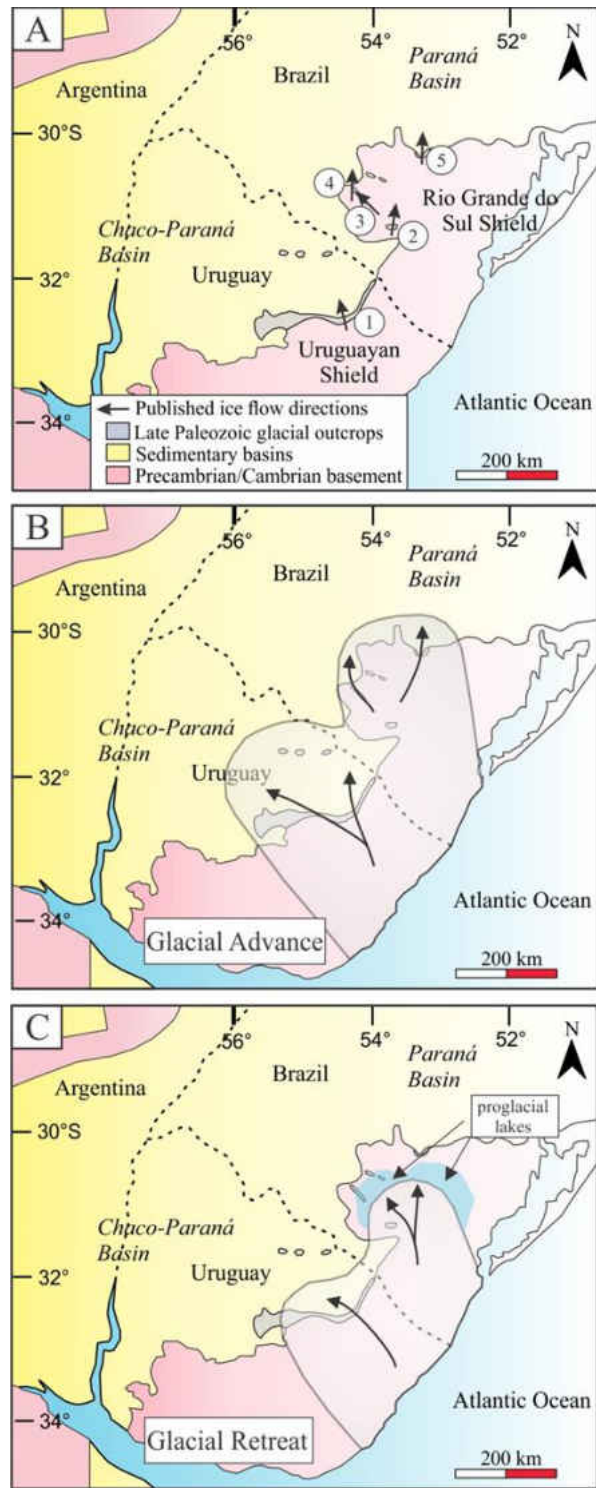
Fig. 3.14. Interpretation of glaciation on Rio Grande do Sul during late Carboniferous. (A) Published ice flow directions from grooved surfaces and ice-contact deformation indicated by black arrows. (1) Assine et al., 2018. (2) Tomazelli and Soliani Júnior (1982). (3) This study. (4) Tomazelli and Soliani Júnior (1997). (5) Tomazelli and Soliani Júnior (1982). (B) "Uruguayan Ice Center" paleogeographic reconstruction during glacial advance phase. Such an ice center may have originated in Cargonian Highlands of Africa. After Crowell and Frakes (1975) and Assine et al. (2018). (C) Interpretation of "Uruguayan Ice Center" during glacial retreat phase. After Crowell and Frakes (1975) and Assine et al. (2018).

135

Chapter 4. Provenance of late Paleozoic glacial/post-glacial deposits in the eastern Chaco-Paraná Basin, Uruguay and southernmost Paraná Basin, Brazil

Abstract

The Paraná Basin, Brazil and the Chaco-Paraná Basin, Uruguay both contain sedimentary records that are critical to reconstructing late Paleozoic ice centers in central Gondwana. The orientations of subglacial erosional features and glaciotectonic deformation features suggest that late Paleozoic glacial deposits in the eastern Chaco-Paraná Basin and the southernmost Paraná Basin are genetically related. However, the location and extent of the ice center responsible for depositing these sediments is unclear. Furthermore, changes in drainage patterns between glacial, inter-glacial, and post-glacial intervals are not understood for this region. Therefore, this study utilized U-Pb detrital zircon geochronology to assess the provenance of glacial and post-glacial sediments from the eastern Chaco-Paraná Basin (San Gregorio, Cerro Pelado, Tres Islas Fms.) and the southernmost Paraná Basin (Itararé Gp.). Results show dominant age peaks at ~520-555 Ma, ~625 Ma, 750-780 Ma, and 900-1000 Ma in all samples from the eastern Chaco-Paraná Basin. These zircons are interpreted to have been derived from sources in the Cuchilla Dionisio Terrane, Punta del Este Terrane, and Namaqua Belt located in southeastern Uruguay and southern Namibia. Another important source was likely Devonian sedimentary rocks of the Durazno Gp. in eastern Uruguay. Meanwhile, a sample of the glaciogenic Itararé Gp. from the southernmost Paraná Basin contains a different detrital zircon signature with peaks at ~580 Ma, ~780 Ma, ~2110 Ma, and ~2500 Ma that closely resembles underlying sedimentary and meta-sedimentary rocks of the Precambrian/Cambrian Camaquã Basin. Detrital zircon ages in the glacial and post-glacial sediments indicate that local sources were dominant. In contrast, zircon ages from relatively ice-distal glaciomarine intervals reflect more distal sources to the E and SE, which indicates a larger drainage catchment opened up when glaciers retreated. These results

support the hypothesis that an ice center in the highlands of southern Namibia and southeast Uruguay expanded W into the Chaco-Paraná Basin and NW into the Paraná Basin and receded to the SE. This ice center was separated from the ice center responsible for glaciation of the eastern Paraná Basin. Therefore, at least two separate ice centers, based in African highlands, were responsible for depositing glacial sediments in the Paraná and Chaco-Paraná Basins.

4.1. Introduction

The late Paleozoic ice age (LPIA, late Devonian to late Permian) was a time characterized by unique climate conditions relative to most of Earth's history. Glaciers were present in high- to mid-latitude basins across Gondwana, coinciding with the growth of widespread equatorial forests and an atmosphere defined by low pCO_2 and high pO_2 (e.g. Gastaldo et al., 1996, Isbell et al., 2003, 2012; Raymond and Metz, 2004; Montañez and Soreghan, 2006; Fielding et al., 2008; Montañez and Poulsen, 2013; Frank et al., 2015). Interpretations of glaciation during this period have evolved over the past several decades from the original hypothesis of a single, continental-scale ice sheet that persisted for ~100 my to a new paradigm of multiple smaller ice sheets and ice caps that fluctuated in time and space on shorter, ~1-10 my timescales (e.g. Isbell et al., 2003, 2012; Fielding et al., 2008). However, the true nature of the glacial interval, including ice extent, the role of the various climate drivers, and the timing of fluctuations in ice volume, remains unclear.

Considerable work has been done on the LPIA glacial record of individual basins across Gondwana, providing new levels of insight into the sedimentary processes and intrabasinal correlations (e.g. Lopez-Gamundi, 1997; Visser, 1997a; Vesely and Assine, 2006; Fielding et al.,

2010). Despite these advances, the temporal and physical connections between strata in adjacent basins remain been poorly constrained due to the lack of reliable radiometric ages and dispersed biostratigraphic zonations. However, the introduction of detrital zircon geochronology as a tool to assess the provenance of glacial strata allows for improved understanding of paleo-drainage patterns, ice extent, and the interbasinal connections between seemingly disparate deposits (e.g. Canile et al., 2016; Linol et al., 2016; Griffis et al., 2019; Craddock et al., 2019). In particular, one critical area to this problem is the cross-Atlantic correlation of late Paleozoic glacial sediments in Africa and South America. Two basins relevant to this question are the Paraná and Chaco-Paraná Basins, which were located on the border between present-day Africa and South America during the late Paleozoic (Fig. 4.1).

The Paraná Basin is an intracratonic sedimentary basin located in Brazil, Paraguay, Uruguay, and Argentina while the Chaco-Paraná Basin is located to the south and southwest in Uruguay, Paraguay, and Argentina (e.g. França and Potter, 1991; Goso, 1995; De Santa Ana, 2004; De Santa Ana et al., 2006a, 2006b; Holz et al., 2010; Vesely et al., 2015; Assine et al., 2018). The Chaco-Paraná Basin is connected to the main body of the Paraná Basin near the Brazil/Uruguay/Argentina border (Fig. 4.1) (Winn Jr. and Steinmatz, 1998). Both basins contain a Permo-Carboniferous glacial record and are thought to have a closely related depositional history (e.g. Assine et al., 2018). However, the glacial record in the Chaco-Paraná Basin is significantly understudied compared to the Paraná Basin due to poor surficial exposure of outcrops (e.g. Winn Jr. and Steinmatz, 1998). The basins are partially separated by a paleotopographic high known as the Rio Grande do Sul Shield (RGS) that contains isolated outcrops of Carboniferous glacial sediments (Fig. 4.2) (e.g. Tomazelli and Soliani Júnior 1982, 1997; Fedorchuk et al., 2019a).

Northeast of the RGS, on the eastern margin of the Paraná Basin (Brazil), the primarily E-W orientations of subglacial grooves and striations, combined with paleocurrent orientations and ice marginal deformation structures, have long implied that a northern Namibia-based ice center drained west into the eastern Paraná Basin (e.g. Frakes and Crowell, 1972; Crowell and Frakes, 1975; Rocha-Campos et al., 2008, Vesely et al., 2015; Rosa et al., 2016, 2019). In support of this hypothesis, recent detrital zircon geochronology studies have indicated that the glacial sediments on the eastern margin of the Paraná basin indeed have an African provenance (e.g. Canile et al., 2016; Griffis et al., 2019). In contrast, detrital zircons from the southernmost margin of the Paraná Basin, collected from the RGS, have a completely different age distribution from those on the eastern margin of the Paraná Basin and southern samples do not appear to have an African source (Griffis et al., 2019, Fedorchuk et al., 2019b). When this distinction is combined with the mostly N and NW flow directions of grooved surfaces and other ice-flow indicators located on the RGS, a separate ice center has been suggested for the southernmost Paraná Basin (and by extension, the Chaco-Paraná Basin) compared to the eastern margin of the Paraná basin (e.g. Tomazelli and Soliani Júnior 1982, 1997; Fedorchuk et al., 2019a). Despite this, the location and extent of this separate ice center remain unclear.

Although there are scattered outcrops of LPIA glacial deposits in the eastern Chaco-Paraná Basin (Fig. 4.2), no previous study has analyzed the provenance of these sediments. Therefore, detrital zircon samples were collected from these sediments in Uruguay and on the RGS for U-Pb dating by laser ablation inductively-coupled-plasma mass spectrometry (LA-ICP-MS). The goals of this project were to: (1) test the hypothesis that an ice center, separate from the eastern margin of the Paraná Basin, flowed into the Chaco-Paraná Basin and the southern Paraná Basin, (2) constrain ice extent and location by comparing the detrital zircon age

distributions to other studies to determine whether glacial sediments in the Chaco-Paraná Basin

have a local provenance, an African provenance, or a provenance from elsewhere in South

America, and (3) determine if the provenance of the sediments changed during the shift from

glacial to post-glacial conditions, reflecting a widespread shift in paleo-ice-drainage patterns.

4.2. Geologic Setting

Late Paleozoic glacial strata in the Paraná Basin of Brazil are part of the Itararé Gp (Fig.

4.3), which consists of three formations: the Lagoa Azul, Campo Mourão, and Taciba Fms (e.g.

França and Potter, 1991). Only the youngest of these, the Taciba Fm., is exposed on the

southernmost part of the basin (e.g. França and Potter, 1991; Holz et al., 2010). Meanwhile,

LPIA glacial strata in the Chaco-Paraná Basin (Uruguay) are known as the San Gregorio Fm.

(Fig. 4.3) (e.g. Goso, 1995; De Santa Ana, 2004; De Santa Ana et al., 2006a, 2006b; Assine et

al., 2018). Both the Itararé Gp. and San Gregorio Fm. are characterized by glacially-influenced

facies associations that include sandstones, rhythmites with dropstones, grooved/striated surfaces

interpreted as subglacial erosional features, conglomerates, and diamictites with striated and

faceted clasts (e.g. De Santa Ana, 2004; De Santa Ana et al., 2006a, 2006ba; Rocha-Campos et

al., 2008; Vesely et al., 2015). On the RGS, the Itararé Gp. overlies Precambrian igneous and

metamorphic terranes including the Taquarembó Block, the Porongos Belt, the São Gabriel

Terrane, and the Pelotas Batholith, as well as Neoproterozoic and Cambrian sedimentary rocks

of the Camaquã Basin (Fig. 4.3) (e.g. Gastal et al., 2005; Saalmann et al., 2005, 2006, 2011;

Hartmann et al., 2011). In Uruguay, outcrops of the San Gregorio Fm. overlie several

Precambrian igneous and metamorphic terranes including the Cuchilla Dionisio Terrane, the

Nico Pérez Terrane, and the Piedra Alta Terrane (e.g. Santos et al., 2003; Mallmann et al., 2007;

Gaucher et al., 2008; Saalmann et al., 2011). The San Gregorio Fm. also rests on Devonian sedimentary rocks of the Durazno Group (Fig. 4.3) (e.g. Uriz et al., 2016).

On the RGS, the postglacial unit that directly overlies the Itararé Group is the coal bearing Rio Bonito Fm (e.g. Holz, 2003; Holz et al., 2006). Radiogenic U-Pb ages of zircons have been measured from ash fall beds within the Rio Bonito Fm. These ages place the Itararé Gp./Rio Bonito Fm. contact very close to the Gzhelian/Asselian boundary (Fig. 4.3), thus constraining glaciation on the RGS to the Carboniferous (e.g. Cagliari et al., 2016; Griffis et al., 2018). In Uruguay, the San Gregorio Fm. interfingers with and is topped by glaciomarine sediments of the Cerro Pelado Fm. and the postglacial, fluvial-deltaic Tres Islas Fm. that pinches out to the west (e.g. De Santa Ana, 2004; De Santa Ana et al., 2006a, 2006ba). The lack of ash beds in the San Gregorio, Cerro Pelado, or Tres Islas Fms. means that the only age constraints on the glaciation are placed by biostratigraphy. Some researchers consider the glacial deposits of the San Gregorio Fm. to have been deposited entirely in the Carboniferous, while others consider deposition to have extended into the early Permian (e.g. Closs, 1967a, 1967b, 1969; Marques-Toigo, 1970, 1974; Beltan, 1981; Braun et al., 2003; Beri et al., 2011, 2015).

Several hypotheses exist for the location and extent of an ice center that supplied sediment to the RGS and the Chaco-Paraná Basin. One scenario, which is typical of traditional views of the late Paleozoic ice age, suggests that a single massive ice center over Africa or Antarctica spread westward into the Chaco-Paraná and Paraná Basins (Gesicki et al., 1998; Gesicki et al., 2002; Starck and Papa, 2006; Holz et al., 2008). Another hypothesis illustrates at least two separate ice centers that spread multiple unconfined lobes onto the eastern and southern margins of the Paraná Basin (e.g. Frakes and Crowell, 1972; Crowell and Frakes, 1975; Assine et al., 2018). This hypothesis commonly portrays a northern ice center over the Winhoek Highlands

in northern Namibia and a southern ice center over the Cargonian Highlands in southern Namibia and South Africa (Fig. 4.1). A third hypothesis envisions ice that entered the Chaco-Paraná Basin and southernmost Paraná Basin to have been confined to a network of paleofjords draining off Africa (e.g. Tedesco et al., 2016; Fallgatter and Paim, 2017). Finally, a fourth hypothesis depicts multiple small ice caps or sheets on locally uplifted areas around South American Basins (e.g. Santos et al., 1996; Rocha-Campos et al., 2008). Potential sediment source areas for the southernmost Paraná Basin and eastern Chaco-Paraná Basin that have been interpreted as paleotopographic highs include the RGS (Brazil), the Pampean Arch (Argentina), and the Cargonian Highlands (southern Namibia) (e.g. Winn Jr. and Steinmetz, 1998; Visser, 1997b; Rocha-Campos et al., 2008). Each of these areas has a distinct detrital zircon age signature that can be compared to samples collected on the RGS and in the eastern Chaco-Paraná Basin.

4.3. Location

Samples were collected from a total of four localities that include one location on the RGS (Paraná Basin, Brazil) and three locations in the eastern Chaco-Paraná Basin, Uruguay (Fig. 4.2). The RGS sample was collected from a glaciotectonized complex of Itararé Gp. sediments in the Lavras do Sul Municipality, Rio Grande do Sul State (Location 1) (Fig. 4.2). The sedimentology and stratigraphy of this locality were described in detail by Tomazelli and Solianí Jr (1997) and Fedorchuk et al. (2019a) (Fig. 4.4). The mean orientation of paleocurrents at Location 1 is to the NW at 312.2±10.2° (1σ) (Fig. 4.4). Two of the Uruguayan localities (Locations 2 and 3) are situated in the Cerro Largo Department, outside the city of Melo (~ 50 km from the Brazil/Uruguay border) (Fig. 4.2). Location 2 was described in detail by Assine et al. (2018) and contains large subglacially carved "whaleback" structures, oriented between 320°

142

and 340° carved into igneous basement. Sandstones and diamictites of the San Gregorio Fm. overlie these whalebacks and contain multi-directional iceberg keel marks carved into bedding planes (Fig. 4.4). This location also contains an outcrop of the postglacial Tres Islas Fm. that overlies the glaciogenic sediments. Paleocurrent data collected from the Tres Islas Fm. at Location 2 indicates flow towards the SE at 155±12.8° (1σ) (Fig. 4.4). Meanwhile, Location 3 was described by Goso (1995) and contains outcrops of the Cerro Pelado Fm. overlain by coarse fluvial sandstones of the Tres Islas Fm. (Figs. 4.2 and 4.4). Measurements of paleocurrents in the Tres Islas Fm. at Location 3 reveal flow to the SW at 251±23.6° (1σ) (Fig. 4.4). Finally, Location 4 is a quarry outside of Andresito (Uruguay, ~300 km SW of Locations 2 and 3) that contains the San Gregorio Fm. (Figs. 4.2 and 4.4).

4.4. Methods

In total, six samples were collected and analyzed for provenance in this study (SUS-1, LMF-2, LMF-3, LMF-5, LP-3, and AND-1). Sample SUS-1 is from a clast-rich sandy diamicite of the Itararé Gp. at Location 1 (RGS, Brazil) (Fig. 4.4) (e.g. Hambrey and Glasser, 2003). LMF-2 and LMF-3 are from the San Gregorio Fm. at Location 2 (Uruguay) (Fig. 4.4). LMF-3 is a sample of clast-rich intermediate diamictite that immediately overlies striated whaleback structures. LMF-2 was collected from a medium, quartz sandstone bed with soft-sediment grooves (interpreted as iceberg keel marks) that is located stratigraphically ~15 m above LMF-3 (Fig. 4.4). LMF-5 was taken from a cross-bedded, arksosic, medium sandstone of the post-glacial Tres Islas Fm. at Location 2 that is located stratigraphically ~10 m above LMF-2 (Fig. 4.4). LP-3 is from a very fine quartz sandstone bed in the glaciomarine Cerro Pelado Fm. at Location 3

(Uruguay) (Fig. 4.4). Finally, AND-1 is from a fine quartz sandstone bed in the San Gregorio Fm. at Location 4 (Uruguay) (Fig. 4.4).

The provenance of these samples was determined by U-Pb detrital zircon geochronology. The samples were all analyzed by laser ablation inductively coupled plasma mass spectrometry (LA-ICP-MS) at the University of California, Davis. A complete description of the zircon separation and ablation methods and complete data is found in Appendices A and B. Samples were compared to each other and to possible sources using the Kolmogorov-Smirnov (K-S) Test with error in the Cumulative Distribution Function (CDF), cross-correlation coefficients from probability density plots (PDPs) of the samples, and multidimensional scaling (MDS) (e.g. Saylor and Sundell, 2016; Vermeeesch et al., 2016). For the K-S Test, a P-value of <0.05 indicates with 95% confidence that the two age distributions are not the same. However, this test cannot assess if the samples have the same provenance (e.g. Berry et al., 2001; DeGraaff-Surpless et al., 2003; Saylor and Sundell, 2016). The Cross-correlation coefficient is the coefficient of determination of a cross-plot of two PDPs for the same age range (e.g. Saylor et al., 2012, 2013; Saylor and Sundell, 2016). For this test, an R^2 value will range from 0 to 1 whereby a value close to 1 means that the PDPs are very similar, with closely matching age peaks and peak heights. Kernel Density Plots (KDEs) with adaptive bandwidths were used for visual comparison of samples since their peaks are smoother than PDPs and less likely to contain small peaks that make it difficult to identify broad patterns (Figs. 4.5, 4.6, 4.7) (e.g. Saylor and Sundell, 2016; Vermeesch et al., 2016). Multidimensional scaling (MDS) is similar to a principle component analysis. This test reproduces relative ranks of dissimilarity between samples so that samples more similar to each other plot closer together and samples more dissimilar to each other plot farther apart (e.g. Vermeesch et al., 2016).

144

To place detrital zircon samples in their proper stratigraphic context, most samples were collected from measured sections describe in previous studies (i.e. Locations 1, 2, and 3). Location 4 is from a previously undescribed section so a new stratigraphic column was measured. The stratigraphic position of each sample is shown next to the stratigraphic column of the locality from which it was collected.

4.5. Results

Sample SUS-1 (Location 1, Itararé Gp., Paraná Basin)

Sample SUS-1 was collected from a clast-rich sandy diamictite of the Itararé Gp. at Location 1. The KDE (N=53) of this sample shows a dominant Neoproterozoic peak at ~580 Ma with much smaller (and broader) secondary peaks at ~780 Ma, ~2110 Ma, and ~2500 Ma (Fig. 4.5). In this sample, 2% of the zircons analyzed were Ordovician, 0% were Cambrian, 74% were Neoproterozoic, 2% were Mesoproterozoic, 22% were Paleoproterozoic, and 0% were Archean (Fig. 4.8).

Sample LMF-3 (Location 2, San Gregorio Fm., Chaco-Paraná Basin)

Sample LMF-3 was collected from a clast-rich intermediate diamictite bed of the San Gregoio Fm. at Location 2. Stratigraphically, this bed is <1 m above a whaleback structure carved into crystalline basement. The KDE of LMF-3 (N=59) exhibits a dominant peak at ~625

Ma and a secondary peak at ~520 Ma. Less constrained peaks occur at ~750 Ma, ~990 Ma, and ~1850 Ma (Fig. 4.6). LMF-3 contains 0% Ordovician grains, 24% Cambrian grains, 63% Neoproterozoic grains, 7% Mesoproterozoic grains, 5% Paleoproterozoic grains, and 1% Archean grains (Fig. 4.8).

Sample LMF-2 (Location 2, San Gregorio Fm., Chaco-Paraná Basin)

Sample LMF-2 was collected from a medium quartz sandstone bed within the San Gregorio Fm. at Location 2. This sandstone bed is ~15 m higher in the measured section than sample LMF-3 and contains soft sediment grooves interpreted as iceberg keel marks. The KDE of this sample (*N*=73) has a primary peak at ~555 Ma and a secondary peak at ~650 Ma. Smaller and broader peaks occur at ~780 Ma, ~1250 Ma, and ~1890 Ma (Fig. 4.6). LMF-2 contains 0% Ordovician grains, 16% Cambrian grains, 72% Neoproterozoic grains, 4% Mesoproterozoic grains, 8% Paleoproterozoic grains, and 0% Archean grains (Fig. 4.8).

Sample LMF-5 (Location 2, Tres Islas Fm., Chaco-Paraná Basin)

Sample LMF-5 was collected from a medium grained, arkosic sandstone within the Tres Islas Fm. at Location 2. Stratigraphically, this bed is ~10 m above sample LMF-2. The KDE of this sample (*N*=50) shows a primary peak at ~625 Ma and a secondary peak at ~555 Ma (Fig. 4.6). LMF-5 has a less diverse zircon population when compared to most other samples, with 0% Ordovician grains, 4% Cambrian grains, 96% Neoproterozoic grains, 0% Mesoproterozoic grains, 0% Paleoproterozoic grains, and 0% Archean grains (Fig. 4.8).

Sample LP-3 (Location 3, Cerro Pelado Fm., Chaco-Paraná Basin)

Sample LP-3 was collected from a very fine quartz sandstone bed within the Cerro Pelado Fm. at Location 3. The KDE of this sample (N=37) shows a primary peak at ~525 Ma and a secondary peak at ~640 Ma. Smaller and broader third-order peaks are located at ~755 Ma, ~1010 Ma, and ~2050 Ma (Fig. 4.6). Sample LP-3 contains 0% Ordovician grains, 35% Cambrian grains, 46% Neoproterozoic grains, 8% Mesoproterozoic grains, 11% Paleoproterozoic grains, and 0% Archean grains (Fig. 4.8).

Sample AND-1 (Location 4, San Gregorio Fm., Chaco-Paraná Basin)

Sample AND-1 is from a fine quartz sandstone bed that is located within the San Gregorio Fm. at Location 4. The KDE of this sample (N=127) exhibits a strong primary peak at ~1010 Ma with secondary peaks at ~525 Ma and ~620 Ma. Smaller, less constrained peaks are located at ~850 Ma, 1080 Ma, ~1280 Ma, and ~1960 Ma (Fig. 4.7). AND-1 contains 0% Ordovician grains, 14% Cambrian grains, 41% Neoproterozoic grains, 34% Mesoproterozoic grains, 10% Paleoproterozoic grains, and 1% Archean grains (Fig. 4.8).

4.5.1. Statistical comparison of samples

Samples were compared to each other using the K-S test (Table 4.1), the cross-correlation coefficient (Table 4.2), and MDS (Fig. 4.9) to assess potential source regions and variations in

drainage. Although all of these statistical comparisons are useful, it should be noted that in relatively small-N samples and samples with variable N, such as those in this study, the cross-correlation coefficient is considered a more sensitive metric of similarity (e.g. Saylor and Sundell, 2016). For visual comparison, in Table 4.1, K-S P-values > 0.05 (samples that cannot be distinguished) are highlighted in yellow and in Table 4.2 cross-correlation coefficients (R^2) > 0.5 (an arbitrary cutoff for visual comparison) are highlighted in yellow. In Table 4.2, values that meet the criteria of K-S P-values > 0.05 and R^2 > 0.5 have solid red squares around them to indicate samples that are most similar to each other. To examine possible source regions for the samples, their age distributions were compared to detrital zircon samples from several prior studies that vary geographically and temporally (Tables 4.1 and 4.2, Fig. 4.9). These comparative detrital zircon studies include: Carboniferous (Itararé Gp.) rocks from the Paraná Basin in Brazil (Sample STR, Griffis et al., 2019), Neoproterozoic sedimentary rocks (Nomtsas Fm.) from the Nama Basin in southern Namibia (Sample NOM, Blanco et al., 2011), Neoproterozoic metasedimentary rocks (Guaritas Group) from the Camaquã on the RGS, Brazil (Sample GG, Oliveira et al., 2014), Devonian sedimentary rocks (Durazno Gp.) from the Chaco-Paraná Basin in Uruguay (Sample UC-13, Uriz et al., 2016), and Ordovician metasedimentary rocks (Ambato metamorphic complex) from the Sierras Pampeanas in Argentina (Sample CEB-392, Verdecchia et al., 2011).

Sample SUS-1 (Location 1, Itararé Gp., Paraná Basin)

The K-S test indicates that the detrital zircon age distribution of sample SUS-1 cannot be distinguished from samples LMF-3 (San Gregorio Fm.), LMF-2 (San Gregorio Fm.), LMF-5

(Tres Islas Fm.), and UP-12 (Durazno Gp.) (i.e. P-value > 0.05) (Table 4.1). Similarly, MDS indicates SUS-1 is most closely related to LMF-2 and LMF-3 (Fig. 4.9). A comparison to all other samples exhibits a P-value of < 0.05 and, therefore, it can be said with 95% confidence that the other samples have a different zircon population than SUS-1. In direct contrast to these K-S test and MDS results, sample STR (Itararé Gp.) from Griffis et al. (2019) has the highest cross-correlation coefficient (R^2=0.63) compared to SUS-1 (Table 4.2). Although this result contradicts the K-S test and MDS, the relatively high R^2 value would seem logical since SUS-1 and STR are both samples of the Itararé Gp. collected on the RGS. The reason for the contradictory result may be that the small sample sizes of both SUS-1 and STR make the K-S test overly sensitive to their differences. No samples had both cross-correlation coefficients > 0.5 and K-S test P-values > 0.05 when compared to SUS-1 (Table 4.2).

Sample LMF-3 (Location 2, San Gregorio Fm., Chaco-Paraná Basin)

The detrital zircon population of sample LMF-3 cannot be distinguished from samples SUS-1 (Itararé Gp.), LMF-2 (San Gregorio Fm.), LMF-5 (Tres Islas Fm.) and LP-3 (Cerro Pelado Fm.) using the K-S test (Table 4.1). All the other samples have P-values < 0.05 and therefore are likely to have different provenance. Only sample LMF-5 has a cross-correlation coefficient > 0.5 (R^2=0.57) with sample LMF-3 (Table 4.2). Based on the agreement of the K-S test and the cross-correlation coefficient, it is hypothesized that the zircon provenance of sample LMF-5 is most similar to sample LMF-3. This is supported by the MDS, which also indicates that LMF-5 is most similar to LMF-3 (Fig. 4.9).

149

Sample LMF-2 (Location 2, San Gregorio Fm., Chaco-Paraná Basin)

The detrital zircon population of LMF-2 cannot be distinguished from those of samples SUS-1 (Itararé Gp.), LMF-3 (San Gregorio Fm.), LMF-5 (Tres Islas Fm.), and LP-3 (Cerro Pelado Fm.) using the K-S test (P-values > 0.05) (Table 4.1). Samples LP-3 and UP-12 (Durazno Gp.) have cross-correlation coefficients that are > 0.5 when compared to LMF-2 (Table 4.2). Sample LP-3 has an R^2 value of 0.68 and UP-12 has an R^2 value of 0.70 versus LMF-2. Based on the agreement of the K-S test and the cross-correlation coefficient for sample LP-3, it is hypothesized that the provenance of sample LMF-2 is most similar to sample LP-3. Similarly, the MDS shows that LP-3 is closely related to LMF-2 (Fig. 4.9).

Sample LMF-5 (Location 2, Tres Islas Fm., Chaco-Paraná Basin)

The detrital zircon population of LMF-5 cannot be distinguished from samples SUS-1 (Itararé Gp.), LMF-3 (San Gregorio Fm.), and LMF-2 (San Gregorio Fm.) based on the K-S test (Table 4.1). However, samples LMF-3, STR (Itararé Gp.), and GG (Gauritas Gp.) all have cross-correlation coefficient's > 0.5 that stand out from the rest of the samples (Table 4.2). Sample LMF-3 has a R^2 value of 0.58, STR has a R^2 value of 0.55, and GG has a R^2 of 0.56 compared to sample LMF-5. However, only LMF-3 has both a K-S test P-value > 0.05 and a R^2 > 0.5, which suggests that LMF-3 has a provenance most similar to LMF-5 (Table 4.2). Supporting this, the MDS connects LMF-5 to LMF-3 as its nearest neighbor (Fig. 4.9).

Sample LP-3 (Location 3, Cerro Pelado Fm., Chaco-Paraná Basin)

150

The detrital zircon population of LP-3 cannot be distinguished from samples LMF-3 (San Gregorio Fm.), LMF-2 (San Gregorio Fm.), and UP-12 (Durazno Gp.) based on the K-S test (Table 4.1). Both samples LMF-2 and UP-12 also have cross-correlation coefficients that are > 0.5 and are significantly larger than all other samples (Table 4.2). LMF-2 has a R^2 value of 0.68 and UP-12 has an R^2 value of 0.61 in relation to LP-3. Since both LMF-2 and UP-12 have K-S P-values > 0.05 and R^2 values in agreement, these two samples are interpreted to have the most similar provenance to sample LP-3 (Table 4.2). The MDS connects LP-3 to LMF-2 as its nearest neighbor (Fig. 4.9).

Sample AND-1 (Location 4, San Gregorio Fm., Chaco-Paraná Basin)

The detrital zircon population of AND-1 cannot be distinguished from samples NOM (Nomtsas Fm.) and UC-13 (Durazno Gp.) using the K-S test (Table 4.1). Both NOM and UC-13 also have cross-correlation coefficients > 0.5 when compared to AND-1. NOM has an R^2 value of 0.57 and UC-13 has an R^2 value of 0.60 (Table 4.2). Both of these R^2 values are significantly higher than any other samples that were compared to AND-1. Therefore, samples NOM and UC-13 are considered to have similar provenance to AND-1 (Table 4.2). This interpretation is further supported by the MDS which shows nearest neighbor lines connecting AND-1 to both UC-13 and NOM (Fig. 4.9).

4.6. Discussion

Based on the U-Pb detrital zircon results presented here, the most likely source region for the glacial sediments (San Gregorio Fm.) deposited in the eastern Chaco-Paraná Basin is the Cuchilla Dionisio terrane (Uruguay), the Punta del Este terrane (Uruguay) and, by extension, the Namaqua Belt in Africa, which would have been directly connected to the Punta del Este terrane during the late Paleozoic (Figs 4.1 and 4.2) (Basei et al., 2011). These terranes were located to the southeast and east of the basin and were likely connected to the Cargonian Highlands that stretched across southern Africa (Fig. 4.1) (e.g. Visser, 1997b). A comparison of the detrital zircon signature from glacial (ice-proximal), glaciomarine (relatively ice-distal), and postglacial samples exhibits an interesting trend whereby glacial sediments reflect highly local erosion of underlying sediments or crystalline basement. Meanwhile, more diverse detrital zircon ages from distal sources are found under glaciomarine conditions. Post-glacial fluvial sediments reflect incision of local underlying units and a return to highly local provenance that is similar to that of ice-proximal sediments.

4.6.1. Comparison of samples to likely source regions

The Cuchilla Dionisio Terrane and Punta del Este Terrane are interpreted as extensions of the Gariep Belt and Namaqua Belt in southern Africa that were formed by the collision of the Río de la Plata and Kalahari Cratons during final assembly of SW Gondwana in the Neoproterozoic (Fig. 4.1) (the Brasiliano Orogeny, e.g. Gaucher et al., 2008). These terranes have been previously depicted as highlands that supplied the sediments of the Devonian Durazno

Gp. in eastern Uruguay (e.g Uriz et al., 2016) and were likely connected to the Cargonian

Highlands of southern Africa, a paleotopographic high formed by subduction under the southern

margin of Gondwana (Fig. 4.1) (e.g. Visser, 1997b).

Based on the detrital zircon ages described here, the Cuchilla Dionisio and Punta del Este

Terranes are considered here as the most likely source of sediment to the eastern Chaco-Paraná

Basin during the LPIA. For example, in the samples from the Chaco-Paraná Basin that were

analyzed (i.e. samples LMF-3, LMF-2, LMF-5, LP-3, AND-1) the two most common age peaks

were ~520-555 Ma and ~625 Ma. The ~625 Ma ages are typical of syn-tectonic granites of the

Cuchilla Dionisio Terrane (Uruguay) which directly underlies the study Locations 2 and 3 and is

therefore the most plausible source of zircons (e.g. Blanco, 2009, Basei et al., 2011). Meanwhile,

the ~520-555 Ma ages are consistent with post-tectonic granite intrusions (Fig. 4.2B) to the south

and east in the Punta del Este Terrane (Uruguay) such as the El Pintor Granite, José Ignacio

Granite, the Rocha Granite, and the Santa Teresa Granite (e.g. Blanco et al., 2009, Basei et al.,

2011). Grenvillian ages of ~900-1000 Ma are also found within gneisses of the Cerro Olivo

Complex, part of the Punta del Este Terrane and, correlatively, the Namaqua Belt (e.g. Blanco et

al., 2009, Basei et al., 2011). Finally, pre-tectonic Brasiliano ages of ~750-780 Ma are found in

migmatites of the Punta del Este Terrane (e.g. Bossi and Gaucher, 2004; Blanco et al., 2009).

Critically, in all the samples analyzed from the eastern Chaco-Paraná Basin, the relatively low

abundance (<12%) of Paleoproterozoic grains, which are typical to the Nico Pérez and the Piedra

Alta Terranes (Fig. 4.2B) indicates that rocks to the SW and W of the Uruguayan Shield were

not a significant source of sediment.

Along with the Cuchilla Dionisio Terrane and Punta del Este Terrane, another important

source of zircons for the Chaco-Paraná Basin samples (LMF-3, LMF-2, LMF-5, LP-3, AND-1)

appears to be recycled Devonian sediments on the Rio de la Plata Craton whose provenance was described by Uriz et al. (2016). This is particularly true of sample AND-1, which is from an outcrop of the San Gregorio Fm. located just west of Devonian Durazno Gp. outcrops (Fig. 4.2B). The age distribution of zircons in sample AND-1 is quite different from the other Chaco-Paraná Basin samples that were analyzed, with a higher percentage of Mesoproterozoic grains (34% compared to 7%, 4%, 0%, and 8%) (Fig. 4.8) but is very similar to sample UC-13 (Uriz et al., 2016) of the Durazno Gp., which was collected ~80 km from AND-1. Both the K-S test and cross-correlation coefficient (R^2=0.60) support the likelihood that the Durazno Gp. was the primary source of sediments in AND-1 (Table 4.2). This indicates a different drainage network, flowing towards the west, for Location 4. Interestingly, AND-1 also has similar provenance to NOM (Nomtsas Fm.) from the Nama Basin in Namibia (Table 4.2) (Blanco et al., 2011). In particular the ~1080 Ma peak is most similar to the ~1065 Ma peak in sample NOM (Fig. 4.7). The likely explanation for the similarity is that Devonian Durazno Gp. and the Cambrian Nomtsas Fm. have similar provenance with both samples consisting of zircons derived from elevated areas of the Cuchilla Dionisio Terrane and Namaqua Terrane. It also seems plausible that the Nama Basin sediments were eroded and resedimented into the eastern Chaco-Paraná Basin during the LPIA and were possibly mixed with resedimented Devonian sediments.

Alternative source areas for the Chaco-Paraná Basin sediments in Uruguay that had to be ruled out include the RGS in southern Brazil and the Sierra Pampeanas located in Argentina. When looking at the RGS, the primary Neoproterozoic peak detected from sample SUS-1 (Itararé Gp.) is ~680 Ma with a secondary peak at ~780 Ma. These peaks and their relative heights are similar to sample STR (Itararé Gp.) from Griffis et al. (2019) and sample GG (Guaritas Group) from Oliveira et al. (2014), which are also from the RGS (Fig. 4.5). The

relatively high cross-correlation coefficients support a similar provenance for SUS-1, STR, and GG (Table 4.2). Thus, it seems most likely that the Precambrian/Cambrian Camaquã Basin sediments (Guaritas Group) were easily eroded by glaciers and resedimented across the RGS during the late Paelozoic.

The K-S test indicates different provenance for the RGS samples and the Chaco-Paraná Basin samples (Table 4.1). Only LMF-5 (the post-glacial Tres Islas Fm.) has a relatively high cross-correlation coefficient when compared to the RGS (Table 4.2). Furthermore, the RGS samples (SUS-1, GG, and STR) lack the slightly younger ~520-555 Ma peak common in the Chaco-Paraná Basin samples (LMF-3, LMF-2, LMF-5, LP-3, AND-1) (Figs. 4.5 and 4.6). The RGS samples also contain more Paleoproterozoic grains compared to the Chaco-Paraná Basin samples (Fig. 4.8). Based on this data, we hypothesize that the RGS was not a major source of sediment to the Chaco-Paraná Basin samples analyzed here. However, it should be noted that the MDS indicates similarity between SUS-1 and samples LMF-3 and LMF-2 (the San Gregorio Fm.) from Uruguay (Fig. 4.9). This may indicative that some sediment from Uruguay was transported N onto the RGS during glaciation and mixed with the Camaquã Basin sediments, although this connection seems tenuous. Meanwhile, none of the samples from the Chaco-Paraná Basin or the RGS (LMF-3, LMF-2, LMF-5, LP-3, AND-1, SUS-1) have K-S P-values or cross-correlation coefficients that support a similar provenance to sample CEB-392 from the Sierra Pampeanas (Table 4.2) (Verdecchia et al., 2011).

4.6.2. Late Paleozoic drainage patterns in southern Brazil and Uruguay

Trends in the detrital zircon age distributions demonstrate shifts in drainage between ice-proximal, relatively ice-distal, and post-glacial sediments. For example, in the sample LMF-3 (Location 2) of diamictite from the San Gregorio Fm. that directly overlies glacially carved basement features (i.e. ice-proximal sediments), there is a higher proportion of ages that reflect the underlying syn-tectonic granites (Figs. 4.2B and 4.6). This supports local erosion and deposition. In the KDE, this is represented by a dominance of the older ~625 Ma peak over the younger ~520-555 Ma peak (post-tectonic granites) (Figs. 4.2B and 4.6) (Blanco, 2009, Basei et al., 2011). Meanwhile, sample LMF-2 was collected in the slightly more ice-distal (glaciomarine) sandstones of the San Gregorio Fm. at the sample location that contain iceberg keel marks and are stratigraphically ~15 m above sample LMF-3 (Fig. 4.4). In contrast to sample LMF-3, LMF-2 contains a dominant younger ~520-555 Ma peak which is probably derived from zircons of the post-tectonic granite intrusions to the E and SE of the study area (Figs. 4.2B and 4.6). This indicates that when ice retreated to the E and SE a wider drainage catchment opened up and more young zircons were eroded, transported, and deposited at Location 2. This interpretation is also supported by sample LP-3 which is from the glaciomarine Cerro Pelado Fm. at Location 3. Similar to LMF-2, LP-3 also shows a dominant younger ~520-555 Ma peak over the older ~625 Ma peak, which supports a wider drainage for this glaciomarine sample (Figs. 4.2B and 4.6). The similar provenance of samples LMF-2 and LP-3 is supported by the K-S test (Table 4.1), the MDS (Fig. 4.9), and the cross-correlation coefficient (R^2=0.68) (Table 4.2), which indicate that these samples are most similar to each other. A strikingly similar trend was observed for ice-proximal/ice-distal sediments in the eastern Paraná Basin by Griffis et al. (2019). The study by Griffis et al. (2019) also noted the shift to more diverse and exotic zircons

from Africa in ice-distal glaciomarine facies and less diverse and more local South American zircons in ice-proximal facies.

At Location 2, the postglacial Tres Islas Fm. is comprised of arkosic, cross-bedded, fluvial sandstones. Sample LMF-5 was collected from one of these sandstones ~12 m above the glaciomarine sample LMF-2 (Fig. 4.4). The detrital zircon age distribution shows a similarity to the ice-proximal sample LMF-3 with a dominant ~625 Ma peak and lack of diverse grains (Fig. 4.6). The K-S P-value and cross-correlation coefficient (R^2=0.57) both support a close relationship between LMF-5 and LMF-3 (Table 4.2). This similarity reflects a return to primarily local provenance (Fig. 4.2B). The abundance of locally sourced sediment may be the result of fluvial incision driven by a drop in base level, tectonically driven uplift, or glacial rebound (isostatic uplift) during postglacial times.

4.6.3. Ice center and paleogeographic reconstructions

The detrital zircon ages measured from the eastern Chaco-Paraná Basin at Locations 2, 3, and 4 all reflect sources in eastern and southeastern Uruguay (Fig. 4.2B), and possibly southwestern Namibia (Fig. 4.1A). This indicates that sediments were likely transported towards the W and NW, out of present Africa during the late Paleozoic. Grooved surfaces and whalebacks at Location 2 also indicate fast-flowing ice moved towards the NW (Fig. 4.10A) (e.g. Assine et al., 2018). This is further supported by previous studies of glacial deposits and grooved surfaces in Africa that show an ice center in the Cargonian Highlands of Africa that drained radially into adjacent basins, including a westward flow towards the Chaco-Paraná Basin (Fig. 4.10B) (e.g. Visser, 1989, 1997b). The detrital zircon ages detailed here represent a similar

drainage pattern to that responsible for deposition of the Devonian Durazno Gp. As reported by Uriz et al. (2016), which also hypothesizes that sediments were sourced in highlands of southeastern Uruguay and southern Namibia. This implies that this area was a persistent source area since the Devonian.

Meanwhile, grooved surfaces and glaciotectonic deformation on the RGS (southernmost Brazil) show a pattern of radial ice flow to the N, NE, and NW (Fig. 4.10A) (e.g. Tomazelli and Soliani Júnior 1982, 1997; Fedorchuk et al., 2019a). This aligns with the hypothesis that the southern Namibian based ice center extended N across SE Uruguay and onto the RGS as an unconfined lobe (Fig. 4.10B). However, the detrital zircon ages from the San Gregorio Fm. in the eastern Chaco-Paraná Basin are quite different from the Itararé Gp. on the RGS. Some authors have proposed a small isolated ice center on the RGS that drained radially outward (e.g. Santo et al., 1996; Rocha-Campos et al., 2008). However, based on this study and the abundance of paleo-ice flow indicators showing flow to the north, the most likely explanation for the different provenance is that the abundance of easily-erodible Precambrian/Cambrian Camaquã Basin sediments contributed most of zircons to the Itararé Gp. on the RGS and erased any Uruguayan signature. Meanwhile, previous detrital zircon studies have suggested that the Itararé Gp. on the eastern margin of the Paraná Basin (north of the RGS) have a northern Namibian provenance (e.g. Canile et al., 2016; Griffis et al., 2019). These samples from the eastern Paraná Basin have dominant Mesoproterozoic peaks that are quite different than those from both the RGS (e.g. Griffis et al., 2019) and the eastern Chaco-Paraná Basin. This supports the interpretation that the RGS was a paleotopographic divide between the Paraná and Chaco-Paraná Basins.

In conclusion, the results from this study help create a link between the glacial deposits in SW Namibia, eastern Uruguay, and southernmost Brazil. This supports the hypothesis that

158

unconfined ice extended out of the Cargonian Highlands (southwestern Namibia and southeastern Uruguay) into the eastern Chaco-Paraná Basin and southernmost Paraná Basin (Fig. 4.10B). This glacier was likely from a different ice center than the Windhoek ice center that was responsible for glacial sediments on the eastern margin of the Paraná Basin (Fig. 4.10B) (e.g. Frakes and Crowell, 1972; Crowell and Frakes, 1975). This contradicts both the hypothesis of a single massive ice center and the hypothesis of a small isolated ice cap on the RGS (e.g. Santos et al., 1996; Gesicki et al., 1998; Gesicki et al., 2002; Rocha-Campos et al., 2008). The presence of two topographically controlled ice centers in Africa is evidence that glaciers preferentially persisted in some areas, and emenated out of these areas when paleoclimate cooled. This reinforces the Equilibrium Line Altitude (ELA) as an important control on where glaciers nucleated and spread from during the LPIA (Fig. 4.10B). Furthermore, while the detrital zircon ages described in this study primarily reflected local sources, clear differences in drainage were noted between ice-proximal, relatively ice-distal glaciomarine, and post-glacial sediments. This may be related to isostatic adjustments such as the formation of an iostatic trough during glacial advance and rebound of this trough as ice retreated. This may have occurred in conjunction with the blockage and opening of preglacial drainage systems as ice advanced and retreated over the study area. These environment-specific differences in detrital zircon signatures may have important implications for how detrital zircons are interpreted in glacially-influenced margins. Therefore, future detrital zircon studies of late Paleozoic glacial deposits should account for the possibility of regional and environmental variability when making broad interpretations of sediment provenance.

4.7. Conclusions

(1) The San Gregorio and Cerro Pelado Fms., as well as the Tres Islas Fm. from the eastern Chaco-Paraná Basin in Uruguay have a different provenance than the glacial sediments (Itararé Gp.) on the RGS in southernmost Brazil.

(2) The detrital zircon samples collected from late Paleozoic strata in the Chaco-Paraná Basin primarily reflect source terranes in E and SE Uruguay or Africa such as the the Cuchilla Dionisio Terrane, Punta del Este Terrane, and Namaqua Belt. The Devonian Durazno Gp. is also a likely source for these sediments.

(3) The detrital zircon sample (SUS-1) of the Itararé Gp. collected from the RGS has a similar provenance to another Itararé Gp. sample collected from elsewhere on the RGS reported by Griffis et al. (2019). This sample also has a similar provenance to the Precambrian/Cambrian Guaritas Gp. sample (Oliviera et al., 2014) from the Camaquã Basin on the RGS. Therefore, it is hypothesized that glaciers easily eroded the Camaquã Basin strata on the RGS and redeposited those sediments across the RGS during the Carboniferous.

(4) Based on the provenance of the late Paleozoic sediments from the eastern Chaco-Paraná Basin and southernmost Paraná Basin, combined with paleo-ice flow directions from other studies, the most likely scenario is that an ice center was located over highlands in SE Uruguay, southern Namibia, and northern South Africa. An unconfined lobe likely flowed NW onto the RGS and W into the Chaco-Paraná Basin from this ice center. The detrital zircon ages do not support an isolated ice center over the RGS or an eastward flowing ice-center from the Sierra Pampeanas.

(5) Comparison of the detrital zircon age distribution from ice-proximal, relatively ice-distal glaciomarine, and post-glacial strata indicates that changes in drainage occurred during ice advance/retreat. Ice-proximal and post-glacial fluvial strata primarily have zircons sources from local igneous basement (~625 Ma), while the relatively ice-distal glaciomarine strata contain more younger zircons (~520-555 Ma) from a larger drainage catchment to the E and SE of the study area.

(6) This study supports the hypothesis that at least two topographically controlled ice centers located over different highlands in Africa supplied sediments to the Paraná and Chaco-Paraná Basins in Brazil and Uruguay. One ice center was likely located over the Windhoek Highlands in northern Namibia and another was located in the Cargonian Highlands of southern Namibia, northern South Africa, and southeast Uruguay.

References

Assine, M. L., de Santa Ana, H., Veroslavsky, G., Vesely, F. F., 2018. Exhumed subglacial landscape in Uruguay; erosional landforms, depositional environments, and paleo-ice flow in the context of the late Paleozoic Gondwanan glaciation. Sedimentary Geology 369, 1-12.

Basei, M. A. S., Peel, E., Sanchez Bettucci, L., Preciozzi, F., Nutman, A. P., 2011. The basement of the Punta del Este Terrane (Uruguay); an African Mesoproterozoic fragment at the eastern border of the South American Rio de La Plata Craton. International Journal of Earth Sciences = Geologische Rundschau 100, 289-304.

Beltan, L., 1981. Coccocephalichthys tessellatus n. sp. (Pisces, Actinopterygii) from the Upper Carboniferous of Uruguay. 2nd Congresso Latino-Americano de Paleontologia, Porto Alegre, pp. 95–105.

Beri, Á., Gutiérrez, P., Balarino, L., 2011. Palynostratigraphy of the late Palaeozoic of Uruguay, Paraná Basin. Review of Palaeobotany and Palynology 167, 16–29.

Beri, Á., Gutiérrez, P.R., Balarino, M.L., 2015. The late Paleozoic palynological diversity in southernmost Paraná (Uruguay), Claromecó and Paganzo basins (Argentina), Western Gondwana. Journal of South American Earth Sciences 64, 183–189.

Berry, R.F., Jenner, G.A., Meffre, S., Tubrett, M.N., 2001. A North American provenance for Neoproterozoic to Cambrian sandstones in Tasmania? Earth and Planetary Science Letters 192, 207-222.

Blanco, G., Germs, G. J. B., Rajesh, H. M., Chemale, F., Jr., Dussin, I. A., Justino, D., 2011. Provenance and paleogeography of the Nama Group (Ediacaran to early Palaeozoic, Namibia); petrography, geochemistry and U/Pb detrital zircon geochronology. Precambrian Research 187, 15-32.

Blanco, G., Rajesh, H. M., Gaucher, C., Germs, G. J. B., Chemale, F., Jr., 2009. Provenance of the Arroyo del Soldado Group (Ediacaran to Cambrian, Uruguay); implications for the paleogeographic evolution of southwestern Gondwana. Precambrian Research 171, 57-73.

Bossi, J., Gaucher, C., 2004. The Cuchilla Dionisio Terrane, Uruguay; an allochthonous block accreted in the Cambrian to SW-Gondwana. Gondwana Research 7, 661-674.

Braun, A., Sprechmann, P., Gaucher, C., 2003. Stratigraphic age of phosphorite-nodules from the San Gregorio Formation of Uruguay. Neues Jahrbuch für Geologie und Paläontologie Monatshefte 12, 739–748.

Cagliari, J., Philipp, R. P., Buso, V. V., Netto, R. G., Klaus Hillebrand, P., da Cunha Lopes, R., Stipp Basei, M. A., Faccini, U. F., 2016. Age constraints of the glaciation in the Paraná Basin: evidence from new U–Pb dates. Journal of the Geological Society 173, 871-874.

Canile, F. M., Babinski, M., Rocha-Campos, A. C., 2016. Evolution of the Carboniferous-Early Cretaceous units of Parana Basin from provenance studies based on U-Pb, Hf and O isotopes from detrital zircons. Gondwana Research 40, 142-169.

Closs, D., 1967a. Orthocone cephalopods from the Upper Carboniferous of Argentina and Uruguay. Ameghiniana 5, 123–129.

Closs, D., 1967b,. Upper Carboniferous anaptychi from Uruguay. Ameghiniana 5, 145–148.

Closs, D., 1969. Intercalation of goniatites in the Gondwanic glacial beds of Uruguay. Gondwana Stratigraphy, IUGS 1st Gondwana Symposium. UNESCO, Paris, Buenos Aires, pp. 197–212.

Craddock, J. P., Ojakangas, R. W., Malone, D. H., Konstantinou, A., Mory, A., Bauer, W., Thomas, R. J., Affinati, S. C., Pauls, K., Zimmerman, U., Botha, G., Rochas-Campos, A., Tohver, E., Riccomini, C., Martin, J., Redfern, J., Horstwood, M., Gehrels, G., 2019. Detrital zircon provenance of Permo-Carboniferous glacial diamictites across Gondwana. Earth-Science Reviews.

Crowell, J., Frakes, L., 1975. The late Paleozoic glaciation. Gondwana geology 3, 313-331.

DeGraaff-Surpless, K., Mahoney, J.B., Wooden, J.L., McWilliams, M.O., 2003,. Lithofacies control in detrital zircon provenance studies: insights from the Cretaceous Methow Basin, southern Canadian Cordillera. Geological Society of America Bulletin 115, 899-915.

De Santa Ana, H., 2004. Análise Tectono-Estratigráfica das Seqüências Permotriassica e Jurocretácea da Bacia Chacoparanense Uruguaia ("Cuenca Norte") (PhD Dissertation). Universidade Estadual Paulista (Unesp), Rio Claro. Brasil, 274 pp.

De Santa Ana, H., Goso, C., Daners, G., 2006a. Cuenca Norte: estratigrafía del Carbonífero-Pérmico. In: Veroslavsky, G., Ubilla, M., Martinez, S. (Eds.), Cuencas Sedimentarias de Uruguay. Geología, Paleontología y Recursos Minerales. Facultad de Ciencias, Montevideo, pp. 147–208.

De Santa Ana, H., Veroslavsky, G., Fulfaro, V.J., Rossello, E.A., 2006b.Cuenca Norte: Evolución tectónica y sedimentaria del Carbonífero-Pérmico. In: Veroslavsky, G., Ubilla, M., Martinez, S. (Eds.), Cuencas Sedimentarias de Uruguay. Geología, Paleontología y Recursos Minerales. Facultad de Ciencias, Montevideo, pp. 209–256.

Fallgatter, C., Paim, P. S. G., 2017. On the origin of the Itararé Group basal nonconformity and its implications for the Late Paleozoic glaciation in the Paraná Basin, Brazil. Palaeogeography, Palaeoclimatology, Palaeoecology (in press). https://doi.org/10.1016/j.palaeo.2017.02.039.

Fedorchuk, N.D., Isbell, J.L., Griffis N.P, Vesely, F.F., Rosa, E.L.M., Montãnez, I.P., Mundil R., Yin, Q-Z., Iannuzzi, R., Roesler, G., Pauls, K.N., 2019a. Carboniferous glaciotectonized sediments in the southernmost Paraná Basin, Brazil. Ice marginal dynamics and paleoclimate indicators: Sedimentary Geology (in review).

Fedorchuk, N. D., Isbell, J. L., Griffis, N. P., Montañez, I. P., Vesely, F. F., Iannuzzi, R., Mundil, R., Yin, Q.-Z., Pauls, K. N., Rosa, E. L. M., 2019b. Origin of paleovalleys on the Rio Grande do Sul Shield (Brazil): Implications for the extent of late Paleozoic glaciation in

west-central Gondwana. Palaeogeography, Palaeoclimatology, Palaeoecology, (in press). https://doi.org/10.1016/j.palaeo.2018.04.013.

Fielding, C. R., Frank, T. D., Isbell, J. L., 2008. The late Paleozoic ice age--A review of current understanding and synthesis of global climate patterns. In: Fielding, C. R., Frank, T. D., Isbell, J. L. (Eds.), Resolving the Late Paleozoic Ice Age in Time and Space. Geological Society of America Special Paper 441, pp. 343-354.

Fielding, C. R., Frank, T. D., Isbell, J. L., Henry, L. C., Domack, E. W., 2010. Stratigraphic signature of the late Palaeozoic ice age in the Parmeener Supergroup of Tasmania, SE Australia, and inter-regional comparisons. Palaeogeography, Palaeoclimatology, Palaeoecology 298, 70-90.

Frakes, L., Crowell, J., 1972. Late Paleozoic glacial geography between the Paraná Basin and the Andean geosyncline. Anais da Academia Brasileira de Ciências 44, 139-145.

Franca, A. B., Potter, P. E., 1991. Stratigraphy and reservoir potential of glacial deposits of the Itarare Group (Carboniferous-Permian), Parana Basin, Brazil. American Association of Petroleum Geologists Bulletin 75, 62-85.

Frank, T. D., Shultis, A. I., Fielding, C. R., 2015. Acme and demise of the late Palaeozoic ice age: A view from the southeastern margin of Gondwana. Palaeogeography, Palaeoclimatology, Palaeoecology 418, 176-192.

Gastal, M. d. C. P., Lafon, J. M., Hartmann, L. A., Koester, E., 2005. Sm/Nd isotopic compositions as a proxy for magmatic processes during the Neoproterozoic of the southern Brazilian Shield. Journal of South American Earth Sciences 18, 255-276.

Gastaldo, R. A., DiMichele, W. A., Pfefferkorn, H. W., 1996. Out of the icehouse into the greenhouse; a late Paleozoic analog for modern global vegetational change. Geological Society America Today 6, 1-7.

Gaucher, C., Finney, S. C., Poire, D. G., Valencia, V. A., Grove, M., Blanco, G., Pamoukaghlian, K., Gomez Peral, L., 2008. Detrital zircon ages of Neoproterozoic sedimentary successions in Uruguay and Argentina; insights into the geological evolution of the Rio de la Plata Craton. Precambrian Research 167, 150-170.

Gesicki, A. L. D., Riccomini, C., Boggiani, P. C., 2002. Ice flow direction during late Paleozoic glaciation in western Paraná Basin, Brazil. Journal of South American Earth Sciences 14, 933-939.

Gesicki, A. L. D., Riccomini, C., Boggiani, P. C., Coimbra, A. M., 1998. The Aquidauana Formation (Parana Basin) in the context of late Palaeozoic glaciation in western Gondwana. Journal of African Earth Sciences 27, 81-82.

Goso, C., 1995. Análise estratigráfica da Formação San Gregorio na borda leste da Bacia Norte Uruguaia (Masters Thesis). Unesp - Univeridade Estadual Paulista, Rio Claro, Brazil, 214 pp.

Griffis, N. P., Mundil, R., Montañez, I. P., Isbell, J., Fedorchuk, N., Vesely, F., Iannuzzi, R., Yin, Q.-Z., 2018,. A new stratigraphic framework built on U-Pb single-zircon TIMS ages and

implications for the timing of the penultimate icehouse (Paraná Basin, Brazil). Geological Society of America Bulletin 130, 848-858.

Griffis, N. P., Montañez, I. P., Fedorchuk, N., Isbell, J., Mundil, R., Vesely, F., Weinshultz, L., Iannuzzi, R., Gulbranson, E., Taboada, A., Pagani, A., Sanborn, M. E., Huyskens, M., Wimpenny, J., Linol, B., Yin, Q.-Z., 2019. Isotopes to ice: Constraining provenance of glacial deposits and ice centers in west-central Gondwana. Palaeogeography, Palaeoclimatology, Palaeoecology (in press). https://doi.org/10.1016/j.palaeo.2018.04.020.

Gulbranson, E. L., Montanez, I. P., Schmitz, M. D., Limarino, C. O., Isbell, J. L., Marenssi, S. A., Crowley, J. L., 2010. High-precision U-Pb calibration of Carboniferous glaciation and climate history, Paganzo Group, NW Argentina. Geological Society of America Bulletin 122, 1480-1498.

Hambrey, M. J., Glasser, N. F., 2003. Glacial sediments: processes, environments and facies. In: Middleton, G.V. (Ed.), Encyclopedia of Sediments and Sedimentary Rocks: Kluwer, Dordrecht, pp. 316-331.

Hartmann, L. A., Philipp, R. P., Santos, J. O. S., McNaughton, N. J., 2011. Time frame of 753–680Ma juvenile accretion during the São Gabriel orogeny, southern Brazilian Shield. Gondwana Research 19, 84-99.

Holz, M., 2003. Sequence stratigraphy of a lagoonal estuarine system; an example from the Lower Permian Rio Bonito Formation, Parana Basin, Brazil. Sedimentary Geology 162, 305-331.

Holz, M., Franca, A. B., Souza, P. A., Iannuzzi, R., Rohn, R., 2010. A stratigraphic chart of the Late Carboniferous/Permian succession of the eastern border of the Parana Basin, Brazil, South America. Journal of South American Earth Sciences 29, 381-399.

Holz, M., Küchle, J., Philipp, R. P., Bischoff, A. P., Arima, N., 2006. Hierarchy of tectonic control on stratigraphic signatures: Base-level changes during the Early Permian in the Paraná Basin, southernmost Brazil. Journal of South American Earth Sciences 22, 185-204.

Holz, M., Souza, P. A., Iannuzzi, R., 2008. Sequence stratigraphy and biostratigraphy of the Late Carboniferous to Early Permian glacial succession (Itarare Subgroup) at the eastern-southeastern margin of the Parana Basin, Brazil. Special Paper - Geological Society of America 441,115-129.

Isbell, J.L., Miller, M.F., Wolfe, K.L., Lenaker, P.A., 2003. Timing of late Paleozoic glaciation in Gondwana: Was glaciation responsible for the development of northern hemisphere cyclothems? In: Chan, M.A., Archer, A.W. (Eds.), Extreme depositional environments: Mega end members in geologic time. Geological Society of America Special Paper 370, 5-24.

Isbell, J. L., Henry, L. C., Gulbranson, E. L., Limarino, C. O., Fraiser, M. L., Koch, Z. J., Ciccioli, P. L., Dineen, A. A., 2012,. Glacial paradoxes during the late Paleozoic ice age:

Evaluating the equilibrium line altitude as a control on glaciation. Gondwana Research 22, 1-19.

Lopez Gamundi, O. R., 1997. Glacial-postglacial transition in the late Paleozoic basins of southern South America, Oxford University Press, New York, NY.

Mallmann, G., Chemale, F., Jr., Avila, J. N., Kawashita, K., Armstrong, R. A., 2007. Isotope geochemistry and geochronology of the Nico Perez Terrane, Rio de la Plata Craton, Uruguay. Gondwana Research 12, 489-508.

Marques-Toigo, M., 1970. Anabaculites nov. gen., a new miospore genus from San Gregorio Formation of Uruguay. Ameghiniana 7, 79–82.

Marques-Toigo, M., 1974. Some new species of spores and pollens of Lower Permian age from the San Gregorio Formation in Uruguay. Anais Academia Brasileira de Ciências 46, 601–616.

Montanez, I.P., Soreghan, G., 2006. Earth's fickle climate: lessons learned from deep-time ice ages. Geotimes 51, 24.

Montañez, I. P., Poulsen, C. J., 2013. The Late Paleozoic Ice Age: An Evolving Paradigm. Annual Review of Earth and Planetary Sciences 41, 629-656.

Oliveira, C. H. E., Chemale, F., Jelinek, A. R., Bicca, M. M., Philipp, R. P., 2014. U–Pb and Lu–Hf isotopes applied to the evolution of the late to post-orogenic transtensional basins of the dom feliciano belt, Brazil. Precambrian Research 246, 240-255.

Raymond, A. L., Metz, C., Parrish, J. T., 2004. Ice and its consequences; glaciation in the Late Ordovician, Late Devonian, Pennsylvanian-Permian, and Cenozoic compared. Journal of Geology 112, 655-670.

Rocha-Campos, A. C., dos Santos, P. R., Canuto, J. R., 2008. Late Paleozoic glacial deposits of Brazil; Parana Basin. Special Paper - Geological Society of America 441, 97-114.

Rosa, E. L. M., Vesely, F. F., Isbell, J. L., Kipper, F., Fedorchuk, N. D., Souza, P. A., 2019. Constraining the timing, kinematics and cyclicity of Mississippian-Early Pennsylvanian glaciations in the Paraná Basin, Brazil. Sedimentary Geology 384, p29-49.

Rosa, E. L. M. d., Vesely, F. F., França, A. B., 2016. A review on late Paleozoic ice-related erosional landforms in the Paraná Basin: origin and paleogeographical implications. Brazilian Journal of Geology 46, 147-166.

Saalmann, K., Gerdes, A., Lahaye, Y., Hartmann, L. A., Remus, M. V. D., aLaeufer, A., 2011. Multiple accretion at the eastern margin of the Rio de la Plata Craton; the prolonged Brasiliano Orogeny in southernmost Brazil. International Journal of Earth Sciences = Geologische Rundschau 100, 355-378.

Saalmann, K., Remus, M. V. D., Hartmann, L. A., 2005. Geochemistry and crustal evolution of volcano-sedimentary successions and orthogneisses in the Sao Gabriel Block, southernmost Brazil; relics of Neoproterozoic magmatic arcs. Gondwana Research 8, 143-161.

Saalmann, K., Remus, M. V. D., Hartmann, L. A., 2006. Tectonic evolution of the Neoproterozoic Sao Gabriel Block, southern Brazil; constraints on Brasiliano orogenic evolution of the Rio de la Plata cratonic margin. Journal of South American Earth Sciences, 21, 204-227.

Santos, P. R., Rocha-Campos, A. C., Canuto, J. R., 1996. Patterns of late Palaeozoic deglaciation in the Paraná Basin, Brazil. Palaeogeography, Palaeoclimatology, Palaeoecology125, 165-184.

Saylor, J. E., Knowles, J. N., Horton, B. K., Nie, J., Mora, A., 2013. Mixing of source populations recorded in detrital zircon U-Pb age spectra of modern river sands. Journal of Geology 121, 17-33.

Saylor, J. E., Stockli, D. F., Horton, B. K., Nie, J., Mora, A., 2012. Discriminating rapid exhumation from syndepositional volcanism using detrital zircon double dating; implications for the tectonic history of the Eastern Cordillera, Colombia. Geological Society of America Bulletin 124, 762-779.

Saylor, J. E., Sundell, K. E., 2016. Quantifying comparison of large detrital geochronology data sets. Geosphere (Boulder, CO) 12, 203-220.

Schneider Santos, J. O., Hartmann, L. A., Bossi, J., Campal, N., Schipilov, A., Pineyro, D., and McNaughton, N. J., 2003. Duration of the Trans-Amazonian cycle and its correlation within South America based on U-Pb SHRIMP geochronology of the La Plata Craton, Uruguay. International Geology Review 45, 27-48.

Starck, D., Papa, C. d., 2006. The northwestern Argentina Tarija Basin: Stratigraphy, depositional systems, and controlling factors in a glaciated basin. Journal of South American Earth Sciences 22, 169-184.

Stollhofen, H., Werner, M., Stanistreet, I. G., Armstrong, R. A., 2008. Single-zircon U-Pb dating of Carboniferous-Permian tuffs, Namibia, and the intercontinental deglaciation cycle framework. Special Paper - Geological Society of America 441, 83-96.

Tedesco, J., Cagliari, J., Coitinho, J. d. R., da Cunha Lopes, R., Lavina, E. L. C., 2016. Late Paleozoic paleofjord in the southernmost Parana Basin (Brazil); geomorphology and sedimentary fill:. Geomorphology 269, 203-214.

Tomazelli, L.J., Soliani Júnior, E., 1982. Evidências de atividade glacial no Paleozóico Superior do Rio Grande do Sul, Brasil. Anais II Congresso Brasileiro de Geologia, Salvador 4, 1378-1389.

Tomazelli, L.J., Soliani Júnior, E., 1997. Sedimentary facies and depositional environments related to Gondwana glaciation in Batovi and Suspiro Regions, Rio Grande do Sul, Brazil. Journal of South American Earth Sciences 10, 295-303.

Uriz, N. J., Cingolani, C. A., Basei, M. A. S., Blanco, G., Abre, P., Portillo, N. S., Siccardi, A., 2016. Provenance and paleogeography of the Devonian Durazno Group, southern Parana Basin in Uruguay. Journal of South American Earth Sciences 66, 248-267.

Verdecchia, S. O., Casquet, C., Baldo, E. G., Pankhurst, R. J., Rapela, C. W., Fanning, M., Galindo, C., 2011. Mid- to Late Cambrian docking of the Rio de la Plata Craton to

southwestern Gondwana; age constraints from U-Pb SHRIMP detrital zircon ages from Sierras de Ambato and Velasco (Sierras Pampeanas, Argentina). Journal of the Geological Society of London 168, 1061-1071.

Vermeesch, P., Resentini, A., Garzanti, E., 2016. An R package for statistical provenance analysis. Sedimentary Geology 336, 14-25.

Vesely, F. F., Assine, M. L., 2006. Deglaciation sequences in the Permo-Carboniferous Itarare Group, Parana Basin, southern Brazil. Journal of South American Earth Sciences 22, 156-168.

Vesely, F. F., Trzaskos, B., Kipper, F., Assine, M. L., Souza, P. A., 2015. Sedimentary record of a fluctuating ice margin from the Pennsylvanian of western Gondwana; Parana Basin, southern Brazil. Sedimentary Geology 326, 45-63.

Visser, J. N. J., 1989. The Permo-Carboniferous Dwyka Formation of Southern Africa: Deposition by a predominantly subpolar marine ice sheet. Palaeogeography, Palaeoclimatology, Palaeoecology 70, 377-391.

Visser, J. N. J., 1997a. Deglaciation sequences in the Permo-Carboniferous Karoo and Kalahari basins of Southern Africa; a tool in the analysis of cyclic glaciomarine basin fills. Sedimentology 44, 507-521.

Visser, J.N.J., 1997b, A review of the Permo-Carboniferous glaciation in Africa. In: Martini, I.P. (Ed.), Late glacial and postglacial environmental changes: Quaternary, Carboniferous-Permian, and Proterozoic. Oxford, UK, Oxford University Press, pp. 169–191.

Winn Jr., R.D., Steinmetz, J.C., 1998. Upper Paleozoic strata of the Chaco-Paraná basin, Argentina, and the great Gondwana glaciation. Journal of South American Earth Sciences 11, 153-168.
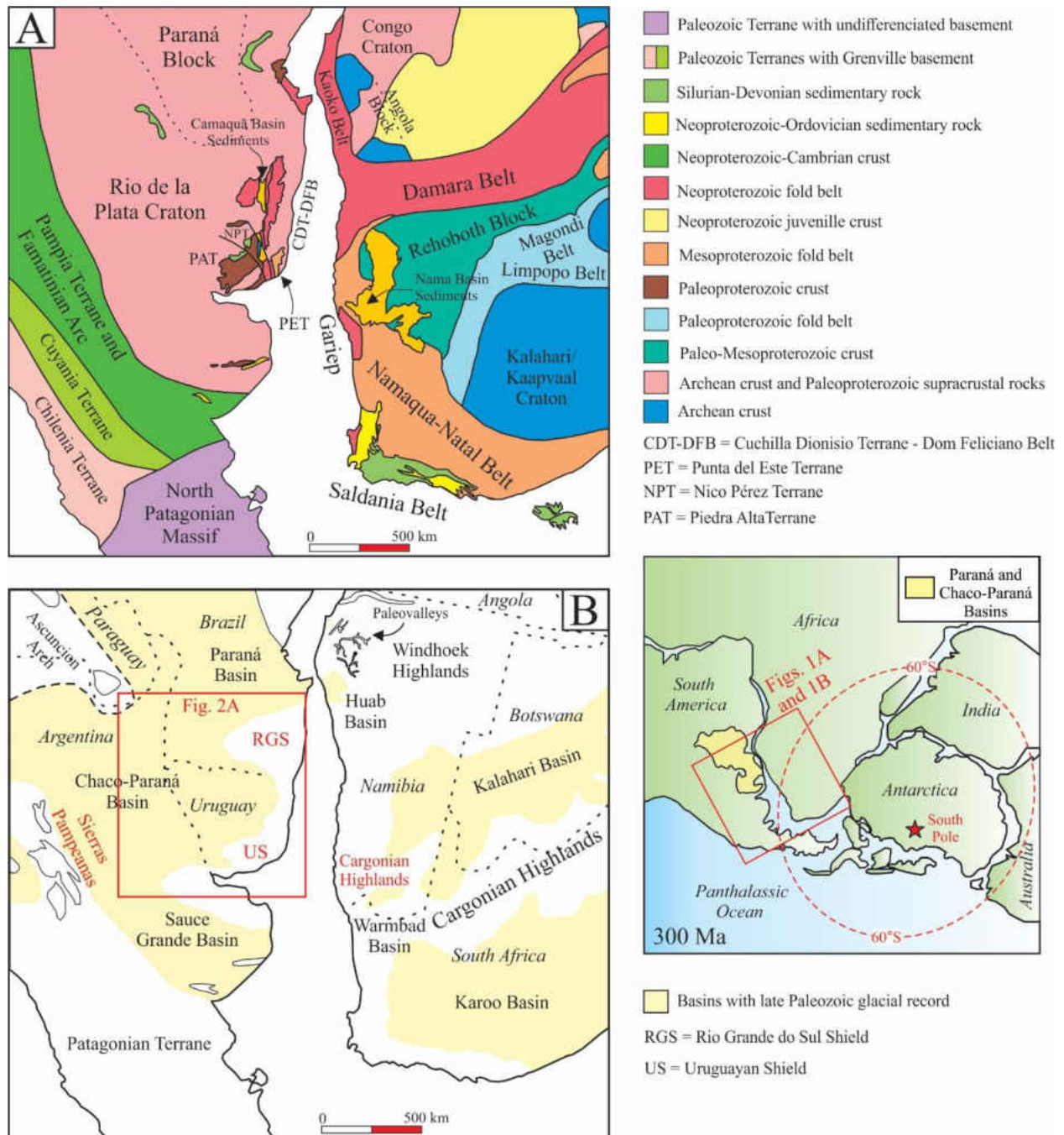
Fig. 4.1. Paleogeography of southernmost Paraná Basin and Chaco-Paraná Basin during late Carboniferous. (A) Simplified map of possible source terranes and their ages in South America and southern Africa after Uriz et al. (2016). (B) Map of study area showing late Paleozoic sedimentary basins and paleotopographic highs after Visser (1997b), Winn Jr. and Steinmetz (1998), and Uriz et al. (2016). Possible source areas for sediments examined in this study are in red. Red box indicates location of Fig. 3.2A.

169
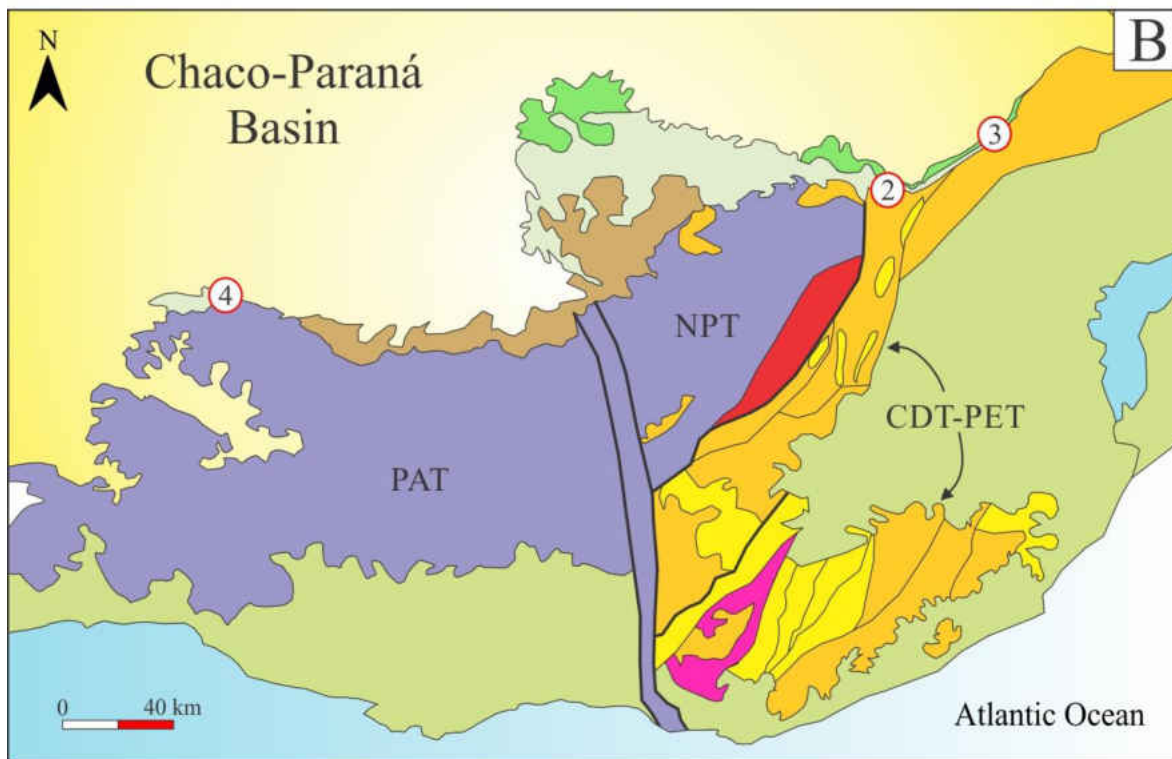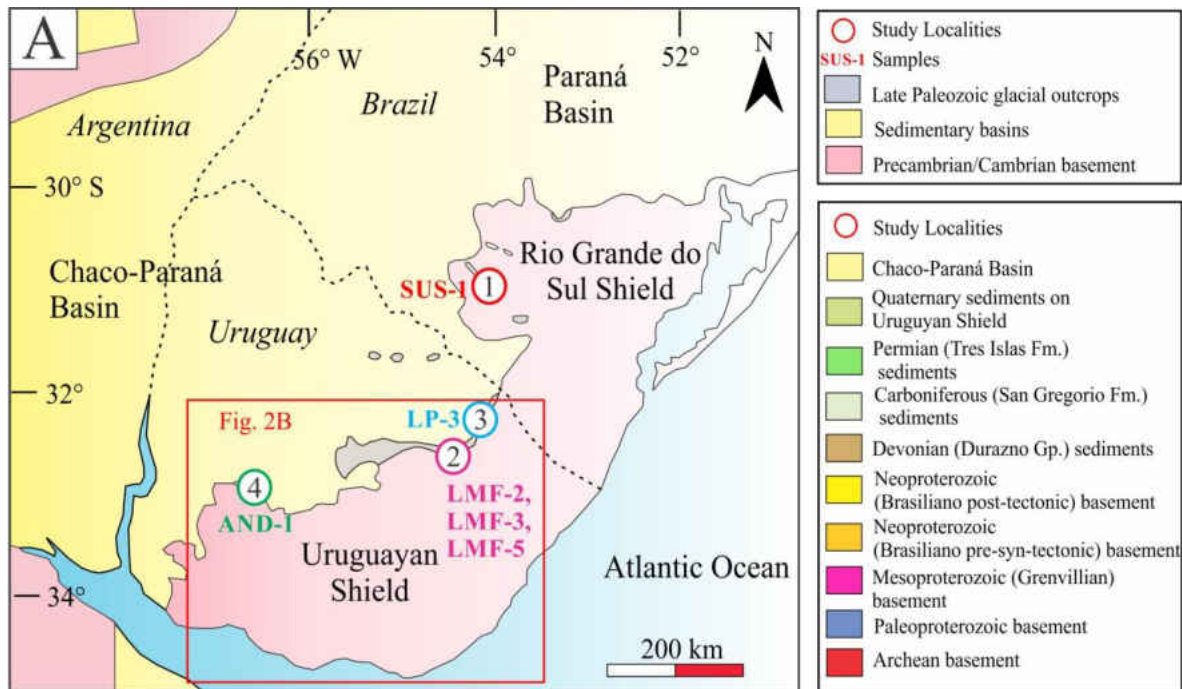
Fig. 4.2. Study area on Rio Grande do Sul Shield and Uruguayan Shield. (A) Study area with late Paleozoic glacial outcrops in gray after Assine et al. (2018). Study locations indicated by colored circles and samples collected from each location labeled in matching color. (B) Possible source terranes within Uruguayan Shield. CDT =Cuchilla Dionisio Terrane, PET=Punta del Este Terrane, NPT= Nico Pérez Terrane, PAT = Piedra Alta Terrane.
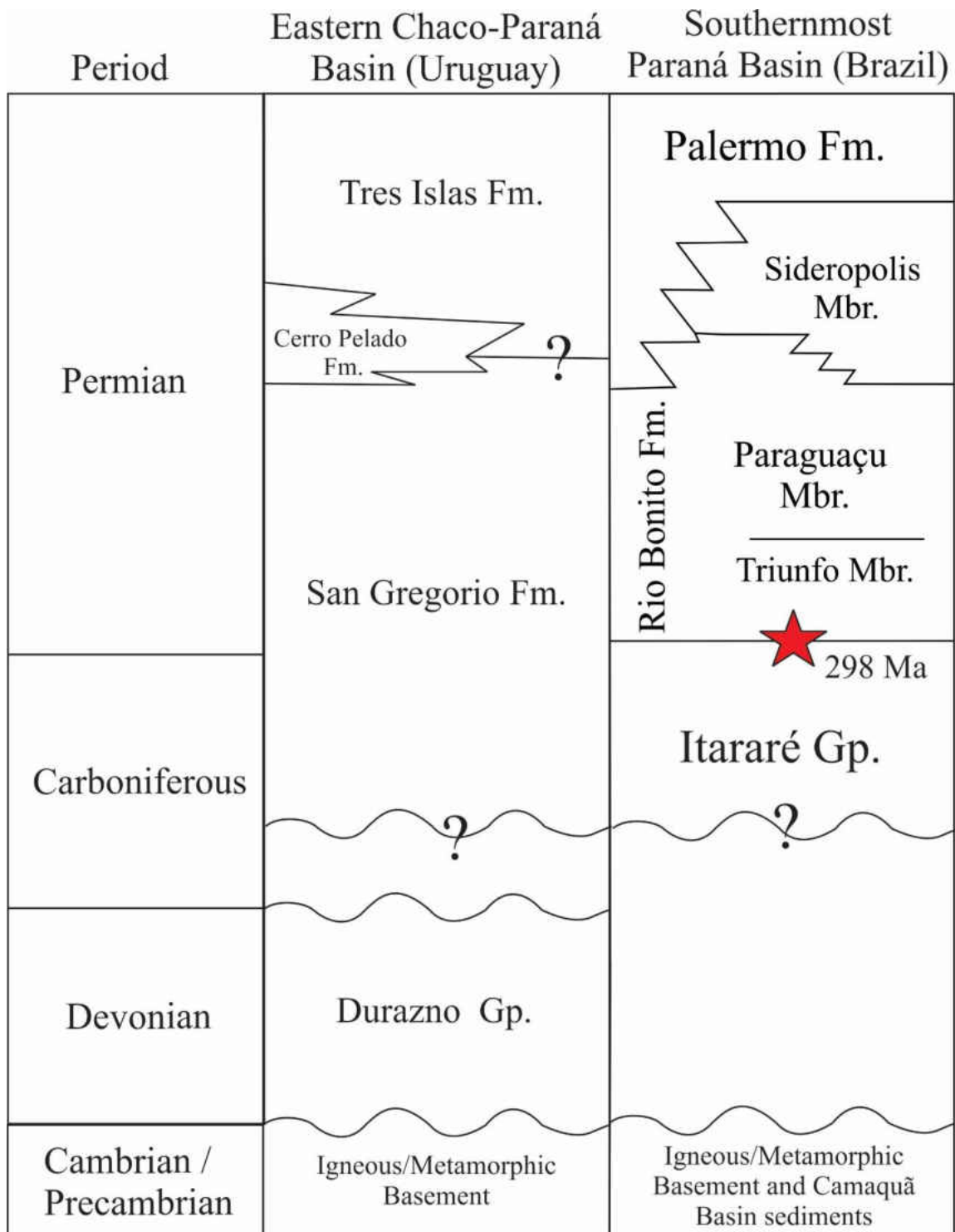
Fig. 4.3. Stratigraphy of southernmost Paraná Basin and eastern Chaco-Paraná Basin after de Santa Ana (2004, 2006a) and Holz et al. (2006). Red star indicates U-Pb zircon age collected by Griffis et al. (2018).
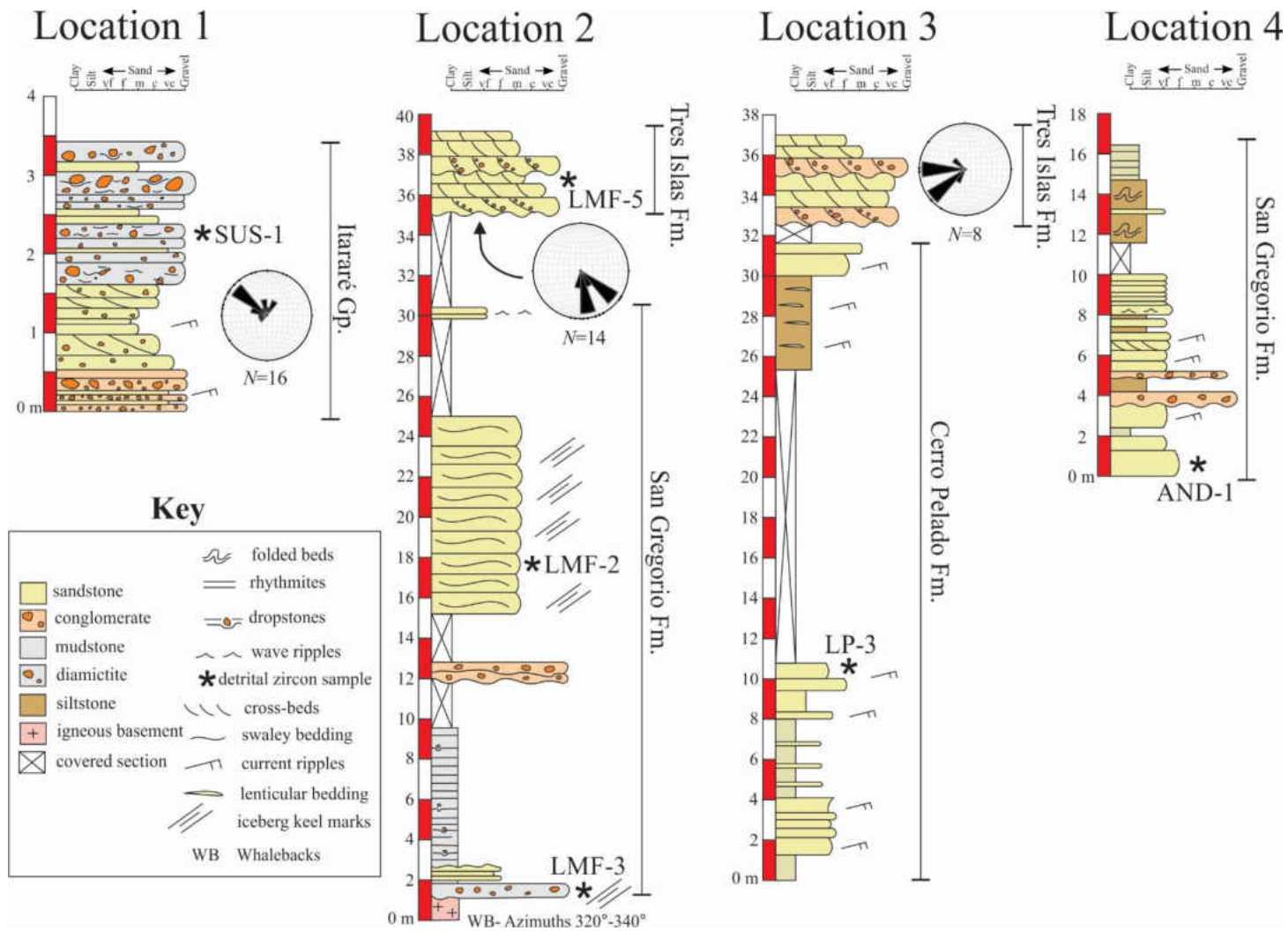
Fig. 4.4. Stratigraphic columns from study sample locations after Goso (1995), Assine et al. (2018), and Fedorchuk et al. (2019a). Detrital zircon sample locations shown with asterisks and paleocurrent orientations collected from cross-stratification depicted using rose diagrams.
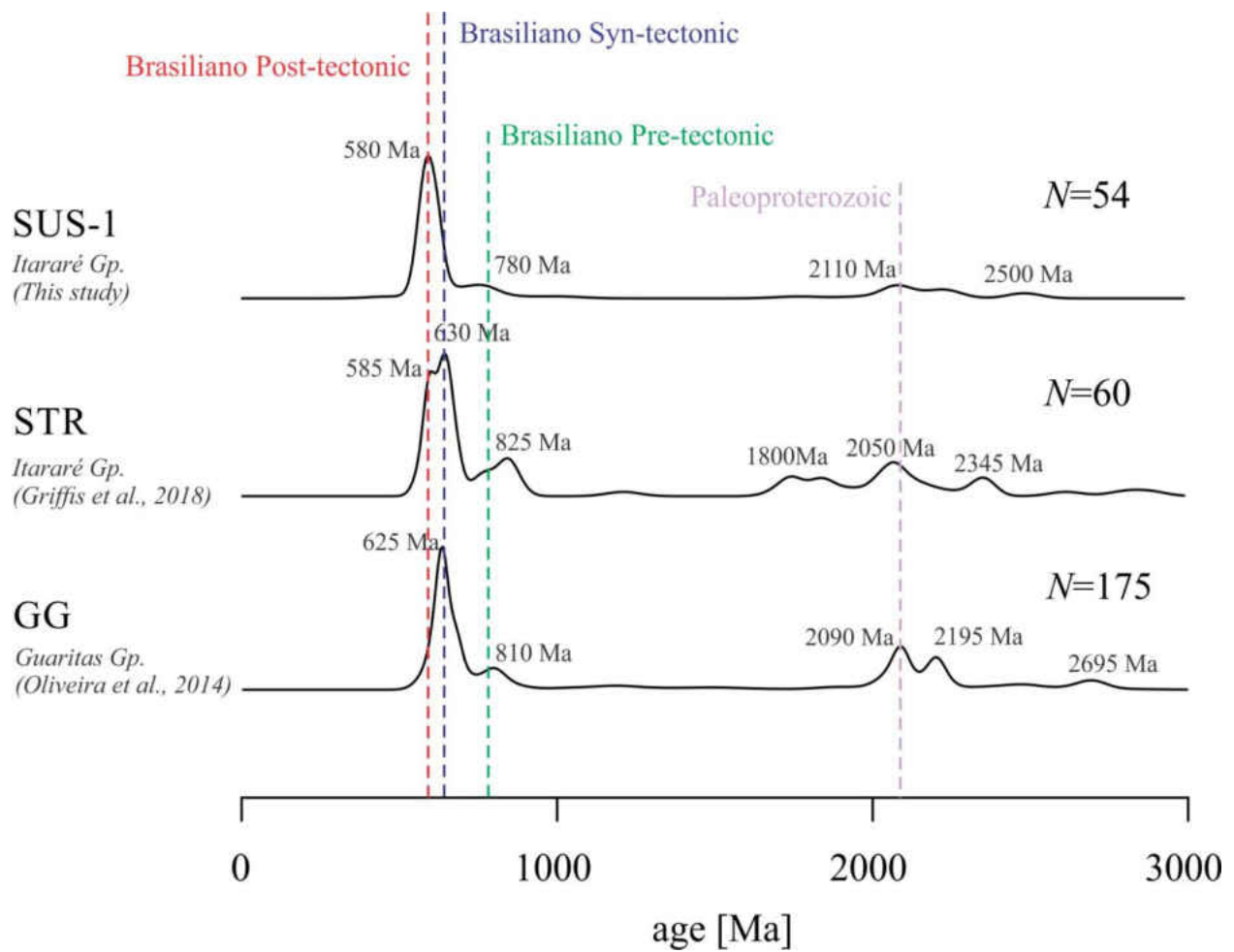
Fig. 4.5. Kernel density plot of sample SUS-1 compared to other samples from Rio Grande do Sul Shield including sample STR (Griffis et al., 2018) and sample GG (Oliveira et al., 2014). Similar peaks and relative peaks heights indicates a close relationship between these samples.
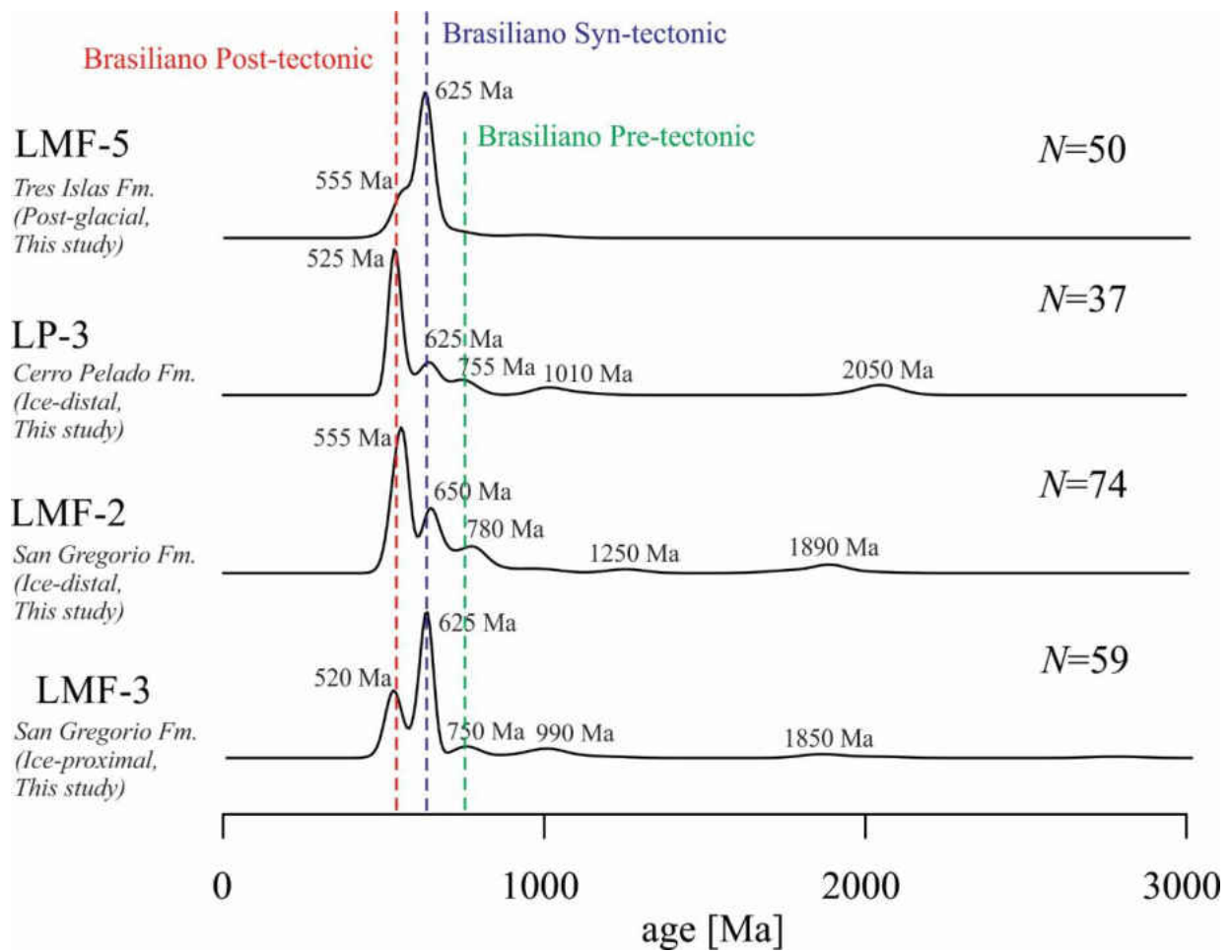
Fig. 4.6. Kernel density plots of samples LMF-5, LMF-3, LMF-2, and LP-3. Relative changes in the amount of syn-tectonic and post-tectonic zircons between ice-proximal, relatively ice-distal, and post-glacial environments reflects changes to drainage patterns.

174
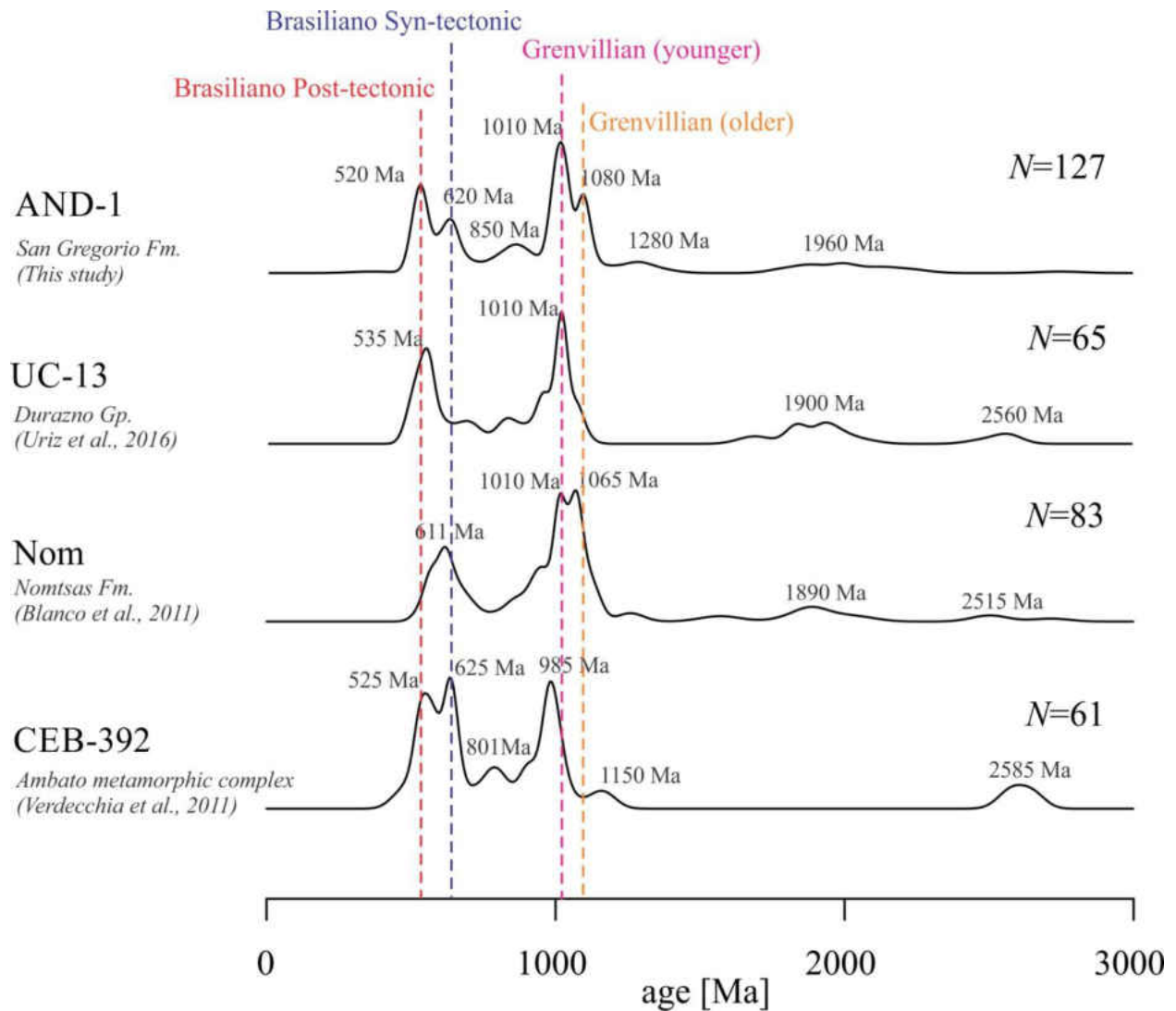
Fig. 4.7. Kernel density plots of samples AND-1, UC-13 (Uriz et al., 2016), NOM (Blanco et al., 2011), and CEB-392 (Verdecchia et al., 2011). Sample AND-1 has similar peaks to both sample UC-13 from Devonian Durazno Gp. and sample NOM from Cambrian Nomtsas Fm.
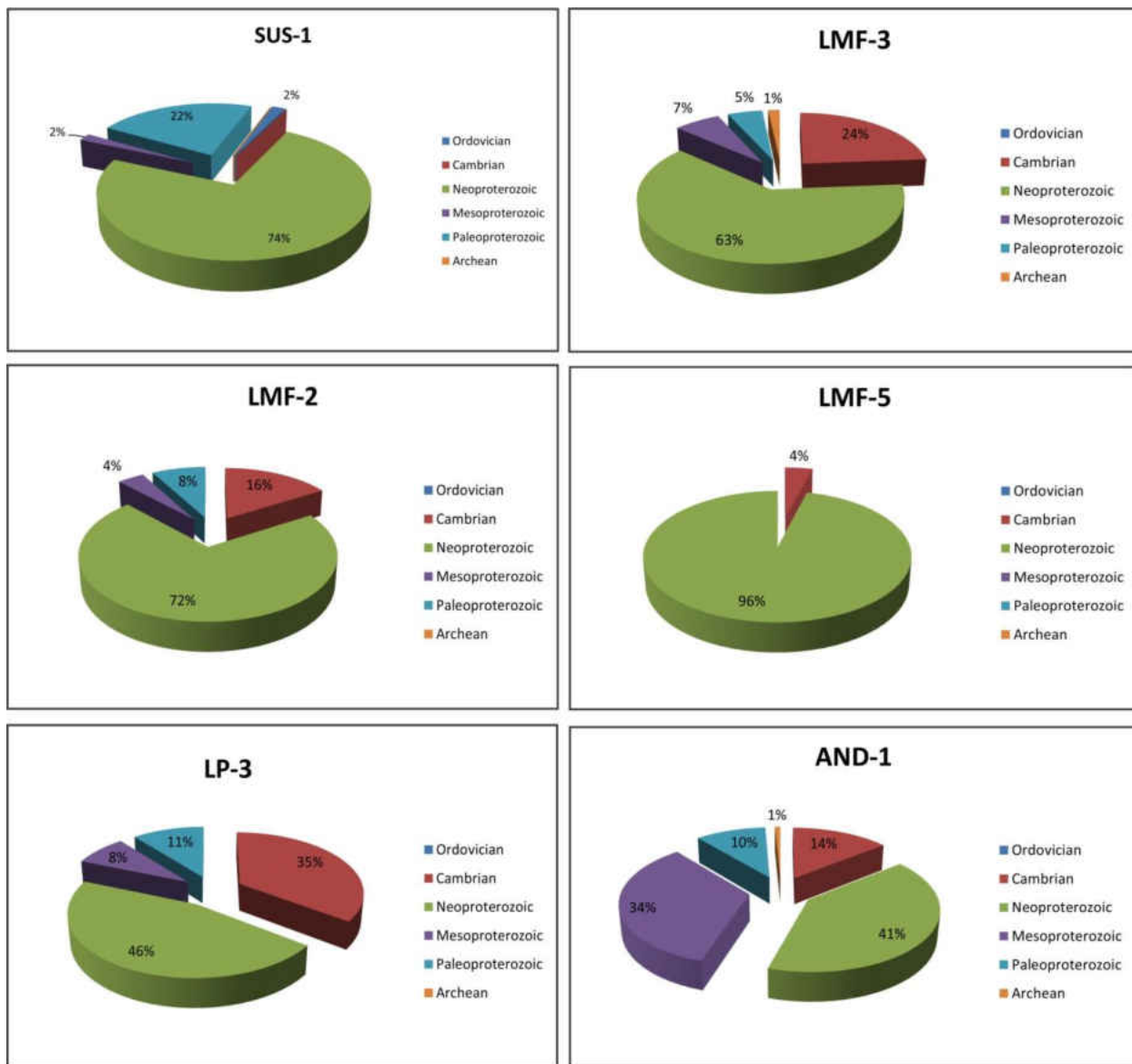
Fig. 4.8. Pie charts showing percentage of Ordovician, Cambrian, Neoproterozoic, Mesoproterozoic, Paleoproterozoic, and Archean grains in each detrital zircon sample. Note sample LMF-5 has a lack of diverse grains and sample AND-1 is unique for its abundance of Mesoproterozoic grains.

176

	SUS-1	LMF-3	LMF-2	LMF-5	LP-3	AND-1	STR	GG	Nom	CEB-392	UC-13
SUS-1		0.14	0.15	0.06	0.01	0.00	0.00	0.00	0.00	0.05	0.00
LMF-3	0.14		0.21	0.30	0.12	0.00	0.00	0.00	0.00	0.00	0.00
LMF-2	0.15	0.21		0.06	0.39	0.00	0.00	0.00	0.00	0.01	0.00
LMF-5	0.06	0.30	0.06		0.04	0.00	0.00	0.00	0.00	0.00	0.00
LP-3	0.01	0.12	0.39	0.04		0.00	0.00	0.00	0.00	0.03	0.00
AND-1	0.00	0.00	0.00	0.00	0.00		0.00	0.00	0.30	0.02	0.73
STR	0.00	0.00	0.00	0.00	0.00	0.00		0.80	0.01	0.00	0.17
GG	0.00	0.00	0.00	0.00	0.00	0.00	0.80		0.00	0.00	0.00
Nom	0.00	0.00	0.00	0.00	0.00	0.30	0.01	0.00		0.00	0.21
CEB-392	0.05	0.00	0.01	0.00	0.03	0.02	0.00	0.00	0.00		0.10
UC-13	0.00	0.00	0.00	0.00	0.00	0.73	0.17	0.00	0.21	0.10	
UP-12	0.23	0.01	0.01	0.00	0.10	0.01	0.07	0.00	0.00	0.14	0.04

Table 4.1. Comparison of K-S P-values between samples analyzed in this study and other studies. P-values < 0.05 indicate that two samples were drawn from different populations (i.e. have different provenance). P-values > 0.05 (highlighted in yellow) indicate samples cannot be clearly distinguished as having separate provenance.

	SUS-1	LMF-3	LMF-2	LMF-5	LP-3	AND-1	STR	GG	Nom	CEB-392	UC-13
SUS-1		0.29	0.32	0.43	0.11	0.07	0.63	0.47	0.12	0.26	0.08
LMF-3	0.29		0.18	0.58	0.25	0.22	0.36	0.37	0.11	0.28	0.09
LMF-2	0.32	0.18		0.38	0.68	0.17	0.32	0.23	0.10	0.49	0.27
LMF-5	0.43	0.58	0.38		0.20	0.10	0.55	0.56	0.14	0.37	0.08
LP-3	0.11	0.25	0.68	0.20		0.25	0.12	0.10	0.06	0.38	0.27
AND-1	0.07	0.22	0.17	0.10	0.25		0.08	0.08	0.57	0.49	0.60
STR	0.63	0.36	0.32	0.55	0.12	0.08		0.87	0.13	0.31	0.06
GG	0.47	0.37	0.23	0.56	0.10	0.08	0.87		0.12	0.27	0.03
Nom	0.12	0.11	0.10	0.14	0.06	0.57	0.13	0.12		0.34	0.46
CEB-392	0.26	0.28	0.49	0.37	0.38	0.49	0.31	0.27	0.34		0.43
UC-13	0.08	0.09	0.27	0.08	0.27	0.60	0.06	0.03	0.46	0.43	
UP-12	0.29	0.27	0.70	0.38	0.61	0.33	0.36	0.28	0.22	0.50	0.35

Table 4.2. Comparison of cross-correlation coefficients (R^2) between samples analyzed in this study and other studies. Samples where R^2 is > 0.50 are highlighted in yellow. Samples in red have both R^2 values > 0.50 and K-S P-values > 0.05.
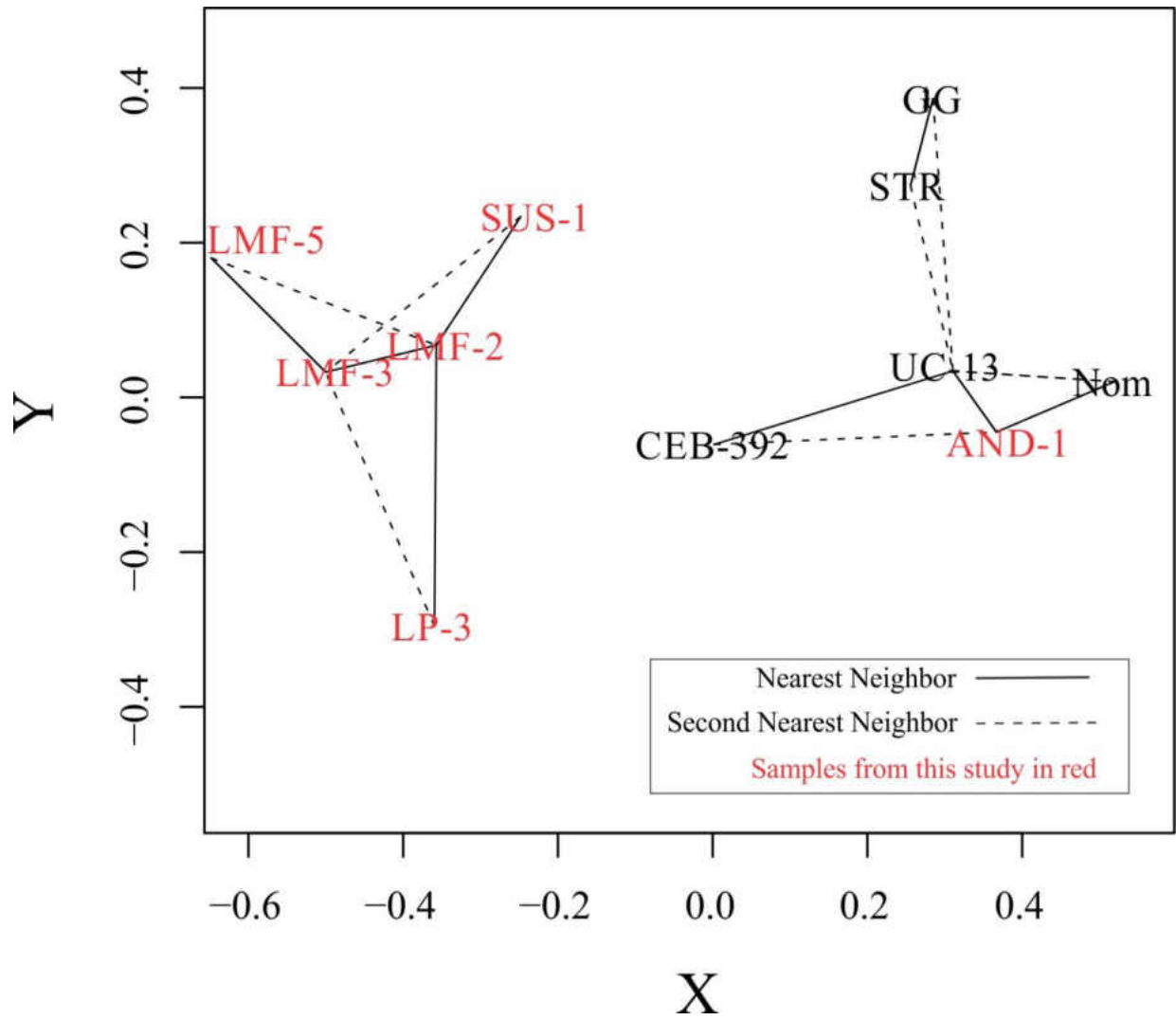
Fig. 4.9. Multidimensional scaling analysis of samples analyzed in this study and other studies. Samples more similar to each other plot closer together and samples more dissimilar to each other plot farther apart.
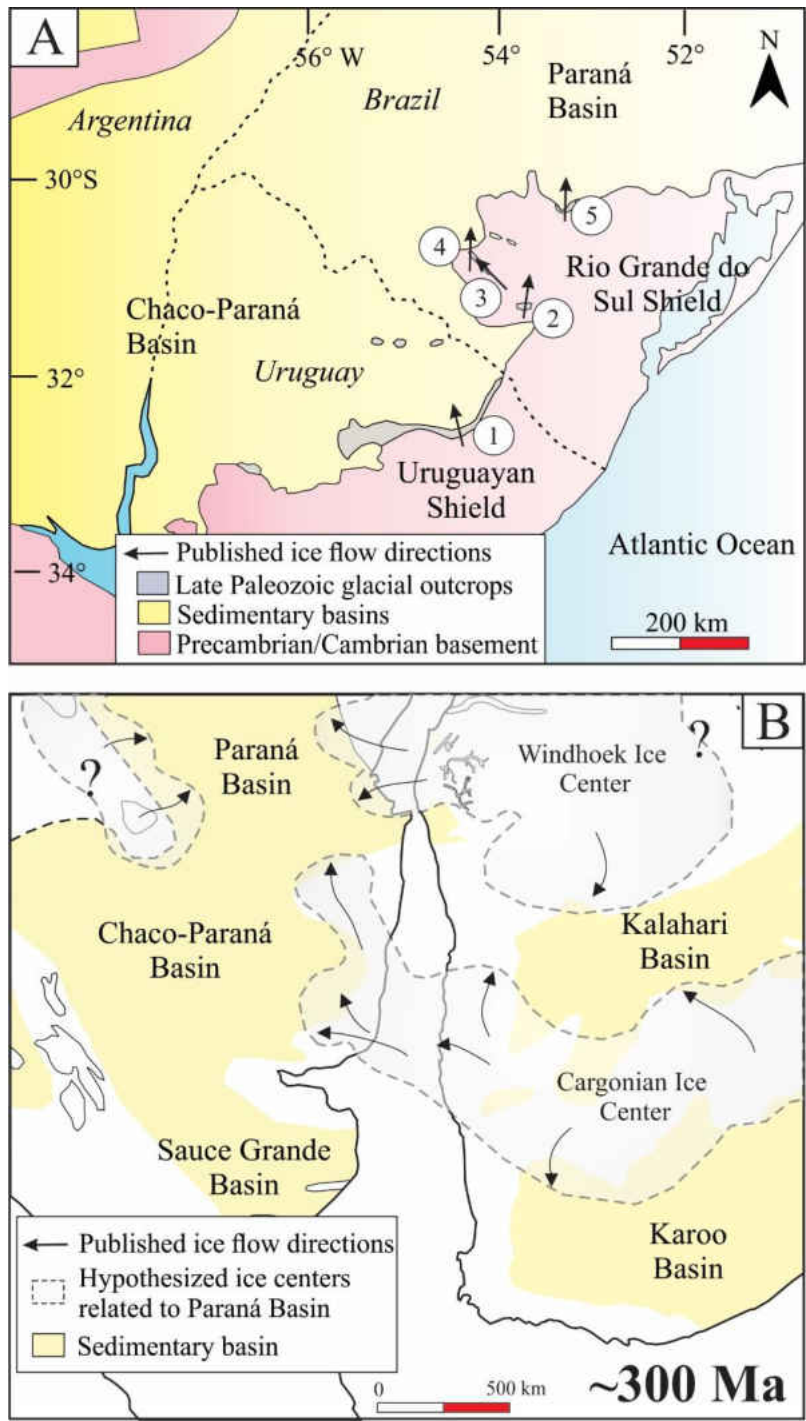
Fig. 4.10. Paleogeographic reconstruction of ice centers that affected the Paraná Basin and eastern Chaco-Paraná Basin. (A) Map of study area showing published ice flow directions. (1) Assine et al. (2018). (2) Tomazelli and Soliani Júnior (1982). (3) Fedorchuk et al. (2019a). (4) Tomazelli and Soliani Júnior (1997). (5) Tomazelli and Soliani Júnior (1982). (B) Reconstruction of two hypothesized ice centers over African highlands draining into Paraná and Chaco-Paraná Basins during the Carboniferous. After Visser (1997b), Rocha-Campos et al. (2008), Uriz et al. (2016), and Assine et al. (2018).

180

Chapter 5. Conclusions

5.1. Outcomes of stated project objectives

1. *Conduct a sedimentologic and stratigraphic analysis of glaciogenic deposits in the southern Paraná Basin to determine the presence, size, extent, timing, depositional environments, and thermal regime of the glaciation.*

- The Mariana Pimentel and Leão Paleovalleys on the eastern Rio Grande do Sul Shield are not glacially-carved fjords draining off Africa.

- The depositional fill of the paleovalleys is consistent with the post-glacial Rio Bonito and Palermo Fms. This suggests that this area may not have been glaciated during the Carboniferous and was certainly not glaciated during the early Permian.

- Sediments in the paleovalleys represent a transition from an estuarine/lacustrine environment, to a fluvial-dominated environment, to an estuarine environment formed by a marine transgression. Some of these base level changes were likely driven by active tectonism (reactivation of basement structures) during the late Paleozoic.

- Ice did not flow directly W from the Windhoek Highlands in Namibia onto the RGS as confined valley glaciers.

- Deformed glacial (Itararé Gp.) strata on the western Rio Grande do Sul Shield are consistent with a late Paleozoic push-moraine complex formed by a grounded, fluctuating ice margin.

- Proglacial sediments from the western Rio Grande do Sul Shield exhibit evidence of a temperate paleoclimate and warm-based glaciation. Some of these sediments were likely deposited in proglacial lakes on the RGS, supporting a terrestrial glacial environment in some areas.

- Deformation structures and grooved surfaces on the Rio Grande do Sul Shield indicate that ice flowed radially NNW and NNE across the RGS. This supports the hypothesis that an unconfined lobe advanced out of Uruguay as proposed by Crowell and Frakes (1975).

2. *Constrain the location and size of ice centers affecting the study area by determining the provenance of glaciogenic units.*

- U-Pb detrital zircon geochronology revealed that sediments located in the Mariana Pimentel and Leão Paleovalleys did not originate from Africa. This helped constrain the size of the ice center that advanced over the RGS by demonstrating that it was separate from the ice center that extended into the eastern margin of the Paraná Basin.

- Detrital zircon samples from glacial sediments on the western RGS (Itararé Gp.) were discussed in Chapter 4 and in Griffis et al. (2019). These indicate that the late Paleozoic sediments on the RGS were primarily derived from local sources. The most significant source of these sediments was the easily erodible, Precambrian/Cambrian Camaquã Basin located on the RGS.

- The provenance of these sediments from the RGS are different than those on the eastern margin of the Paraná Basin, which have an African source in the highlands of northern Namibia (e.g. Canile et al., 2016).

3. *Compare and contrast the provenance and sedimentology of glaciogenic sediments within the study area to related localities in the Chaco-Paraná Basin, Uruguay in order to evaluate drainage patterns during the late Paleozoic.*

- Subglacially-carved whalebacks were described south of the RGS on the eastern margin of the Chaco-Paraná Basin, Uruguay (Assine et al., 2018). These features have orientations that imply thick, fast-flowing ice that moved towards the NW. This supports the hypothesis that an unconfined lobe flowed out of the Chaco-Paraná Basin in Uruguay and into the southernmost Paraná Basin (e.g. Crowell and Frakes, 1975).
- Detrital zircon samples collected from the Chaco-Paraná Basin in Uruguay indicate that sediment was sourced from igneous and metamorphic terranes in SE Uruguay and likely SW Namibia. This is consistent with an ice center over the Cargonian Highlands in southern Namibia, SE Uruguay, and northern South Africa that was separate from the Windhoek Highlands in northern Namibia that fed the eastern Paraná Basin.
- Detrital zircon signatures differ between ice-proximal glacial settings, more ice-distal environments, and post-glacial environments. This is interpreted to reflect differences in drainage catchments as ice advanced and retreated, possibly due to isostatic adjustments and the blockage/release of preglacial fluvial networks. Zircons ages reflect more local sources when ice extended further into the basin and more distal sources when ice has

retreated further back. Post-glacial zircons reflect a return to local sources, likely due to incision of underlying basement material.

5.2. Implications for the late Paleozoic ice volume paradox

The results of this project are broadly consistent with the interpretation that an unconfined lobe(s), originating from an ice center in the Cargonian Highlands of southern Africa, extended out into the Chaco-Paraná Basin and onto the RGS (e.g. Frakes and Crowell, 1972; Crowell and Frakes, 1975; Assine et al., 2018). Based on the orientations of subglacially grooved surfaces in Africa, such an ice center was likely separate from the ice center located over the Windhoek Highlands that supplied ice to the eastern margin of the Paraná Basin (Visser, 1997). Therefore, this project is clear evidence for the emerging view of glaciation during the late Paleozoic as consisting of multiple, distinct, topographically controlled ice centers. However, this work did not support the most limited interpretation of glaciation on the RGS, which envisioned a small, isolated, ice cap (e.g. Santos et al., 1996; Rocha-Campos et al., 2008). This implies that glaciation during the late Paleozoic was significantly more complex than previously believed, in which topographically controlled ice centers waxed and waned under the influence of various drivers and emanated (in some cases 100s-1000s of kms) out into various depositional basins. Nevertheless, the combined ice-volume from these ice-centers could simply not contain enough water volume to produce 100s of m of eustatic sea-level change (c.f. Crowley and Baum, 1992; Isbell, 2003). For example, as discussed in Chapter 2, two massive ice centers over both northern and southern Namibia would only create ~3.9 m of global sea-level change

even if they completely grew to their maximum extension and then disappeared over Milankovitch timespans.

This study further contradicts the hypothesis of a single, massive, long-lived glaciation by illustrating that peak glaciation did not occur everywhere at the same time. Chapter 3 of this study shows that the southernmost margin of the Paraná Basin experienced frequent changes in ice-marginal positions during the Carboniferous and Chapter 2 demonstrates that the RGS was deglaciated by the early Permian. Both of these data points indicate that a massive ice sheet or ice-shelf could not have persisted over the study area through the early Permian. Despite this, the early Permian appears to represent a time of widespread glaciation in Africa (e.g.Visser, 1997; Fielding et al., 2008; Stollhofen et al., 2008). Meanwhile, glaciers in various basins in western South America had disappeared long prior to those that deposited sediments on the RGS (e.g. Fielding et al., 2008; Isbell et al., 2012). A record of widespread, time-equivalent ice cover does not appear to exist across Gondwana.

This begs the question: what was the true nature of eustatic sea-level fluctuations during the late Paleozoic? The answer to this question is beyond the scope of this study but the results presented here show the complexity involved with interpreting base-level changes. For example, in Chapter 2, the depositional fill of the paleovalleys in question were likely influenced by (at a minimum) some combination of local tectonism, regional tectonism, and eustatic fluctuations. This was likely the case for many sedimentary basins during the LPIA, which implies that previous interpretations of eustatic changes may be need to be reconsidered. When combined, all of the evidence points towards the influence of multiple drivers of climate and base level fluctuations that include but are not limited to the drift of the continents, local and regional tectonism, $p\mathrm{CO}_2$, orbital parameters, ocean and atmospheric circulation, and plant and animal

evolution (e.g. Heckel, 1977; Isbell et al., 2012; Montañez and Poulsen, 2013). These drivers were likely operating at different frequencies to control glaciation during the late Paleozoic but their exact roles remain an important topic of discussion.

5.3. Future Directions

There are several areas where this project could be expanded. Firstly, more work is needed on the sedimentology and stratigraphy of the glacial and post-glacial record of the Chaco-Paraná Basin in Uruguay. The stratigraphic record of glacial advance/retreat cycles is generally unknown for the Chaco-Paraná Basin and some effort is required to correlate the cycles to those recognized in the Paraná Basin (e.g. Vesely and Assine, 2006). Although most of the stratigraphic record for the Chaco-Paraná Basin is located in the subsurface, cores do exist (e.g. Winn Jr. and Steinmetz, 1998). It is unclear if glaciation persisted longer in the Chaco-Paraná Basin compared to the Paraná Basin. Additionally, it is unclear if the depositional processes and environments are different from the southern margin of the Paraná Basin.

Secondly, the glacial records in the eastern Chaco-Paraná Basin and eastern Paraná basin also need to be better tied to their respective ice centers in Africa. The Windhoek Highlands of northern Namibia contain westward draining paleovalleys with a late Paleozoic glaciogenic fill (Dwyka Gp.) (e.g. Martin, 1981; Visser, 1997). These stratigraphy and sedimentology of the fill needs to be examined to determine if glaciers were confined to the valleys or if they overtopped the valley walls as massive unconfined lobes that drained west into the Paraná Basin. This can help determine whether or not glaciers that entered the eastern Paraná Basin were confined to fjords as suggested by some authors (e.g. Fallgatter and Paim, 2016) or existed as unconfined

lobes as proposed by other authors (e.g. Crowell and Frakes, 1975). The provenance of these sediments should also be examined to determine how similar they are to those on the eastern margin of the Paraná Basin and to possible source regions in Namibia or further east in Africa. Finally, more work is needed on the glacial record bordering the Cargonian Highlands in Namibia and South Africa. Here, the paleo ice-flow indicators and detrital zircon (U-Pb) geochronology should be re-examined for the Dwyka Gp. to see how well these sediments correspond to those described here from the eastern Chaco-Paraná Basin.

In conclusion, the LPIA continues to be one of the most interesting and relevant time periods in Earth's history and an important point of reference for understanding modern Earth systems. The late Paleozoic saw the beginnings of widespread, complex terrestrial plant and animal life. This time interval also saw some of the most dramatic climatic shifts of the entire Phanerozoic. The results of this work in the southernmost Paraná Basin represent one temporally and geographically small piece of the interpretations into this time. Therefore, continued research into the LPIA is needed to ground truth the glacial record in basins across Gondwana. Hopefully, this can lead to an improved understanding of how current human activities might interact with Earth's complex, deep-time climate drivers.

References

Assine, M. L., de Santa Ana, H., Veroslavsky, G., Vesely, F. F., 2018. Exhumed subglacial landscape in Uruguay; erosional landforms, depositional environments, and paleo-ice flow in the context of the late Paleozoic Gondwanan glaciation. Sedimentary Geology 369, 1-12.

Canile, F. M., Babinski, M., Rocha-Campos, A. C., 2016. Evolution of the Carboniferous-Early Cretaceous units of Parana Basin from provenance studies based on U-Pb, Hf and O isotopes from detrital zircons. Gondwana Research 40, 142-169.

Crowell, J.C., Frakes, L.A., 1975. The late Paleozoic glaciation. In: Campbell, K.S.W. (Ed.), Gondwana Geology. Australian National University Press, Canberra, pp. 313-331.

Crowley, T.J., Baum, S.K., 1992, Modeling late Paleozoic glaciation. Geology 20, 507-510.

Fallgatter, C., Paim, P. S. G., 2017. On the origin of the Itararé Group basal nonconformity and its implications for the Late Paleozoic glaciation in the Paraná Basin, Brazil. Palaeogeography, Palaeoclimatology, Palaeoecology (in press). https://doi.org/10.1016/j.palaeo.2017.02.039.

Fielding, C. R., Frank, T. D., Isbell, J. L., 2008. The late Paleozoic ice age-A review of current understanding and synthesis of global climate patterns. In: Fielding, C. R., Frank, T. D., Isbell, J. L. (Eds.), Resolving the Late Paleozoic Ice Age in Time and Space. Geological Society of America Special Publication 441, pp. 343-354.

Frakes, L.A., Crowell, J.C., 1972. Late Paleozoic glacial geography between the Paraná Basin and the Andean Geosyncline. Anais. Academia Brasileira de Ciencias 44, pp. 139- 145.

Griffis, N. P., Montañez, I. P., Fedorchuk, N., Isbell, J., Mundil, R., Vesely, F., Weinshultz, L., Iannuzzi, R., Gulbranson, E., Taboada, A., Pagani, A., Sanborn, M. E., Huyskens, M., Wimpenny, J., Linol, B., Yin, Q.-Z., 2019. Isotopes to ice: Constraining provenance of glacial deposits and ice centers in west-central Gondwana. Palaeogeography, Palaeoclimatology, Palaeoecology (in press). https://doi.org/10.1016/j.palaeo.2018.04.020.

Heckel, P. H., 1977. Origin of phosphatic black shale facies in Pennsylvanian cyclothems of mid-continent North America. American Association of Petroleum Geologists Bulletin 61, 1045-1068.

Isbell, J.L., Miller, M.F., Wolfe, K.L., Lenaker, P.A., 2003. Timing of late Paleozoic glaciation in Gondwana: Was glaciation responsible for the development of northern hemisphere cyclothems? In: Chan, M.A., Archer, A.W. (Eds.), Extreme depositional environments: Mega end members in geologic time. Geological Society of America Special Paper 370, 5-24.

Isbell, J. L., Henry, L. C., Gulbranson, E. L., Limarino, C. O., Fraiser, M. L., Koch, Z. J., Ciccioli, P. L., Dineen, A. A., 2012,. Glacial paradoxes during the late Paleozoic ice age:

Evaluating the equilibrium line altitude as a control on glaciation. Gondwana Research 22, 1-19.

Martin, H., 1981. The late Palaeozoic Dwyka Group of the South Kalahari Basin in Namibia and Botswana and the subglacial valleys of the Kaokoveld in Namibia. In: Hambrey, M.J., Harland, W.B. (Eds.), Earth's Pre-Pleistocene Glacial Record. Cambridge University Press, Cambridge, pp. 61-66.

Montañez, I. P., Poulsen, C. J., 2013. The late Paleozoic ice age: an evolving paradigm. Annual Review of Earth & Planetary Sciences 41, 1-28.

Rocha-Campos, A. C., dos Santos, P. R., Canuto, J. R., 2008. Late Paleozoic glacial deposits of Brazil; Parana Basin. Special Paper - Geological Society of America 441, 97-114.

Santos, P. R., Rocha-Campos, A. C., Canuto, J. R., 1996. Patterns of late Palaeozoic deglaciation in the Paraná Basin, Brazil. Palaeogeography, Palaeoclimatology, Palaeoecology 125, 165-184.

Stollhofen, H., Werner, M., Stanistreet, I. G., Armstrong, R. A., 2008. Single-zircon U-Pb dating of Carboniferous-Permian tuffs, Namibia, and the intercontinental deglaciation cycle framework. Special Paper - Geological Society of America 441, 83-96.

Vesely, F. F., Assine, M. L., 2006. Deglaciation sequences in the Permo-Carboniferous Itarare Group, Parana Basin, southern Brazil. Journal of South American Earth Sciences 22, 156-168.

Visser, J.N.J., 1997, A review of the Permo-Carboniferous glaciation in Africa. In: Martini, I.P. (Ed.), Late glacial and postglacial environmental changes: Quaternary, Carboniferous-Permian, and Proterozoic. Oxford, UK, Oxford University Press, pp. 169–191.

Winn Jr., R.D., Steinmetz, J.C., 1998. Upper Paleozoic strata of the Chaco-Paraná basin, Argentina, and the great Gondwana glaciation. Journal of South American Earth Sciences 11, 153-168.

Appendices

Appendix A: Detrital zircon methods

A1. Supplemental U-Pb detrital zircon methods (Chapter 2)

Detrital zircon samples were crushed and sieved to separate out the 63-250 μm fraction. A density separation was performed using lithium sodium tungstate (LST) and zircons were picked from the heavy fraction under a binocular scope. Careful attention was paid to not bias zircon picks based on size, morphology, or color. Zircons were mounted in an epoxy resin, polished, and imaged using back scattered electrons to check for fractures, inherited cores, rims, zonation, and inclusions that were avoided when possible. However, in many cases, these features were unavoidable due to their prevalence in the complex (recycled) zircons analyzed in this study (Figs. A1.1 and A1.2). All zircons picked, regardless of appearance, were ablated in order to not bias the data.
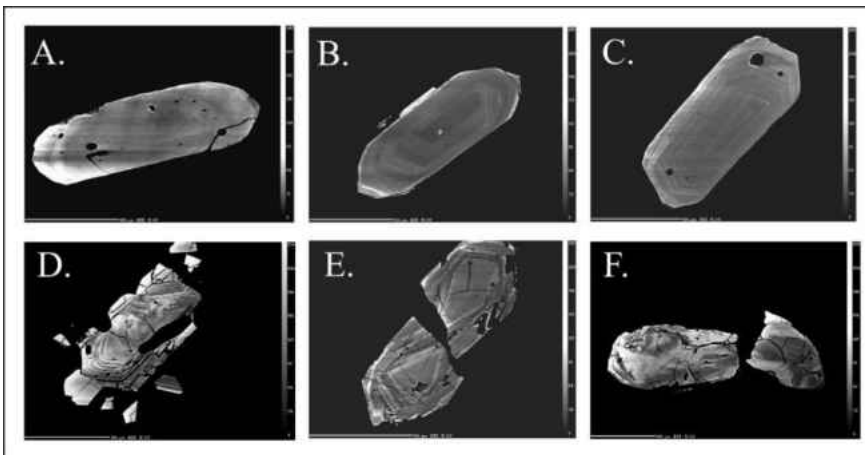
Fig. A1.1. Back scattered electron images of zircons analyzed in this study. (A-C) Examples of zircons that produced concordant data meeting quality standards. (D-E) Examples of zircons producing data below quality standards excluded from dataset. A=MDP15_6_21; B=MDP15_6_91; C=MDP15_6_72; D=MDP15_6_2; E=MDP15_6_71; F=MDP15_6_22.

Fig. A1.2. Spot MDP15_6_96 (white circle) of inherited core. Produced concordant age of 1257 Ma (Fig. A1.3).

U-Th-Pb data was collected via laser-ablation inductively coupled plasma mass spectrometry (LA-ICP-MS) using a Photon Machines Analyte 193H excimer laser (193 nm) connected to an Element XR HR-ICP-MS at the University of California, Davis. Counts were measured of ^{204}(Pb+Hg), ^{206}Pb, ^{207}Pb, ^{208}Pb, ^{232}Th, and ^{238}U. ^{207}Pb/^{235}U ratios were calculated by using a natural abundance ratio of ^{235}U/^{238}U equal to 1/137.88. Runs consisted of 20 seconds of background measurement, 60 seconds of analysis, followed by another 20 seconds of background. Every 10 unknown samples was bracketed by two measurements of the 91500 (1065 Ma; Wiedenbeck et al., 1995) reference standard, which was used for calibration, downhole fractionation correction, and machine drift correction during data reduction. GJ-1 (609 Ma; Jackson et al., 2004), Temora (417 Ma; Black et al.; 2003), and Plesovitch (337 Ma; Slama et al., 2008) were also measured as check standards between every 10 unknowns (Fig. A1.3).
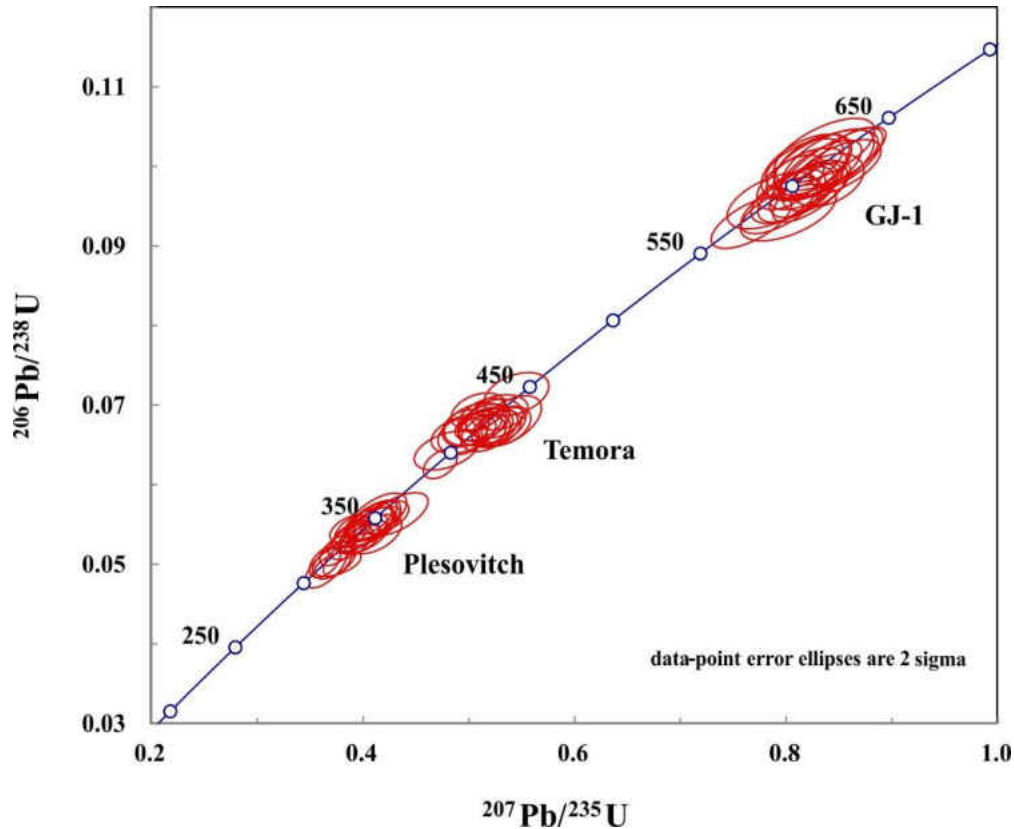
Fig. A1.3. Check standards from analysis of MDP6. Plesovitch=337 Ma, Temora=417 Ma, GJ-1=609 Ma.

Data reduction was performed offline using the *Iolite* add-on for *Igor Pro* (U-Pb Geochronology3 DRS with automatic splines) according to Hellstrom et al. (2008) and Paton et al. (2010; 2011). Analytical uncertainties were propagated through the analytical session (Paton, 2010). In the absence of [204]Hg measurements, Common Pb was corrected for using the Andersen et al. (2002) method via the *CommonPbCorr#3 Excel* macro. Error ellipses (2σ) were plotted on concordia diagrams using the *Isoplot 4.15* add-on for *Excel* (Ludwig, 2008).

Analysis were filtered for data quality purposes after Gehrels and Pecha (2014) and Spencer et al. (2016). Only data that met the following criteria was used (Figs. A1.4 and A1.5):

1.) Uncertainty (1σ) of $^{206}Pb*/^{238}U$ age is <10%

2.) Uncertainty (1σ) of $^{207}Pb*/^{206}Pb*$ age is <15%

3.) 204 intensity is <500 cps

4.) Analytical uncertainty (2σ) must overlap concordia on Wetherill diagram

*indicates common Pb corrected age
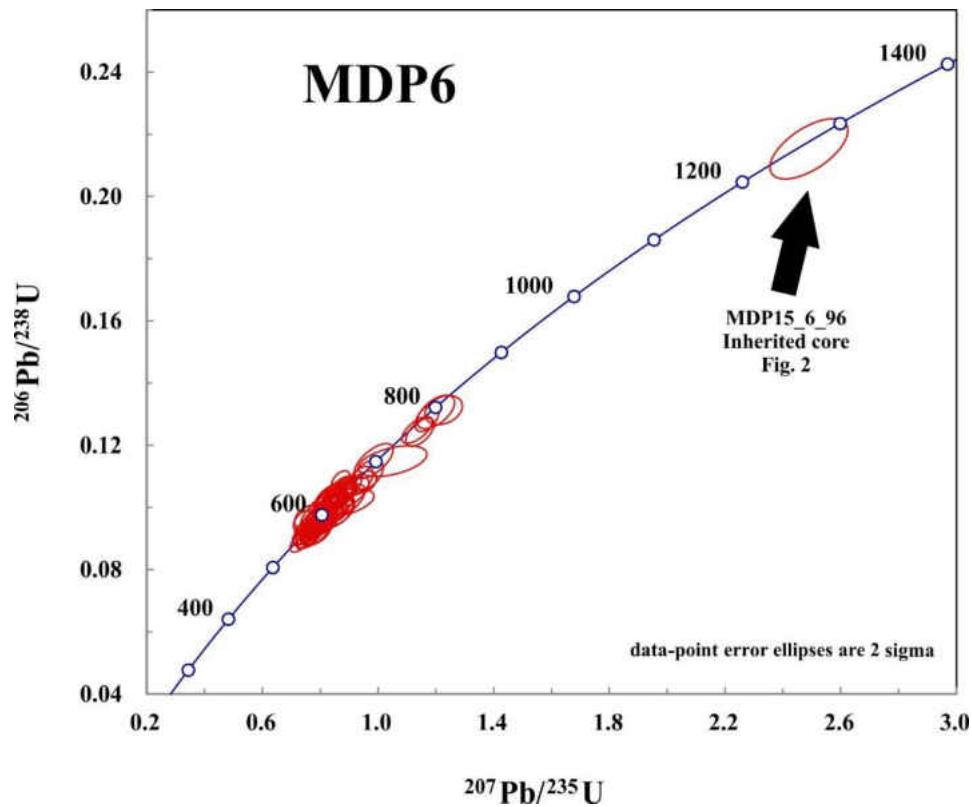
Fig. A1.4. Wetherill concordia diagram of analyses included for sample MDP6. Black arrow indicates spot MDP15_6_96 taken of inherited core.
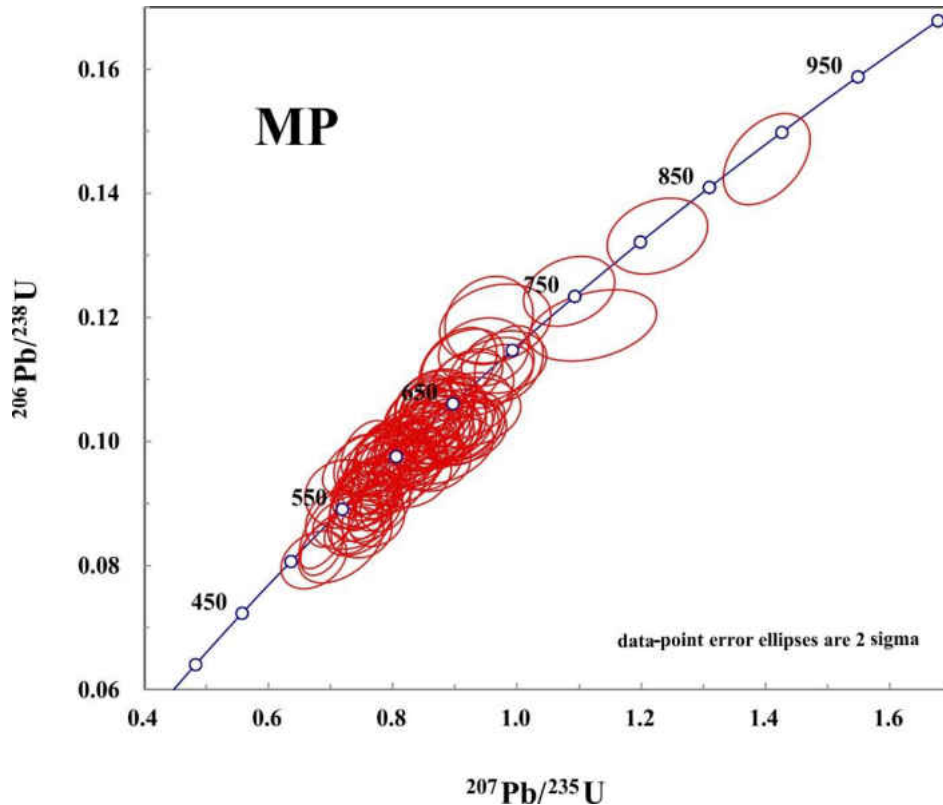
Fig. A1.5. Wetherill concordia diagram of analyses included for sample MP.

When ages are >1.5 Ga ^{207}Pb/^{206}Pb ages are recommended as best ages and for ages <1.5 Ga ^{206}Pb/^{238}U ages are recommended as best ages (Spencer et al., 2016). In this study, all concordant ages were less than 1.5 Ga so ^{206}Pb/^{238}U ages were used. Kernel density estimate plots were created using adaptive bandwidths on *DensityPlotter* (i.e. Vermeesch, 2012) and *provenance*, a free package for *R* (Vermeesch et al., 2016). A Kolmogorov-Smirnov (K-S) test using error in the Cumulative Distribution Function (CDF) was applied to evaluate the heterogeneity between the age distributions. If p is <0.05 it can be established with 95% confidence that two age distributions are not the same. However, this test cannot determine if the samples have the same provenance (e.g. Berry et al., 2001; DeGraaff-Surpless et al., 2003).

References

Berry, R.F., Jenner, G.A., Meffre, S., Tubrett, M.N., 2001. A North American provenance for Neoproterozoic to Cambrian sandstones in Tasmania? Earth and Planetary Science Letters 192, 207-222.

Black, L.P., Kamo, S.L., Allen, C.M., Aleinikoff, J.N., Davis, D.W., Korsch, R.J., Foudoulis, C., 2003. TEMORA 1: a new zircon standard for Phanerozoic U-Pb geochronology. Chemical Geology 200, 155-170.

DeGraaff-Surpless, K., Mahoney, J.B., Wooden, J.L., McWilliams, M.O., 2003. Lithofacies control in detrital zircon provenance studies: insights from the Cretaceous Methow Basin, southern Canadian Cordillera. Geological Society of America Bulletin 115, 899-915.

Gehrels, G., Pecha, M., 2014. Detrital zircon U-Pb geochronology and Hf isotope geochemistry of Paleozoic and Triassic passive margin strata of western North America. Geosphere 10, 49-65.

Hellstrom, J.C., Paton, C., Woodhead, J.D., Hergt, M., 2008. Iolite: Software for spatially resolved LA-(quad and MC) ICP-MS analysis. In: Sylvester, P. (Ed.), Laser ablation ICP-MS in the earth sciences: current practices and outstanding issues. Mineralogical Association of Canada, short course, pp. 343-348.

Jackson, S.E., Pearson, N.J., Griffin, W.L., Belousova, E.A., 2004. The application of laser ablation-inductively coupled plasma mass spectrometry to in situ U-Pb zircon geochronology. Chemical Geology 211, 47-69.

Ludwig, K.R., 2008. User's Manual for Isoplot. Berkeley Geochronology Center Special Publication 474, No. 4, Berkeley, CA.

Paton, C., Hellstrom, J., Paul, B., Woodhead, J., Hergt, J., 2011. Iolite: freeware for the visualization and processing of mass spectrometric data. Journal of Analytical Atomic Spectrometry 26, 2508-2518.

Paton, C., Woodhead, J.D., Hellstrom, J.C., Hergt, J.M., Greig, A., Maas, R., 2010. Improved laser ablation U-Pb zircon geochronology through robust downhole fractionation correction. Geochemistry, Geophysics, Geosystems 11, 1-36.

Sláma, J., Košler, J., Condon, D.J., Crowley, J.L., Gerdes, A., Hanchar, J.M., Horstwood, M.S.A., Morris, G.A., Nasdala, L., Norberg, N., Schaltegger, U., Schoene, B., Tubrett, M.N., Whitehouse, M.J., 2008. Plešovice zircon–A new natural reference material for U–Pb and Hf isotopic microanalysis. Chemical Geology 249, 1-35.

Spencer, C.J., Kirkland, C.L., Taylor, R.J.M, 2016. Strategies towards statistically robust interpretations of in situ U–Pb zircon geochronology. Geoscience Frontiers 7, 581-589.

Vermeesch, P., 2012. On the visualisation of detrital age distributions. Chemical Geology 312-313, 190-194.

Vermeesch, P., Resentini, A., Garzanti, E., 2016. An R package for statistical provenance analysis. Sedimentary Geology 336, 14-25.

Wiedenbeck, M., Allé, P., Corfu, F., Griffin, W.L., Meier, M., Oberli, F., Von Quadt, A., Roddick, J.C., Spiegel, W., 1995. Three natural zircon standards for U-Th-Pb, Lu-Hf, trace element and REE analyses. Geostandards and Geoanalytical Research 19, 1-23.

A2. Supplemental U-Pb detrital zircon methods (Chapter 4)

Detrital zircon samples were crushed and sieved to separate out the 63-250 μm fraction. A density separation was performed using lithium sodium tungstate (LST) and zircons were picked from the heavy fraction under a binocular scope. Careful attention was paid to not bias zircon picks based on size, morphology, or color. Zircons were mounted in an epoxy resin, polished, and imaged using back scattered electrons to check for fractures, inherited cores, rims, zonation, and inclusions that were avoided when possible. However, in many cases, these features were unavoidable due to their prevalence in the complex (recycled) zircons analyzed in this study.

U-Th-Pb data was collected via laser-ablation inductively coupled plasma mass spectrometry (LA-ICP-MS) using a Photon Machines Analyte 193H excimer laser (193 nm) connected to an Element XR HR-ICP-MS at the University of California, Davis. Counts were measured of ^{204}(Pb+Hg), ^{206}Pb, ^{207}Pb, ^{208}Pb, ^{232}Th, and ^{238}U. ^{207}Pb/^{235}U ratios were calculated by using a natural abundance ratio of ^{235}U/^{238}U equal to 1/137.88. Runs consisted of 20 seconds of background measurement, 30 seconds of analysis, followed by another 20 seconds of background. Every 10 unknown samples was bracketed by two measurements of the 91500 (1065 Ma; Wiedenbeck et al., 1995) reference standard, which was used for calibration, downhole fractionation correction, and machine drift correction during data reduction. GJ-1 (609 Ma; Jackson et al., 2004), Temora (417 Ma; Black et al.; 2003), and Plesovitch (337 Ma; Slama et al., 2008) were also measured as check standards between every 10 unknowns (Fig. 3).

Data reduction was performed offline using the *Iolite* add-on for *Igor Pro* (U-Pb Geochronology3 DRS with automatic splines) according to Hellstrom et al. (2008) and Paton et

al. (2010; 2011). Analytical uncertainties were propagated through the analytical session (Paton, 2010). In the absence of ^{204}Hg measurements, Common Pb was corrected for using the Andersen et al. (2002) method via the *CommonPbCorr#3 Excel* macro. Error ellipses (2σ) were plotted on concordia diagrams using the *Isoplot 4.15* add-on for *Excel* (Ludwig, 2008).

Analysis were filtered for data quality purposes after Gehrels and Pecha (2014) and Spencer et al. (2016). Only data that met the following criteria was used:

1.) Uncertainty (1σ) of ^{206}Pb*/^{238}U age is <10%

2.) Uncertainty (1σ) of ^{207}Pb*/^{206}Pb* age is <15%

3.) 204 intensity is <500 cps

4.) Discordance was < 25%

*indicates common Pb corrected age

When ages are >1.5 Ga ^{207}Pb/^{206}Pb ages are recommended as best ages and for ages <1.5 Ga ^{206}Pb/^{238}U ages are recommended as best ages (Spencer et al., 2016). In this study, all concordant ages were less than 1.5 Ga so ^{206}Pb/^{238}U ages were used. Kernel density estimate plots and multidimensional scaling plots (MDS) were created using adaptive bandwidths on *DensityPlotter* (i.e. Vermeesch, 2012) and *provenance*, a free package for *R* (Vermeesch et al., 2016). A Kolmogorov-Smirnov (K-S) test using error in the Cumulative Distribution Function (CDF) was applied to evaluate the heterogeneity between the age distributions. If p is <0.05 it can be established with 95% confidence that two age distributions are not the same. However, this test cannot determine if the samples have the same provenance (e.g. Berry et al., 2001; DeGraaff-

Surpless et al., 2003). Cross-correlation coefficients were calculated using the *DZ Stats* compiler

for *Matlab* (e.g. Saylor and Sundell, 2016).

References

Berry, R.F., Jenner, G.A., Meffre, S., Tubrett, M.N., 2001. A North American provenance for Neoproterozoic to Cambrian sandstones in Tasmania? Earth and Planetary Science Letters 192, 207-222.

Black, L.P., Kamo, S.L., Allen, C.M., Aleinikoff, J.N., Davis, D.W., Korsch, R.J., Foudoulis, C., 2003. TEMORA 1: a new zircon standard for Phanerozoic U-Pb geochronology. Chemical Geology 200, 155-170.

DeGraaff-Surpless, K., Mahoney, J.B., Wooden, J.L., McWilliams, M.O., 2003. Lithofacies control in detrital zircon provenance studies: insights from the Cretaceous Methow Basin, southern Canadian Cordillera. Geological Society of America Bulletin 115, 899-915.

Gehrels, G., Pecha, M., 2014. Detrital zircon U-Pb geochronology and Hf isotope geochemistry of Paleozoic and Triassic passive margin strata of western North America. Geosphere 10, 49-65.

Hellstrom, J.C., Paton, C., Woodhead, J.D., Hergt, M., 2008. Iolite: Software for spatially resolved LA-(quad and MC) ICP-MS analysis. In: Sylvester, P. (Ed.), Laser ablation ICP-MS in the earth sciences: current practices and outstanding issues. Mineralogical Association of Canada, short course, pp. 343-348.

Jackson, S.E., Pearson, N.J., Griffin, W.L., Belousova, E.A., 2004. The application of laser ablation-inductively coupled plasma mass spectrometry to in situ U-Pb zircon geochronology. Chemical Geology 211, 47-69.

Ludwig, K.R., 2008. User's Manual for Isoplot. Berkeley Geochronology Center Special Publication 474, No. 4, Berkeley, CA.

McHenry, L.J., 2009. Element mobility during zeolitic and argillic alteration of volcanic ash in a closed-basin lacustrine environment: case study Olduvai Gorge, Tanzania. Chemical Geology 265, 540-552.

Paton, C., Hellstrom, J., Paul, B., Woodhead, J., Hergt, J., 2011. Iolite: freeware for the visualization and processing of mass spectrometric data. Journal of Analytical Atomic Spectrometry 26, 2508-2518.

Paton, C., Woodhead, J.D., Hellstrom, J.C., Hergt, J.M., Greig, A., Maas, R., 2010. Improved laser ablation U-Pb zircon geochronology through robust downhole fractionation correction. Geochemistry, Geophysics, Geosystems 11, 1-36.

Saylor, J.E., Sundell, K.E., 2016. Qunatifying comparison of large detrital geochronology data sets. Geossphere 12, 203-220.

Sláma, J., Košler, J., Condon, D.J., Crowley, J.L., Gerdes, A., Hanchar, J.M., Horstwood, M.S.A., Morris, G.A., Nasdala, L., Norberg, N., Schaltegger, U., Schoene, B., Tubrett, M.N., Whitehouse, M.J., 2008. Plešovice zircon–A new natural reference material for U–Pb and Hf isotopic microanalysis. Chemical Geology 249, 1-35.

Spencer, C.J., Kirkland, C.L., Taylor, R.J.M, 2016. Strategies towards statistically robust interpretations of *in situ* U–Pb zircon geochronology. Geoscience Frontiers 7, 581-589.

Vermeesch, P., 2012. On the visualisation of detrital age distributions. Chemical Geology 312-313, 190-194.

Vermeesch, P., Resentini, A., Garzanti, E., 2016. An R package for statistical provenance analysis. Sedimentary Geology 336, 14-25.

Wiedenbeck, M., Allé, P., Corfu, F., Griffin, W.L., Meier, M., Oberli, F., Von Quadt, A.,

Roddick, J.C., Spiegel, W., 1995. Three natural zircon standards for U-Th-Pb, Lu-Hf, trace

element and REE analyses. Geostandards and Geoanalytical Research 19, 1-23.

Appendix B: Detrital zircon data

Table B1. Sample MDP6

| | Location: 30°18'27.78''S, 51°38'35.22''W | | | | | | | | | | | | | | | |
Spot	Pb^{207}/U^{235}	1σ	Pb^{206}/U^{238}	1σ	ρ	Pb^{207}/Pb^{206}	1σ	Pb^{206}/U^{238} age	1σ	Pb^{207}/Pb^{206} age	1σ	Pb^{207}/U^{235} age	1σ	%disc	Best Age	2σ
MDP15_6_1	0.843	0.015	0.098	0.0013	0.44	0.0615	0.00104	603	8	657	37	621	8	-8.22	603	16
MDP15_6_4	1.17	0.017	0.1288	0.0018	0.51	0.0655	0.00092	781	10	790	30	787	8	-1.14	781	20
MDP15_6_5	0.814	0.016	0.0958	0.00155	0.50	0.0602	0.0011	590	9	611	40	605	9	-3.44	590	18
MDP15_6_7	0.854	0.015	0.0988	0.00155	0.58	0.0628	0.00096	607	9	701	33	627	8	-13.41	607	18
MDP15_6_10	0.915	0.022	0.105	0.0019	0.62	0.0619	0.00118	644	11	671	42	660	12	-4.02	644	22
MDP15_6_12	1.145	0.02	0.1242	0.00185	0.58	0.0667	0.00101	755	11	828	32	775	9	-8.82	755	22
MDP15_6_16	0.776	0.019	0.0934	0.0018	0.58	0.0588	0.00121	576	11	560	46	583	11	2.86	576	22
MDP15_6_17	1.05039	0.0485	0.11489	0.00201	0.46	0.06631	0.00236	701	12	816	76	729	24	-14.09	701	24
MDP15_6_18	0.789	0.0185	0.0923	0.00175	0.57	0.06	0.00121	569	10	604	44	591	11	-5.79	569	20
MDP15_6_21	0.86	0.014	0.103	0.00135	0.33	0.0612	0.00105	632	8	646	38	630	8	-2.17	632	16
MDP15_6_23	0.952	0.0175	0.1081	0.00145	0.37	0.0636	0.00116	662	8	728	39	679	9	-9.07	662	16
MDP15_6_24	0.767	0.0135	0.0926	0.00135	0.58	0.0599	0.0009	571	8	600	33	578	8	-4.83	571	16
MDP15_6_27	0.806	0.0155	0.0959	0.0015	0.65	0.0606	0.00091	590	9	625	33	600	9	-5.60	590	18
MDP15_6_29	1.2	0.0265	0.1307	0.0022	0.57	0.0658	0.00123	792	13	800	40	801	12	-1.00	792	26
MDP15_6_30	0.794	0.015	0.0938	0.0015	0.63	0.0613	0.00094	578	9	650	33	593	8	-11.08	578	18

MDP15_6_31	0.865	0.02	0.1006	0.00175	0.61	0.0633	0.00118	618	10	718	40	633	11	-13.93	618	20
MDP15_6_34	0.78	0.0195	0.097	0.00195	0.54	0.0593	0.0013	597	11	578	49	585	11	3.29	597	22
MDP15_6_36	0.901	0.017	0.1063	0.0016	0.66	0.0602	0.00087	651	9	611	32	652	9	6.55	651	18
MDP15_6_38	0.903	0.021	0.1027	0.00195	0.57	0.062	0.00124	630	11	674	44	653	11	-6.53	630	22
MDP15_6_41	0.8	0.0145	0.0951	0.00135	0.43	0.0609	0.00107	586	8	636	38	597	8	-7.86	586	16
MDP15_6_44	0.781	0.0125	0.0942	0.0013	0.46	0.0596	0.00093	580	8	589	34	586	7	-1.53	580	16
MDP15_6_45	0.789	0.015	0.0946	0.00145	0.55	0.0609	0.00101	583	9	636	36	591	9	-8.33	583	18
MDP15_6_46	0.825	0.019	0.1027	0.00185	0.59	0.0593	0.00113	630	11	578	42	611	11	9.00	630	22
MDP15_6_48	0.842	0.0165	0.1029	0.00165	0.61	0.0587	0.00095	631	10	556	36	620	9	13.49	631	20
MDP15_6_49	0.78	0.0175	0.0932	0.00175	0.62	0.0602	0.0011	574	10	611	40	585	10	-6.06	574	20
MDP15_6_50	0.811	0.0165	0.0973	0.0017	0.61	0.0611	0.00104	599	10	643	37	603	9	-6.84	599	20
MDP15_6_51	0.85	0.017	0.1025	0.0017	0.55	0.0607	0.00107	629	10	629	39	625	9	0.00	629	20
MDP15_6_53	0.877	0.014	0.1037	0.0014	0.52	0.0616	0.00089	636	8	660	32	639	8	-3.64	636	16
MDP15_6_55	0.936	0.019	0.1085	0.0019	0.52	0.0621	0.00116	664	11	678	41	671	10	-2.06	664	22
MDP15_6_58	0.79	0.013	0.0981	0.00145	0.61	0.0589	0.00081	603	9	563	31	591	7	7.10	603	18
MDP15_6_59	0.832	0.02	0.1024	0.0016	0.45	0.0582	0.00128	628	9	537	49	615	11	16.95	628	18
MDP15_6_60	0.888	0.0145	0.106	0.0014	0.26	0.0607	0.0011	649	8	629	40	645	8	3.18	649	16
MDP15_6_61	0.845	0.0155	0.1019	0.0019	0.59	0.0597	0.00101	626	11	593	37	622	9	5.56	626	22
MDP15_6_62	0.831	0.019	0.0999	0.00185	0.57	0.0613	0.0012	614	11	650	43	614	11	-5.54	614	22
MDP15_6_63	0.964	0.022	0.1104	0.00205	0.50	0.0629	0.00132	675	12	705	45	685	11	-4.26	675	24
MDP15_6_64	0.876	0.019	0.1058	0.00175	0.53	0.0608	0.00116	648	10	632	42	639	10	2.53	648	20
MDP15_6_65	0.825	0.017	0.0995	0.00165	0.56	0.0613	0.00109	611	10	650	39	611	9	-6.00	611	20

MDP15_6_66	0.766	0.0195	0.0925	0.00175	0.67	0.0599	0.00113	570	10	600	42	577	11	-5.00	570	20
MDP15_6_67	0.779	0.0165	0.094	0.00165	0.61	0.0608	0.00106	579	10	632	38	585	9	-8.39	579	20
MDP15_6_68	0.863	0.0205	0.0985	0.00175	0.47	0.0638	0.00118	606	10	755	47	632	11	-19.74	606	20
MDP15_6_69	0.849	0.014	0.1044	0.00145	0.39	0.0644	0.00142	640	8	593	37	624	8	7.93	640	16
MDP15_6_72	0.862	0.014	0.1021	0.00145	0.55	0.0597	0.00101	627	8	632	30	631	8	-0.79	627	16
MDP15_6_73	0.761	0.02	0.0963	0.00175	0.22	0.06439	0.00525	593	10	549	60	575	12	8.01	593	20
MDP15_6_75	0.818	0.016	0.095	0.00135	0.43	0.0596	0.00093	585	8	735	38	607	9	-20.41	585	16
MDP15_6_76	0.843	0.0175	0.1024	0.00165	0.58	0.0608	0.00089	628	10	618	36	621	10	1.62	628	20
MDP15_6_77	0.871	0.0135	0.1082	0.00145	0.42	0.0585	0.00167	662	8	589	32	636	7	12.39	662	16
MDP15_6_82.	0.856	0.0165	0.0987	0.00135	0.38	0.0633	0.0012	607	8	718	41	628	9	-15.46	607	16
MDP15_6_85	0.753	0.0145	0.0896	0.0012	0.60	0.0597	0.00093	553	7	593	35	570	8	-6.75	553	14
MDP15_6_87	0.784	0.016	0.0963	0.0014	0.62	0.0589	0.00095	593	8	563	36	588	9	5.33	593	16
MDP15_6_89	0.74	0.0145	0.0909	0.00125	0.46	0.0585	0.00105	561	7	549	40	562	8	2.19	561	14
MDP15_6_90	0.763	0.0135	0.0917	0.00125	0.68	0.0597	0.00078	566	7	593	29	576	8	-4.55	566	14
MDP15_6_91	0.826	0.016	0.0994	0.00145	0.55	0.0607	0.00101	611	9	629	37	611	9	-2.86	611	18
MDP15_6_93	0.777	0.014	0.0945	0.00125	0.45	0.0601	0.00102	582	7	607	38	584	8	-4.12	582	14
MDP15_6_95	0.728	0.013	0.0887	0.00125	0.56	0.0599	0.00092	548	7	600	34	555	8	-8.67	548	14
MDP15_6_96	2.49	0.055	0.2153	0.00395	0.61	0.0847	0.00153	1257	21	1309	36	1269	16	-3.97	1257	42
MDP15_6_97	0.78568	0.03019	0.09423	0.00121	0.61	0.06047	0.00183	581	7	620	67	589	17	-6.29	581	14
MDP15_6_98	0.787	0.014	0.0971	0.0012	0.52	0.0592	0.00092	597	7	574	35	589	8	4.01	597	14
MDP15_6_100	0.737	0.0125	0.0907	0.0011	0.46	0.0592	0.00093	560	7	574	35	561	7	-2.44	560	14
MDP15_6_102	0.774	0.015	0.0915	0.00135	0.56	0.0616	0.00102	564	8	660	36	582	9	-14.55	564	16

MDP15_6_103	0.869	0.02	0.1039	0.0016	0.52	0.0608	0.00122	637	9	632	44	635	11	0.79	637	18
MDP15_6_106	0.787	0.014	0.093	0.0011	0.53	0.0617	0.00095	573	6	664	34	589	8	-13.70	573	12
MDP15_6_107	0.779	0.0175	0.0911	0.0012	0.43	0.0607	0.00125	562	7	629	46	585	10	-10.65	562	14
MDP15_6_108	0.822	0.015	0.0974	0.0013	0.47	0.0617	0.00104	599	8	664	37	609	8	-9.79	599	16
MDP15_6_109	0.808	0.014	0.0983	0.0011	0.28	0.06	0.00107	604	6	604	40	601	8	0.00	604	12
MDP15_6_112	1.135	0.0215	0.1249	0.00175	0.65	0.0653	0.00094	759	10	784	31	770	10	-3.19	759	20
MDP15_6_114	1.227	0.0265	0.1313	0.0019	0.29	0.0675	0.0015	795	11	853	48	813	12	-6.80	795	22
MDP15_6_118	0.756	0.013	0.0936	0.0011	0.60	0.0598	0.00083	577	6	596	31	572	8	-3.19	577	12
MDP15_6_119	0.86	0.022	0.1008	0.0015	0.10	0.0626	0.00177	619	9	695	62	630	12	-10.94	619	18
MDP15_6_121	0.745	0.0155	0.0958	0.0014	0.48	0.0577	0.00109	590	8	518	43	565	9	13.90	590	16
MDP15_6_126	0.748	0.0165	0.0899	0.0012	0.24	0.0603	0.00138	555	7	614	51	567	10	-9.61	555	14
MDP15_6_128	0.848	0.016	0.1016	0.0014	0.56	0.0604	0.00097	624	8	618	36	624	9	0.97	624	16
MDP15_6_129	0.77	0.014	0.0937	0.00125	0.65	0.0597	0.00083	577	7	593	31	580	8	-2.70	577	14
MDP15_6_131	0.831	0.0155	0.1029	0.00135	0.50	0.0585	0.00097	631	8	549	37	614	9	14.94	631	16
MDP15_6_133	0.791	0.014	0.0944	0.0012	0.50	0.0619	0.00098	582	7	671	32	592	8	-13.26	582	14
MDP15_6_134	0.778	0.0135	0.0937	0.00115	0.53	0.0601	0.0009	577	7	607	31	584	8	-4.94	577	14
MDP15_6_135	0.76	0.0135	0.0933	0.0011	0.53	0.0595	0.00091	575	6	585	31	574	8	-1.71	575	12
MDP15_6_137	0.812	0.0155	0.0977	0.0013	0.53	0.0604	0.00099	601	8	618	33	604	9	-2.75	601	16
MDP15_6_138	0.876	0.021	0.1045	0.0018	0.55	0.0596	0.00122	641	11	589	42	639	11	8.83	641	22
MDP15_6_139	0.883	0.0185	0.1041	0.0015	0.60	0.0603	0.00102	638	9	614	34	643	10	3.91	638	18
MDP_15_6_293	0.828	0.0215	0.0989	0.0017	0.53	0.0598	0.00134	608	10	596	49	613	12	2.01	608	20
MDP_15_6_294	0.793	0.0255	0.0953	0.0021	0.48	0.059	0.0017	587	12	567	64	593	14	3.53	587	24

Spot	Pb207/U235	1σ	Pb206/U238	1σ	ρ	Pb207/Pb206	1σ	Pb206/U238 age	1σ	Pb207/Pb206 age	1σ	Pb207/U235 age	1σ	%disc		
MDP_15_6_296	0.851	0.028	0.0986	0.0022	0.51	0.059	0.00171	606	13	567	64	625	15	6.88	606	26
MDP_15_6_297	0.985	0.0275	0.1149	0.0023	0.66	0.0612	0.0013	701	13	646	46	696	14	8.51	701	26
MDP_15_6_298	0.786	0.021	0.0915	0.00155	0.57	0.0611	0.00135	564	9	643	48	589	12	-12.29	564	18
MDP_15_6_301	0.87304	0.04634	0.10134	0.00189	0.49	0.06248	0.00246	622	11	691	85	637	25	-9.99	622	22

Notes:

Error= 1 sigma (except best age error= 2 sigma)

Rho (ρ)= error correlation

% discordance = (1-(206/238 age)/(207/206 age))*-100

red colored data (highlighted below) = data below quality standards

all data corrected for common Pb

Spot	Pb207/U235	1σ	Pb206/U238	1σ	ρ	Pb207/Pb206	1σ	Pb206/U238 age	1σ	Pb207/Pb206 age	1σ	Pb207/U235 age	1σ	%disc		
MDP15_6_2	3.9	0.6	0.175	0.0215	0.98	0.1259	0.00498	1040	118	2041	72	1614	124	-49.04		
MDP15_6_3	0.87864	0.06163	0.07106	0.0012	0.92	0.08968	0.0051	443	7	1419	112	640	33	-68.78		
MDP15_6_6	1.216	0.0215	0.1268	0.00195	0.51	0.0683	0.00113	770	11	878	35	808	10	-12.30		
MDP15_6_8	0.963	0.021	0.1056	0.0019	0.65	0.0653	0.00111	647	11	784	36	685	11	-17.47		
MDP15_6_9	0.83105	0.04041	0.08835	0.00179	0.61	0.06822	0.0024	546	11	875	74	614	22	-37.60		
MDP15_6_11	27.8	2.5	0.86	0.08	0.94	0.2396	0.00772	4000	277	3117	52	3412	88	28.33		
MDP15_6_13	0.893	0.0225	0.0924	0.0016	0.44	0.069	0.00162	570	9	899	49	648	12	-36.60		
MDP15_6_14	1.137	0.0275	0.0819	0.00175	0.40	0.099	0.00249	507	10	1605	48	771	13	-68.41		

MDP15_6_15	0.998	0.0285	0.1071	0.0021	0.38	0.0669	0.00186	656	12	835	59	703	14	-21.44		
MDP15_6_19	0.924	0.032	0.0886	0.00225	0.56	0.0776	0.00228	547	13	1137	60	664	17	-51.89		
MDP15_6_20	1.125	0.031	0.0886	0.0017	0.35	0.0896	0.00246	547	10	1417	53	765	15	-61.40		
MDP15_6_22	1.128	0.017	0.0869	0.0012	0.44	0.0936	0.00143	537	7	1500	29	767	8	-64.20		
MDP15_6_25	0.80854	0.03397	0.09057	0.00136	0.23	0.06475	0.00222	559	8	766	74	602	19	-27.02		
MDP15_6_26	0.941	0.027	0.0985	0.0018	0.52	0.0695	0.00171	606	11	914	52	673	14	-33.70		
MDP15_6_28	1.384	0.0315	0.1209	0.0019	0.29	0.0823	0.00194	736	11	1253	47	882	13	-41.26		
MDP15_6_32	44.2	2.9	1.23	0.085	0.94	0.2709	0.00634	5170	246	3311	37	3870	65	56.15		
MDP15_6_33	1.232	0.0415	0.0805	0.0018	0.95	0.1076	0.00153	499	11	1759	26	815	19	-71.63		
MDP15_6_35	0.86	0.0185	0.0822	0.00135	0.68	0.0736	0.00117	509	8	1031	33	630	10	-50.63		
MDP15_6_37	1.10078	0.03179	0.08382	0.00119	0.71	0.09524	0.00188	519	7	1533	38	754	15	-66.14		
MDP15_6_39	0.93	0.0205	0.1016	0.00175	0.65	0.0655	0.00112	624	10	790	36	668	11	-21.01		
MDP15_6_40	0.855	0.0125	0.0926	0.0013	0.13	0.0675	0.00128	571	8	853	40	627	7	-33.06		
MDP15_6_42	2.89	0.235	0.118	0.01	0.98	0.1894	0.0034	719	58	2737	30	1379	61	-73.73		
MDP15_6_43	0.98	0.0185	0.0865	0.00135	0.43	0.0835	0.00155	535	8	1281	37	694	9	-58.24		
MDP15_6_47	1.74815	0.3128	0.1017	0.00365	0.67	0.12467	0.01862	624	21	2024	291	1026	116	-69.17		
MDP15_6_52	1.6616	1.02283	0.17935	0.0257	0.97	0.06719	0.03328	1063	140	844	964	994	390	25.95		
MDP15_6_54	1.238	0.0205	0.0718	0.00105	0.02	0.1267	0.00277	447	6	2053	39	818	9	-78.23		
MDP15_6_56	0.868	0.015	0.0923	0.0013	0.53	0.068	0.00105	569	8	869	32	634	8	-34.52		
MDP15_6_57	1.53558	0.59948	0.09412	0.01055	0.98	0.11832	0.0337	580	62	1931	654	945	240	-69.96		
MDP15_6_70	0.86287	0.08073	0.09719	0.00189	0.58	0.0604	0.00106	598	11	755	168	632	44	-20.79		
MDP15_6_71	0.843	0.02	0.0629	0.0013	0.52	0.0967	0.00212	393	8	1561	40	621	11	-74.82		

MDP15_6_74	1.177	0.23584	0.10975	0.00281	0.93	0.07778	0.01373	671	16	1141	363	790	110	-41.19		
MDP15_6_78	13.68566	2.57188	0.43103	0.04992	0.99	0.23028	0.01915	2310	225	3054	135	2728	178	-24.36		
MDP15_6_79	0.91113	0.05162	0.06321	0.00176	0.92	0.10454	0.00383	395	11	1706	65	658	27	-76.85		
MDP15_6_80	0.872	0.018	0.0899	0.00145	0.56	0.0719	0.00128	555	9	983	35	637	10	-43.54		
MDP15_6_81	0.82	0.0145	0.0868	0.0012	0.47	0.0671	0.00111	537	7	841	36	608	8	-36.15		
MDP15_6_84	0.82	0.0165	0.0769	0.00125	0.56	0.0765	0.00133	478	7	1108	36	608	9	-56.86		
MDP15_6_86	7.5	0.8	0.296	0.0325	0.98	0.1944	0.00382	1671	162	2780	33	2173	96	-39.89		
MDP15_6_88	0.98639	0.06176	0.08239	0.00186	0.58	0.08683	0.00408	510	11	1357	94	697	32	-62.42		
MDP15_6_92	0.828	0.0185	0.0953	0.00165	0.66	0.0625	0.00106	587	10	691	37	613	10	-15.05		
MDP15_6_94	0.929	0.0175	0.0812	0.00115	0.60	0.0832	0.00128	503	7	1274	31	667	9	-60.52		
MDP15_6_99	0.876	0.0215	0.0918	0.00165	0.56	0.0688	0.00142	566	10	893	44	639	12	-36.62		
MDP15_6_101	0.84206	0.0397	0.07955	0.00184	0.01	0.07677	0.00306	493	11	1115	82	620	22	-55.78		
MDP15_6_104	0.85	0.0165	0.0959	0.00145	0.68	0.0649	0.00093	590	9	771	31	625	9	-23.48		
MDP15_6_105	0.87	0.018	0.0936	0.0013	0.51	0.0691	0.00125	577	8	902	38	636	10	-36.03		
MDP15_6_110	4.4	0.5	0.141	0.016	0.97	0.2198	0.00634	850	90	2979	48	1712	94	-71.47		
MDP15_6_111	0.952	0.017	0.1038	0.00115	0.51	0.0662	0.00103	637	7	813	33	679	9	-21.65		
MDP15_6_113	1.826	0.0325	0.1485	0.0024	0.60	0.0883	0.00134	893	13	1389	30	1055	12	-35.71		
MDP15_6_115	0.89	0.0155	0.097	0.00125	0.48	0.0677	0.00108	597	7	859	34	646	8	-30.50		
MDP15_6_116	0.849	0.0175	0.0951	0.00115	0.41	0.0661	0.00127	586	7	810	41	624	10	-27.65		
MDP15_6_117	0.894	0.02	0.089	0.0014	0.35	0.0716	0.0016	550	8	975	47	649	11	-43.59		
MDP15_6_120	0.85	0.018	0.0978	0.0014	0.45	0.0633	0.00123	602	8	718	43	625	10	-16.16		
MDP15_6_122	0.87477	0.03225	0.08919	0.00154	0.40	0.07113	0.00215	551	9	961	63	638	17	-42.66		

MDP15_6_123	4.44	0.095	0.2349	0.0044	0.80	0.1394	0.00181	1360	23	2220	23	1720	18	-38.74	
MDP15_6_124	0.91227	0.0806	0.10121	0.00172	0.44	0.06537	0.00505	622	10	786	171	658	43	-20.87	
MDP15_6_125	1.12	0.055	0.0981	0.00155	0.64	0.0815	0.00333	603	9	1234	83	763	26	-51.13	
MDP15_6_127	4.9	0.65	0.159	0.021	0.98	0.2321	0.00599	951	117	3067	43	1802	112	-68.99	
MDP15_6_130	1.46	0.125	0.0951	0.0032	0.97	0.114	0.00609	586	19	1864	100	914	52	-68.56	
MDP15_6_132	1.115	0.0185	0.0692	0.00115	0.44	0.1228	0.00217	431	7	1997	32	761	9	-78.42	
MDP15_6_136	0.749	0.0185	0.0946	0.0013	0.27	0.057	0.00141	583	8	492	52	568	11	18.50	
MDP15_6_140	1.209	0.0275	0.0759	0.00145	0.65	0.1148	0.00206	472	9	1877	30	805	13	-74.85	
MDP_15_6_290	1.00823	0.04628	0.07758	0.00164	0.39	0.09425	0.0033	482	10	1513	67	708	23	-68.14	
MDP_15_6_291	0.916	0.0205	0.094	0.0014	0.52	0.0723	0.0014	579	8	994	40	660	11	-41.75	
MDP_15_6_292	0.761	0.022	0.0874	0.0016	0.52	0.0628	0.00156	540	9	701	53	575	13	-22.97	
MDP_15_6_295	0.50494	0.02708	0.0374	0.00071	0.02	0.09793	0.00445	237	4	1585	86	415	18	-85.05	
MDP_15_6_299	0.869	0.0245	0.0887	0.00155	0.43	0.071	0.00185	548	9	957	54	635	13	-42.74	
MDP_15_6_300	0.77272	0.06837	0.06919	0.0019	0.47	0.081	0.00602	431	11	1221	151	581	39	-64.70	
MDP_15_6_302	0.828	0.024	0.0867	0.00175	0.15	0.0696	0.00228	536	10	917	68	613	13	-41.55	
MDP_15_6_303	0.74728	0.06608	0.09214	0.0018	0.60	0.05882	0.00437	568	11	560	167	567	38	1.43	
MDP_15_6_304	0.86412	0.03963	0.08577	0.00143	0.57	0.07307	0.00248	530	8	1016	70	632	22	-47.83	
MDP_15_6_305	0.788	0.0205	0.0928	0.0016	0.52	0.0603	0.00136	572	9	614	49	590	12	-6.84	

Table B2. Sample MDP6 check standards

Spot	Pb^{207}/U^{235}	1σ	Pb^{206}/U^{238}	1σ	ρ	Pb^{207}/Pb^{206}	1σ	Pb^{206}/U^{238} age	1σ	Pb^{207}/Pb^{206} age	1σ	Pb^{207}/U^{235} age	1σ
GJ1_1	0.857	0.014	0.1011	0.00155	0.66	0.06	0.00079	621	9	604	29	628	8
TEM-1	0.516	0.0095	0.0665	0.00095	0.36	0.0549	0.00103	415	6	408	43	422	6
Ples_1	0.376	0.0055	0.0504	0.0008	0.53	0.0536	0.0008	317	5	354	34	324	4
GJ1_2	0.824	0.015	0.0968	0.00155	0.72	0.0615	0.0008	596	9	657	28	610	8
TEM-2	0.526	0.0095	0.067	0.00095	0.41	0.0554	0.00099	418	6	428	40	429	6
Pleso-2	0.365	0.008	0.0496	0.00105	0.64	0.0531	0.00097	312	6	333	42	316	6
GJ1_3	0.816	0.013	0.097	0.0014	0.56	0.0609	0.00087	597	8	636	31	606	7
Tem-3	0.533	0.0085	0.0675	0.0009	0.47	0.056	0.00086	421	5	452	34	434	6
Pleso-3	0.409	0.0095	0.0554	0.00105	0.65	0.0527	0.00096	348	6	316	42	348	7
GJ1_1_2	0.827	0.0125	0.0976	0.0013	0.5	0.0612	0.00088	600	8	646	31	612	7
TEM-1_2	0.506	0.012	0.0676	0.0011	0.36	0.0532	0.00125	422	7	337	54	416	8
Ples_1_2	0.413	0.0115	0.056	0.0012	0.61	0.0529	0.0012	351	7	325	52	351	8
GJ1_2_2	0.839	0.014	0.0983	0.00135	0.37	0.0615	0.00106	604	8	657	38	619	8
TEM-2_2	0.494	0.0095	0.0661	0.00095	0.23	0.0538	0.00114	413	6	363	49	408	6
Pleso-2_2	0.37616	0.00896	0.05007	0.00065	0.54	0.05449	0.00102	315	4	391	43	324	7
GJ1_3_2	0.804	0.013	0.098	0.0014	0.56	0.0597	0.00086	603	8	593	32	599	7
Tem-3_2	0.524	0.011	0.0683	0.001	0.26	0.0567	0.00126	426	6	480	50	428	7
Pleso-3_2	0.364	0.006	0.0503	0.0008	0.5	0.0532	0.00086	316	5	337	37	315	4
GJ1_1_3	0.805	0.013	0.0963	0.00135	0.59	0.0608	0.00084	593	8	632	30	600	7
TEM-1_3	0.534	0.01	0.0674	0.001	0.38	0.0575	0.00109	420	6	511	43	434	7
Ples_1_3	0.412	0.01	0.0538	0.001	0.5	0.0539	0.00119	338	6	367	50	350	7
GJ1_2_3	0.832	0.016	0.0995	0.00155	0.68	0.0605	0.00087	611	9	622	31	615	9
TEM-2_3	0.518	0.0115	0.0673	0.001	0.31	0.0559	0.00126	420	6	448	51	424	8
Pleso-2_3	0.39	0.007	0.0542	0.0008	0.51	0.0531	0.00087	340	5	333	38	334	5

GJ1_3_3	0.825	0.015	0.1002	0.00155	0.54	0.0603	0.00098	616	9	614	36	611	8
Tem-3_3	0.516	0.0105	0.0672	0.00095	0.35	0.056	0.00114	419	6	452	46	422	7
Pleso-3_3	0.411	0.008	0.0551	0.00085	0.49	0.0541	0.00097	346	5	375	41	350	6
GJ1_1_4	0.795	0.0155	0.0951	0.00145	0.66	0.0609	0.00091	586	9	636	32	594	9
TEM-1_4	0.473	0.0065	0.0626	0.00075	0.45	0.0555	0.00075	391	5	432	31	393	4
Ples_1_4	0.376	0.007	0.0518	0.0008	0.58	0.0531	0.00084	326	5	333	36	324	5
GJ1_2_4	0.839	0.018	0.1004	0.00175	0.62	0.06	0.00105	617	10	604	36	619	10
TEM-2_4	0.495	0.0125	0.0664	0.001	0.38	0.0555	0.00133	414	6	432	51	408	8
Pleso-2_4	0.388	0.0085	0.0528	0.0009	0.53	0.0529	0.00103	332	6	325	42	333	6
GJ1_3_4	0.818	0.017	0.1	0.00165	0.54	0.0592	0.00108	614	10	574	38	607	9
Tem-3_4	0.497	0.009	0.0671	0.00095	0.24	0.0543	0.00109	419	6	384	43	410	6
Pleso-3_4	0.373	0.0085	0.0505	0.00095	0.55	0.054	0.00108	318	6	371	43	322	6
GJ1_1_5	0.838	0.02	0.1008	0.00155	0.59	0.0583	0.00112	619	9	541	43	618	11
TEM-1_5	0.545	0.0125	0.0714	0.0011	0.37	0.0547	0.00122	445	7	400	52	442	8
Ples_1_5	0.42	0.0095	0.0559	0.00085	0.51	0.0543	0.00107	351	5	384	46	356	7
GJ1_2_5	0.819	0.014	0.0975	0.0012	0.62	0.0597	0.00081	600	7	593	30	607	8
TEM-2_5	0.509	0.0105	0.0692	0.00095	0.33	0.0545	0.00113	431	6	392	48	418	7
Pleso-2_5	0.409	0.011	0.0548	0.001	0.64	0.0539	0.00111	344	6	367	48	348	8
GJ1_3_5	0.817	0.015	0.1003	0.0013	0.57	0.0594	0.00091	616	8	582	34	606	8
Tem-3_5	0.513	0.009	0.0668	0.0008	0.2	0.0564	0.00108	417	5	468	44	420	6
Pleso-3_5	0.408	0.008	0.0557	0.0008	0.56	0.0524	0.00087	349	5	303	39	347	6
GJ1_1_6	0.848	0.017	0.0998	0.00145	0.63	0.0602	0.00094	613	8	611	35	624	9
TEM-1_6	0.538	0.0125	0.068	0.0013	0.52	0.0587	0.00124	424	8	556	47	437	8
Ples_1_6	0.411	0.01	0.0556	0.001	0.59	0.0527	0.00105	349	6	316	47	350	7
GJ1_2_6	0.767	0.0155	0.093	0.00135	0.66	0.0592	0.0009	573	8	574	34	578	9
TEM-2_6	0.512	0.009	0.0688	0.00085	0.53	0.0541	0.00083	429	5	375	35	420	6
Pleso-2_6	0.401	0.009	0.0542	0.00085	0.63	0.0526	0.00092	340	5	312	41	342	7
GJ1_3_6	0.819	0.0155	0.099	0.00135	0.53	0.06	0.00099	609	8	604	37	607	9
Tem-3_6	0.529	0.011	0.0691	0.0009	0.25	0.056	0.00121	431	5	452	50	431	7
Pleso-3_6	0.4	0.0095	0.0535	0.00085	0.53	0.0527	0.00107	336	5	316	48	342	7

GJ1_1_7	0.806	0.016	0.0964	0.00145	0.63	0.0622	0.00097	593	9	681	34	600	9
Ples_1_7	0.397	0.008	0.0531	0.00075	0.56	0.0545	0.00092	334	5	392	39	339	6
GJ1_2_7	0.836	0.0195	0.102	0.00165	0.62	0.0598	0.0011	626	10	596	41	617	11
TEM-2_7	0.514	0.01	0.0678	0.00095	0.42	0.0549	0.00102	423	6	408	43	421	7
Pleso-2_7	0.432	0.012	0.0563	0.0011	0.6	0.0535	0.0012	353	7	350	52	365	9
GJ1_3_7	0.844	0.0205	0.1004	0.00185	0.8	0.0597	0.00086	617	11	593	30	621	11
Tem-3_7	0.509	0.009	0.0674	0.00075	0.41	0.0543	0.0009	420	5	384	35	418	6
Pleso-3_7	0.387	0.0075	0.0545	0.0007	0.52	0.0507	0.00085	342	4	227	37	332	5
Ples_1_2	0.393	0.009	0.0536	0.0008	0.50077	0.0523	0.00105	337	5	299	46	337	7
GJ1_2_2	0.787	0.0175	0.0957	0.00145	0.54224	0.0591	0.00112	589	9	571	42	589	10
Pleso-2_2	0.405	0.0095	0.0551	0.00085	0.55545	0.0531	0.00104	346	5	333	45	345	7
GJ1_3_2	0.802	0.0185	0.0942	0.00145	0.55751	0.0605	0.00117	580	9	622	42	598	10
Tem-3_2	0.479	0.0125	0.0643	0.001	0.43917	0.0548	0.0013	402	6	404	54	397	9
Pleso-3_2	0.407	0.0095	0.0551	0.00085	0.44948	0.053	0.00114	346	5	329	49	347	7
Notes:													
Error= 1 sigma													
Rho (ρ)= error correlation													
all data corrected for common Pb													
Pleso=Plesovitch (337 Ma)													
Tem=Temora (417 Ma)													
GJ-1= 609 Ma													

Table B3. Sample MP

Spot	Pb^{207}/U^{235}	1σ	Pb^{206}/U^{238}	1σ	ρ	Pb^{207}/Pb^{206}	1σ	Pb^{206}/U^{238} age	1σ	Pb^{207}/Pb^{206} age	1σ	Pb^{207}/U^{235} age	1σ	%disc	Best Age	2σ
	Location: 30°19'40.91''S, 51°35'47.15''W															
MP_001	0.852	0.0175	0.1048	0.00225	0.37	0.0591	0.00139	642	13	571	52	626	10	12.43	642	26
MP_002	0.859	0.021	0.103	0.0023	0.27	0.0619	0.00175	632	13	671	62	630	11	-5.81	632	26
MP_003	0.788	0.0185	0.0963	0.00215	0.33	0.0596	0.00159	593	13	589	59	590	11	0.68	593	26
MP_004	0.89	0.018	0.1054	0.0023	0.47	0.0616	0.00133	646	13	660	48	646	10	-2.12	646	26
MP_005	0.76	0.0175	0.0982	0.0021	0.35	0.0576	0.00146	604	12	515	57	574	10	17.28	604	24
MP_008	0.771	0.015	0.0975	0.00225	0.49	0.0598	0.0013	600	13	596	48	580	9	0.67	600	26
MP_009	0.854	0.018	0.1052	0.00225	0.33	0.06	0.00148	645	13	604	55	627	10	6.79	645	26
MP_010	0.917	0.026	0.102	0.0024	0.35	0.0666	0.00199	626	14	825	64	661	14	-24.12	626	28
MP_011	0.903	0.0195	0.1021	0.00215	0.37	0.0624	0.0015	627	13	688	53	653	10	-8.87	627	26
MP_012	0.775	0.0145	0.0901	0.00185	0.37	0.0609	0.00134	556	11	636	49	583	8	-12.58	556	22
MP_013	0.843	0.022	0.1033	0.00235	0.21	0.0589	0.00181	634	14	563	69	621	12	12.61	634	28
MP_014	0.751	0.0165	0.0904	0.00195	0.33	0.0589	0.00148	558	12	563	56	569	10	-0.89	558	24
MP_017	0.747	0.017	0.0962	0.002	0.26	0.0586	0.00155	592	12	552	59	566	10	7.25	592	24
MP_021	0.866	0.026	0.1019	0.00225	0.28	0.0624	0.002	626	13	688	70	633	14	-9.01	626	26
MP_022	0.905	0.0255	0.1121	0.00255	0.35	0.0605	0.00177	685	15	622	65	654	14	10.13	685	30
MP_023	0.7422	0.01684	0.08672	0.00197	0.39	0.06207	0.00147	536	12	677	52	564	10	-20.83	536	24
MP_026	0.774	0.017	0.0923	0.00195	0.17	0.0615	0.00171	569	12	657	61	582	10	-13.39	569	24
MP_027	0.773	0.016	0.0932	0.002	0.41	0.0606	0.00139	574	12	625	51	581	9	-8.16	574	24
MP_028	0.777	0.0155	0.0977	0.00205	0.31	0.0579	0.00139	601	12	526	54	584	9	14.26	601	24
MP_029	1.402	0.0285	0.1455	0.003	0.42	0.0706	0.00156	876	17	946	46	890	12	-7.40	876	34
MP_030	0.765	0.0145	0.0887	0.0018	0.49	0.0632	0.00125	548	11	715	43	577	8	-23.36	548	22
MP_031	0.774	0.0185	0.0876	0.00185	0.18	0.0617	0.00179	541	11	664	64	582	11	-18.52	541	22

MP_032	0.749	0.021	0.0893	0.0022	0.33	0.0593	0.00181	551	13	578	68	568	12	-4.67	551	26
MP_033	0.788	0.0165	0.0901	0.0019	0.26	0.0625	0.00159	556	11	691	56	590	9	-19.54	556	22
MP_034	0.889	0.0175	0.1043	0.00215	0.37	0.0608	0.00137	640	13	632	50	646	9	1.27	640	26
MP_036	0.955	0.029	0.1195	0.0029	0.16	0.0625	0.00224	728	17	691	70	681	15	5.35	728	34
MP_037	0.696	0.019	0.0861	0.0027	0.65	0.0626	0.00156	532	16	695	49	536	11	-23.45	532	32
MP_043	0.912	0.024	0.1022	0.00215	0.19	0.0636	0.00194	627	13	728	59	658	13	-13.87	627	26
MP_044	0.72	0.025	0.0915	0.00225	0.09	0.0587	0.00239	564	13	556	82	551	15	1.44	564	26
MP_047	0.756	0.0215	0.0912	0.00205	0.21	0.0593	0.00191	563	12	578	64	572	12	-2.60	563	24
MP_048	0.844	0.0175	0.0972	0.00205	0.28	0.062	0.00155	598	12	674	49	621	10	-11.28	598	24
MP_049	0.699	0.016	0.0875	0.00185	0.30	0.0577	0.00151	541	11	518	53	538	10	4.44	541	22
MP_050	0.767	0.02	0.0886	0.002	0.45	0.064	0.00165	547	12	742	50	578	11	-26.28	547	24
MP_051	0.86264	0.02066	0.09719	0.00204	0.23	0.06437	0.00166	598	12	754	50	632	11	-20.69	598	24
MP_052	0.832	0.0215	0.098	0.00215	0.06	0.0619	0.00204	603	13	671	65	615	12	-10.13	603	26
MP_053	0.74729	0.02106	0.08586	0.00189	0.06	0.06312	0.00208	531	11	712	64	567	12	-25.42	531	22
MP_054	0.879	0.025	0.1012	0.0023	0.22	0.0615	0.00198	621	13	657	63	640	14	-5.48	621	26
MP_056	0.832	0.0255	0.0949	0.00225	0.17	0.0624	0.0022	584	13	688	69	615	14	-15.12	584	26
MP_058	0.888	0.026	0.1044	0.00245	0.23	0.0643	0.00213	640	14	752	64	645	14	-14.89	640	28
MP_059	0.987	0.0225	0.1125	0.0025	0.26	0.0638	0.00174	687	14	735	53	697	11	-6.53	687	28
MP_060	0.686	0.014	0.0827	0.00175	0.40	0.0626	0.00142	512	10	695	44	530	8	-26.33	512	20
MP_061	0.867	0.024	0.0965	0.00185	0.16	0.0664	0.00206	594	11	819	63	634	13	-27.47	594	22
MP_062	0.797	0.022	0.0926	0.00175	0.25	0.0629	0.00184	571	10	705	60	595	12	-19.01	571	20
MP_064	0.861	0.023	0.1065	0.002	0.35	0.0582	0.00155	652	12	537	56	631	13	21.42	652	24
MP_066	0.839	0.028	0.0996	0.00205	0.20	0.0612	0.00218	612	12	646	74	619	15	-5.26	612	24
MP_068	0.837	0.022	0.1012	0.00185	0.51	0.0598	0.00138	621	11	596	48	617	12	4.19	621	22
MP_069	0.857	0.0235	0.0998	0.0019	0.38	0.0623	0.00167	613	11	684	55	628	13	-10.38	613	22
MP_071	0.823	0.0335	0.0985	0.0023	0.25	0.0615	0.00255	606	13	657	86	610	19	-7.76	606	26
MP_072	1.226	0.033	0.1331	0.0025	0.26	0.0647	0.00185	806	14	765	58	813	15	5.36	806	28
MP_074	0.79	0.022	0.098	0.00185	0.39	0.0579	0.00156	603	11	526	57	591	12	14.64	603	22
MP_076	0.827	0.0225	0.0985	0.00185	0.20	0.0597	0.00178	606	11	593	62	612	13	2.19	606	22
MP_077	1.084	0.03	0.1242	0.0023	0.27	0.0623	0.0018	755	13	684	60	746	15	10.38	755	26

MP_078	0.771	0.021	0.0954	0.0017	0.40	0.058	0.0015	587	10	530	55	580	12	10.75	587	20
MP_081	0.816	0.0245	0.0979	0.002	0.37	0.0594	0.00174	602	12	582	61	606	14	3.44	602	24
MP_082	0.946	0.0295	0.1144	0.00225	0.13	0.059	0.00205	698	13	567	73	676	15	23.10	698	26
MP_083	0.851	0.0235	0.1016	0.0019	0.26	0.0605	0.00175	624	11	622	60	625	13	0.32	624	22
MP_084	0.818	0.0215	0.0991	0.0018	0.41	0.0593	0.00149	609	11	578	53	607	12	5.36	609	22
MP_085	0.871	0.0235	0.1046	0.002	0.35	0.0599	0.00162	641	12	600	56	636	13	6.83	641	24
MP_086	0.744	0.022	0.0861	0.00185	0.38	0.0641	0.00188	532	11	745	60	565	13	-28.59	532	22
MP_087	0.822	0.0215	0.0967	0.00175	0.43	0.0612	0.0015	595	10	646	51	609	12	-7.89	595	20
MP_088	0.93	0.0265	0.1093	0.0021	0.10	0.061	0.002	669	12	639	68	668	14	4.69	669	24
MP_090	0.784	0.0225	0.094	0.00175	0.32	0.0607	0.00175	579	10	629	60	588	13	-7.95	579	20
MP_091	0.979	0.028	0.1128	0.00205	0.19	0.0632	0.00195	689	12	715	63	693	14	-3.64	689	24
MP_092	0.815	0.0225	0.0957	0.00185	0.45	0.0618	0.00158	589	11	667	53	605	13	-11.69	589	22
MP_093	0.917	0.0245	0.11	0.002	0.41	0.0604	0.00153	673	12	618	53	661	13	8.90	673	24
MP_095	0.852	0.0325	0.101	0.00215	0.18	0.0606	0.00244	620	13	625	85	626	18	-0.80	620	26
MP_097	0.866	0.0255	0.1065	0.0021	0.30	0.0592	0.00178	652	12	574	64	633	14	13.59	652	24
MP_098	0.861	0.026	0.1003	0.002	0.38	0.0614	0.0018	616	12	653	62	631	14	-5.67	616	24
MP_101	0.717	0.028	0.0833	0.0025	0.45	0.0619	0.00229	516	15	671	78	549	17	-23.10	516	30
MP_102	1.122	0.042	0.1187	0.00235	0.34	0.0695	0.0025	723	14	914	73	764	20	-20.90	723	28
MP_103	0.911	0.0295	0.1014	0.00205	0.23	0.0639	0.00217	623	12	738	71	658	16	-15.58	623	24
MP_104	0.959	0.028	0.1115	0.00215	0.33	0.0636	0.00186	681	12	728	61	683	15	-6.46	681	24
MP_105	0.96	0.027	0.1105	0.0021	0.37	0.0619	0.0017	676	12	671	58	683	14	0.75	676	24
MP_106	0.768	0.023	0.0955	0.0018	0.23	0.0587	0.00184	588	11	556	67	579	13	5.76	588	22
MP_109	0.913	0.0255	0.1017	0.00205	0.42	0.0654	0.00174	624	12	787	55	659	14	-20.71	624	24
MP_111	0.747	0.0245	0.0964	0.00205	0.51	0.058	0.00166	593	12	530	62	566	14	11.89	593	24
MP_112	0.965	0.0365	0.119	0.0026	0.22	0.0588	0.00231	725	15	560	84	686	19	29.46	725	30
MP_113	0.884	0.032	0.0985	0.0022	0.37	0.0659	0.0023	606	13	803	72	643	17	-24.53	606	26
MP_114	0.673	0.0215	0.0809	0.0019	0.30	0.0613	0.00205	501	11	650	71	523	13	-22.92	501	22
MP_115	0.815	0.0235	0.0941	0.0018	0.35	0.0626	0.00178	580	11	695	60	605	13	-16.55	580	22
MP_117	0.796	0.022	0.0993	0.0019	0.42	0.0591	0.00155	610	11	571	56	595	12	6.83	610	22
MP_119	0.913	0.027	0.1126	0.00225	0.33	0.0603	0.00179	688	13	614	63	659	14	12.05	688	26

Spot	Pb^{207}/U^{235}	1σ	Pb^{206}/U^{238}	1σ	ρ	Pb^{207}/Pb^{206}	1σ	Pb^{206}/U^{238} age	1σ	Pb^{207}/Pb^{206} age	1σ	Pb^{207}/U^{235} age	1σ	%disc		
MP_120	0.78	0.023	0.0962	0.002	0.47	0.0585	0.00157	592	12	549	58	585	13	7.83	592	24
MP_121	0.85	0.026	0.1048	0.0021	0.42	0.0601	0.00172	642	12	607	61	625	14	5.77	642	24
MP_122	0.757	0.023	0.0926	0.00195	0.44	0.0597	0.0017	571	12	593	61	572	13	-3.71	571	24
MP_124	0.894	0.0275	0.1014	0.00205	0.43	0.0629	0.0018	623	12	705	60	649	15	-11.63	623	24
MP_125	0.771	0.026	0.092	0.00195	0.30	0.0611	0.00208	567	12	643	72	580	15	-11.82	567	24
MP_126	0.764	0.0215	0.0925	0.00175	0.38	0.0585	0.0016	570	10	549	59	576	12	3.83	570	20
MP_128	0.85	0.025	0.1031	0.00215	0.48	0.0594	0.00158	633	13	582	57	625	14	8.76	633	26
MP_129	0.753	0.022	0.0904	0.00185	0.40	0.061	0.00172	558	11	639	60	570	13	-12.68	558	22
MP_130	0.773	0.0225	0.093	0.00195	0.26	0.0592	0.00184	573	12	574	66	581	13	-0.17	573	24
MP_132	0.918	0.036	0.1047	0.0023	0.17	0.0624	0.0026	642	13	688	87	661	19	-6.69	642	26
MP_133	0.784	0.0235	0.0976	0.00205	0.41	0.0586	0.00168	600	12	552	62	588	13	8.70	600	24
MP_134	0.859	0.0255	0.1032	0.00205	0.50	0.0622	0.00163	633	12	681	55	630	14	-7.05	633	24
MP_136	0.92	0.0295	0.1058	0.00215	0.27	0.0632	0.00208	648	13	715	69	662	16	-9.37	648	26
MP_137	0.882	0.025	0.1013	0.00205	0.33	0.0632	0.00183	622	12	715	60	642	13	-13.01	622	24
MP_139	0.892	0.0295	0.1032	0.0021	0.25	0.0635	0.00217	633	12	725	71	647	16	-12.69	633	24
MP_140	0.735	0.026	0.087	0.0018	0.28	0.0605	0.00216	538	11	622	76	559	15	-13.50	538	22
Notes:																
Error= 1 sigma (except best age error= 2 sigma)																
Rho (ρ)= error correlation																
% discordance = (1-(206/238 age)/(207/206 age))*-100																
red colored data (highlighted below) = data below quality standards																
all data corrected for common Pb																
Spot	Pb^{207}/U^{235}	1σ	Pb^{206}/U^{238}	1σ	ρ	Pb^{207}/Pb^{206}	1σ	Pb^{206}/U^{238} age	1σ	Pb^{207}/Pb^{206} age	1σ	Pb^{207}/U^{235} age	1σ	%disc		
MP_006	0.694	0.0165	0.0776	0.00185	0.36	0.0682	0.00184	482	11	875	57	535	10	-44.91		

MP_007	1.08226	0.02191	0.11392	0.00252	0.50	0.0689	0.00135	695	15	896	41	745	11	-22.43		
MP_015	0.696	0.0175	0.0797	0.00195	0.36	0.0629	0.00177	494	12	705	61	536	10	-29.93		
MP_016	0.68695	0.02323	0.07641	0.00227	0.41	0.06521	0.00212	475	14	781	70	531	14	-39.18		
MP_018	2.32635	0.04567	0.15963	0.0034	0.51	0.1057	0.00199	955	19	1726	35	1220	14	-44.67		
MP_019	0.655	0.0135	0.0776	0.0017	0.62	0.0647	0.00121	482	10	765	40	512	8	-36.99		
MP_020	0.70623	0.014	0.07016	0.00156	0.50	0.07301	0.00148	437	9	1014	42	543	8	-56.90		
MP_024	0.67587	0.01296	0.06268	0.00131	0.54	0.0782	0.00146	392	8	1152	38	524	8	-65.97		
MP_025	0.563	0.013	0.0442	0.00115	0.72	0.0944	0.00177	279	7	1516	36	453	8	-81.60		
MP_035	0.819	0.0185	0.0921	0.002	0.22	0.0641	0.00177	568	12	745	60	607	10	-23.76		
MP_038	0.822	0.0175	0.1085	0.0023	0.27	0.0589	0.00151	664	13	563	51	609	10	17.94		
MP_039	0.786	0.0165	0.1019	0.00215	0.50	0.0594	0.00125	626	13	582	42	589	9	7.56		
MP_040	1.246	0.0295	0.1462	0.00325	0.36	0.0658	0.00171	880	18	800	50	822	13	10.00		
MP_041	0.76722	0.0184	0.07403	0.00165	0.45	0.07516	0.0017	460	10	1073	42	578	11	-57.13		
MP_042	0.673	0.0215	0.0856	0.00225	0.06	0.0575	0.0023	529	13	511	81	523	13	3.52		
MP_045	0.648	0.0175	0.0654	0.00155	0.09	0.0732	0.00252	408	9	1019	64	507	11	-59.96		
MP_046	0.533	0.0105	0.0478	0.00115	0.53	0.0795	0.00172	301	7	1185	39	434	7	-74.60		
MP_055	0.46823	0.02021	0.02747	0.0015	0.99	0.12364	0.00166	175	9	2009	21	390	14	-91.29		
MP_057	0.70886	0.01643	0.07476	0.00174	0.40	0.06876	0.00163	465	10	892	45	544	10	-47.87		
MP_063	0.67	0.0225	0.0758	0.00165	0.16	0.0652	0.00241	471	10	781	75	521	14	-39.69		
MP_065	0.539	0.029	0.0637	0.00195	0.22	0.063	0.00351	398	12	708	116	438	19	-43.79		
MP_067	0.78	0.023	0.0844	0.0018	0.44	0.0661	0.00183	522	11	810	56	585	13	-35.56		
MP_070	0.66	0.0175	0.0685	0.0015	0.63	0.0704	0.00149	427	9	940	42	515	11	-54.57		
MP_073	0.51188	0.04641	0.06053	0.00153	0.49	0.06133	0.00456	379	9	651	159	420	31	-41.78		
MP_075	2.07	0.085	0.1511	0.00425	0.93	0.0948	0.00175	907	24	1524	33	1139	28	-40.49		
MP_079	4.24382	0.16717	0.26788	0.00494	0.59	0.1149	0.00334	1530	25	1878	51	1683	32	-18.53		
MP_080	0.79396	0.08807	0.08044	0.00186	0.32	0.07159	0.00725	499	11	974	209	593	50	-48.77		
MP_089	0.88	0.0285	0.1118	0.00215	0.24	0.0559	0.00187	683	12	448	72	641	15	52.46		
MP_094	0.57814	0.03231	0.0578	0.00119	0.58	0.07254	0.00314	362	7	1001	87	463	21	-63.84		
MP_096	0.664	0.019	0.07	0.0015	0.53	0.0686	0.00172	436	9	887	51	517	12	-50.85		

Spot	Pb^{207}/U^{235}	1σ	Pb^{206}/U^{238}	1σ	ρ	Pb^{207}/Pb^{206}	1σ	Pb^{206}/U^{238} age	1σ	Pb^{207}/Pb^{206} age	1σ	Pb^{207}/U^{235} age	1σ		
MP_099	0.83485	0.05482	0.09912	0.00217	0.45	0.06109	0.00313	609	13	642	108	616	30	-5.14	
MP_100	5.87	0.155	0.335	0.0065	0.63	0.1241	0.00256	1863	31	2016	36	1957	23	-7.59	
MP_107	0.782	0.0215	0.0838	0.0015	0.34	0.0675	0.00184	519	9	853	56	587	12	-39.16	
MP_108	0.761	0.0235	0.0857	0.00185	0.42	0.0629	0.00185	530	11	705	61	575	14	-24.82	
MP_110	0.38086	0.05069	0.04599	0.00138	0.62	0.06007	0.00657	290	8	606	233	328	37	-52.15	
MP_116	1.015	0.029	0.1107	0.00245	0.89	0.067	0.00091	677	14	838	28	711	15	-19.21	
MP_118	1.20997	0.0505	0.10894	0.0024	0.67	0.08055	0.0023	667	14	1211	55	805	23	-44.92	
MP_123	1.16	0.055	0.1126	0.0023	0.48	0.0739	0.00308	688	13	1039	83	782	26	-33.78	
MP_127	0.772	0.031	0.0739	0.00205	0.64	0.0753	0.00232	460	12	1077	61	581	18	-57.29	
MP_131	0.672	0.02	0.0754	0.0017	0.57	0.0661	0.00165	469	10	810	51	522	12	-42.10	
MP_135	0.735	0.0225	0.0769	0.00165	0.42	0.0693	0.00202	478	10	908	59	559	13	-47.36	
MP_138	0.67355	0.04911	0.07421	0.00153	0.60	0.06583	0.00403	461	9	801	126	523	30	-42.45	

Table B4. Sample MP check standards

Spot	Pb^{207}/U^{235}	1σ	Pb^{206}/U^{238}	1σ	ρ	Pb^{207}/Pb^{206}	1σ	Pb^{206}/U^{238} age	1σ	Pb^{207}/Pb^{206} age	1σ	Pb^{207}/U^{235} age	1σ
GJ1_1	0.815	0.0165	0.1019	0.0022	0.42198	0.0583	0.00131	626	13	541	51	605	9
TEM-1	0.508	0.012	0.0649	0.0016	0.40287	0.0564	0.00149	405	10	468	60	417	8
Ples_1	0.392	0.008	0.0541	0.00115	0.39661	0.0516	0.00118	340	7	268	54	336	6
GJ1_2	0.859	0.018	0.1034	0.0022	0.3784	0.0599	0.00141	634	13	600	52	630	10
TEM-2	0.512	0.018	0.0632	0.00165	0.19669	0.0587	0.00232	395	10	556	88	420	12
Pleso-2	0.378	0.0085	0.0505	0.0011	0.77548	0.0528	0.00078	318	7	320	35	326	6
GJ1_3	0.824	0.0175	0.0998	0.00215	0.32562	0.0614	0.00153	613	13	653	55	610	10
Tem-3	0.484	0.012	0.0659	0.00145	0.23045	0.0548	0.0016	411	9	404	67	401	8
Pleso-3	0.407	0.009	0.0545	0.0012	0.37135	0.0544	0.00135	342	7	388	57	347	6
GJ1_1_2	0.849	0.019	0.1025	0.00225	0.51672	0.0605	0.00132	629	13	622	48	624	10

TEM-1_2	0.502	0.0165	0.0635	0.0015	0.26026	0.0588	0.00207	397	9	560	79	413	11
Ples_1_2	0.392	0.009	0.0535	0.00115	0.34696	0.0546	0.00139	336	7	396	58	336	7
GJ1_2_2	0.762	0.0165	0.0907	0.00195	0.41227	0.0595	0.00139	560	12	585	52	575	10
TEM-2_2	0.459	0.0125	0.0605	0.0013	0.31196	0.0545	0.00158	379	8	392	67	384	9
Pleso-2_2	0.4	0.009	0.0538	0.0012	0.51841	0.0521	0.00115	338	7	290	52	342	7
GJ1_3_2	0.813	0.0165	0.1038	0.0022	0.33175	0.0592	0.00142	637	13	574	48	604	9
Tem-3_2	0.523	0.0145	0.0688	0.00155	0.29916	0.0562	0.00169	429	9	460	61	427	10
Pleso-3_2	0.399	0.0085	0.0566	0.0012	0.4085	0.0526	0.00122	355	7	312	48	341	6
GJ1_1_3	0.779	0.017	0.096	0.002	0.42211	0.0589	0.00135	591	12	563	46	585	10
TEM-1_3	0.46	0.0125	0.062	0.0013	0.27995	0.0542	0.00159	388	8	379	60	384	9
Ples_1_3	0.374	0.0085	0.0522	0.0012	0.85681	0.0511	0.00063	328	7	245	26	323	6
GJ1_2_3	0.763	0.016	0.0908	0.0019	0.48033	0.0596	0.00127	560	11	589	42	576	9
Pleso-2_3	0.361	0.0085	0.0491	0.00115	0.88474	0.0523	0.00059	309	7	299	24	313	6
GJ1_3_3	0.785	0.0165	0.0978	0.002	0.39663	0.0595	0.00136	602	12	585	45	588	9
Tem-3_3	0.49	0.017	0.0656	0.00165	0.36634	0.0548	0.0019	410	10	404	71	405	12
Pleso-3_3	0.382	0.009	0.0517	0.00125	0.9076	0.0545	0.00056	325	8	392	21	329	7
GJ1_1	0.753	0.02	0.0935	0.00165	0.28958	0.0596	0.00163	576	10	589	57	570	12
TEM-1	0.51703	0.02459	0.06627	0.00132	0.16572	0.05658	0.00246	414	8	475	93	423	16
Ples_1	0.351	0.0095	0.0505	0.001	0.67803	0.0512	0.00102	318	6	250	44	305	7
GJ1_2	0.809	0.022	0.0958	0.00175	0.42378	0.0595	0.00152	590	10	585	53	602	12
TEM-2	0.46314	0.02032	0.06217	0.00112	0.1517	0.05403	0.00222	389	7	372	90	386	14
Pleso-2	0.363	0.0105	0.0497	0.001	0.91033	0.0517	0.0007	313	6	272	30	314	8
GJ1_3	0.79	0.021	0.0946	0.00175	0.34911	0.0595	0.00158	583	10	585	56	591	12
Tem-3	0.455	0.0125	0.0603	0.0011	0.34136	0.0551	0.0015	377	7	416	59	381	9
Pleso-3	0.36	0.0095	0.0489	0.0009	0.35797	0.0538	0.00141	308	6	363	57	312	7
GJ1_1_2	0.824	0.0225	0.0984	0.0018	0.42684	0.0597	0.00153	605	11	593	53	610	13
TEM-1_2	0.512	0.0155	0.0658	0.0013	0.31232	0.0555	0.0017	411	8	432	66	420	10
Ples_1_2	0.375	0.0105	0.0521	0.00095	0.36951	0.0516	0.0014	327	6	268	60	323	8
GJ1_2_2	0.828	0.022	0.1019	0.00185	0.26981	0.0596	0.00166	626	11	589	58	613	12
TEM-2_2	0.496	0.0145	0.0651	0.00125	0.2242	0.0565	0.00176	407	8	472	67	409	10

Pleso-2_2	0.379	0.01	0.0513	0.00095	0.2499	0.0541	0.00153	322	6	375	61	326	7
GJ1_3_2	0.78	0.021	0.0942	0.0017	0.24052	0.0595	0.0017	580	10	585	61	585	12
Tem-3_2	0.46196	0.01929	0.05988	0.00118	0.2829	0.05595	0.00199	375	7	450	77	386	13
Pleso-3_2	0.355	0.0095	0.0483	0.0009	0.43421	0.0524	0.00132	304	6	303	56	308	7
GJ1_1_3	0.837	0.023	0.0987	0.0018	0.40588	0.0605	0.00158	607	11	622	55	617	13
TEM-1_3	0.519	0.0145	0.0679	0.0014	0.40647	0.0563	0.00153	423	8	464	59	424	10
Ples_1_3	0.419	0.013	0.0569	0.00135	0.95564	0.0534	0.00058	357	8	346	24	355	9
GJ1_2_3	0.876	0.0245	0.1051	0.002	0.51485	0.0613	0.0015	644	12	650	52	639	13
TEM-2_3	0.495	0.013	0.0661	0.0012	0.39341	0.0542	0.00138	413	7	379	56	408	9
Pleso-2_3	0.385	0.0105	0.0538	0.00115	0.96658	0.0525	0.00045	338	7	307	19	331	8
GJ1_3_3	0.851	0.024	0.1032	0.002	0.46071	0.0601	0.00155	633	12	607	55	625	13
Pleso-3_3	0.417	0.0115	0.0555	0.00105	0.40882	0.0541	0.00142	348	6	375	58	354	8
GJ1_1_4	0.797	0.022	0.0978	0.00185	0.39126	0.0587	0.00157	602	11	556	57	595	12
TEM-1_4	0.506	0.0165	0.0675	0.0013	0.033614	0.055	0.00205	421	8	412	82	416	11
Ples_1_4	0.384	0.011	0.0524	0.001	0.47274	0.0537	0.00139	329	6	358	57	330	8
GJ1_2_4	0.865	0.025	0.1028	0.002	0.66234	0.061	0.00132	631	12	639	46	633	14
TEM-2_4	0.566	0.019	0.0722	0.00145	0.11191	0.0575	0.00214	449	9	511	80	455	12
Pleso-2_4	0.401	0.0115	0.0547	0.0011	0.86409	0.0527	0.0008	343	7	316	34	342	8
GJ1_3_4	0.801	0.0225	0.0981	0.0019	0.42519	0.0603	0.0016	603	11	614	56	597	13
Tem-3_4	0.5	0.013	0.0661	0.0012	0.33913	0.056	0.00147	413	7	452	57	412	9
Pleso-3_4	0.397	0.011	0.0539	0.001	0.47891	0.0546	0.00136	338	6	396	55	339	8
Notes:													
Error= 1 sigma													
Rho (ρ)= error correlation													
all data corrected for common Pb													

Pleso=Plesovitch (337 Ma)														
Tem=Temora (417 Ma)														
GJ-1= 609 Ma														

Table B5. Sample AND-1

220

Spot	Location: 33° 9' 22''S, 57° 10' 29.37 W Pb^{207}/U^{235}	1σ	Pb^{206}/U^{238}	1σ	ρ	Pb^{207}/Pb^{206}	1σ	Pb^{206}/U^{238} age	1σ	Pb^{207}/Pb^{206} age	1σ	Pb^{207}/U^{235} age	1σ	%disc	Best Age	2σ
AND1_1.FIN2	1.417	0.0205	0.1444	0.0017	0.41226	0.07114	0.000335	869	9.5	959	10	896	8.5	-9.38478	869	19
AND1_2.FIN2	1.38	0.02	0.1359	0.0016	0.63709	0.07365	0.000285	821	9	1031	7.5	881	8.5	-20.3686	821	18
AND1_3.FIN2	0.647	0.0095	0.0779	0.0009	0.36906	0.05999	0.00029	483	5.5	601	10.5	507	6	-19.6339	483	11
AND1_4.FIN2	1.059	0.0155	0.1162	0.00135	0.41534	0.06584	0.00032	708	8	804	10	733	7.5	-11.9403	708	16
AND1_5.FIN2	2.721	0.0395	0.2198	0.00255	0.4412	0.0896	0.000385	1282	13.5	1417	8.5	1334	10.5	-9.52717	1282	27
AND1_6.FIN2	2.45	0.0365	0.207	0.00245	0.28979	0.0851	0.0005	1212	13	1322	12	1256	10.5	-8.32073	1212	26
AND1_7.FIN2	0.815	0.0125	0.0965	0.00115	0.20423	0.06105	0.00042	594	6.5	631	15	606	7	-5.86371	594	13
AND1_9.FIN2	1.8	0.026	0.1699	0.002	0.48495	0.07652	0.00035	1012	11	1107	9	1044	9.5	-8.58175	1012	22
AND1_10.FIN2	4.37	0.065	0.292	0.00345	0.4785	0.1088	0.0005	1652	17	1779	8.5	1706	12	-7.13884	1779	17
AND1_11.FIN2	1.679	0.0255	0.1633	0.00195	0.24087	0.07442	0.00046	975	10.5	1062	12.5	1000	9.5	-8.19209	975	21
AND1_12.FIN2	0.722	0.011	0.087	0.001	0.27021	0.06013	0.00037	538	6	605	13.5	551	6.5	-11.0744	538	12

AND1_13.FIN2	1.675	0.025	0.1638	0.0019	0.31643	0.07403	0.0004	978	10.5	1048	10.5	999	9.5	-6.67939	978	21
AND1_14.FIN2	1.788	0.027	0.1688	0.002	0.28244	0.07698	0.00048	1005	11	1121	12	1041	9.5	-10.3479	1005	22
AND1_15.FIN2	8.81	0.125	0.3754	0.00435	0.58821	0.1703	0.0006	2054	20	2560	6	2319	13	-19.7656	2560	12
AND1_16.FIN2	5.64	0.08	0.3339	0.00395	0.61963	0.1225	0.0005	1857	19	1994	7.5	1922	12.5	-6.87061	1994	15
AND1_17.FIN2	1.138	0.018	0.1205	0.00145	0.3289	0.0689	0.0005	734	8.5	891	15	772	8.5	-17.6207	734	17
AND1_18.FIN2	2.949	0.044	0.2342	0.00275	0.27275	0.0907	0.00055	1357	14.5	1438	11.5	1394	11.5	-5.63282	1357	29
AND1_19.FIN2	1.734	0.025	0.1628	0.0019	0.55029	0.07748	0.00031	972	10.5	1133	8	1021	9	-14.2101	972	21
AND1_20.FIN2	1.036	0.016	0.1036	0.00125	0.7838	0.07271	0.0003	635	7.5	1004	8.5	722	8	-36.753	635	15
AND1_21.FIN2	1.372	0.022	0.145	0.00175	0.25047	0.069	0.0006	874	9.5	886	17.5	876	9.5	-1.3544	874	19
AND1_23.FIN2	0.625	0.011	0.0799	0.00095	0.1847	0.0564	0.0006	496	6	450	23.5	491	7	10.22222	496	12
AND1_24.FIN2	0.701	0.011	0.0852	0.001	0.24074	0.05993	0.000435	527	6	595	15.5	539	6.5	-11.4286	527	12
AND1_25.FIN2	0.67	0.0105	0.085	0.001	0.21325	0.05711	0.00043	526	6	495	16.5	520	6.5	6.262626	526	12
AND1_26.FIN2	1.531	0.023	0.1557	0.00185	0.33954	0.0716	0.0004	933	10	975	11.5	943	9	-4.30769	933	20
AND1_27.FIN2	1.805	0.03	0.1645	0.002	0.29834	0.0794	0.0007	981	11	1180	17	1043	10.5	-16.8644	981	22
AND1_28.FIN2	0.833	0.0125	0.0991	0.00115	0.2491	0.06122	0.00032	609	6.5	645	11	615	6.5	-5.5814	609	13
AND1_29.FIN2	0.815	0.015	0.0937	0.0011	0.58153	0.0634	0.00065	577	6.5	690	19	600	7.5	-16.3768	577	13
AND1_30.FIN2	1.559	0.024	0.1543	0.0019	0.52871	0.07275	0.000425	925	10.5	1006	11.5	954	9.5	-8.05169	925	21
AND1_31.FIN2	6.7	0.095	0.3704	0.00435	0.57157	0.1316	0.0005	2031	20.5	2119	7	2073	13	-4.1529	2119	14
AND1_32.FIN2	0.648	0.0095	0.0805	0.00095	0.2594	0.05846	0.00035	499	5.5	545	13	507	6	-8.44037	499	11
AND1_33.FIN2	0.635	0.0095	0.0809	0.00095	0.32957	0.05698	0.00032	502	5.5	486	12	499	6	3.292181	502	11
AND1_34.FIN2	1.356	0.02	0.1399	0.0016	0.36823	0.07032	0.000345	844	9	931	10	870	8.5	-9.34479	844	18
AND1_35.FIN2	0.632	0.01	0.0803	0.00095	0.26645	0.05757	0.00049	498	6	505	19	497	6.5	-1.38614	498	12

Pleso_4.FIN2	0.398	0.006	0.0541	0.00065	0.35001	0.05317	0.000265	339.5	3.85	337	11.5	339.9	4.25	0.74184	339.5	7.7
AND1_36.FIN2	0.618	0.0105	0.0794	0.00095	0.14309	0.057	0.00055	492	5.5	466	21	487	6.5	5.579399	492	11
AND1_37.FIN2	1.773	0.0265	0.1729	0.00205	0.52917	0.07449	0.000375	1028	11.5	1052	10	1035	9.5	-2.28137	1028	23
AND1_38.FIN2	0.853	0.013	0.1031	0.0012	0.32719	0.06014	0.000385	632	7	610	13.5	626	7	3.606557	632	14
AND1_39.FIN2	0.889	0.0135	0.1025	0.0012	0.35797	0.06278	0.000365	629	7	701	12.5	647	7	-10.271	629	14
AND1_41.FIN2	0.683	0.01	0.0814	0.001	0.28504	0.0605	0.000365	504	6	623	13	529	6	-19.1011	504	12
AND1_42.FIN2	5.81	0.085	0.3468	0.00405	0.57468	0.12144	0.000455	1920	19.5	1978	6.5	1947	12.5	-2.93225	1978	13
AND1_43.FIN2	1.761	0.0265	0.1736	0.00205	0.32433	0.07312	0.000425	1031	11	1019	12	1030	9.5	1.177625	1031	22
AND1_44.FIN2	1.655	0.025	0.1653	0.00195	0.38776	0.07226	0.000445	986	11	987	13	991	9.5	-0.10132	986	22
AND1_45.FIN2	5.27	0.075	0.3325	0.0039	0.34295	0.1144	0.00055	1852	19	1872	8.5	1864	12.5	-1.06838	1872	17
AND1_46.FIN2	0.682	0.0105	0.0842	0.001	0.31403	0.05843	0.000375	521	6	544	14	528	6.5	-4.22794	521	12
AND1_47.FIN2	1.665	0.0295	0.17	0.0021	0.16162	0.0709	0.0008	1013	11.5	936	23	994	11	8.226496	1013	23
AND1_49.FIN2	1.863	0.0285	0.1839	0.0022	0.17522	0.0731	0.00055	1089	12	1016	14.5	1068	10.5	7.185039	1089	24
AND1_50.FIN2	1.77	0.026	0.1715	0.00205	0.47874	0.07452	0.00035	1020	11	1053	9.5	1034	9.5	-3.1339	1020	22
AND1_51.FIN2	1.732	0.0445	0.1697	0.0025	0.34343	0.0734	0.0012	1012	13.5	1023	34	1021	16.5	-1.07527	1012	27
AND1_52.FIN2	1.689	0.0435	0.1687	0.0025	0.29688	0.0719	0.0012	1006	13.5	987	33.5	1004	16	1.925025	1006	27
AND1_53.FIN2	0.653	0.0175	0.084	0.00125	0.1332	0.0565	0.00105	520	7.5	444	40	509	10.5	17.11712	520	15
AND1_54.FIN2	2.15	0.055	0.196	0.00285	0.57277	0.0789	0.0013	1154	15.5	1168	32	1166	17.5	-1.19863	1154	31
AND1_55.FIN2	1.894	0.048	0.1798	0.00265	0.45307	0.0755	0.00125	1066	14.5	1082	32.5	1079	17	-1.47874	1066	29
AND1_56.FIN2	0.435	0.0115	0.0571	0.00085	0.16603	0.055	0.00105	358	5	399	42	366	8.5	-10.2757	358	10
AND1_57.FIN2	1.95	0.05	0.1853	0.00275	0.37106	0.0762	0.0013	1096	15	1093	33.5	1097	17	0.274474	1096	30
AND1_58.FIN2	0.667	0.017	0.085	0.00125	0.30047	0.0571	0.00095	526	7.5	497	38	519	10.5	5.83501	526	15

AND1_59.FIN2	1.218	0.031	0.1255	0.0019	0.71675	0.0712	0.0012	762	11	962	33.5	809	14.5	-20.79	762	22
AND1_60.FIN2	1.906	0.0485	0.1825	0.0027	0.43432	0.0762	0.00125	1080	14.5	1098	33	1083	17	-1.63934	1080	29
AND1_61.FIN2	2.62	0.065	0.2292	0.00335	0.386	0.0839	0.0014	1330	17.5	1286	32.5	1307	18.5	3.421462	1330	35
AND1_62.FIN2	1.778	0.045	0.1746	0.0026	0.50169	0.075	0.00125	1038	14	1067	33.5	1037	16.5	-2.7179	1038	28
AND1_63.FIN2	1.609	0.041	0.1608	0.00235	0.36487	0.0735	0.0012	962	13	1027	33.5	974	15.5	-6.32911	962	26
AND1_64.FIN2	0.662	0.0175	0.0824	0.00125	0.50542	0.06	0.00105	510	7.5	601	38.5	516	10.5	-15.1414	510	15
AND1_65.FIN2	2.55	0.07	0.2014	0.0032	0.8463	0.0934	0.00155	1182	17	1495	31	1284	19.5	-20.9365	1182	34
AND1_66.FIN2	0.679	0.0175	0.0807	0.0012	0.58171	0.0615	0.001	500	7	652	35.5	526	10.5	-23.3129	500	14
AND1_67.FIN2	4.43	0.115	0.277	0.00425	0.72122	0.1176	0.00195	1575	21.5	1919	29.5	1719	22	-17.926	1919	59
AND1_68.FIN2	1.734	0.044	0.167	0.00245	0.43911	0.0755	0.00125	995	13.5	1078	33	1021	16.5	-7.69944	995	27
AND1_69.FIN2	1.68	0.043	0.1654	0.00245	0.36501	0.074	0.00125	986	13.5	1041	33	1001	16	-5.28338	986	27
AND1_71.FIN2	1.706	0.044	0.1688	0.0025	0.30215	0.0729	0.00125	1005	14	1004	34.5	1010	16.5	0.099602	1005	28
AND1_72.FIN2	2.26	0.06	0.1987	0.00295	0.36259	0.0823	0.0014	1168	16	1254	33	1201	18	-6.85805	1168	32
AND1_73.FIN2	1.766	0.045	0.1729	0.00255	0.3051	0.0743	0.00125	1028	14	1053	33.5	1033	16.5	-2.37417	1028	28
AND1_74.FIN2	1.243	0.0325	0.1301	0.00195	0.49424	0.0694	0.0012	789	11.5	910	34.5	820	14.5	-13.2967	789	23
AND1_75.FIN2	1.325	0.0345	0.1391	0.00215	0.60978	0.0696	0.0012	839	12.5	923	35	855	15.5	-9.10076	839	25
AND1_76.FIN2	1.669	0.0425	0.1673	0.0025	0.49113	0.0725	0.0012	997	13.5	998	33.5	997	16	-0.1002	997	27
AND1_77.FIN2	0.68	0.0185	0.0856	0.0013	0.08508	0.0573	0.0011	529	7.5	489	41	527	11	8.179959	529	15
AND1_78.FIN2	1.526	0.039	0.1498	0.0022	0.49843	0.0739	0.0012	900	12.5	1035	33.5	940	15.5	-13.0435	900	25
AND1_79.FIN2	0.707	0.0185	0.0871	0.0013	0.27663	0.0583	0.001	538	7.5	542	37.5	543	11	-0.73801	538	15
AND1_80.FIN2	1.98	0.05	0.1811	0.0027	0.30441	0.0796	0.0014	1073	14.5	1185	35	1106	17.5	-9.45148	1073	29
AND1_81.FIN2	1.81	0.0465	0.1754	0.0026	0.34867	0.0741	0.00125	1042	14	1037	33.5	1050	16.5	0.48216	1042	28

AND1_8 2.FIN2	0.725	0.0185	0.0884	0.0013	0.33594	0.0592	0.001	546	8	573	36.5	553	11	-4.71204	546	16
AND1_8 3.FIN2	1.267	0.0345	0.1366	0.0021	0.16217	0.0663	0.0013	825	12	826	41.5	830	15.5	-0.12107	825	24
AND1_8 5.FIN2	0.919	0.024	0.1011	0.0016	0.70362	0.0656	0.0011	621	9.5	789	36	662	12.5	-21.2928	621	19
AND1_8 6.FIN2	1.771	0.0455	0.1724	0.00255	0.24964	0.0738	0.00125	1025	14	1033	34	1034	17	-0.77444	1025	28
AND1_8 7.FIN2	0.685	0.018	0.086	0.0013	0.24656	0.0573	0.001	532	7.5	503	37.5	529	10.5	5.765408	532	15
AND1_8 8.FIN2	0.932	0.024	0.1082	0.0016	0.31925	0.0617	0.00105	662	9	669	36	668	12.5	-1.04634	662	18
AND1_8 9.FIN2	0.866	0.0225	0.1026	0.00155	0.26977	0.0609	0.00105	630	9	632	36.5	633	12.5	-0.31646	630	18
AND1_9 0.FIN2	0.932	0.025	0.1027	0.00155	0.20509	0.0658	0.0012	630	9	794	38	668	13	-20.6549	630	18
AND1_9 1.FIN2	1.085	0.028	0.1217	0.0018	0.29321	0.0638	0.0011	740	10.5	736	36.5	745	13.5	0.543478	740	21
AND1_9 2.FIN2	1.666	0.0425	0.1647	0.00245	0.36798	0.0731	0.0012	983	13.5	1012	34	997	16.5	-2.86561	983	27
AND1_9 3.FIN2	0.693	0.0175	0.0853	0.00125	0.38556	0.0586	0.001	528	7.5	549	36	535	10.5	-3.82514	528	15
AND1_9 4.FIN2	1.176	0.031	0.125	0.00185	0.24827	0.0673	0.0012	760	11	843	37.5	788	14.5	-9.84579	760	22
AND1_9 5.FIN2	7.68	0.195	0.4	0.006	0.56479	0.1378	0.00225	2170	27	2198	28	2195	23	-1.27389	2198	56
AND1_9 6.FIN2	5.3	0.135	0.3272	0.0048	0.53687	0.1159	0.0019	1825	23.5	1894	29	1869	21.5	-3.64308	1894	58
AND1_9 7.FIN2	1.336	0.0345	0.1402	0.0021	0.38668	0.0683	0.00115	846	12	869	36	860	15	-2.64672	846	24
AND1_9 8.FIN2	1.763	0.046	0.1677	0.0025	0.36593	0.0756	0.0013	1000	14	1080	34.5	1034	17	-7.40741	1000	28
AND1_9 9.FIN2	0.657	0.017	0.0815	0.0012	0.28073	0.0576	0.001	505	7	515	36.5	513	10.5	-1.94175	505	14
AND1_1 00.FIN2	0.813	0.021	0.0976	0.00145	0.33058	0.0596	0.001	600	8.5	578	36.5	603	11.5	3.806228	600	17
AND1_1 02.FIN2	5.31	0.135	0.336	0.005	0.60484	0.1142	0.00185	1870	24	1866	29	1869	21.5	0.214362	1866	58
AND1_1 03.FIN2	1.227	0.031	0.1312	0.00195	0.57683	0.0685	0.00115	794	11	887	34	813	14	-10.4848	794	22
AND1_1 04.FIN2	1.275	0.035	0.1326	0.0022	0.90939	0.0698	0.0012	804	12.5	918	35	832	16	-12.4183	804	25
AND1_1 05.FIN2	2.56	0.065	0.2185	0.00325	0.44745	0.0858	0.00145	1274	17	1334	32.5	1290	19	-4.49775	1274	34

AND1_1 06.FIN2	1.745	0.0445	0.1718	0.00255	0.42933	0.0744	0.00125	1022	14	1050	33.5	1025	16.5	-2.66667	1022	28
AND1_1 07.FIN2	4.73	0.12	0.3172	0.00465	0.62392	0.1093	0.0018	1776	22.5	1789	29	1772	21.5	-0.72666	1789	58
AND1_1 08.FIN2	1.385	0.036	0.1451	0.00215	0.40124	0.07	0.0012	874	12.5	925	34.5	883	15	-5.51351	874	25
AND1_1 09.FIN2	1.703	0.0435	0.1686	0.0025	0.5019	0.0744	0.0012	1004	13.5	1052	33	1010	16	-4.56274	1004	27
AND1_1 10.FIN2	6.74	0.17	0.377	0.0055	0.56389	0.1304	0.00215	2063	26	2103	28.5	2078	22.5	-1.90204	2103	57
AND1_1 11.FIN2	2.52	0.065	0.2165	0.0032	0.43278	0.0843	0.0014	1263	17	1299	32.5	1279	18.5	-2.77136	1263	34
AND1_1 12.FIN2	0.9	0.0235	0.1047	0.0016	0.5835	0.0623	0.0011	642	9.5	679	37	652	12.5	-5.44919	642	19
AND1_1 13.FIN2	13.65	0.345	0.519	0.0075	0.62963	0.1896	0.0031	2696	32.5	2737	27	2727	23.5	-1.49799	2737	54
AND1_1 14.FIN2	1.742	0.0455	0.1709	0.00255	0.22092	0.0738	0.0013	1017	14	1032	36	1023	17	-1.45349	1017	28
AND1_1 15.FIN2	3.74	0.095	0.2481	0.0038	0.79085	0.1087	0.0018	1429	19.5	1779	30.5	1579	21	-19.674	1429	39
AND1_1 16.FIN2	1.925	0.049	0.1824	0.0027	0.43849	0.0762	0.00125	1080	14.5	1096	33	1090	17	-1.45985	1080	29
AND1_1 18.FIN2	1.96	0.05	0.1862	0.0028	0.27094	0.0759	0.0013	1100	15	1087	34.5	1101	17.5	1.195952	1100	30
AND1_1 19.FIN2	0.781	0.021	0.0895	0.00135	0.31403	0.0632	0.00115	552	8	698	37.5	586	12	-20.9169	552	16
AND1_1 20.FIN2	1.907	0.049	0.1818	0.00275	0.53888	0.0763	0.0013	1077	15	1103	34	1084	17.5	-2.35721	1077	30
AND1_1 21.FIN2	0.697	0.018	0.089	0.0013	0.24575	0.0571	0.001	549	8	486	38.5	537	11	12.96296	549	16
AND1_1 22.FIN2	1.762	0.045	0.1751	0.0026	0.34447	0.0742	0.00125	1040	14.5	1045	34	1031	16.5	-0.47847	1040	29
AND1_1 23.FIN2	1.672	0.0425	0.166	0.00245	0.47317	0.074	0.0012	990	13.5	1042	32.5	998	16.5	-4.9904	990	27
AND1_1 24.FIN2	6.25	0.16	0.365	0.0055	0.58748	0.1259	0.00205	2005	25.5	2042	28	2012	22	-1.81195	2042	56
AND1_1 25.FIN2	0.809	0.0215	0.0953	0.00145	0.30301	0.0626	0.00115	587	8.5	661	37.5	600	12	-11.1952	587	17
AND1_1 26.FIN2	0.87	0.022	0.1017	0.0015	0.3957	0.0621	0.001	624	8.5	677	35.5	636	12	-7.82866	624	17
AND1_1 27.FIN2	2.04	0.05	0.1896	0.0028	0.28932	0.0782	0.0013	1119	15	1152	33	1130	17.5	-2.86458	1119	30
AND1_1 28.FIN2	1.634	0.0425	0.1629	0.00245	0.53898	0.0729	0.0012	972	13.5	1010	33	983	16	-3.76238	972	27

AND1_1 29.FIN2	1.924	0.049	0.1827	0.0027	0.48872	0.0759	0.00125	1082	14.5	1095	34	1089	17	-1.18721	1082	29
AND1_1 30.FIN2	1.98	0.05	0.1862	0.00275	0.40788	0.0767	0.00125	1101	15	1108	33.5	1109	17	-0.63177	1101	30
AND1_1 31.FIN2	2	0.05	0.1859	0.00275	0.47817	0.0777	0.0013	1099	15	1136	33.5	1118	17.5	-3.25704	1099	30
AND1_1 32.FIN2	5.88	0.15	0.349	0.005	0.5294	0.1215	0.002	1928	24.5	1979	29.5	1958	22	-2.57706	1979	59
AND1_1 33.FIN2	2.02	0.05	0.1873	0.0028	0.35629	0.0778	0.0013	1107	15	1142	34	1121	17.5	-3.0648	1107	30
AND1_1 34.FIN2	0.954	0.0245	0.1114	0.00165	0.2477	0.062	0.00105	681	9.5	669	36.5	680	13	1.793722	681	19
AND1_1 35.FIN2	1.776	0.046	0.1739	0.00265	0.53768	0.0743	0.00125	1033	14.5	1048	34.5	1038	16.5	-1.4313	1033	29
AND1_1 36.FIN2	0.779	0.02	0.0919	0.00135	0.38123	0.0618	0.00105	567	8	666	34.5	585	11.5	-14.8649	567	16
AND1_1 37.FIN2	1.917	0.0495	0.1833	0.00275	0.2908	0.0759	0.0013	1084	15	1089	34.5	1089	17	-0.45914	1084	30
AND1_1 40.FIN2	0.876	0.0225	0.1039	0.00155	0.42086	0.0613	0.001	637	9	659	36	638	12	-3.33839	637	18
AND1_1 41.FIN2	0.781	0.02	0.0945	0.0014	0.46633	0.06	0.001	582	8	603	36	586	11.5	-3.48259	582	16
AND1_1 42.FIN2	0.964	0.0245	0.1105	0.00165	0.5352	0.0634	0.00105	675	9.5	717	35	685	12.5	-5.85774	675	19
AND1_1 44.FIN2	1.91	0.048	0.1817	0.00265	0.55984	0.076	0.00125	1076	14.5	1094	32.5	1085	17	-1.64534	1076	29
AND1_1 45.FIN2	1.556	0.04	0.1503	0.0023	0.64292	0.0746	0.00125	903	13	1065	33	953	16	-15.2113	903	26
AND1_1 46.FIN2	8.02	0.205	0.413	0.006	0.53969	0.1404	0.0023	2230	28.5	2230	28.5	2233	23	0	2230	57
AND1_1 47.FIN2	1.795	0.046	0.1731	0.00255	0.57844	0.0744	0.0012	1029	14	1050	33.5	1044	17	-2	1029	28
AND1_1 48.FIN2	1.641	0.046	0.1653	0.00265	0.3529	0.0714	0.00145	987	14.5	966	41.5	979	17.5	2.173913	987	29
AND1_1 49.FIN2	1.926	0.049	0.1839	0.0027	0.5487	0.0754	0.00125	1088	15	1078	32.5	1090	17	0.927644	1088	30
AND1_1 50.FIN2	0.889	0.023	0.1021	0.0015	0.30391	0.0626	0.00105	627	9	695	36.5	648	12.5	-9.78417	627	18
AND1_1 51.FIN	0.855	0.022	0.1025	0.00155	0.039538	0.0597	0.00105	629	9	593	38	627	12	6.070826	629	18
Notes:																

Error= 1 sigma (except best age error= 2 sigma)															
Rho (ρ)= error correlation															
% discordance = (1-(206/238 age)/(207/206 age))*-100															
red colored data (highlighted below) = data below quality standards															
all data corrected for common Pb															
AND1_8.FIN2	1.998	0.0295	0.1454	0.00175	0.7913	0.09967	0.000375	875	10	1618	7	1115	10	-45.9209	
AND1_22.FIN2	0.664	0.01	0.0779	0.0011	0.65142	0.06319	0.000395	484	6.5	714	13	517	6	-32.2129	
AND1_40.FIN2	1.092	0.019	0.0961	0.00165	0.92571	0.08369	0.000425	590	10	1282	10	745	9	-53.9782	
AND1_48.FIN2	0.861	0.0165	0.0934	0.00115	0.40784	0.0672	0.00085	576	7	790	25.5	625	8.5	-27.0886	
AND1_70.FIN2	0.676	0.0175	0.0742	0.0011	0.34175	0.066	0.0011	462	6.5	803	35.5	524	10.5	-42.4658	
AND1_84.FIN2	0.81	0.0205	0.085	0.0013	0.59527	0.0685	0.00115	526	7.5	880	34	602	11.5	-40.2273	
AND1_101.FIN2	1.63	0.05	0.1459	0.00385	0.9768	0.0819	0.00135	870	22	1241	33	957	21.5	-29.8952	
AND1_117.FIN2	0.711	0.018	0.0783	0.00115	0.30699	0.0653	0.0011	486	7	780	35	545	10.5	-37.6923	
AND1_138.FIN2	1.159	0.0305	0.1098	0.0017	0.72819	0.0771	0.0013	672	10	1123	33.5	780	14.5	-40.1603	
AND1_139.FIN2	0.661	0.017	0.0715	0.0012	0.75405	0.0671	0.00115	445	7.5	837	35	515	10.5	-46.8339	
AND1_143.FIN2	6.68	0.31	0.2716	0.0047	0.80145	0.163	0.0055	1545	24	2250	65	1914	41.5	-31.3333	

Table B6. Sample AND-1 check standards

Spot	Pb^{207}/U^{235}	1σ	Pb^{206}/U^{238}	1σ	ρ	Pb^{207}/Pb^{206}	1σ	Pb^{206}/U^{238} age	1σ	Pb^{207}/Pb^{206} age	1σ	Pb^{207}/U^{235} age	1σ
Pleso-1.FIN2	0.387	0.0055	0.0519	0.0006	0.27351	0.05362	0.000285	326	3.7	348	12	331.7	4.15
Temora-1.FIN2	0.47	0.0085	0.0634	0.00075	0.12075	0.0536	0.0007	396	4.65	342	27	391	6
GJ1-1.FIN2	0.806	0.012	0.0962	0.0011	0.35069	0.06044	0.000315	592	6.5	623	11	601	6.5
Pleso_3.FIN2	0.385	0.0055	0.0525	0.0006	0.30775	0.05333	0.00027	329.8	3.75	340	11.5	330.4	4.15
Pleso_4.FIN2	0.398	0.006	0.0541	0.00065	0.35001	0.05317	0.000265	339.5	3.85	337	11.5	339.9	4.25
temora-3.FIN2	0.488	0.008	0.0667	0.0008	0.18385	0.05296	0.00048	416.4	4.85	322	20	403	5.5
Pleso_5.FIN2	0.406	0.006	0.0555	0.00065	0.232	0.05263	0.00027	348.2	3.95	307	11.5	345.5	4.3
GJ1_4.FIN2	0.853	0.0125	0.1031	0.0012	0.29272	0.05912	0.000305	633	7	572	11.5	626	7
Temora-5.FIN2	0.5	0.0085	0.0681	0.0008	0.12528	0.0527	0.00055	424.8	4.9	290	22.5	411	6
Pleso-1.FIN2	0.384	0.01	0.0525	0.00075	0.38264	0.053	0.0009	329.8	4.75	327	36.5	330	7
Temora-1.FIN2	0.549	0.015	0.0675	0.001	0.13177	0.0583	0.0011	421	6	544	42	444	10
GJ1-1.FIN2	0.828	0.021	0.0988	0.00145	0.43683	0.0605	0.001	608	8.5	619	36	613	12
Pleso_3.FIN2	0.366	0.0095	0.0509	0.00075	0.36201	0.053	0.0009	319.8	4.55	327	38.5	317	7
Pleso_4.FIN2	0.398	0.01	0.054	0.0008	0.35064	0.0528	0.00085	339	4.85	320	37	341	7.5
Pleso_5.FIN2	0.4	0.01	0.0539	0.0008	0.38308	0.0529	0.00085	338.4	4.85	323	37	341	7.5
GJ1_4.FIN2	0.849	0.0215	0.1008	0.0015	0.38248	0.0603	0.001	619	8.5	615	35	624	12
Temora-5.FIN2	0.503	0.0135	0.0665	0.001	0.20127	0.0541	0.001	415	6	357	39.5	413	9
Pleso_6.FIN2	0.396	0.01	0.0545	0.0008	0.35834	0.0531	0.0009	342.3	4.9	327	37.5	339	7.5
gj1-7.FIN2	0.875	0.0225	0.1059	0.00155	0.31121	0.0607	0.001	649	9	627	35.5	639	12
temora-7.FIN2	0.522	0.014	0.0679	0.00105	0.14504	0.0559	0.00105	424	6	436	40.5	426	9.5
Pleso_8.FIN2	0.43	0.011	0.0572	0.00085	0.23217	0.0538	0.0009	359	5	358	37.5	363	8
temora_8.FIN2	0.534	0.0145	0.0711	0.00105	0.20979	0.0535	0.001	443	6.5	342	40.5	435	9.5
GJ1_8.FIN2	0.929	0.024	0.109	0.0016	0.33365	0.0606	0.001	667	9.5	620	36.5	666	12.5

Notes:																	
Error= 1 sigma																	
Rho (ρ)= error correlation																	
all data corrected for common Pb																	
Pleso=Plesovitch (337 Ma)																	
Tem=Temora (417 Ma)																	
GJ-1= 609 Ma																	

Table B7. Sample LMF-2

	Location: 32°39.323 S, 54°34.964 W															
Spot	Pb^{207}/U^{235}	1σ	Pb^{206}/U^{238}	1σ	ρ	Pb^{207}/Pb^{206}	1σ	Pb^{206}/U^{238} age	1σ	Pb^{207}/Pb^{206} age	1σ	Pb^{207}/U^{235} age	1σ	%disc	Best Age	2σ
lmf2_2.FIN2	0.67	0.013	0.0819	0.0014	0.25836	0.0588	0.0005	508	8.5	557	19	521	8	-8.79713	508	17
lmf2_3.FIN2	0.669	0.013	0.0827	0.0014	0.30582	0.0583	0.0005	512	8.5	546	19	520	8	-6.22711	512	17
lmf2_5.FIN2	0.862	0.0165	0.1009	0.0017	0.23045	0.0615	0.00055	620	10	658	19	631	9	-5.77508	620	20
lmf2_7.FIN2	1.171	0.0225	0.1254	0.00215	0.34087	0.0672	0.0006	762	12.5	846	19	787	10.5	-9.92908	762	25
lmf2_8.FIN2	0.73	0.014	0.0887	0.0015	0.25596	0.0593	0.00055	548	9	575	19.5	557	8	-4.69565	548	18
lmf2_9.FIN2	5.17	0.1	0.322	0.0055	0.70481	0.1155	0.0009	1797	27.5	1887	14.5	1846	16.5	-4.76948	1887	29
lmf2_10.FIN2	0.914	0.0185	0.1057	0.00185	0.19507	0.062	0.0007	648	10.5	660	25	658	10	-1.81818	648	21
lmf2_15.FIN2	1.126	0.0215	0.1237	0.0021	0.3772	0.0657	0.00055	752	12	801	17	766	10	-6.11735	752	24
lmf2_16.FIN2	0.755	0.0145	0.0879	0.0015	0.34362	0.061	0.00055	544	9	648	19.5	571	8	-16.0494	544	18

lmf2_21. FIN2	1.105	0.0215	0.1212	0.0021	0.29145	0.0655	0.0006	737	12	788	19.5	756	10	-6.47208	737	24
lmf2_22. FIN2	0.893	0.0185	0.1028	0.0018	0.10887	0.0625	0.00075	631	10.5	687	26.5	647	10	-8.15138	631	21
lmf2_23. FIN2	0.685	0.014	0.0845	0.0015	0.16172	0.0581	0.00075	523	9	551	28.5	531	8.5	-5.08167	523	18
lmf2_24. FIN2	0.737	0.014	0.0884	0.0015	0.27584	0.0602	0.0005	546	9	610	18	560	8	-10.4918	546	18
lmf2_25. FIN2	0.869	0.0175	0.1038	0.0018	0.25604	0.0612	0.00065	636	10.5	645	22	636	9.5	-1.39535	636	21
lmf2_26. FIN2	0.893	0.0175	0.1047	0.0018	0.21285	0.0621	0.0006	642	10.5	667	20.5	647	9	-3.74813	642	21
lmf2_27. FIN2	0.744	0.014	0.0866	0.0015	0.33324	0.0623	0.0005	536	9	684	17.5	565	8	-21.6374	536	18
lmf2_28. FIN2	0.874	0.0175	0.1028	0.00175	0.098558	0.0614	0.00065	631	10.5	643	22	636	9.5	-1.86625	631	21
lmf2_29. FIN2	1.202	0.0235	0.1327	0.00225	0.18313	0.0662	0.00065	803	13	809	20	802	10.5	-0.74166	803	26
lmf2_31. FIN2	0.748	0.0155	0.0877	0.00155	0.27901	0.0625	0.00075	542	9	680	24.5	566	9	-20.2941	542	18
lmf2_33. FIN2	5.25	0.1	0.312	0.0055	0.45578	0.1228	0.00095	1749	26	1996	13.5	1862	15.5	-12.3747	1996	27
lmf2_35. FIN2	4.35	0.085	0.2706	0.0047	0.5804	0.1172	0.00095	1543	23.5	1913	14.5	1702	15.5	-19.3413	1913	29
lmf2_36. FIN2	0.758	0.015	0.0937	0.0016	0.4089	0.0596	0.00055	577	9.5	583	21	574	8.5	-1.02916	577	19
lmf2_37. FIN2	0.756	0.0145	0.0908	0.00155	0.38737	0.0611	0.00055	560	9.5	634	20	572	8.5	-11.6719	560	19
lmf2_41. FIN2	0.725	0.0145	0.0907	0.00155	0.16135	0.0588	0.0006	560	9	554	22	553	8.5	1.083032	560	18
lmf2_44. FIN2	0.677	0.013	0.0851	0.00145	0.37215	0.0586	0.0005	526	8.5	554	18.5	525	8	-5.05415	526	17
lmf2_45. FIN2	0.693	0.0135	0.0868	0.0015	0.26366	0.0585	0.0005	536	9	547	20	535	8	-2.01097	536	18
lmf2_47. FIN2	0.682	0.0135	0.0854	0.0015	0.32908	0.0586	0.0006	528	9	543	22.5	527	8	-2.76243	528	18
lmf2_48. FIN2	5.26	0.1	0.33	0.0055	0.37408	0.1163	0.0009	1840	27	1899	14	1862	16	-3.1069	1899	28
lmf2_49. FIN2	4.98	0.095	0.316	0.0055	0.51904	0.1155	0.0009	1771	26.5	1887	14	1816	16	-6.14732	1887	28
lmf2_51. FIN2	0.75	0.0145	0.0919	0.00155	0.25345	0.0597	0.00055	567	9.5	590	19.5	568	8.5	-3.89831	567	19
lmf2_52. FIN2	0.746	0.0145	0.0917	0.0016	0.32767	0.0595	0.0006	566	9.5	593	20.5	567	8.5	-4.55312	566	19

lmf2_53. FIN2	0.683	0.014	0.0863	0.0015	0.3152	0.0579	0.0006	534	9	528	24	529	8	1.136364	534	18
lmf2_55. FIN2	4.2	0.08	0.2861	0.00485	0.50321	0.1073	0.0008	1621	24.5	1754	14	1674	15.5	-7.58267	1754	28
lmf2_57. FIN2	0.742	0.0145	0.0903	0.00155	0.1165	0.0594	0.00055	557	9	578	19.5	562	8.5	-3.63322	557	18
lmf2_58. FIN2	1.262	0.0245	0.1364	0.00235	0.3	0.0674	0.0006	824	13.5	853	19	829	11	-3.39977	824	27
lmf2_59. FIN2	0.761	0.0145	0.0915	0.00155	0.19001	0.0604	0.00055	564	9	605	20.5	575	8.5	-6.77686	564	18
lmf2_60. FIN2	0.734	0.0145	0.092	0.0016	0.22787	0.0583	0.0006	568	9.5	522	23	559	8.5	8.812261	568	19
lmf2_61. FIN2	1.196	0.0225	0.1297	0.0022	0.37755	0.0669	0.0005	786	12.5	834	15.5	799	10.5	-5.7554	786	25
lmf2_62. FIN2	0.69	0.0155	0.087	0.00155	0.19061	0.0579	0.00085	538	9	505	30.5	531	9	6.534653	538	18
lmf2_64. FIN2	0.756	0.0145	0.0921	0.00155	0.35637	0.0599	0.0005	568	9.5	600	19.5	572	8.5	-5.33333	568	19
lmf2_66. FIN2	0.907	0.019	0.1072	0.00185	0.25344	0.0614	0.0007	657	11	642	24.5	656	10	2.336449	657	22
lmf2_67. FIN2	0.881	0.0175	0.105	0.0018	0.13596	0.0609	0.00065	644	10.5	629	22	641	9.5	2.384738	644	21
lmf2_68. FIN2	1.012	0.0195	0.1157	0.002	0.31108	0.0635	0.00055	705	11.5	726	18.5	710	10	-2.89256	705	23
lmf2_69. FIN2	0.686	0.013	0.085	0.00145	0.29371	0.0585	0.0005	526	8.5	541	18.5	530	8	-2.77264	526	17
lmf2_70. FIN2	1.121	0.021	0.1169	0.002	0.45775	0.0694	0.00055	713	11.5	915	16.5	764	10	-22.0765	713	23
lmf2_71. FIN2	0.745	0.0145	0.0913	0.00155	0.2177	0.0595	0.0006	563	9	580	21.5	565	8.5	-2.93103	563	18
lmf2_73. FIN2	0.702	0.0135	0.0873	0.0015	0.32905	0.05829	0.000485	540	9	543	18	541	8	-0.55249	540	18
lmf2_74. FIN2	0.762	0.015	0.0925	0.00165	0.26168	0.0601	0.0007	570	9.5	596	24.5	574	9	-4.36242	570	19
lmf2_75. FIN2	0.702	0.014	0.0881	0.00155	0.38078	0.0576	0.0006	544	9.5	516	21	541	8	5.426357	544	19
lmf2_76. FIN2	0.916	0.018	0.104	0.00185	0.43713	0.0636	0.00065	638	11	724	22	659	9.5	-11.8785	638	22
lmf2_77. FIN2	0.912	0.0175	0.106	0.00185	0.49715	0.0622	0.00055	650	10.5	678	18.5	658	9.5	-4.12979	650	21
lmf2_78. FIN2	1.516	0.0295	0.1522	0.0027	0.50729	0.0722	0.00065	914	15	987	18.5	938	12	-7.39615	914	30
lmf2_79. FIN2	0.738	0.0145	0.0907	0.00155	0.31425	0.0588	0.00055	560	9.5	558	20.5	561	8.5	0.358423	560	19

lmf2_80.FIN2	0.785	0.0165	0.0945	0.00175	0.50193	0.0605	0.0007	582	10.5	635	24.5	587	9.5	-8.34646	582	21
lmf2_81.FIN2	0.903	0.0175	0.107	0.0019	0.52282	0.061	0.0006	655	11	641	20	653	9.5	2.184087	655	22
lmf2_83.FIN2	0.733	0.014	0.0909	0.0016	0.32666	0.0581	0.00055	561	9.5	529	20	558	8	6.049149	561	19
lmf2_85.FIN2	0.693	0.0145	0.0846	0.0015	0.36037	0.0589	0.0007	524	9	553	25.5	534	8.5	-5.24412	524	18
lmf2_86.FIN2	1.214	0.023	0.1298	0.00225	0.39559	0.0675	0.00055	787	13	856	17.5	807	10.5	-8.06075	787	26
lmf2_88.FIN2	0.784	0.015	0.0936	0.00165	0.50365	0.0603	0.00055	577	9.5	613	19	587	8.5	-5.87276	577	19
lmf2_89.FIN2	4.45	0.085	0.291	0.005	0.68313	0.11	0.0009	1646	25.5	1801	15	1721	16.5	-8.60633	1801	30
lmf2_91.FIN2	1.201	0.0235	0.1306	0.0023	0.274	0.0662	0.0006	791	13	803	19	800	11	-1.4944	791	26
lmf2_94.FIN2	0.725	0.014	0.0894	0.00155	0.41987	0.0588	0.00055	552	9.5	561	21	553	8	-1.60428	552	19
lmf2_95.FIN2	1.74	0.033	0.1632	0.00285	0.51333	0.0768	0.00065	975	15.5	1118	16.5	1023	12.5	-12.7907	975	31
lmf2_96.FIN2	0.925	0.0185	0.1084	0.0019	0.27628	0.0619	0.0007	663	11	672	24	664	10	-1.33929	663	22
lmf2_97.FIN2	0.933	0.0195	0.1107	0.002	0.28454	0.0619	0.00075	677	11.5	645	27	670	10.5	4.96124	677	23
lmf2_98.FIN2	0.929	0.0185	0.1085	0.0019	0.43352	0.0616	0.0006	665	11.5	665	21	667	9.5	0	665	23
lmf2_99.FIN2	1.407	0.031	0.1397	0.0027	0.68975	0.0732	0.0008	844	15	1012	21.5	893	13	-16.6008	844	30
lmf2_100.FIN2	2.414	0.047	0.2152	0.00385	0.45893	0.0815	0.00075	1258	20.5	1230	18.5	1247	14	2.276423	1258	41
lmf2_101.FIN2	0.694	0.014	0.0861	0.00155	0.32734	0.0579	0.00065	532	9	523	24.5	535	8.5	1.720841	532	18
lmf2_102.FIN2	0.97	0.0185	0.1117	0.00195	0.32792	0.0627	0.00055	682	11	692	19	688	9.5	-1.44509	682	22
lmf2_104.FIN2	2.362	0.045	0.2139	0.00375	0.44769	0.0801	0.0007	1249	20	1198	17	1231	14	4.257095	1249	40
lmf2_106.FIN2	1.016	0.0195	0.1159	0.002	0.24847	0.0633	0.0006	707	11.5	715	19.5	712	10	-1.11888	707	23
lmf2_107.FIN2	0.761	0.015	0.0939	0.00165	0.23045	0.0581	0.0006	579	9.5	528	22	574	8.5	9.659091	579	19
Notes:																

Error= 1 sigma (except best age error= 2 sigma)															
Rho (ρ)= error correlation															
% discordance = (1-(206/238 age)/(207/206 age))*-100															
red colored data (highlighted below) = data below quality standards															
all data corrected for common Pb															
lmf2_1.FIN2	0.953	0.0185	0.1001	0.00175	0.22022	0.0687	0.0007	615	10	892	19.5	679	9.5	-31.0538	
lmf2_4.FIN2	0.989	0.0185	0.0814	0.0014	-0.02631	0.0879	0.0008	504	8.5	1373	18	698	9.5	-63.2921	
lmf2_6.FIN2	1.605	0.03	0.0872	0.00155	0.26048	0.1322	0.0012	539	9	2125	15.5	972	12	-74.6353	
lmf2_11.FIN2	0.841	0.0205	0.1026	0.00185	0.036639	0.0588	0.00105	629	10.5	513	37.5	614	11	22.61209	
lmf2_12.FIN2	0.939	0.0175	0.0993	0.0017	0.12846	0.0674	0.00055	610	10	850	17.5	672	9.5	-28.2353	
lmf2_13.FIN2	1.376	0.026	0.1077	0.0018	0.28795	0.0918	0.00075	659	10.5	1461	15.5	879	11	-54.8939	
lmf2_14.FIN2	1.549	0.029	0.0924	0.0017	0.22512	0.1218	0.0012	570	10	1982	18	950	11.5	-71.2412	
lmf2_17.FIN2	0.748	0.0145	0.0781	0.00135	0.1835	0.0687	0.0007	485	8	893	20.5	566	8.5	-45.6887	
lmf2_18.FIN2	1.508	0.034	0.0762	0.00135	0.66848	0.1424	0.00165	473	8	2244	21.5	930	14	-78.9216	
lmf2_19.FIN2	0.866	0.0165	0.0848	0.0015	0.24171	0.0733	0.0007	525	9	1019	19	633	9	-48.4789	
lmf2_20.FIN2	0.976	0.019	0.0791	0.00135	-0.01354	0.089	0.00095	491	8	1404	19.5	692	10	-65.0285	
lmf2_30.FIN2	0.901	0.018	0.0936	0.0016	0.15052	0.0704	0.0008	577	9.5	929	22.5	650	9.5	-37.8902	
lmf2_32.FIN2	1.16	0.022	0.1268	0.00215	0.23507	0.0666	0.00055	770	12.5	819	18.5	782	10.5	-5.98291	
lmf2_34.FIN2	1.405	0.0265	0.1295	0.00225	0.42438	0.0792	0.00065	785	13	1175	16.5	891	11	-33.1915	
lmf2_38.FIN2	0.829	0.016	0.087	0.0015	0.030218	0.0705	0.0007	538	9	937	20.5	612	9	-42.5827	
lmf2_39.FIN2	0.81	0.0155	0.0892	0.0015	0.16272	0.067	0.00055	551	9	832	17.5	603	8.5	-33.774	
lmf2_40.FIN2	0.771	0.0155	0.0838	0.00145	0.41823	0.0679	0.00065	519	8.5	859	20	580	8.5	-39.5809	

lmf2_42.FIN2	1.471	0.029	0.1379	0.00235	0.59837	0.0777	0.0007	833	13.5	1140	17.5	919	11.5	-26.9298
lmf2_43.FIN2	0.913	0.0215	0.0901	0.00155	0.14702	0.0735	0.00115	556	9	1010	31.5	657	11	-44.9505
lmf2_46.FIN2	0.743	0.0155	0.0904	0.0016	0.19715	0.0611	0.0008	558	9.5	630	28	564	9	-11.4286
lmf2_50.FIN2	0.921	0.018	0.0864	0.0015	0.35196	0.078	0.0007	534	9	1143	19	662	9.5	-53.2808
lmf2_54.FIN2	0.904	0.0175	0.0965	0.00165	0.23499	0.0683	0.0006	594	10	878	18.5	654	9	-32.3462
lmf2_56.FIN2	0.946	0.018	0.102	0.00175	0.30302	0.0677	0.00055	626	10	861	17	675	9.5	-27.2938
lmf2_63.FIN2	1.326	0.025	0.0977	0.00165	0.37952	0.0984	0.0008	601	10	1595	15	857	11	-62.3197
lmf2_65.FIN2	1.836	0.0345	0.1681	0.00285	0.55337	0.0791	0.0006	1002	16	1175	15.5	1058	12.5	-14.7234
lmf2_70.FIN2	1.121	0.021	0.1169	0.002	0.45775	0.0694	0.00055	713	11.5	915	16.5	764	10	-22.0765
lmf2_72.FIN2	0.985	0.019	0.1051	0.0018	0.35114	0.0683	0.0006	644	10.5	876	18	697	9.5	-26.484
lmf2_82.FIN2	1.291	0.0245	0.1034	0.00185	0.5529	0.0907	0.0008	634	11	1440	17	842	11	-55.9722
lmf2_84.FIN2	1.008	0.019	0.085	0.00145	0.51333	0.0858	0.0007	526	8.5	1330	15.5	708	9.5	-60.4511
lmf2_87.FIN2	1.567	0.0295	0.0774	0.00145	0.71781	0.1461	0.0013	481	8.5	2303	15.5	957	11.5	-79.1142
lmf2_90.FIN2	0.868	0.017	0.0858	0.00155	0.36717	0.0723	0.0007	531	9	996	20.5	634	9.5	-46.6867
lmf2_92.FIN2	1.37	0.0265	0.1162	0.002	0.10869	0.0856	0.00085	709	11.5	1323	19.5	876	11.5	-46.4097
lmf2_93.FIN2	4.48	0.17	0.2395	0.0043	0.78827	0.1352	0.00385	1382	22.5	2000	47	1676	29.5	-30.9
lmf2_103.FIN2	1.181	0.024	0.1	0.0018	0.16563	0.0851	0.001	614	10.5	1313	23.5	790	11	-53.2369
lmf2_105.FIN2	1.329	0.026	0.08	0.0014	-0.06735	0.1209	0.00125	496	8.5	1956	19	858	11.5	-74.6421

Table B8. Sample LMF-2 check standards

Spot	Pb^{207}/U^{235}	1σ	Pb^{206}/U^{238}	1σ	ρ	Pb^{207}/Pb^{206}	1σ	Pb^{206}/U^{238} age	1σ	Pb^{207}/Pb^{206} age	1σ	Pb^{207}/U^{235} age	1σ
Pleso-1.FIN2	0.388	0.0075	0.0524	0.0009	0.28685	0.05314	0.000445	329	5.5	328	19	333	5.5
Temora-1.FIN2	0.493	0.01	0.065	0.0011	0.15063	0.0546	0.0006	406	6.5	376	23	406	6.5
GJ1-1.FIN2	0.829	0.016	0.0988	0.0017	0.4405	0.0606	0.0005	607	10	628	18	613	9
Pleso_3.FIN2	0.39	0.0075	0.052	0.0009	0.3429	0.05403	0.00045	327	5.5	369	19	335	5.5
Pleso_4.FIN2	0.397	0.0075	0.054	0.0009	0.23307	0.05335	0.00046	339	5.5	344	19	339	5.5
Pleso_5.FIN2	0.4	0.0075	0.0553	0.00095	0.2794	0.05315	0.00047	347	6	330	20	342	5.5
GJ1_4.FIN2	0.847	0.016	0.1033	0.00175	0.30341	0.06	0.0005	634	10.5	601	18.5	623	9
Pleso_6.FIN2	0.407	0.0075	0.0553	0.00095	0.28594	0.05314	0.00044	347	5.5	329	18.5	346	5.5
gj1-7.FIN2	0.863	0.0165	0.1036	0.00175	0.47011	0.06	0.0005	636	10.5	599	18	632	9
Pleso_8.FIN2	0.412	0.008	0.0552	0.00095	0.26144	0.05392	0.00046	347	5.5	364	19	351	5.5
pleso-9.FIN2	0.411	0.008	0.0559	0.00095	0.23436	0.05311	0.000455	351	6	329	19.5	349	5.5
temora_8.FIN2	0.511	0.0105	0.0676	0.00115	0.10152	0.0548	0.00065	422	7	379	25.5	418	7
GJ1_8.FIN2	0.894	0.017	0.1078	0.00185	0.20344	0.06	0.0005	660	10.5	600	18	648	9
Temora-5.FIN2	0.493	0.0115	0.068	0.0012	0.025489	0.0528	0.00085	424	7	300	31.5	406	7.5
temora-7.FIN2	0.501	0.0105	0.0686	0.0012	0.049713	0.0527	0.00065	428	7	302	25.5	412	7
Notes:													
Error= 1 sigma													

Rho (ρ)= error correlation															
all data corrected for common Pb															
Pleso=Plesovitch (337 Ma)															
Tem=Temora (417 Ma)															
GJ-1= 609 Ma															

Table B9. Sample LMF-3

Spot	Location: 32°39.365' S, 54°35.102' W														
	Pb^{207}/U^{235}	1σ	Pb^{206}/U^{238}	1σ	ρ	Pb^{207}/Pb^{206}	1σ	Pb^{206}/U^{238} age	1σ	Pb^{207}/Pb^{206} age	1σ	Pb^{207}/U^{235} age	1σ	%disc	Best Age	2σ
LMF3_1_2.FIN2	4.778	0.042	0.3038	0.0024	0.60899	0.1138	0.0005	1711	11.5	1861	8	1779	7.5	-8.06018	1861	16
LMF3_1_3.FIN2	0.663	0.0065	0.0829	0.00065	0.36232	0.05802	0.000365	513.7	3.75	536	14	516.3	3.95	-4.16045	513.7	7.5
LMF3_1_4.FIN2	0.881	0.0095	0.1026	0.0008	0.18484	0.0621	0.00055	629.6	4.65	665	18.5	639	5	-5.32331	629.6	9.3
LMF3_1_5.FIN2	0.869	0.0075	0.1021	0.00075	0.2672	0.0615	0.00034	626.8	4.3	654	12	634.8	4.2	-4.15902	626.8	8.6
LMF3_1_6.FIN2	0.877	0.0095	0.103	0.0008	0.068322	0.0617	0.00055	632.3	4.65	654	19	639	5	-3.31804	632.3	9.3
LMF3_1_8.FIN2	0.846	0.008	0.0975	0.00085	0.71215	0.06296	0.000295	599.5	4.95	707	10	621.9	4.5	-15.2051	599.5	9.9
LMF3_1_9.FIN2	0.664	0.0065	0.0834	0.00065	0.31296	0.05765	0.00039	516.6	3.85	510	15	517.6	3.9	1.294118	516.6	7.7
LMF3_1_10.FIN2	0.643	0.006	0.0817	0.0006	0.34629	0.05728	0.00036	506.3	3.55	498	13.5	504	3.8	1.666667	506.3	7.1
LMF3_1_11.FIN2	0.943	0.0105	0.1015	0.00105	0.37973	0.0667	0.0006	623	6	824	19	676	6	-24.3932	623	12
LMF3_1_12.FIN2	0.872	0.0075	0.1021	0.00075	0.43515	0.06165	0.000265	626.6	4.25	664	9	636.7	4	-5.63253	626.6	8.5

LMF3_1_13.FIN2	0.676	0.0055	0.0839	0.0006	0.34402	0.0584	0.00024	519.2	3.55	541	9	525	3.25	-4.02957	519.2	7.1
LMF3_1_14.FIN2	1.11	0.0095	0.122	0.0009	0.44142	0.06631	0.0003	742	5.5	820	9.5	758.8	4.45	-9.5122	742	11
LMF3_1_15.FIN2	0.855	0.009	0.1013	0.00085	0.32422	0.0614	0.0005	621.9	4.9	649	17.5	628.5	4.9	-4.17565	621.9	9.8
LMF3_1_16.FIN2	1.219	0.0115	0.1228	0.00095	0.33208	0.07208	0.000465	747	5.5	986	13	810	5.5	-24.2394	747	11
LMF3_1_17.FIN2	0.686	0.006	0.0853	0.00065	0.2869	0.05793	0.000325	527.6	3.7	532	12	530.8	3.7	-0.82707	527.6	7.4
LMF3_1_18.FIN2	0.677	0.006	0.0834	0.0006	0.41301	0.05878	0.00028	516	3.65	557	10	524.9	3.55	-7.36086	516	7.3
LMF3_1_19.FIN2	0.857	0.0075	0.1004	0.00075	0.16335	0.06189	0.00039	616.6	4.45	660	13.5	630.2	4.2	-6.57576	616.6	8.9
LMF3_1_20.FIN2	0.638	0.0085	0.0825	0.0007	0.093024	0.0559	0.00065	511.3	4.15	423	25	499	5	20.8747	511.3	8.3
LMF3_1_21.FIN2	2.342	0.0215	0.1991	0.00185	0.63345	0.08506	0.000455	1170	10	1316	10.5	1224	6.5	-11.0942	1170	20
LMF3_1_22.FIN2	1.748	0.017	0.1697	0.00125	0.22959	0.0744	0.0005	1010	7	1050	14	1025	6	-3.80952	1010	14
LMF3_1_23.FIN2	0.881	0.008	0.1041	0.0008	0.44719	0.06196	0.000315	638.3	4.6	668	11	641.9	4.2	-4.44611	638.3	9.2
LMF3_1_24.FIN2	0.725	0.007	0.0863	0.00065	0.20162	0.06088	0.00042	533.6	3.75	635	15	553	4.15	-15.9685	533.6	7.5
LMF3_1_25.FIN2	0.742	0.007	0.0884	0.0007	0.27243	0.06098	0.00042	546.2	4.1	634	15	563	4.2	-13.8486	546.2	8.2
LMF3_1_26.FIN2	1.978	0.018	0.1769	0.00145	0.55919	0.08134	0.000415	1050	8	1225	10	1109	6	-14.2857	1050	16
LMF3_1_27.FIN2	0.82	0.0075	0.0962	0.0007	0.21228	0.06173	0.00036	591.9	4.2	663	12	607.9	4.05	-10.724	591.9	8.4
LMF3_1_28.FIN2	0.88	0.008	0.1036	0.0008	0.27311	0.06154	0.000395	635.5	4.55	653	14	640.8	4.45	-2.67994	635.5	9.1
LMF3_1_29.FIN2	1.132	0.0095	0.1235	0.0009	0.55973	0.06641	0.000245	750	5	821	8	768.8	4.5	-8.64799	750	10
LMF3_1_30.FIN2	0.664	0.0065	0.0815	0.0006	0.23258	0.05901	0.00042	504.8	3.6	562	15.5	516.3	4.1	-10.1779	504.8	7.2
LMF3_1_31.FIN2	0.864	0.0085	0.1016	0.0008	0.31642	0.06163	0.00045	623.8	4.55	660	15.5	632.3	4.65	-5.48485	623.8	9.1
LMF3_1_34.FIN2	0.865	0.0075	0.1005	0.00075	0.32349	0.06229	0.00029	617	4.3	690	10.5	632.2	4.05	-10.5797	617	8.6
LMF3_1_35.FIN2	0.669	0.0065	0.0839	0.0006	0.10285	0.05785	0.00042	519.1	3.7	521	15.5	519	3.95	-0.36468	519.1	7.4
LMF3_1_36.FIN2	0.823	0.009	0.0973	0.0008	0.24779	0.0609	0.0005	598.3	4.65	642	17	609	4.95	-6.80685	598.3	9.3

LMF3_1_37.FIN2	0.864	0.008	0.1012	0.00075	0.27653	0.06127	0.00036	621.1	4.3	645	13	632.2	4.35	-3.70543	621.1	8.6
LMF3_1_40.FIN2	1.183	0.01	0.124	0.0009	0.40648	0.06833	0.000295	753	5	877	9	792.6	4.7	-14.1391	753	10
LMF3_1_41.FIN2	4.287	0.0345	0.2768	0.00205	0.54439	0.1124	0.000415	1575	10.5	1839	7	1690	6.5	-14.3556	1839	14
LMF3_1_42.FIN2	0.649	0.0055	0.0819	0.0006	0.32213	0.05684	0.00028	507.5	3.5	485	11	507.9	3.45	4.639175	507.5	7
LMF3_1_43.FIN2	0.87	0.0095	0.1033	0.0008	0.27042	0.0608	0.0005	634.2	4.75	627	18	635	5	1.148325	634.2	9.5
LMF3_1_44.FIN2	1.598	0.0125	0.1556	0.0011	0.54764	0.07385	0.00023	932	6	1037	6.5	969.1	4.85	-10.1254	932	12
LMF3_1_45.FIN2	0.636	0.006	0.0785	0.0006	0.3781	0.0594	0.000335	487.1	3.55	583	12.5	500.6	3.7	-16.4494	487.1	7.1
LMF3_1_46.FIN2	0.711	0.006	0.0871	0.00065	0.39049	0.05899	0.000305	538.2	3.75	561	11.5	545.1	3.6	-4.06417	538.2	7.5
LMF3_1_48.FIN2	0.862	0.0075	0.1021	0.0007	0.28627	0.06143	0.00032	626.9	4.2	648	11	631.2	4.15	-3.25617	626.9	8.4
LMF3_1_49.FIN2	0.7	0.006	0.0858	0.00065	0.34132	0.05943	0.000305	530.3	3.75	579	11.5	538.6	3.7	-8.41105	530.3	7.5
LMF3_1_51.FIN2	2.07	0.0215	0.1729	0.00165	0.83749	0.08698	0.000375	1027	9	1361	8.5	1139	7	-24.5408	1027	18
LMF3_1_52.FIN2	0.815	0.007	0.0927	0.0007	0.49559	0.06344	0.00032	571.5	4.1	724	10.5	604.8	4	-21.0635	571.5	8.2
LMF3_1_53.FIN2	0.89	0.008	0.1037	0.00075	0.37922	0.06208	0.000345	635.9	4.4	684	12	646.7	4.35	-7.03216	635.9	8.8
LMF3_1_54.FIN2	0.853	0.0085	0.1022	0.00075	0.11506	0.06071	0.00047	627.4	4.5	624	16.5	626.2	4.6	0.544872	627.4	9
LMF3_1_55.FIN2	1.674	0.014	0.1633	0.00115	0.40197	0.07438	0.00032	975	6.5	1054	8.5	999	5.5	-7.49526	975	13
LMF3_1_56.FIN2	0.905	0.008	0.1035	0.00075	0.29074	0.06323	0.000365	634.6	4.35	717	12.5	653.2	4.4	-11.4923	634.6	8.7
LMF3_1_57.FIN2	1.742	0.022	0.1683	0.0014	0.26501	0.0752	0.00075	1002	7.5	1063	20	1022	8.5	-5.73848	1002	15
LMF3_1_59.FIN2	0.815	0.007	0.0965	0.0007	0.37238	0.0612	0.000315	594.1	4.2	645	11	604.4	3.95	-7.89147	594.1	8.4
LMF3_1_60.FIN2	0.845	0.0075	0.0999	0.000495	0.30391	0.0613	0.0005	613.7	2.9	654	18	623.9	3.9	-6.16208	613.7	5.8
LMF3_1_61.FIN2	1.079	0.009	0.1211	0.0006	0.33763	0.0648	0.00055	737	3.5	762	17	742.2	4.35	-3.28084	737	7
LMF3_1_62.FIN2	2.177	0.0235	0.1813	0.00175	0.84655	0.0862	0.0006	1076	9.5	1343	13.5	1173	7.5	-19.8809	1076	19
LMF3_1_63.FIN2	7.42	0.08	0.3686	0.00305	0.74919	0.1454	0.00115	2021	14.5	2295	13.5	2164	9.5	-11.939	2295	27

LMF3_1_64.FIN2	0.869	0.007	0.1026	0.00065	0.4673	0.06169	0.00048	629.4	3.9	666	16.5	634.8	3.65	-5.4955	629.4	7.8
LMF3_1_65.FIN2	13.78	0.1	0.4966	0.00315	0.63339	0.1983	0.0013	2601	13.5	2811	11	2735	7	-7.47065	2811	22
LMF3_1_67.FIN2	0.853	0.0075	0.0999	0.00065	0.42762	0.0612	0.00055	613.5	3.7	655	19	624.9	4.2	-6.33588	613.5	7.4
LMF3_1_68.FIN2	0.848	0.0065	0.0997	0.0006	0.49184	0.06103	0.000445	612.2	3.45	639	15	623.5	3.6	-4.19405	612.2	6.9
LMF3_1_70.FIN2	0.853	0.012	0.0982	0.0007	0.1805	0.0619	0.00095	603.9	4	660	31.5	624	6.5	-8.5	603.9	8
LMF3_1_71.FIN2	0.888	0.0115	0.1038	0.0009	0.36899	0.061	0.0008	636	5.5	631	29.5	645	6	0.792393	636	11
LMF3_1_72.FIN2	0.919	0.0095	0.1009	0.00085	0.53004	0.0655	0.0006	619.8	4.9	788	19	662.2	4.95	-21.3452	619.8	9.8
LMF3_1_73.FIN2	1.406	0.0165	0.1432	0.0015	0.61878	0.0704	0.0007	862	8.5	941	20.5	889	7	-8.39532	862	17
LMF3_1_74.FIN2	0.828	0.0065	0.0966	0.0006	0.55015	0.06211	0.000485	594.5	3.6	673	16	612.8	3.8	-11.6642	594.5	7.2
LMF3_1_75.FIN2	1.293	0.026	0.1303	0.0021	0.87177	0.0722	0.00075	790	12	978	21.5	838	11	-19.2229	790	24
LMF3_1_76.FIN2	0.829	0.0075	0.0996	0.00065	0.29846	0.0609	0.0006	611.8	3.75	634	21	613.4	4.1	-3.50158	611.8	7.5
LMF3_1_78.FIN2	0.728	0.007	0.0884	0.00065	0.49666	0.0598	0.00055	545.8	3.85	594	20	555.5	4.1	-8.11448	545.8	7.7
LMF3_1_79.FIN2	13.39	0.1	0.504	0.0032	0.66331	0.1935	0.00135	2631	14	2769	11.5	2706	7	-4.98375	2769	23
Notes:																
Error= 1 sigma (except best age error= 2 sigma)																
Rho (ρ)= error correlation																
% discordance = (1-(206/238 age)/(207/206 age))*-100																
red colored data (highlighted below) = data below quality standards																
all data corrected for common Pb																
LMF3_1_1.FIN2	0.621	0.0085	0.0712	0.0006	0.32474	0.0623	0.0007	443.4	3.75	697	23	491	5.5	-36.3845		

Spot	Pb²⁰⁷/U²³⁵	1σ	Pb²⁰⁶/U²³⁸	1σ	ρ	Pb²⁰⁷/Pb²⁰⁶	1σ	Pb²⁰⁶/U²³⁸ age	1σ	Pb²⁰⁷/Pb²⁰⁶ age	1σ	Pb²⁰⁷/U²³⁵ age	1σ		
LMF3_1_7.FIN2	0.803	0.007	0.0892	0.00065	0.46724	0.06511	0.000315	550.9	3.95	776	10.5	598.8	4.05	-29.0077	
LMF3_1_32.FIN2	0.75	0.02	0.0662	0.00085	0.80152	0.0801	0.0013	413	5	1133	29	559	11	-63.5481	
LMF3_1_33.FIN2	0.617	0.005	0.0692	0.0005	0.54807	0.06507	0.00026	431.1	3.1	774	8.5	487.7	3.25	-44.3023	
LMF3_1_38.FIN2	0.687	0.0065	0.0798	0.00065	0.47542	0.06256	0.000385	494.8	3.95	698	13	530.7	4.05	-29.1117	
LMF3_1_39.FIN2	0.879	0.0075	0.0914	0.00075	0.63408	0.06923	0.000305	563.4	4.5	907	9	639.8	4.05	-37.8831	
LMF3_1_47.FIN2	0.74	0.0065	0.084	0.0006	0.21771	0.06379	0.00032	519.9	3.55	730	10.5	562.1	3.7	-28.7808	
LMF3_1_50.FIN2	0.955	0.008	0.1027	0.00075	0.37819	0.06711	0.000305	630	4.25	846	9.5	680	4.25	-25.5319	
LMF3_1_58.FIN2	1.16	0.0095	0.1145	0.0009	0.58635	0.07338	0.000305	699	5	1023	8.5	782.1	4.5	-31.6716	
LMF3_1_66.FIN2	0.975	0.0075	0.0991	0.00065	0.66037	0.07106	0.000495	608.7	3.7	958	14	691.2	3.8	-36.4614	
LMF3_1_69.FIN2	0.796	0.006	0.0846	0.0007	0.66744	0.0677	0.0005	524.1	4.3	858	16	594.4	3.5	-38.9161	
LMF3_1_77.FIN2	0.609	0.015	0.0697	0.00205	0.84905	0.0678	0.00105	432	12.5	835	33.5	479	9.5	-48.2635	

Table B10. Sample LMF-3 check standards

Spot	Pb²⁰⁷/U²³⁵	1σ	Pb²⁰⁶/U²³⁸	1σ	ρ	Pb²⁰⁷/Pb²⁰⁶	1σ	Pb²⁰⁶/U²³⁸ age	1σ	Pb²⁰⁷/Pb²⁰⁶ age	1σ	Pb²⁰⁷/U²³⁵ age	1σ
Pleso_1.FIN2	0.3859	0.0033	0.05229	0.000385	0.42905	0.05356	0.00025	328.6	2.35	352	10.5	331.4	2.45
temora_1.FIN2	0.489	0.006	0.0649	0.00055	0.44819	0.0544	0.00055	405	3.2	368	20.5	403.1	4.15
Gj1_1.FIN2	0.776	0.0065	0.0938	0.0007	0.35356	0.06014	0.000295	577.8	4.05	611	10.5	583.4	3.75
GJ1_2.FIN2	0.795	0.007	0.0954	0.0007	0.34944	0.06008	0.000305	587.1	4.1	609	11	594.8	3.9
Pleso_2.FIN2	0.3891	0.00325	0.05306	0.00039	0.4176	0.05308	0.00024	333.3	2.4	330	10.5	333.9	2.35

Temora_2.FIN2	0.506	0.0065	0.0668	0.0006	0.28588	0.055	0.0006	416.7	3.5	387	23.5	415.1	4.3
Pleso_3.FIN2	0.3945	0.0033	0.05332	0.00039	0.37346	0.05418	0.00025	334.9	2.4	374	10.5	337.5	2.4
GJ1_3.FIN2	0.776	0.0065	0.0933	0.0007	0.37078	0.0604	0.000295	575.2	4	614	10.5	582.6	3.75
Pleso_4.FIN2	0.3873	0.0032	0.05222	0.000375	0.57923	0.05393	0.000195	328.1	2.3	365	8.5	332.2	2.35
GJ1_4.FIN2	0.79	0.007	0.0947	0.0007	0.43859	0.06072	0.00031	582.9	4.2	622	11	591.5	3.85
Pleso_5.FIN2	0.4022	0.0034	0.05383	0.000395	0.37232	0.05419	0.00026	338	2.4	382	10.5	343.4	2.45
Pleso_1.FIN2	0.3821	0.0026	0.05236	0.00023	0.34675	0.05321	0.00036	329	1.4	334	15	328.4	1.9
temora_1.FIN2	0.49	0.005	0.06391	0.00037	0.14201	0.0554	0.0006	399.3	2.25	422	23.5	404.2	3.45
Gj1_1.FIN2	0.784	0.0055	0.0949	0.000415	0.29112	0.0601	0.000425	584.4	2.45	608	15	588.7	3.1
GJ1_2.FIN2	0.792	0.0055	0.09503	0.000415	0.31433	0.06027	0.00041	585.1	2.45	611	14.5	592.6	3.15
Pleso_2.FIN2	0.3791	0.0026	0.05152	0.00021	0.39414	0.0535	0.00035	323.8	1.3	344	15	326.2	1.95
Temora_2.FIN2	0.492	0.0055	0.06421	0.00035	0.11987	0.0552	0.0006	401.5	2.1	403	24	406.3	3.85
Pleso_3.FIN2	0.3832	0.0026	0.05209	0.000215	0.26989	0.05343	0.00036	327.3	1.3	340	15.5	329.2	1.9
GJ1_3.FIN2	0.798	0.006	0.09551	0.00042	0.32451	0.0606	0.000445	588	2.45	626	16	595.2	3.35
Notes:													
Error= 1 sigma													
Rho (ρ)= error correlation													
all data corrected for common Pb													
Pleso=Plesovitch (337 Ma)													
Tem=Temora (417 Ma)													
GJ-1= 609 Ma													

Table B11. Sample LMF-5

Spot	Pb^{207}/U^{235}	1σ	Pb^{206}/U^{238}	1σ	ρ	Pb^{207}/Pb^{206}	1σ	Pb^{206}/U^{238} age	1σ	Pb^{207}/Pb^{206} age	1σ	Pb^{207}/U^{235} age	1σ	%disc	Best Age	2σ
Location: 32°39.612' S, 54° 34.433' W																
LMF5_2.FIN2	0.911	0.0095	0.1043	0.00105	0.48731	0.0639	0.0006	639	6	733	20	657	5	-12.824	639	12
LMF5_4.FIN2	0.714	0.0075	0.089	0.00085	0.28052	0.0581	0.00055	550	5	527	21	546.1	4.45	4.364326	550	10
LMF5_7.FIN2	0.75	0.0075	0.0914	0.0009	0.2967	0.0599	0.00055	563	5	610	19.5	567.2	4.4	-7.70492	563	10
LMF5_8.FIN2	0.824	0.008	0.098	0.0009	0.22281	0.0615	0.00055	603	5.5	656	18.5	609.5	4.35	-8.07927	603	11
LMF5_9.FIN2	0.857	0.008	0.1014	0.00095	0.27608	0.0619	0.0005	622	5.5	671	18	628.3	4.45	-7.30253	622	11
LMF5_11.FIN2	0.839	0.01	0.1023	0.0011	0.3722	0.0601	0.00065	628	6.5	618	24	620	5.5	1.618123	628	13
LMF5_12.FIN2	0.78	0.0075	0.0917	0.0009	0.49159	0.0618	0.0005	565	5.5	670	18	585	4.25	-15.6716	565	11
LMF5_13.FIN2	1.069	0.013	0.1147	0.00125	0.76546	0.0678	0.0006	699	7	855	18	738	6.5	-18.2456	699	14
LMF5_14.FIN2	0.744	0.008	0.0909	0.0009	0.28298	0.0593	0.0006	561	5	575	21	565.7	4.5	-2.43478	561	10
LMF5_15.FIN2	0.854	0.0115	0.1047	0.00105	0.20015	0.0592	0.00075	641	6	548	28	624	6.5	16.9708	641	12
LMF5_16.FIN2	0.868	0.0115	0.1052	0.00105	0.18977	0.0594	0.00075	644	6.5	575	28	632	6.5	12	644	13
LMF5_18.FIN2	0.705	0.0075	0.088	0.00085	0.28087	0.0583	0.0006	543	5	539	22.5	541.8	4.6	0.742115	543	10
LMF5_19.FIN2	0.852	0.01	0.1016	0.00105	0.16037	0.0603	0.0007	624	6	597	25.5	625	5.5	4.522613	624	12
LMF5_21.FIN2	0.73	0.0075	0.0899	0.00085	0.28749	0.0584	0.00055	556	5	545	20.5	556.1	4.4	2.018349	556	10
LMF5_22.FIN2	0.836	0.008	0.0941	0.0009	0.37545	0.0638	0.00055	579	5.5	736	17.5	616.3	4.4	-21.3315	579	11

LMF5_23.FIN2	0.718	0.0095	0.0892	0.00095	0.28757	0.0576	0.0007	550	5.5	511	27	550	5.5	7.632094	550	11
LMF5_24.FIN2	0.881	0.01	0.1048	0.00105	0.31745	0.0607	0.0006	643	6	625	21.5	642	5.5	2.88	643	12
LMF5_25.FIN2	0.882	0.009	0.1048	0.001	0.19541	0.0607	0.0006	642	6	629	20.5	641.9	4.9	2.066773	642	12
LMF5_27.FIN2	0.856	0.008	0.0975	0.0009	0.34476	0.064	0.00055	600	5.5	736	17	627.7	4.35	-18.4783	600	11
LMF5_29.FIN2	0.814	0.008	0.093	0.0009	0.36553	0.0642	0.00055	573	5	747	17.5	604.3	4.35	-23.2932	573	10
LMF5_30.FIN2	0.964	0.0095	0.1051	0.001	0.049852	0.0669	0.00065	644	6	836	19.5	684.8	4.9	-22.9665	644	12
LMF5_31.FIN2	1.217	0.011	0.1299	0.0012	0.42496	0.0681	0.00055	787	7	870	16.5	808	5	-9.54023	787	14
LMF5_32.FIN2	0.88	0.011	0.1064	0.00105	0.078787	0.0604	0.00075	652	6	595	25.5	639	6	9.579832	652	12
LMF5_33.FIN2	0.959	0.0125	0.1043	0.00125	0.35118	0.0664	0.0009	639	7.5	836	27.5	682	6.5	-23.5646	639	15
LMF5_35.FIN2	0.664	0.007	0.0829	0.0008	0.38973	0.0584	0.00055	513.2	4.75	546	20	516.5	4.15	-6.00733	513.2	9.5
LMF5_37.FIN2	0.833	0.0085	0.0991	0.00095	0.32305	0.0615	0.0006	609	5.5	658	20	614.9	4.85	-7.44681	609	11
LMF5_38.FIN2	0.927	0.0095	0.1098	0.0011	0.28667	0.0617	0.00055	671	6.5	667	19.5	665.9	4.9	0.5997	671	13
LMF5_39.FIN2	0.861	0.0115	0.1032	0.00105	0.06636	0.0605	0.0008	633	6	604	27.5	628	6	4.801325	633	12
LMF5_41.FIN2	0.907	0.0085	0.1045	0.001	0.34381	0.0626	0.00055	640	6	695	18	656.1	4.5	-7.91367	640	12
LMF5_42.FIN2	0.696	0.0075	0.0845	0.0009	0.41339	0.0595	0.0006	523	5.5	579	22	536	4.55	-9.67185	523	11
LMF5_43.FIN2	0.865	0.009	0.1026	0.001	0.17203	0.061	0.0006	630	5.5	635	21	632.4	4.8	-0.7874	630	11
LMF5_44.FIN2	0.731	0.008	0.0901	0.0009	0.2613	0.0583	0.0006	556	5	539	23	556.3	4.7	3.153989	556	10
LMF5_47.FIN2	1.64	0.0165	0.1642	0.0016	0.41003	0.0727	0.00065	980	9	1005	18	986	6.5	-2.48756	980	18
LMF5_49.FIN2	0.904	0.009	0.1018	0.00095	0.37563	0.0649	0.00055	625	5.5	769	17.5	653.8	4.7	-18.7256	625	11
LMF5_50.FIN2	0.858	0.0095	0.1027	0.001	0.33728	0.061	0.0006	631	6	635	21.5	629	5	-0.62992	631	12
LMF5_51.FIN2	0.82	0.0105	0.0994	0.00105	0.174	0.0614	0.0008	610	6	630	27.5	607	6	-3.1746	610	12
LMF5_52.FIN2	0.863	0.0095	0.1036	0.001	0.16484	0.0615	0.00065	635	6	643	23	631	5.5	-1.24417	635	12

LMF5_5 3.FIN2	0.864	0.0135	0.1011	0.0012	0.19061	0.0629	0.001	621	7	711	32	631	7.5	-12.6582	621	14
LMF5_5 4.FIN2	0.847	0.012	0.1012	0.00105	0.21303	0.0618	0.00085	623	6	633	29	621	6.5	-1.57978	623	12
LMF5_5 5.FIN2	1.634	0.0175	0.1545	0.00165	0.50031	0.0779	0.00075	926	9	1143	18.5	984	7	-18.9851	926	18
LMF5_5 7.FIN2	1.094	0.011	0.1193	0.00115	0.36076	0.0677	0.0006	727	6.5	862	18.5	750	5	-15.6613	727	13
LMF5_5 8.FIN2	0.822	0.0265	0.1	0.0016	-0.08747	0.0611	0.0022	614	9.5	590	75	605	15	4.067797	614	19
LMF5_5 9.FIN2	0.914	0.01	0.1069	0.00105	0.17681	0.0627	0.00065	654	6	695	21	659	5	-5.89928	654	12
LMF5_6 0.FIN2	0.897	0.009	0.1017	0.00095	0.39932	0.0641	0.00055	624	5.5	752	18	650.5	4.75	-17.0213	624	11
LMF5_6 1.FIN2	0.886	0.01	0.1044	0.00105	0.2447	0.0616	0.00065	640	6	652	22.5	645	5.5	-1.84049	640	12
LMF5_6 4.FIN2	0.863	0.0105	0.1004	0.0011	0.40615	0.0625	0.0007	616	6.5	684	23	632	6	-9.94152	616	13
LMF5_6 7.FIN2	0.879	0.0095	0.0999	0.00105	0.27421	0.0628	0.00065	614	6	699	22	641	5	-12.1602	614	12
LMF5_6 8.FIN2	0.742	0.0095	0.0934	0.00095	0.33013	0.0574	0.0007	576	5.5	492	26	564	5.5	17.07317	576	11
LMF5_6 9.FIN2	0.736	0.0075	0.0893	0.00085	0.27634	0.0591	0.00055	552	5	576	20.5	558.9	4.4	-4.16667	552	10
LMF5_7 0.FIN2	0.849	0.0085	0.0994	0.00095	0.44215	0.0618	0.00055	611	5.5	660	19	624.2	4.6	-7.42424	611	11
LMF5_7 1.FIN2	0.859	0.011	0.1012	0.00105	0.24175	0.061	0.0007	621	6	630	25.5	628	6	-1.42857	621	12
LMF5_7 3.FIN2	0.836	0.01	0.101	0.00105	0.27529	0.0608	0.0007	620	6	627	25	617	5.5	-1.11643	620	12
LMF5_7 4.FIN2	0.746	0.0075	0.0907	0.00085	0.22367	0.0602	0.00055	560	5	607	20	565.5	4.3	-7.743	560	10
LMF5_8 0.FIN2	0.917	0.011	0.1012	0.001	0.26057	0.0661	0.00075	621	6	799	23.5	659	6	-22.2778	621	12
LMF5_8 4.FIN2	1.029	0.01	0.118	0.00115	0.36386	0.0631	0.00055	719	6.5	710	18	718	5	1.267606	719	13
LMF5_8 5.FIN2	1.607	0.0155	0.1598	0.00155	0.41264	0.0726	0.0006	955	8.5	1001	17	972	6	-4.5954	955	17
Notes:																
Error= 1 sigma (except best age error= 2 sigma)																

Rho (ρ)= error correlation															
% discordance = (1-(206/238 age)/(207/206 age))*-100															
red colored data (highlighted below) = data below quality standards															
all data corrected for common Pb															
LMF5_1.FIN2	1.157	0.0165	0.0994	0.00095	0.16795	0.0847	0.00115	611	5.5	1278	25.5	778	7.5	-52.1909	
LMF5_3.FIN2	0.913	0.011	0.0898	0.00085	0.15531	0.074	0.00085	554	5	1032	23	658	6	-46.3178	
LMF5_5.FIN2	1.353	0.016	0.1122	0.00125	0.86975	0.088	0.0007	685	7	1382	15.5	869	7	-50.4342	
LMF5_6.FIN2	2.023	0.024	0.0876	0.00095	0.53995	0.1675	0.0017	541	5.5	2538	16.5	1121	8	-78.684	
LMF5_10.FIN2	2.41	0.095	0.109	0.0015	0.92807	0.1583	0.00455	667	8.5	2415	48.5	1212	25.5	-72.381	
LMF5_17.FIN2	1.759	0.018	0.1142	0.0011	0.66056	0.1106	0.0009	698	6.5	1810	15.5	1029	6.5	-61.4365	
LMF5_20.FIN2	0.845	0.0105	0.0906	0.0009	0.20099	0.0669	0.00075	559	5.5	835	24	622	5.5	-33.0539	
LMF5_26.FIN2	0.977	0.011	0.1018	0.00095	0.22316	0.0698	0.0007	625	5.5	907	20	691	5.5	-31.0915	
LMF5_28.FIN2	1.263	0.04	0.0977	0.001	0.8563	0.0909	0.0023	601	6	1310	38.5	793	14	-54.1221	
LMF5_34.FIN2	9.84	0.415	0.2322	0.0043	0.97493	0.279	0.009	1339	22.5	3080	70	2204	48.5	-56.526	
LMF5_36.FIN2	0.776	0.0075	0.0863	0.0008	0.19385	0.0655	0.0006	533.6	4.9	790	18.5	582.5	4.25	-32.4557	
LMF5_40.FIN2	1.889	0.019	0.146	0.0016	-0.62114	0.0948	0.00125	878	9	1504	25	1076	6.5	-41.6223	
LMF5_45.FIN2	0.872	0.01	0.089	0.00085	0.052726	0.07	0.0008	550	5	930	23.5	636	5.5	-40.8602	
LMF5_46.FIN2	0.876	0.011	0.0938	0.0009	0.34769	0.0678	0.00075	578	5.5	842	22.5	637	6	-31.3539	
LMF5_48.FIN2	0.997	0.019	0.0982	0.001	0.47982	0.0729	0.0012	604	6	942	30.5	692	8.5	-35.8811	
LMF5_56.FIN2	2.863	0.0255	0.0683	0.00065	0.39268	0.3099	0.00245	425.6	3.9	3520	12.5	1372	6.5	-87.9091	

Spot	Pb^{207}/U^{235}	1σ	Pb^{206}/U^{238}	1σ	ρ	Pb^{207}/Pb^{206}	1σ	Pb^{206}/U^{238} age	1σ	Pb^{207}/Pb^{206} age	1σ	Pb^{207}/U^{235} age	1σ			
LMF5_62.FIN2	0.927	0.009	0.0883	0.00085	0.078924	0.0762	0.0007	545.2	4.95	1090	19	665.6	4.85	-49.9817		
LMF5_63.FIN2	1.045	0.0135	0.0875	0.0009	-0.2763	0.0869	0.00125	541	5.5	1340	29	726	6.5	-59.6269		
LMF5_65.FIN2	0.791	0.007	0.0875	0.00085	0.35244	0.0648	0.0005	540.7	4.9	767	17	591.6	4.1	-29.5046		
LMF5_66.FIN2	1.004	0.011	0.0904	0.00085	0.32633	0.0795	0.0008	558	5	1184	19.5	705	5.5	-52.8716		
LMF5_72.FIN2	1.055	0.022	0.0882	0.00105	0.37051	0.0872	0.0016	545	6	1365	36	725	10.5	-60.0733		
LMF5_75.FIN2	1.322	0.0215	0.1025	0.0011	0.21816	0.0952	0.00145	629	6.5	1517	29.5	857	9.5	-58.5366		
LMF5_76.FIN2	1.05	0.0125	0.1028	0.0011	0.57836	0.0748	0.0007	630	6.5	1063	19	729	6	-40.7338		
LMF5_77.FIN2	0.795	0.008	0.0832	0.00085	0.46821	0.0697	0.0006	515	5	922	18.5	593.9	4.45	-44.1432		
LMF5_78.FIN2	2.42	0.13	0.1393	0.00195	0.83368	0.126	0.0055	842	10.5	1890	60	1194	30	-55.4497		
LMF5_79.FIN2	39.5	1.05	0.321	0.01	0.73191	0.939	0.022	1779	48.5	5270	50	3732	24.5	-66.2429		
LMF5_81.FIN2	1.108	0.011	0.0894	0.0009	0.49813	0.0898	0.0008	552	5.5	1421	17	757	5.5	-61.1541		
LMF5_82.FIN2	1.182	0.034	0.0978	0.001	0.85928	0.0843	0.0016	601	6	1231	30	763	10.5	-51.1779		
LMF5_83.FIN2	1.097	0.012	0.0933	0.0009	0.12442	0.0853	0.0009	575	5.5	1327	20.5	751	5.5	-56.6692		
LMF5_86.FIN2	0.907	0.0135	0.0975	0.001	0.11962	0.068	0.00105	599	6	834	31.5	652	7	-28.1775		
LMF5_87.FIN2	0.759	0.009	0.0842	0.0009	0.32683	0.0647	0.0007	521	5.5	766	23.5	573	5	-31.9843		

Table B12. Sample LMF-5 check standards

Spot	Pb^{207}/U^{235}	1σ	Pb^{206}/U^{238}	1σ	ρ	Pb^{207}/Pb^{206}	1σ	Pb^{206}/U^{238} age	1σ	Pb^{207}/Pb^{206} age	1σ	Pb^{207}/U^{235} age	1σ
Pleso_1.FIN2	0.4142	0.00395	0.0567	0.00055	0.35078	0.05327	0.000455	355.4	3.25	334	19	352.1	2.85
temora_1.FIN2	0.501	0.007	0.0658	0.0007	0.12027	0.0555	0.0008	410.9	4.2	404	31	411.5	4.9
Gj1_1.FIN2	0.822	0.008	0.099	0.00095	0.3915	0.0605	0.0005	609	5.5	619	18.5	609	4.5

GJ1_2.FIN2	0.831	0.008	0.0999	0.00095	0.29135	0.0608	0.00055	614	5.5	628	19	614.3	4.45
Pleso_2.FIN2	0.4095	0.0039	0.056	0.0005	0.26039	0.05293	0.00046	351.3	3.2	317	19.5	348.7	2.85
Temora_2.FIN2	0.491	0.0075	0.0671	0.0007	0.16636	0.0529	0.0008	418.9	4.35	303	30.5	404	5
Pleso_3.FIN2	0.4163	0.00395	0.0568	0.00055	0.20777	0.05314	0.000465	356.2	3.25	326	20	353.4	2.85
GJ1_3.FIN2	0.819	0.008	0.0981	0.00095	0.44837	0.0606	0.00055	604	5.5	625	19	606.9	4.5
Pleso_4.FIN2	0.4128	0.00395	0.0564	0.00055	0.24628	0.05286	0.000465	353.8	3.25	318	19.5	350.9	2.85
temora-3.FIN2	0.486	0.0065	0.0644	0.0007	0.15709	0.0552	0.00075	402.2	4.1	382	28	400.7	4.55
GJ1_4.FIN2	0.823	0.008	0.0982	0.00095	0.31596	0.0612	0.00055	604	5.5	644	19	609.8	4.4
Pleso_5.FIN2	0.4057	0.00385	0.0554	0.0005	0.30845	0.05327	0.000455	347.7	3.15	335	19.5	345.9	2.85
pleso_6.FIN2	0.4124	0.00395	0.0566	0.00055	0.43453	0.05275	0.00044	354.8	3.2	318	18.5	350.3	2.85
GJ1-5.FIN2	0.808	0.008	0.0985	0.00095	0.26278	0.0593	0.00055	606	5.5	577	19.5	600.9	4.45
Temora-5.FIN2	0.472	0.0065	0.0649	0.00065	0.18201	0.0526	0.0007	405.4	4	290	27.5	392.1	4.3
gj1-6.FIN2	0.806	0.008	0.0986	0.00095	0.37493	0.0606	0.00055	606	5.5	621	19	600	4.45
gj1-7.FIN2	0.832	0.008	0.1003	0.00095	0.28261	0.0602	0.0005	616	5.5	610	19	614.9	4.5
pleso-7.FIN2	0.4194	0.00405	0.0563	0.00055	0.31791	0.05365	0.00046	353.1	3.25	358	20	355.8	2.95
temora-6.FIN2	0.489	0.0065	0.0654	0.00065	0.18371	0.0542	0.0007	408.4	4.05	357	28.5	404.1	4.45
Notes:													
Error= 1 sigma													
Rho (ρ)= error correlation													
all data corrected for common Pb													
Pleso=Plesovitch (337 Ma)													
Tem=Temora (417 Ma)													
GJ-1= 609 Ma													

Table B13. Sample LP-3

Spot	Pb^{207}/U^{235}	1σ	Pb^{206}/U^{238}	1σ	ρ	Pb^{207}/Pb^{206}	1σ	Pb^{206}/U^{238} age	1σ	Pb^{207}/Pb^{206} age	1σ	Pb^{207}/U^{235} age	1σ	%disc	Best Age	2σ
	Location: 32° 23.220' S, 54° 6.34' W															
lp3_1. FIN2	1.757	0.0425	0.1699	0.00415	0.22524	0.0747	0.00044	1011	23	1065	12	1030	16	-5.07042	1011	46
lp3_2. FIN2	6.46	0.155	0.366	0.009	0.38302	0.12703	0.00047	2014	41.5	2057	6.5	2040	21	-2.09042	2057	13
lp3_3. FIN2	5.7	0.135	0.338	0.008	0.56379	0.12196	0.000335	1877	39.5	1984	4.85	1931	20.5	-5.39315	1984	9.7
lp3_4. FIN2	1.075	0.027	0.1197	0.003	0.4248	0.0651	0.00055	729	17	777	16.5	741	13	-6.17761	729	34
lp3_5. FIN2	0.731	0.0185	0.0881	0.00225	0.19415	0.0595	0.00075	544	13.5	594	26.5	557	11	-8.41751	544	27
lp3_6. FIN2	1.141	0.0275	0.1206	0.00295	0.51654	0.06787	0.00023	734	17	864	7	773	13	-15.0463	734	34
lp3_7. FIN2	0.903	0.0225	0.1048	0.00265	0.57822	0.06253	0.00041	642	15.5	693	14	654	12	-7.35931	642	31
lp3_8. FIN2	0.687	0.018	0.0852	0.00215	0.27485	0.0581	0.00065	527	12.5	531	24.5	530	11	-0.7533	527	25
lp3_9. FIN2	1.963	0.048	0.1862	0.00465	0.28607	0.0762	0.0005	1101	25	1099	13	1104	16.5	0.181984	1101	50
lp3_10 .FIN2	1.141	0.0275	0.1254	0.00305	0.4737	0.0657	0.00024	761	17.5	797	8	773	13	-4.51694	761	35
lp3_11 .FIN2	6.57	0.16	0.364	0.009	0.55238	0.1296	0.00055	2002	42	2091	7.5	2056	22	-4.25634	2091	15
lp3_12 .FIN2	1.789	0.043	0.1691	0.00415	0.70451	0.0761	0.000235	1007	23	1098	6	1041	16	-8.2878	1007	46
lp3_13 .FIN2	0.731	0.0175	0.0888	0.00215	0.29207	0.0591	0.00029	549	13	570	10.5	557	10.5	-3.68421	549	26

lp3_14 .FIN2	0.693	0.0175	0.0853	0.00215	0.4042	0.0586	0.00055	527	13	543	20	536	11	-2.94659	527	26
lp3_15 .FIN2	0.681	0.0165	0.0843	0.00205	0.16271	0.05828	0.000325	522	12	549	12	528	10	-4.91803	522	24
lp3_16 .FIN2	0.694	0.017	0.0854	0.0021	0.33057	0.05838	0.00033	528	12.5	539	12	535	10	-2.04082	528	25
lp3_17 .FIN2	0.716	0.018	0.0833	0.00205	0.1722	0.0616	0.0005	516	12	652	17.5	547	10.5	-20.8589	516	24
lp3_18 .FIN2	0.9	0.023	0.1045	0.00255	0.18541	0.062	0.00065	640	15	657	22.5	650	12.5	-2.58752	640	30
lp3_19 .FIN2	0.698	0.017	0.087	0.0021	0.27106	0.0581	0.000315	538	12.5	524	12	537	10	2.671756	538	25
lp3_20 .FIN2	6.11	0.145	0.351	0.0085	0.44771	0.1256	0.0005	1938	41	2033	7.5	1992	21	-4.6729	2033	15
lp3_21 .FIN2	0.88	0.0215	0.1035	0.0025	0.33023	0.06106	0.000345	635	14.5	645	12	641	11.5	-1.55039	635	29
lp3_22 .FIN2	0.882	0.0215	0.1038	0.00255	0.28201	0.06121	0.00031	637	15	648	11	642	11.5	-1.69753	637	30
lp3_23 .FIN2	1.161	0.028	0.1259	0.00305	0.31896	0.06646	0.000315	764	17.5	819	10	783	13.5	-6.71551	764	35
lp3_24 .FIN2	0.691	0.0165	0.0847	0.00205	0.27735	0.05888	0.00034	524	12.5	557	12.5	533	10	-5.9246	524	25
lp3_25 .FIN2	0.681	0.0165	0.0809	0.002	0.33166	0.06086	0.00036	502	12	631	12.5	526	10	-20.4437	502	24
lp3_26 .FIN2	0.784	0.019	0.0945	0.0023	0.27174	0.05995	0.0003	582	13.5	598	11	588	10.5	-2.67559	582	27
lp3_27 .FIN2	0.692	0.0175	0.0857	0.00215	0.31738	0.059	0.0005	530	12.5	565	19	534	10.5	-6.19469	530	25
lp3_28 .FIN2	0.683	0.0165	0.0852	0.00205	0.43898	0.05797	0.00029	527	12.5	526	11	530	10	0.190114	527	25
lp3_29 .FIN2	0.737	0.0195	0.09	0.0023	0.30813	0.0586	0.00065	555	13.5	543	24.5	561	11	2.209945	555	27
lp3_30 .FIN2	0.719	0.0175	0.0868	0.0021	0.44848	0.06004	0.000295	537	12.5	601	10.5	550	10	-10.6489	537	25
lp3_31 .FIN2	0.725	0.0175	0.0892	0.00215	0.34861	0.05937	0.00029	551	13	576	10.5	553	10	-4.34028	551	26
lp3_32 .FIN2	0.685	0.017	0.0862	0.0021	0.23685	0.05759	0.00037	533	12.5	509	14	529	10	4.715128	533	25
lp3_33 .FIN2	0.703	0.0175	0.0848	0.00205	0.26602	0.06054	0.000425	525	12.5	624	15	540	10	-15.8654	525	25
lp3_34 .FIN2	0.683	0.017	0.0858	0.0021	0.26907	0.05826	0.000405	531	12.5	536	15.5	528	10	-0.93284	531	25
lp3_36 .FIN2	0.911	0.022	0.1082	0.00265	0.22765	0.06157	0.00036	663	15.5	657	12.5	657	11.5	0.913242	663	31

Spot	Pb^{207}/U^{235}	1σ	Pb^{206}/U^{238}	1σ	ρ	Pb^{207}/Pb^{206}	1σ	Pb^{206}/U^{238} age	1σ	Pb^{207}/Pb^{206} age	1σ	Pb^{207}/U^{235} age	1σ			
lp3_37.FIN2	0.731	0.018	0.0875	0.00215	0.36895	0.06151	0.00033	540	12.5	653	11.5	557	10.5	-17.3047	540	25
lp3_38.FIN2	1.273	0.0315	0.1251	0.00315	0.7523	0.07465	0.000405	759	18	1059	11	833	14	-28.3286	759	36
lp3_39.FIN2	0.745	0.0185	0.0929	0.00225	0.19118	0.05871	0.00041	572	13.5	548	15.5	565	11	4.379562	572	27
lp3_40.FIN2	0.873	0.021	0.1052	0.00255	0.55224	0.06099	0.000215	645	15	638	7.5	637	11.5	1.097179	645	30
lp3_41.FIN2	0.945	0.024	0.1044	0.00255	0.16329	0.0663	0.00065	640	15	810	20.5	676	12.5	-20.9877	640	30
lp3_42.FIN2	0.734	0.0185	0.0888	0.0022	0.4557	0.0603	0.000445	548	13	615	16	558	10.5	-10.8943	548	26
Notes:																
Error= 1 sigma (except best age error= 2 sigma)																
Rho (ρ)= error correlation																
% discordance = (1-(206/238 age)/(207/206 age))*-100																
red colored data (highlighted below) = data below quality standards																
all data corrected for common Pb																
lp3_35.FIN2	0.863	0.023	0.0922	0.0023	0.3591	0.0688	0.00085	569	13.5	886	24	631	12.5	-35.7788		

Table B14. Sample LP-3 check standards

Spot	Pb^{207}/U^{235}	1σ	Pb^{206}/U^{238}	1σ	ρ	Pb^{207}/Pb^{206}	1σ	Pb^{206}/U^{238} age	1σ	Pb^{207}/Pb^{206} age	1σ	Pb^{207}/U^{235} age	1σ
Pleso-1.FIN2	0.39	0.0095	0.0527	0.0013	0.40389	0.05355	0.000235	331	8	351	10	334	7
Temora-1.FIN2	0.504	0.0125	0.0659	0.0016	0.20405	0.05524	0.00037	412	9.5	425	15	415	8.5

GJ1-1.FIN2	0.828	0.02	0.0997	0.0024	0.4656	0.05996	0.000255	613	14	599	9	612	11
Pleso_3.FIN2	0.393	0.0095	0.0532	0.0013	0.35921	0.05302	0.000225	334	8	327	9.5	336	7
Pleso_4.FIN2	0.4	0.0095	0.0541	0.0013	0.20766	0.05367	0.000285	340	8	356	12	342	7
Notes:													
Error= 1 sigma													
Rho (ρ)= error correlation													
all data corrected for common Pb													
Pleso=Plesovitch (337 Ma)													
Tem=Temora (417 Ma)													
GJ-1= 609 Ma													

Table B15. Sample SUS-1

	Location: 30.76761° S, 54.27878° W															
Spot	Pb^{207}/U^{235}	1σ	Pb^{206}/U^{238}	1σ	ρ	Pb^{207}/Pb^{206}	1σ	Pb^{206}/U^{238} age	1σ	Pb^{207}/Pb^{206} age	1σ	Pb^{207}/U^{235} age	1σ	%disc	Best Age	2σ
sus_1.FIN2	1.123	0.015	0.123	0.0015	0.41518	0.06607	0.000265	748	8.5	810	8.5	764	7	-7.65432	748	17
sus_2.FIN2	0.785	0.011	0.091	0.0011	0.30227	0.06277	0.00036	562	6.5	694	12	587	6.5	-19.0202	562	13
sus_3.FIN2	9.88	0.13	0.439	0.0055	0.63572	0.16309	0.000475	2344	23.5	2486.2	4.9	2423	12	-5.71957	2486.2	9.8
sus_6.FIN2	0.839	0.014	0.1013	0.00125	0.10301	0.0602	0.00065	622	7.5	594	24	617	7.5	4.713805	622	15
sus_7.FIN2	7.09	0.095	0.3601	0.0044	0.61364	0.14251	0.000485	1982	21	2258	6	2122	12	-12.2232	2258	12
sus_9.FIN2	0.754	0.0115	0.091	0.0011	0.14209	0.0601	0.00055	561	6.5	585	19.5	570	7	-4.10256	561	13
sus_10.FIN2	0.987	0.0135	0.1113	0.00135	0.32211	0.06427	0.000335	680	8	746	11	698	7	-8.84718	680	16

sus_11 .FIN2	0.876	0.0125	0.1021	0.00125	0.20755	0.06218	0.00044	627	7.5	683	15	638	7	-8.19912	627	15
sus_13 .FIN2	5.01	0.085	0.2996	0.00405	0.24211	0.12	0.0014	1688	20	1971	20.5	1817	14	-14.3582	1971	41
sus_14 .FIN2	0.753	0.013	0.0936	0.00115	0.033072	0.058	0.0007	576	7	527	26	568	7.5	9.297913	576	14
sus_15 .FIN2	0.865	0.0115	0.0995	0.0012	0.34526	0.06304	0.00027	612	7	706	9	632	6.5	-13.3144	612	14
sus_16 .FIN2	0.686	0.01	0.0823	0.00115	0.4257	0.06133	0.00047	509	7	643	16	530	6	-20.8398	509	14
sus_17 .FIN2	0.734	0.0125	0.0924	0.0012	0.17575	0.0578	0.00065	570	7	493	24.5	559	7.5	15.61866	570	14
sus_18 .FIN2	6.08	0.085	0.3375	0.00415	0.61654	0.1313	0.00055	1875	20	2114	7.5	1985	12	-11.3056	2114	15
sus_21 .FIN2	0.726	0.012	0.0914	0.00115	0.13567	0.0583	0.00065	564	6.5	506	24.5	552	7	11.46245	564	13
sus_22 .FIN2	0.805	0.011	0.0956	0.00115	0.27794	0.06121	0.00028	589	6.5	645	9.5	600	6	-8.68217	589	13
sus_23 .FIN2	5.95	0.08	0.3253	0.0041	0.78415	0.13328	0.000425	1815	20	2140	5.5	1967	12	-15.1869	2140	11
sus_24 .FIN2	0.797	0.0115	0.0959	0.00115	0.10212	0.06075	0.00045	590	7	622	16	595	6.5	-5.14469	590	14
sus_25 .FIN2	7.11	0.095	0.3714	0.00445	0.41481	0.1394	0.00055	2036	21	2219	6.5	2124	12	-8.24696	2219	13
sus_26 .FIN2	0.832	0.016	0.0998	0.00135	0.093409	0.0603	0.0009	614	7.5	564	31.5	612	9	8.865248	614	15
sus_27 .FIN2	6.97	0.095	0.3644	0.0044	0.5172	0.13989	0.00047	2002	20.5	2225	6	2107	12	-10.0225	2225	12
sus_28 .FIN2	0.768	0.011	0.0935	0.00115	0.17406	0.05958	0.000405	576	6.5	594	14.5	578	6.5	-3.0303	576	13
sus_29 .FIN2	0.897	0.0125	0.1038	0.00125	0.18406	0.0627	0.000395	636	7.5	695	13.5	651	7	-8.48921	636	15
sus_30 .FIN2	0.714	0.0115	0.0896	0.0011	0.063874	0.0579	0.00055	553	6.5	525	21.5	546	6.5	5.333333	553	13
sus_31 .FIN2	0.779	0.017	0.0981	0.0013	0.11809	0.0583	0.00105	603	7.5	495	37	581	9.5	21.81818	603	15
sus_32 .FIN2	0.841	0.0115	0.1009	0.0012	0.21761	0.06072	0.00035	620	7	625	12.5	619	6.5	-0.8	620	14
sus_33 .FIN2	0.781	0.011	0.092	0.0011	0.1999	0.0616	0.000335	567	6.5	668	11.5	586	6	-15.1198	567	13
sus_34 .FIN2	0.734	0.0125	0.0921	0.00115	0.10693	0.0582	0.0007	568	7	516	25	557	7	10.07752	568	14
sus_35 .FIN2	0.814	0.0115	0.0963	0.00115	0.29908	0.06188	0.00034	593	7	667	11.5	605	6	-11.0945	593	14

sus_36 .FIN2	0.79	0.011	0.0953	0.00115	0.25593	0.06072	0.00035	587	6.5	629	12	592	6	-6.67727	587	13
sus_37 .FIN2	0.822	0.012	0.0952	0.00115	0.10463	0.0625	0.00055	586	7	689	18.5	608	6.5	-14.9492	586	14
sus_38 .FIN2	4.56	0.065	0.3092	0.0039	0.3176	0.1078	0.00075	1736	19	1763	12.5	1742	12	-1.53148	1763	25
sus_39 .FIN2	0.835	0.0115	0.0952	0.00115	0.39145	0.06382	0.000275	586	7	739	9	616	6.5	-20.7037	586	14
sus_40 .FIN2	0.836	0.0135	0.1003	0.00125	0.37818	0.0598	0.00055	616	7.5	585	20	614	7.5	5.299145	616	15
sus_41 .FIN2	0.902	0.012	0.1051	0.00125	0.32543	0.06201	0.00029	644	7.5	679	10	653	6.5	-5.15464	644	15
sus_44 .FIN2	0.83	0.0115	0.0935	0.0011	0.11115	0.06446	0.000375	576	6.5	751	12.5	614	6.5	-23.3023	576	13
sus_45 .FIN2	0.939	0.013	0.1114	0.00135	0.27698	0.06124	0.00034	681	7.5	647	12	672	7	5.255023	681	15
sus_46 .FIN2	0.703	0.0095	0.0833	0.001	0.078952	0.06229	0.00042	515	6	669	14	540	5.5	-23.0194	515	12
sus_47 .FIN2	0.819	0.0115	0.0995	0.0012	0.20312	0.06012	0.000365	612	7	604	13	607	6.5	1.324503	612	14
sus_49 .FIN2	1.741	0.0245	0.1693	0.00205	0.37704	0.07444	0.00039	1008	11	1046	10.5	1022	9	-3.63289	1008	22
sus_51 .FIN2	0.736	0.01	0.0901	0.0011	0.59901	0.05924	0.00029	556	6.5	576	10.5	559	6	-3.47222	556	13
sus_52 .FIN2	0.761	0.012	0.0913	0.00115	0.1563	0.0606	0.0006	563	6.5	605	20.5	573	7	-6.94215	563	13
sus_53 .FIN2	8.99	0.125	0.403	0.005	0.84911	0.1616	0.00045	2185	23.5	2471.5	4.65	2334	12.5	-11.5922	2471.5	9.3
sus_54 .FIN2	6.03	0.08	0.3453	0.00415	0.5279	0.1273	0.0005	1911	20	2065	7	1980	12	-7.45763	2065	14
sus_55 .FIN2	0.798	0.011	0.0954	0.00115	0.22746	0.06083	0.0003	588	6.5	631	10.5	595	6	-6.81458	588	13
sus_56 .FIN2	0.838	0.0115	0.0977	0.00115	0.2872	0.06193	0.00027	601	7	668	9	618	6	-10.0299	601	14
sus_58 .FIN2	5.38	0.085	0.3061	0.00405	0.38695	0.1277	0.0011	1722	20	2054	15	1881	13.5	-16.1636	2054	30
sus_59 .FIN2	0.807	0.0115	0.0972	0.0012	0.21289	0.0599	0.000415	598	7	597	15	601	6.5	0.167504	598	14
sus_61 .FIN2	1.053	0.014	0.1107	0.00135	0.30809	0.06909	0.000275	677	7.5	900	8	730	7	-24.7778	677	15
sus_62 .FIN2	0.753	0.0105	0.0877	0.00105	0.36587	0.06259	0.0003	542	6	694	10	570	6	-21.902	542	12
sus_63 .FIN2	0.709	0.0105	0.0879	0.00105	0.15893	0.05877	0.000485	543	6.5	547	18	543	6.5	-0.73126	543	13

sus_65 .FIN2	1.17	0.016	0.1293	0.00155	0.23806	0.06579	0.00032	784	9	800	10	787	7.5	-2	784	18
sus_68 .FIN2	6.69	0.09	0.3787	0.00455	0.52607	0.12866	0.000475	2071	21	2080	6.5	2071	12	-0.43269	2080	13
sus_69 .FIN2	1.409	0.0195	0.1406	0.00175	0.67508	0.07311	0.000315	848	10	1017	8.5	892	8.5	-16.6175	848	20
sus_70 .FIN2	0.768	0.012	0.0949	0.0012	0.28123	0.0589	0.0005	584	7	561	19.5	579	7	4.099822	584	14
sus_71 .FIN2	0.833	0.017	0.1011	0.0014	0.14858	0.0597	0.00095	620	8	576	34.5	614	9	7.638889	620	16
sus_74 .FIN2	0.849	0.012	0.1018	0.00125	0.2236	0.06012	0.00039	625	7	601	14	624	6.5	3.993344	625	14
sus_75 .FIN2	0.784	0.0125	0.0963	0.0012	0.072615	0.0588	0.0006	593	7	552	23	587	7	7.427536	593	14
sus_76 .FIN2	1.026	0.015	0.1214	0.0015	0.27986	0.06138	0.000435	738	8.5	650	15	716	7.5	13.53846	738	17
sus_77 .FIN2	1.069	0.0185	0.1275	0.00165	0.094647	0.0613	0.0008	774	9.5	625	26	739	9	23.84	774	19
Notes:																
Error= 1 sigma (except best age error= 2 sigma)																
Rho (ρ)= error correlation																
% discordance = (1-(206/238 age)/(207/206 age))*-100																
red colored data (highlighted below) = data below quality standards																
all data corrected for common Pb																
sus_4. FIN2	0.748	0.01	0.0703	0.00085	0.43377	0.07688	0.000285	438	5	1117	7.5	567	6	-60.7878		
sus_5. FIN2	35.9	0.6	0.365	0.0065	0.49347	0.721	0.009	2012	29	4781	20.5	3664	17.5	-57.9168		
sus_8. FIN2	0.851	0.0125	0.0901	0.0011	0.33597	0.06841	0.000435	556	6.5	885	13	625	6.5	-37.1751		
sus_12 .FIN2	1.319	0.0305	0.1039	0.0014	0.28408	0.0912	0.0016	638	8	1406	33.5	846	13.5	-54.623		
sus_19 .FIN2	1.88	0.085	0.1149	0.0016	0.90125	0.113	0.0039	701	9.5	1650	55	1017	26.5	-57.5152		
sus_20 .FIN2	0.74	0.0105	0.0694	0.00105	0.70764	0.0779	0.00055	433	6.5	1145	14	562	6	-62.1834		
sus_42 .FIN2	0.866	0.0115	0.0708	0.0009	0.29612	0.09	0.00055	441	5.5	1428	11.5	633	6.5	-69.1176		

Spot													
sus_43.FIN2	0.803	0.011	0.0901	0.00115	0.37712	0.06474	0.000365	556	7	768	12	598	6.5	-27.6042
sus_48.FIN2	4.42	0.07	0.2619	0.0039	0.94761	0.12325	0.00033	1497	20	2005.1	4.85	1709	13	-25.3404
sus_50.FIN2	0.895	0.0125	0.076	0.00115	0.55998	0.0868	0.0007	472	7	1351	15.5	649	6.5	-65.0629
sus_57.FIN2	5.86	0.095	0.2199	0.0032	0.95765	0.1928	0.00055	1279	16.5	2767.7	4.55	1950	13.5	-53.7883
sus_60.FIN2	1.74	0.024	0.1205	0.00145	0.3396	0.1043	0.0005	733	8.5	1705	9	1023	9	-57.0088
sus_64.FIN2	0.845	0.012	0.0873	0.0013	0.27422	0.0711	0.0007	539	7.5	948	19.5	621	6.5	-43.1435
sus_66.FIN2	0.78	0.012	0.0654	0.0016	0.8285	0.0974	0.00175	406	10	1472	33	584	7	-72.4185
sus_67.FIN2	0.826	0.011	0.0866	0.00105	0.35099	0.0699	0.000345	535	6	928	10	611	6	-42.3491
sus_72.FIN2	1.22	0.029	0.113	0.0028	0.61669	0.0841	0.0009	688	16	1288	21	800	12	-46.5839
sus_73.FIN2	6.61	0.24	0.277	0.0085	0.14634	0.181	0.0055	1564	41.5	2600	60	2057	32.5	-39.8462

Table B16. Sample SUS-1 check standards

Spot	Pb^{207}/U^{235}	1σ	Pb^{206}/U^{238}	1σ	ρ	Pb^{207}/Pb^{206}	1σ	Pb^{206}/U^{238} age	1σ	Pb^{207}/Pb^{206} age	1σ	Pb^{207}/U^{235} age	1σ
Pleso_1.FIN2	0.39	0.0055	0.0523	0.00065	0.41544	0.05414	0.000255	328.8	3.9	381	10.5	334.7	3.9
temora_1.FIN2	0.49	0.0075	0.0653	0.0008	0.22485	0.0548	0.0005	407.7	4.85	390	20	404	5.5
Gj1_1.FIN2	0.81	0.011	0.0976	0.0012	0.42917	0.06051	0.000275	600	7	621	10	602	6
GJ1_2.FIN2	0.837	0.0115	0.0995	0.0012	0.35541	0.06092	0.0003	611	7	632	10.5	618	6.5
Pleso_2.FIN2	0.383	0.0055	0.0521	0.00065	0.25416	0.05358	0.000285	327.6	3.85	346	12	330	3.85
Temora_2.FIN2	0.475	0.008	0.0643	0.0008	0.043736	0.0535	0.00065	401.9	4.8	343	25	395	5.5
Pleso_3.FIN2	0.38	0.005	0.0517	0.0006	0.31335	0.0534	0.00027	325.2	3.8	338	11.5	327.4	3.85
GJ1_3.FIN2	0.813	0.011	0.0983	0.0012	0.37161	0.06011	0.00028	604	7	601	10.5	604	6
Pleso_4.FIN2	0.407	0.0055	0.0551	0.00065	0.29328	0.05338	0.000255	346	4.05	340	10.5	346.7	3.95

temora-3.FIN2	0.499	0.008	0.0687	0.00085	0.10256	0.0522	0.00055	428	5	295	23	410	5.5
GJ1_4.FIN2	0.851	0.0115	0.1017	0.0012	0.33098	0.06084	0.00029	625	7	633	10	625	6.5
Pleso_5.FIN2	0.405	0.0055	0.0554	0.00065	0.29468	0.05318	0.00026	347.5	4.05	331	11	345.1	4
pleso_6.FIN2	0.402	0.0055	0.0552	0.00065	0.34413	0.05287	0.000245	346.4	4.05	328	10.5	343.4	3.95
GJ1-5.FIN2	0.882	0.012	0.1067	0.00125	0.27427	0.06009	0.000285	653	7.5	606	10.5	642	6.5
Temora-5.FIN2	0.52	0.008	0.0703	0.00085	0.12389	0.05397	0.00046	438	5	356	18.5	426	5
pleso-7.FIN2	0.417	0.0055	0.0559	0.00065	0.3199	0.05402	0.000265	350.9	4.1	370	11	353.5	4.15
gj1-6.FIN2	0.885	0.012	0.1062	0.00125	0.38136	0.06038	0.000275	651	7.5	614	9.5	644	6.5
temora6.FIN2	0.523	0.008	0.0707	0.00085	0.1105	0.05388	0.00048	440	5	351	19.5	427	5
Notes:												
Error= 1 sigma												
Rho (ρ)= error correlation												
all data corrected for common Pb												
Pleso=Plesovitch (337 Ma)												
Tem=Temora (417 Ma)												
GJ-1= 609 Ma												

Fig. B1. MDP6 concordia plot
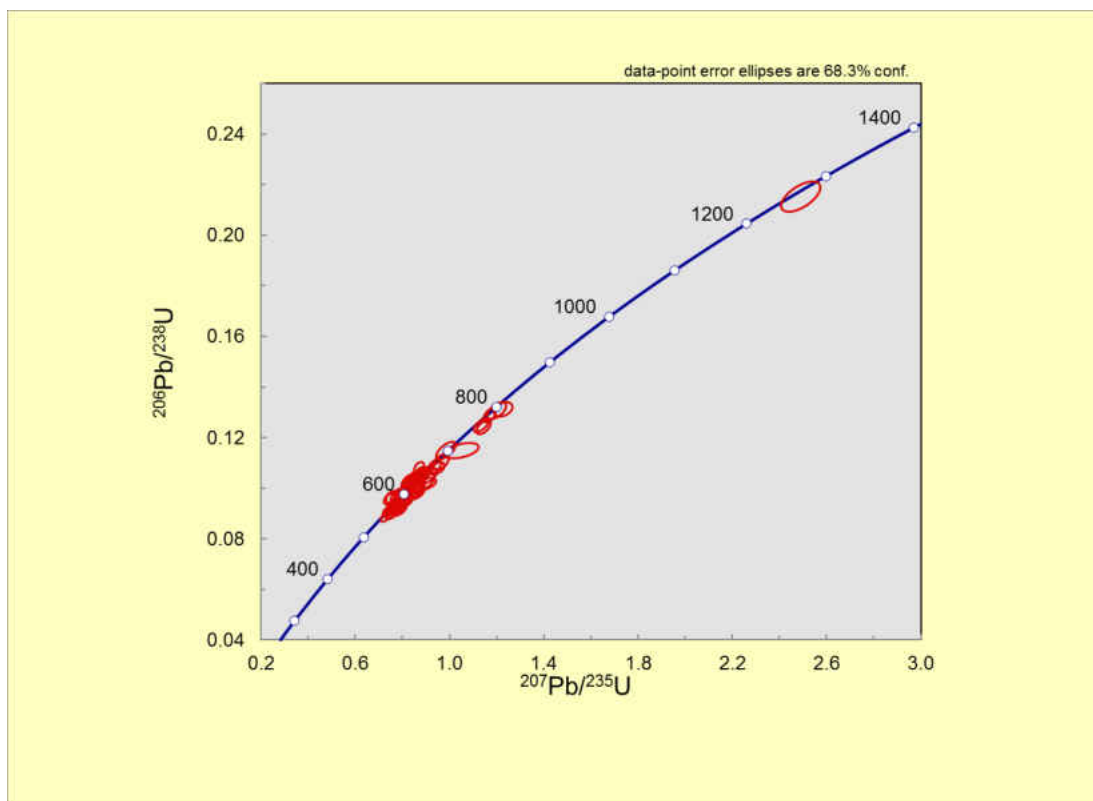
Fig. B2. MDP6 check standards concordia plot

Fig. B3. MP concordia Plot

data-point error ellipses are 68.3% conf.
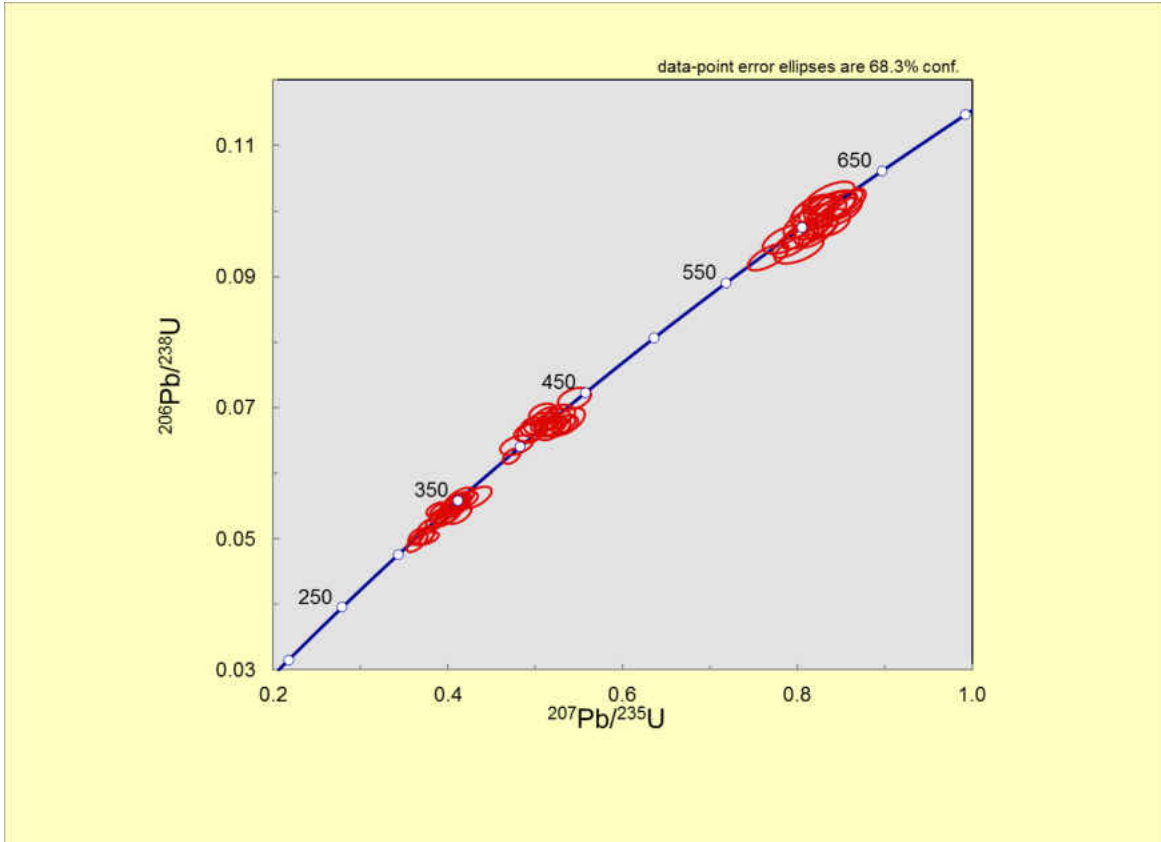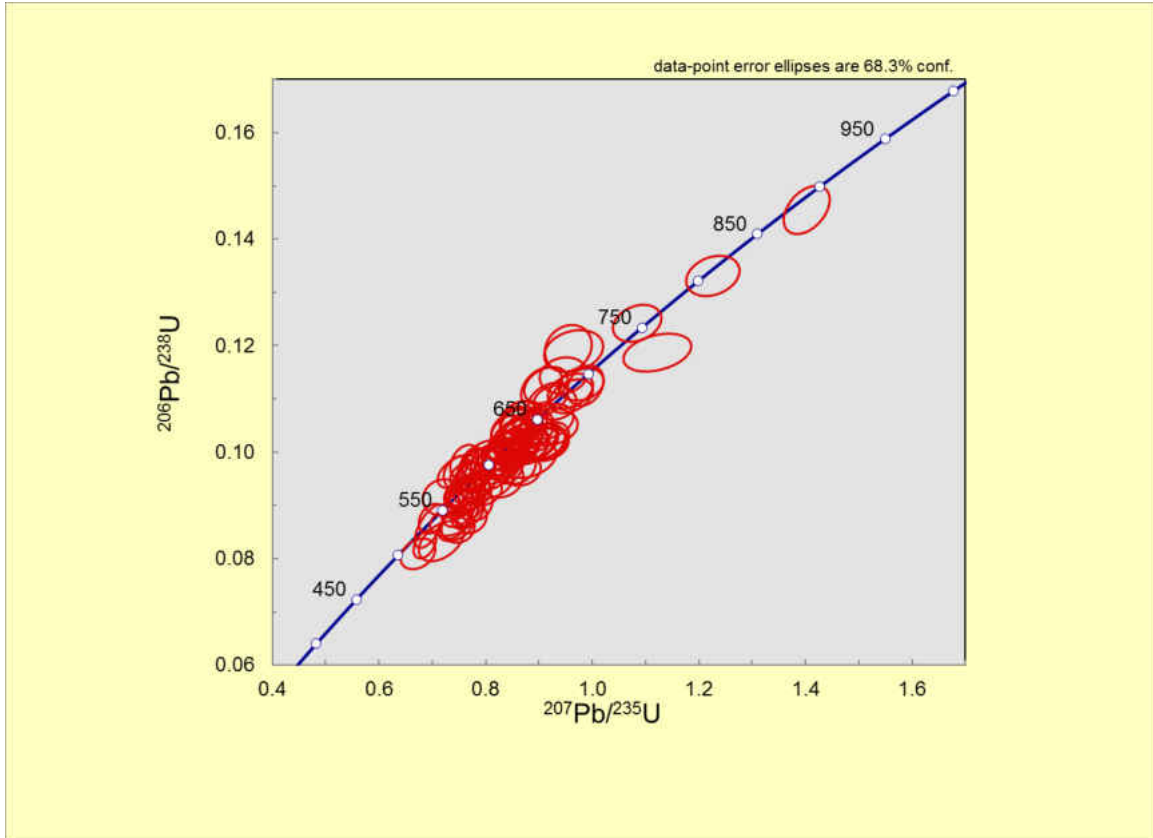
Fig. B4. MP check standards concordia plot
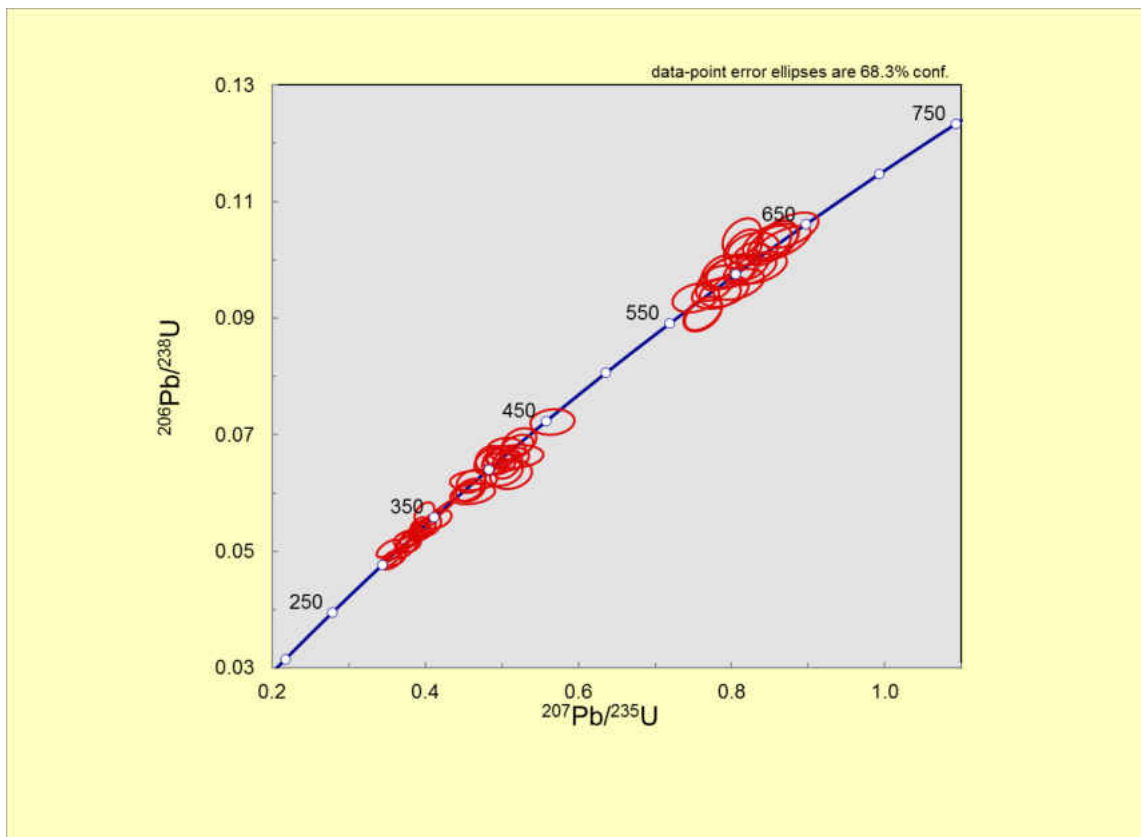
Fig. B5. AND-1 concordia Plot
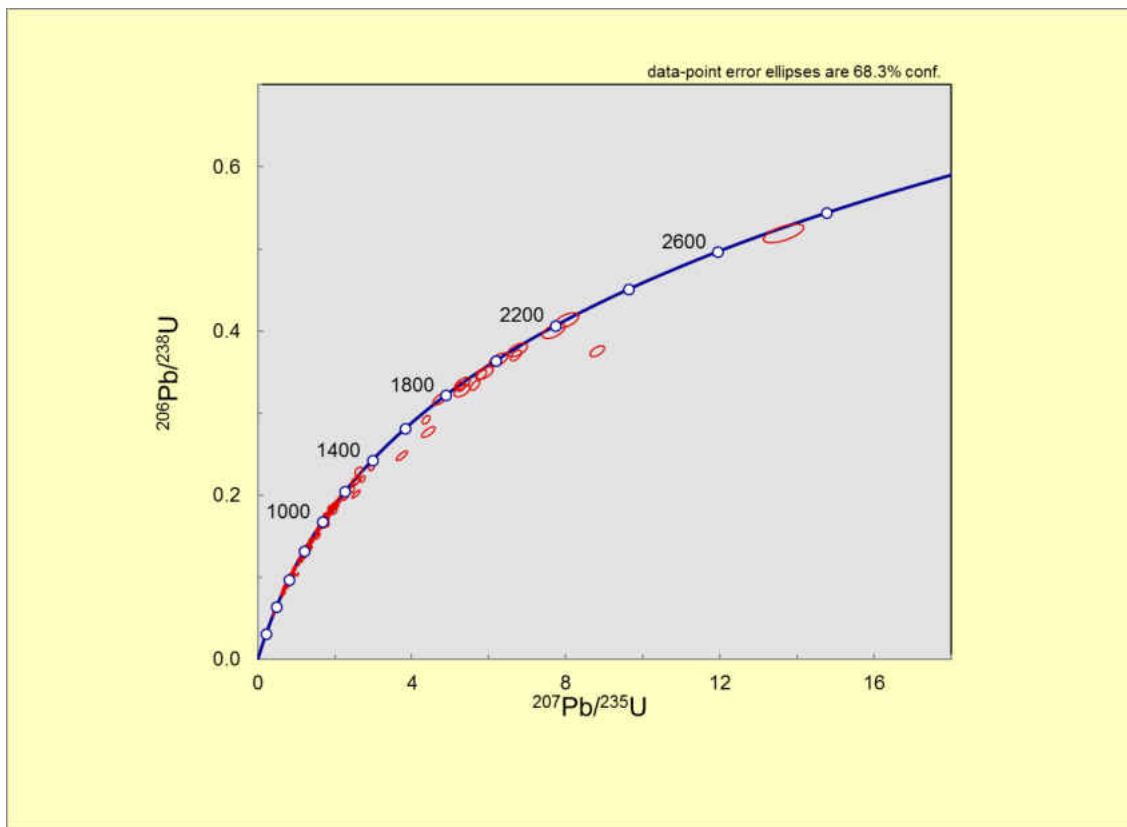
Fig. B6. AND-1 check standards concordia plot
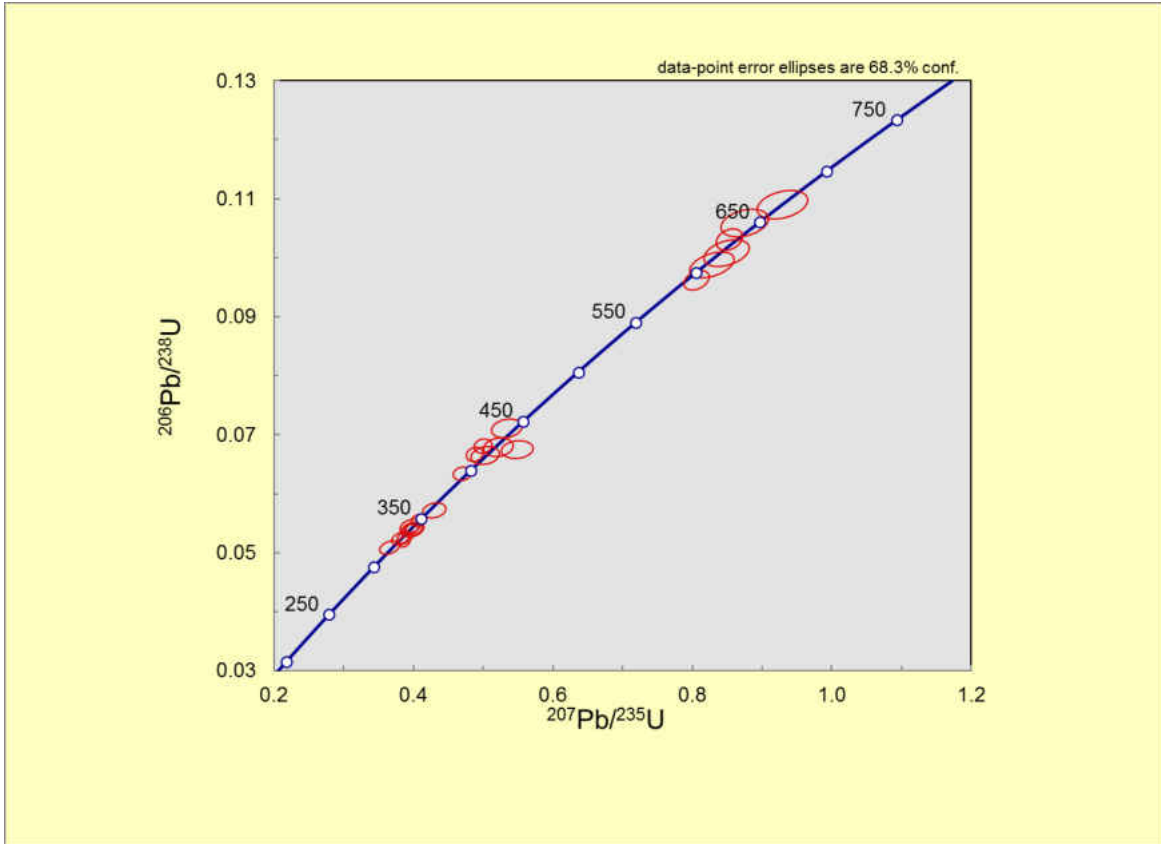
Fig. B7. LMF-2 concordia plot
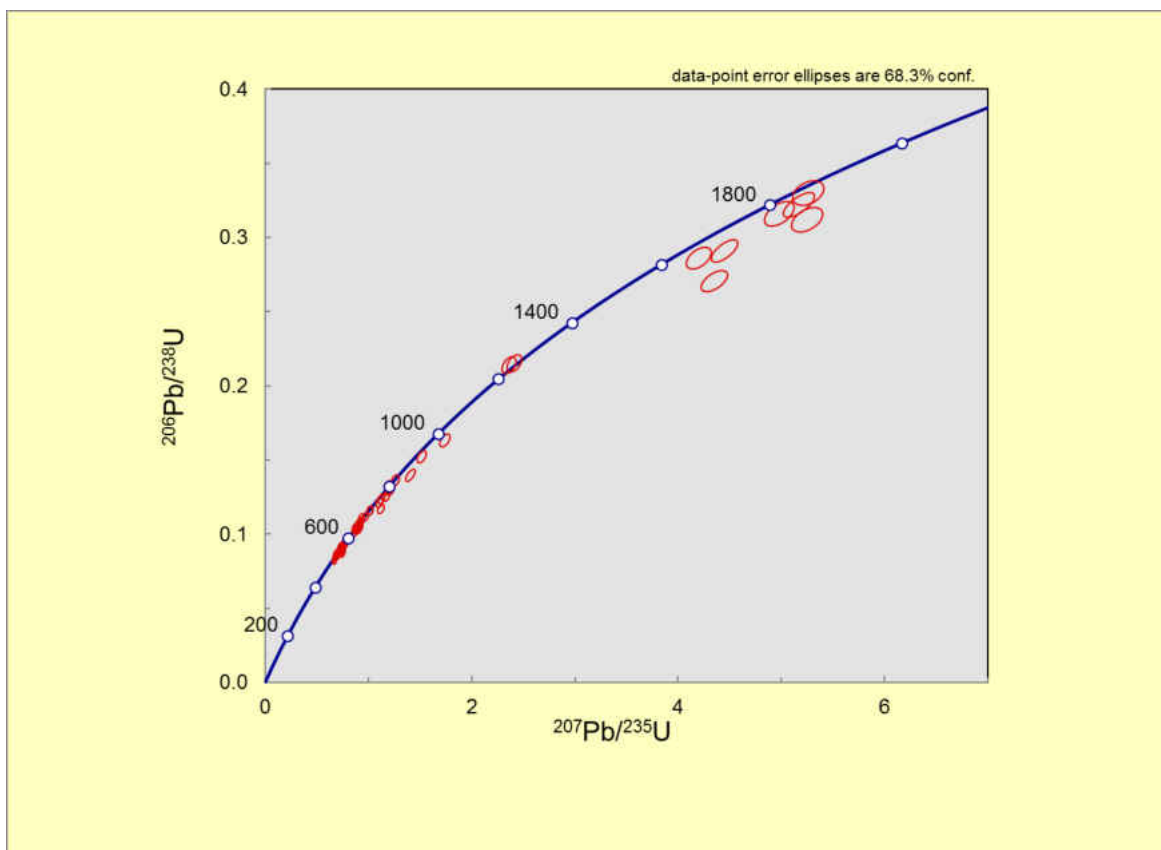
Fig. B8. LMF-2 check standards concordia plot
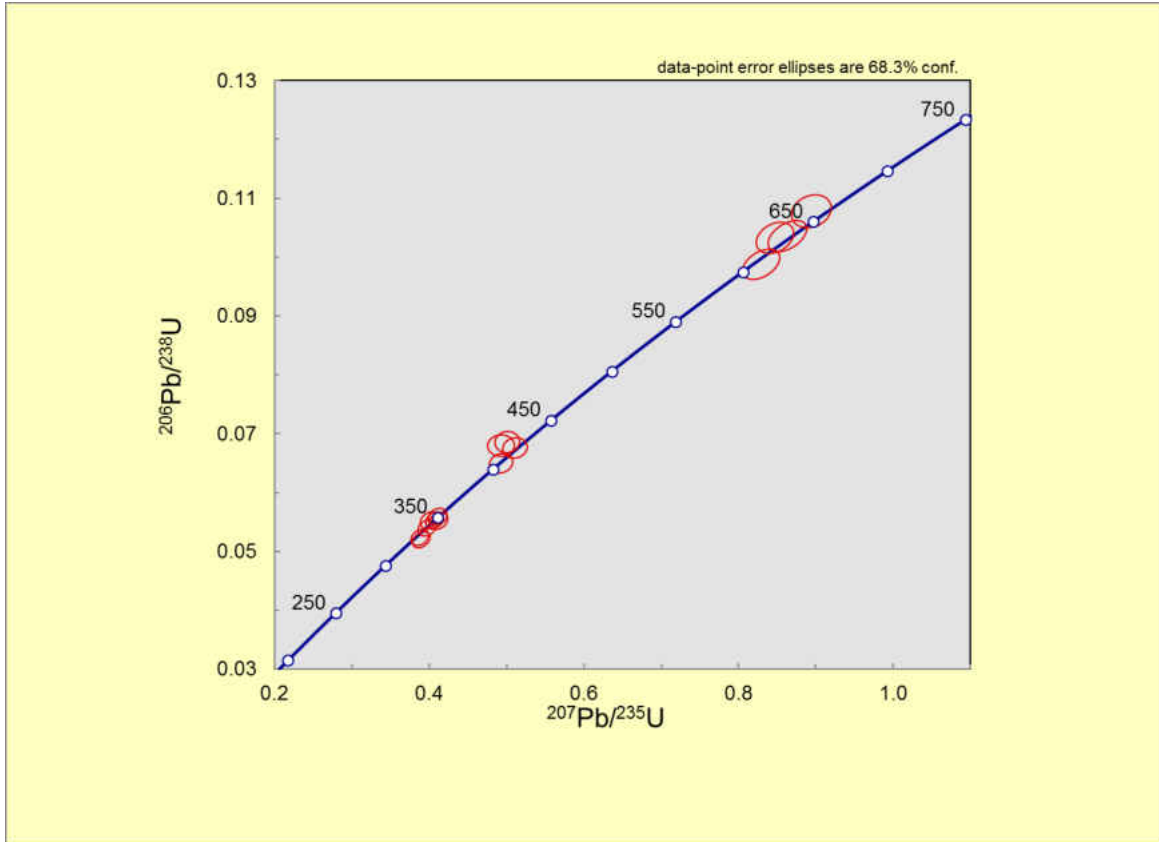
Fig. B9. LMF-3 concordia plot
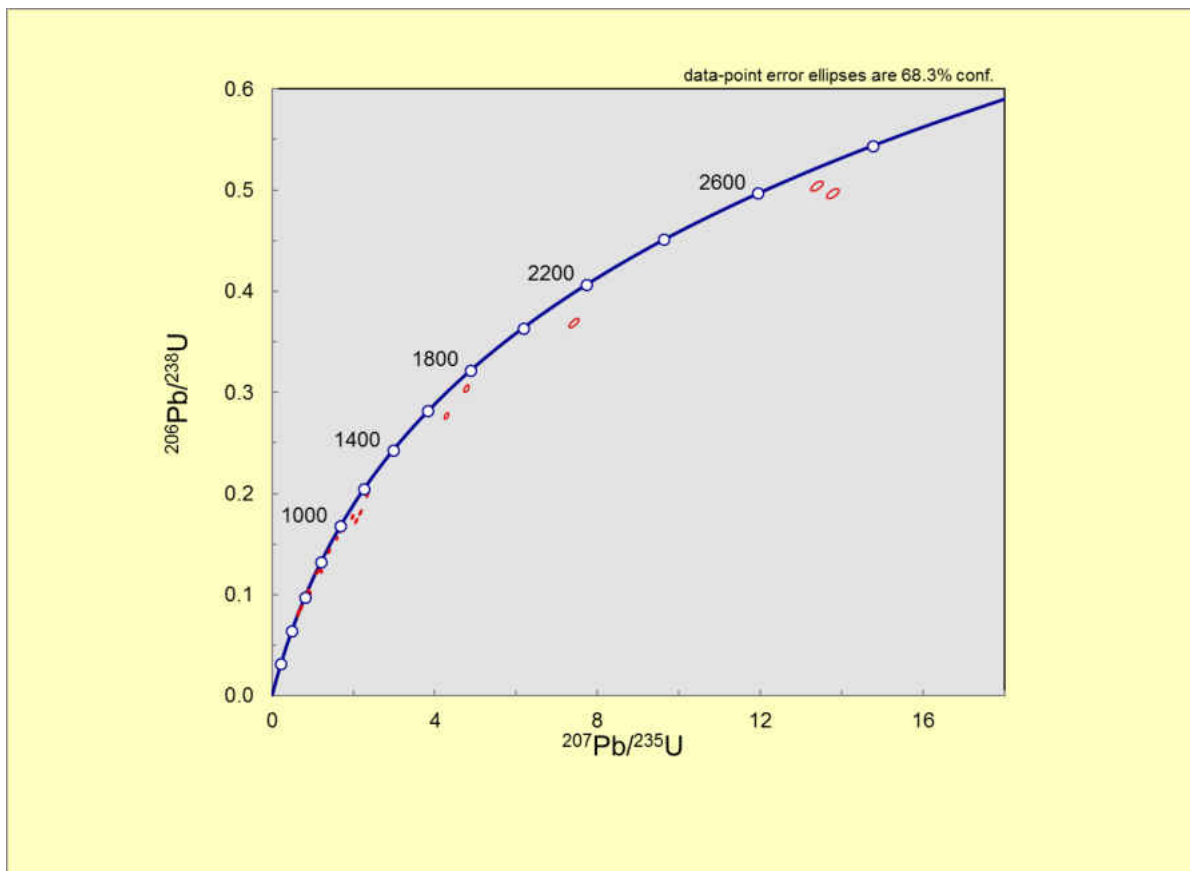
Fig. B10. LMF-3 check standards concordia plot

data-point error ellipses are 68.3% conf.

266
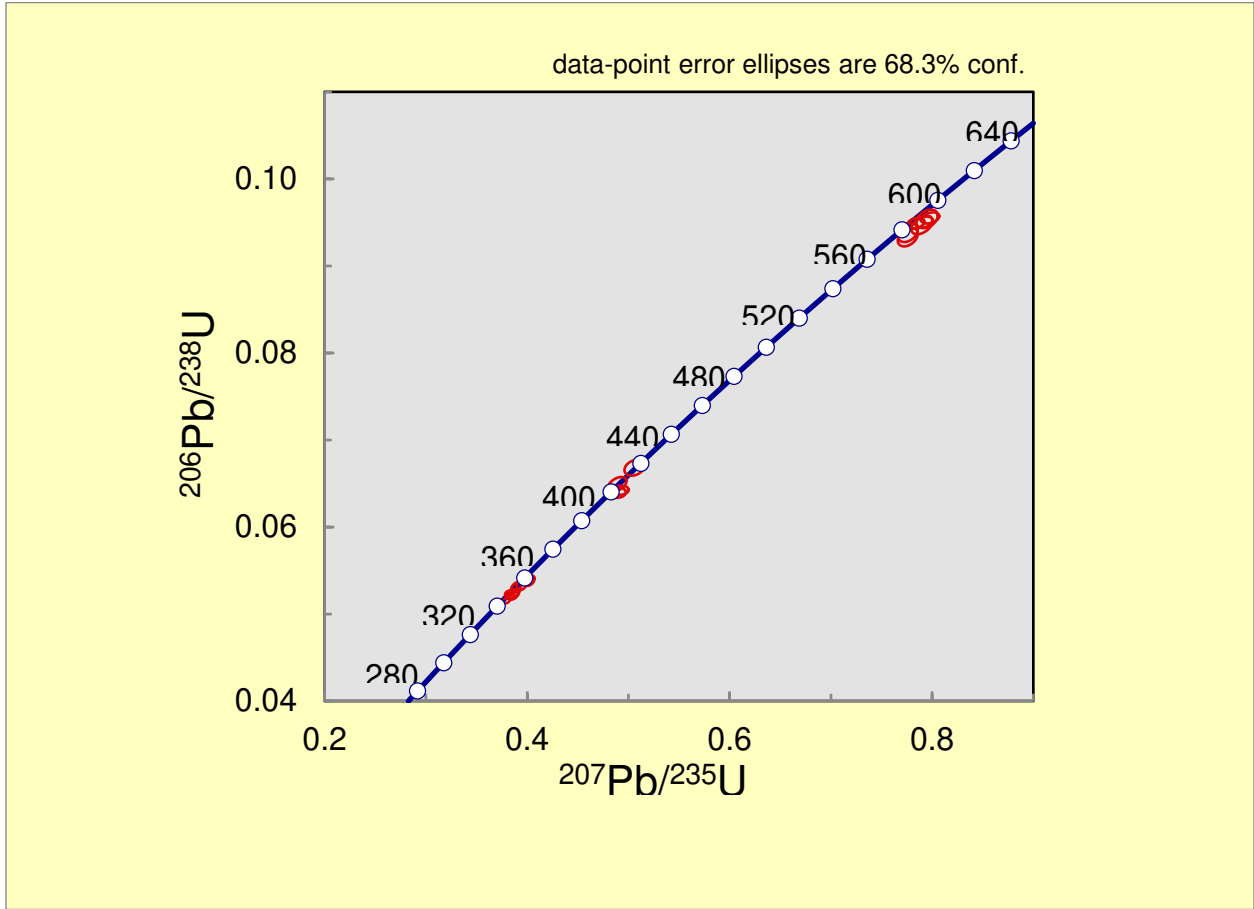
Fig. B11. LMF-5 concordia plot

data-point error ellipses are 68.3% conf.
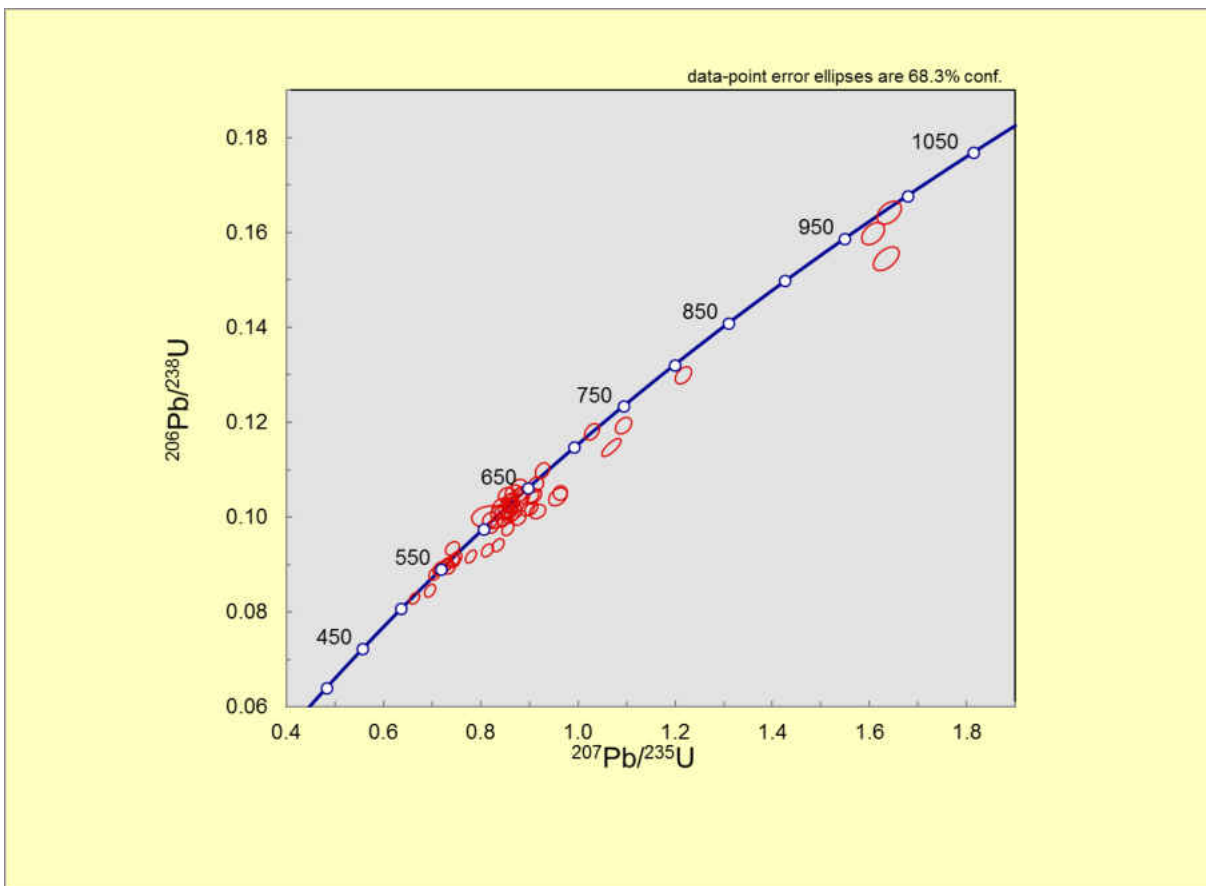
Fig. B12. LMF-5 check standards concordia plot
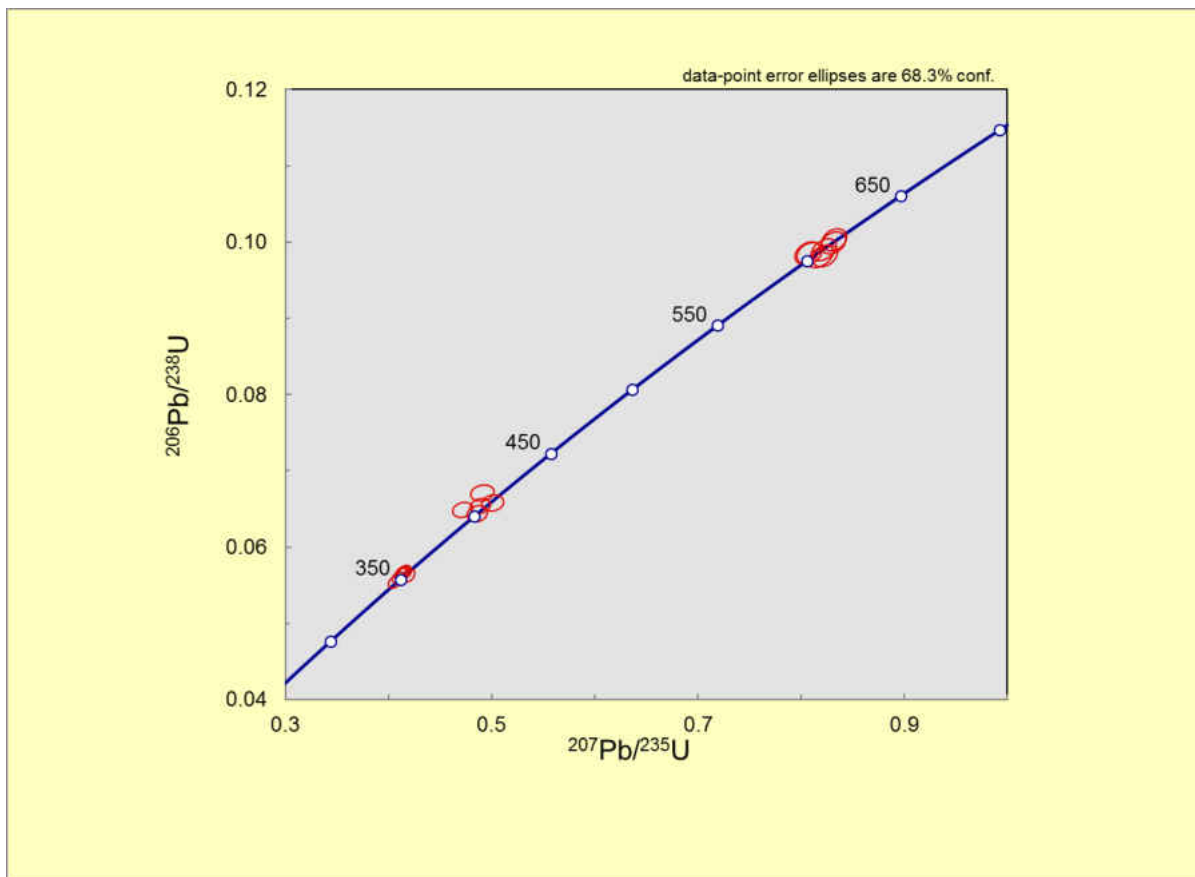
Fig. B13. LP-3 concordia plot

data-point error ellipses are 68.3% conf.
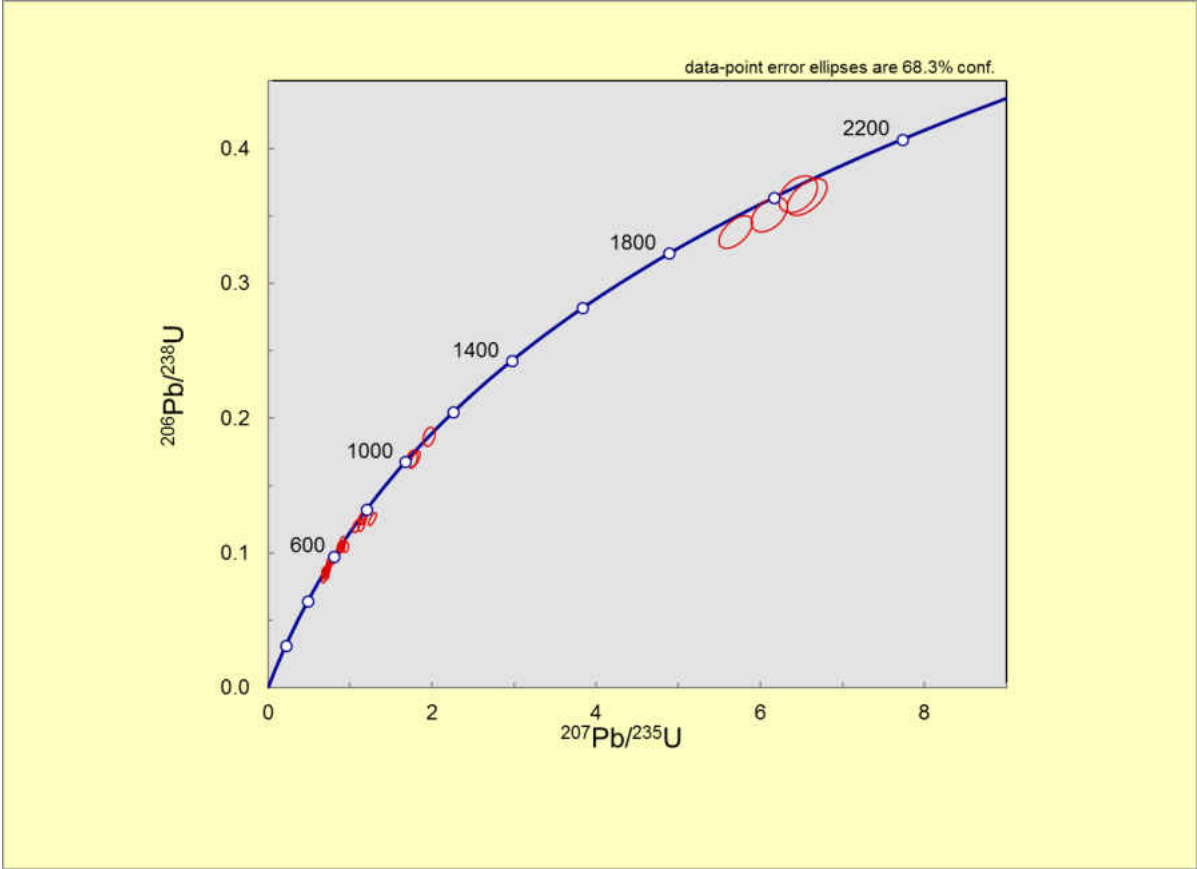
Fig. B14. LP-3 check standards concordia plot
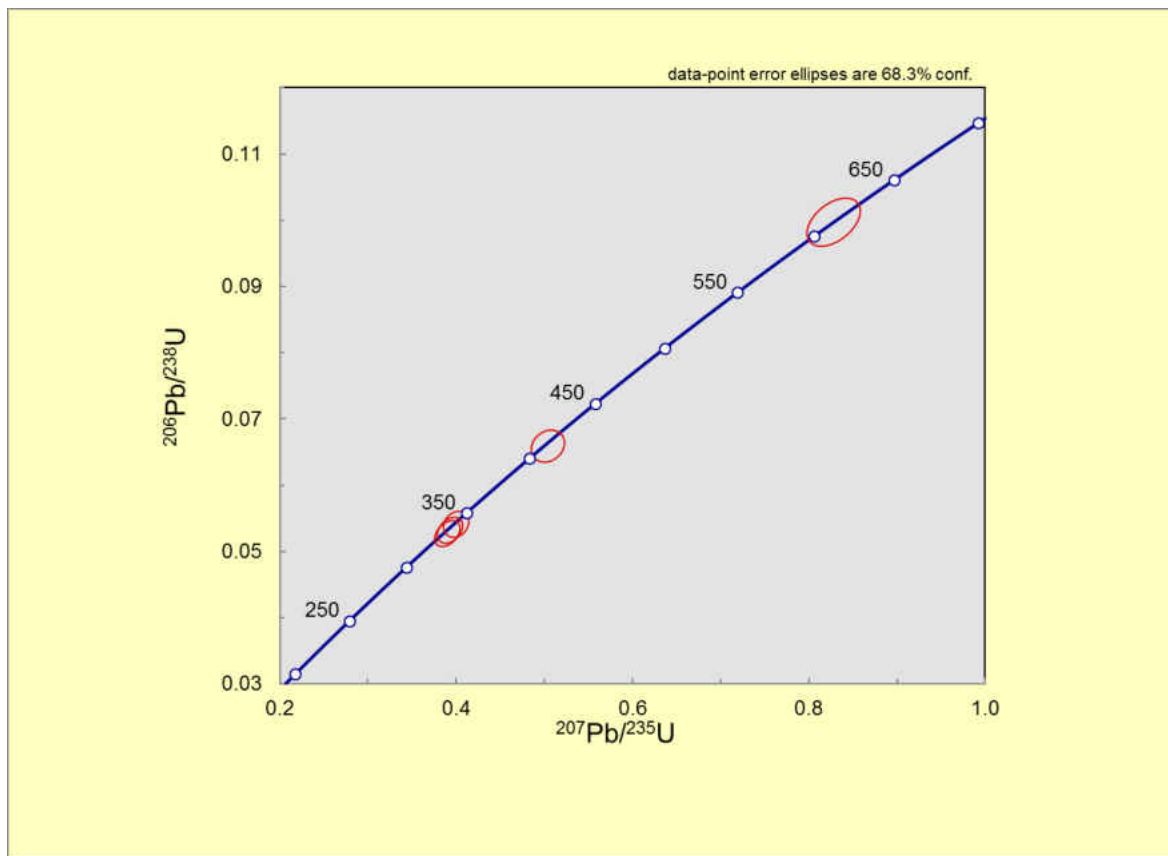
Fig. B15. SUS-1 concordia plot
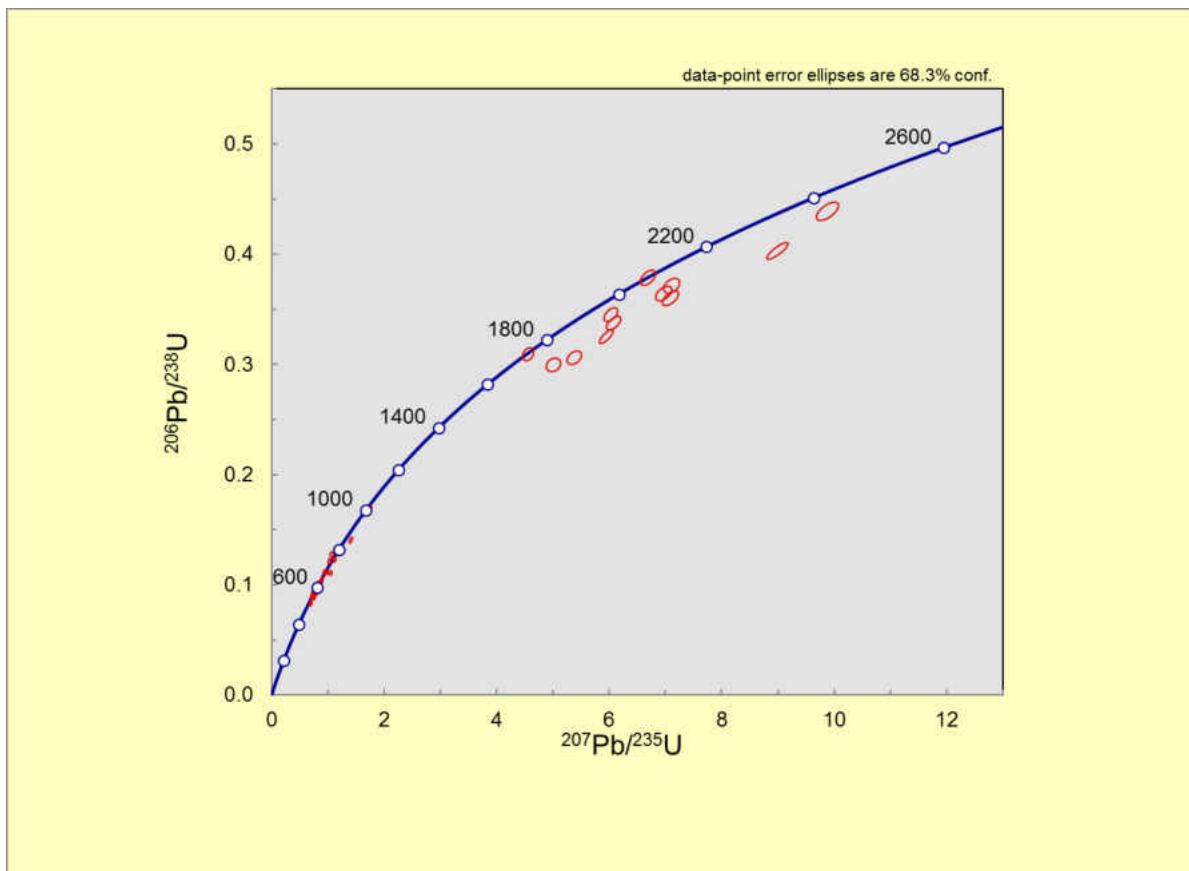
**Fig. B16. SUS-1 check standards concordia plot**
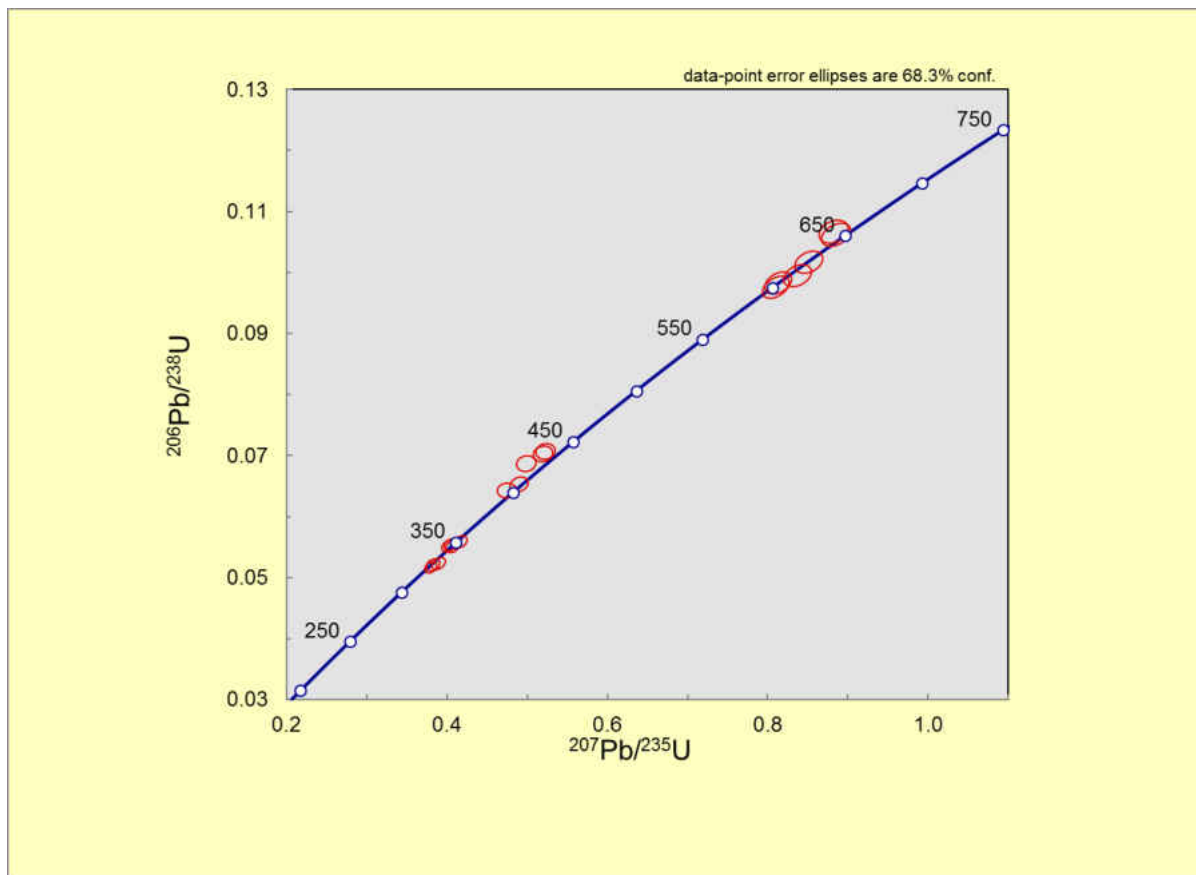
Appendix C: Geochemical data

Table C1. Major element geochemical data (Chapter 3)

Sample	cm from base of rhythmites	SiO₂ (%)	TiO₂ (%)	Al₂O₃ (%)	Fe₂O₃ (%)	MnO (%)	MgO (%)	CaO (%)	Na₂O (%)	K₂O (%)	P₂O₅ (%)	Sum (%)	LOI (%)	CIA
	Location: 30° 45.959' S, 54° 16.852' W													
s14	140	67.78	0.73	15.12	5.06	0.03	1.62	0.36	0.08	4.34	0.03	95.15	4.68	73.6
s13	130	67.29	0.77	15.56	4.99	0.02	1.75	0.39	0.04	4.52	0.04	95.37	4.47	73.6
s12	120	66.14	0.78	16.06	5.36	0.1	1.77	0.4	0.06	4.6	0.04	95.31	4.51	73.5
s11	100	65.22	0.77	16.21	5.39	0.02	1.81	0.4	0.06	4.65	0.03	94.56	5.27	73.7
s10	90	66.01	0.78	16.04	5.15	0.05	1.77	0.4	0.06	4.65	0.03	94.94	4.9	73.5
s9	80	65.34	0.77	15.87	5.1	0.05	1.77	0.4	0.06	4.6	0.03	93.99	5.85	73.5
s8	70	51.92	0.69	13.64	5.39	0.02	1.69	0.4	0.08	4.43	0.02	78.28	21.56	70.9
s7	60	63.72	0.82	16.78	5.84	0.05	1.9	0.44	0.06	4.92	0.03	94.56	5.27	73.2
s6	50	65.85	0.82	15.98	5.62	0.03	1.65	0.39	0.12	4.73	0.02	95.21	4.6	72.8
s5	40	66.88	0.85	14.96	4.93	0.06	1.41	0.35	0.13	4.53	0.03	94.13	5.68	72.5
s4	30	72.67	0.75	13.39	3.11	0.25	0.85	0.22	0.58	3.89	0.03	95.74	4.03	70.9
s3	20	74.59	0.61	13.27	1.89	0.12	0.67	0.18	0.95	3.61	0.08	95.97	3.8	70.3
s2	10	73.65	0.57	12.57	3.56	0.03	0.68	0.22	1.58	3.44	0.09	96.39	3.41	65.9
s1	0	71.84	0.56	12.38	3.49	0.03	0.68	0.22	1.58	3.45	0.08	94.31	5.47	65.4
CIA=chemcial index of alteration after Nesbitt and Young (1982)														
LOI= loss on ignition														
Sum=pre-normalized sum, excluding LOI														
All Fe reported as Fe₂O₃														

Table C2. Trace element geochemical data #1 (Chapter 3)

Sample	Sc (ppm)	V (ppm)	Cr (ppm)	Co (ppm)	Ni (ppm)	Rb (ppm)	Sr (ppm)	Y (ppm)	Zr (ppm)	Nb (ppm)	Cs (ppm)	Ba (ppm)	La (ppm)	Ce (ppm)	Pr (ppm)	Rb/K
s14	13	123	75	8	45	175	80	49	169	17	6	637	45	85	13	0.0049
s13	15	129	81	6	46	185	87	59	171	18	6	666	63	119	20	0.0049
s12	14	135	82	19	67	185	84	47	177	18	6	758	55	130	19	0.0048
s11	15	136	80	6	47	184	83	43	179	18	6	641	45	94	14	0.0048
s10	14	134	82	12	57	184	81	43	178	18	6	659	42	87	12	0.0048
s9	13	131	82	12	57	182	79	40	171	18	6.	642	40	85	12	0.0048
s8	12	137	79	6	49	171	73	32	138	15	5	586	22	37	5.	0.0047
s7	15	163	92	10	65	191	87	40	184	18	6	715	27	45	6	0.0047
s6	13	151	80	8	51	169	91	36	180	18	5	740	25	43	6	0.0043
s5	13	140	88	9	48	150	97	41	190	19	4	854	25	41	7	0.0040
s4	9	90	56	16	60	120	122	30	227	17	2	1188	19	40	5	0.0037
s3	9	58	46	7	22	99	271	29	180	14	1	1032	96	145	16	0.0033
s2	9	77	53	5	27	100	354	26	256	13	2	915	96	154	15	0.0035
s1	8	76	53	5	27	100	361	27	249	13	2	943	98	154	15	0.0035

Table C3. Trace element geochemical data #2 (Chapter 3)

Sample	Nd (ppm)	Sm (ppm)	Eu (ppm)	Gd (ppm)	Tb (ppm)	Dy (ppm)	Ho (ppm)	Er (ppm)	Tm (ppm)	Yb (ppm)	Lu (ppm)	Hf (ppm)	Ta (ppm)	Pb (ppm)	Th (ppm)	U (ppm)
s14	56.44	12.53	2.51	11.34	1.60	1.60	1.72	4.65	0.72	4.40	0.66	4.66	1.38	16.24	18.94	6.79
s13	85.92	19.06	3.60	16.13	2.18	2.18	2.16	5.67	0.85	5.22	0.79	4.89	1.55	13.82	23.28	7.91
s12	80.20	17.46	3.20	13.60	1.78	1.78	1.72	4.65	0.71	4.43	0.67	4.87	1.47	23.56	20.58	7.18
s11	60.93	13.24	2.45	10.73	1.46	1.46	1.53	4.33	0.68	4.26	0.65	4.88	1.47	13.85	20.36	6.66
s10	54.12	11.74	2.21	9.81	1.34	1.34	1.51	4.24	0.67	4.26	0.65	4.82	1.48	15.29	20.04	6.66
s9	51.40	11.07	2.15	9.34	1.29	1.29	1.44	4.02	0.63	4.05	0.61	4.60	1.42	15.25	19.19	6.56
s8	22.92	5.04	1.11	5.11	0.80	0.80	1.09	3.20	0.51	3.34	0.51	3.51	1.16	13.74	16.20	5.25
s7	28.10	6.21	1.33	6.49	1.00	1.00	1.40	4.14	0.66	4.29	0.65	4.80	1.46	16.00	20.38	6.27
s6	29.30	6.33	1.36	6.36	0.96	0.96	1.23	3.55	0.57	3.63	0.55	4.79	1.38	14.60	17.20	5.74
s5	30.71	7.02	1.50	7.22	1.09	1.09	1.35	3.82	0.59	3.68	0.56	5.25	1.42	16.95	15.37	5.79
s4	25.56	5.94	1.32	5.95	0.89	0.89	1.04	2.96	0.46	2.88	0.43	5.99	1.16	20.70	10.53	4.64
s3	56.21	8.72	1.69	6.76	0.91	0.91	0.94	2.50	0.37	2.27	0.34	4.71	0.91	14.91	7.00	3.93
s2	53.48	7.61	1.50	6.09	0.79	0.79	0.91	2.44	0.37	2.33	0.35	6.62	0.95	21.82	10.61	2.06
s1	53.87	7.57	1.52	6.10	0.82	0.82	0.91	2.47	0.37	2.33	0.36	6.45	0.95	21.78	10.72	2.06

Appendix D: Paleocurrent, grooved surfaces, and structural data from study area

Table D1. Paleocurrent measurements from Chapter 2 - Morro do Papaleo

Cross-Stratification, Lower Sandstone Beds (Dip Direction)	Cross-Stratification, Upper Sandstone Beds (Dip Direction)
214	279
219	314
214	224
244	294
249	299
224	304
204	324
184	309
164	314
264	209
214	
304	

Table D2. Paleocurrent and structural measurements from Chapter 3 - Ibaré railroad track succession

Cross-Stratification (Dip direction)	Fold Axes (Trend/Plunge)	Shear Planes (Strike/Dip)
313	31/25	58/25
236	31/28	30/21
279	53/40	38/11
1	66/35	00/45
345	106/35	
26	18/28	
21	16/26	
300	6/18	
292	4/22	
284	44/27	
340	11/26	
305	76/9	
252	21/13	
322	21/10	
302	70/32	
305	106/34	

	61/21	
	98/36	
	78/25	
	81/34	
	166/33	
	40/28	
	46/15	
	56/5	
	76/6	
	72/12	
	46/31	
	246/10	
	226/70	
	246/13	
	226/14	
	85/12	
	77/10	
	72/5	
	271/5	
	64/3	
	92/8	
	85/7	
	270/5	
	88/5	
	72/8	
	68/1	
	42/1	
	195/1	

Table D3. Paleocurrent measurements from Chapter 4

Cross-Stratification, Location 1 (Dip Direction)	Cross-Stratification, Location 2 (Dip Direction)	Cross-Stratification, Location 3 (Dip Direction)
313	152	307
236	162	267
279	192	227
1	177	212
345	187	272
26	127	229
21	157	227

300	122	272
292	124	
284	127	
340	172	
305	127	
252	172	
322	172	
302		
305		

Table D4. Orientations of grooved surfaces in study area

31.29815° S, 53.58142° W	30° 26.219' S, 53° 5.636' W	32° 39.323' S, 54° 34.964' W
Grooved Surface Near Bagé, Brazil (Trend)	Grooved Surface Near Cachoeira do Sul, Brazil (Trend)	Grooved Surfaces Near Melo, Uruguay (Trend)
16	2	212
21	356	212
19	1	210
12	3	210
16	356	210
21	359	212
16	3	208
16	0	212
	3	177
	3	167
	3	247
	0	207
	3	207
	5	207
	357	213
	356	196
	0	206
	4	206
	2	337
	7	328
	4	337
	8	326
	8	327
	1	337

	7	328
	358	328
	2	336
	4	332
	3	337
	1	322
	7	322
	8	321
	8	332
	1	332
	4	330
	5	330
	6	332
	1	337
	2	15
	2	312
	356	
	0	

**Fig. E1. Chapter 3, Location 1 stratigraphic column**
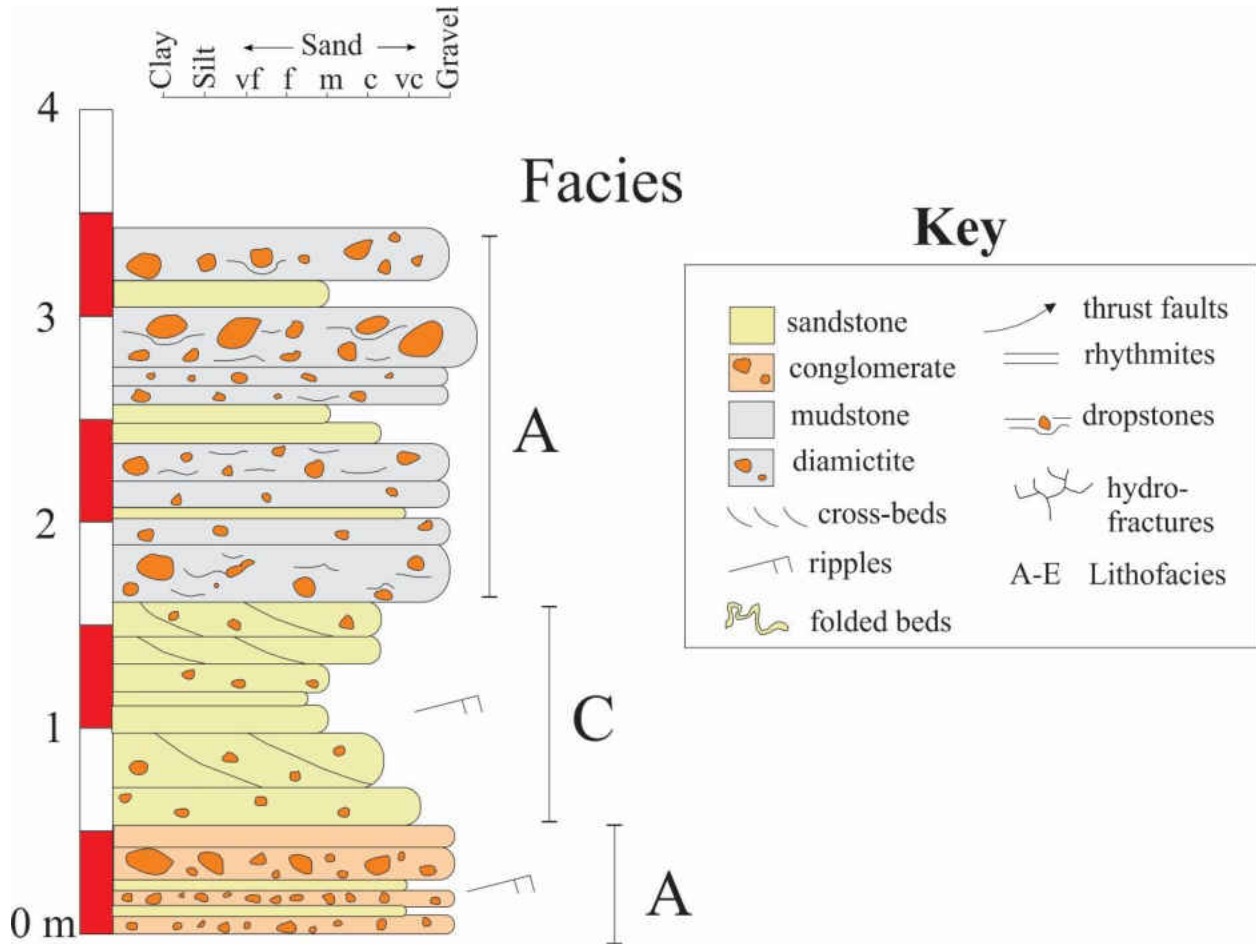
Fig. E2. Chapter 3, Location 2 stratigraphic column
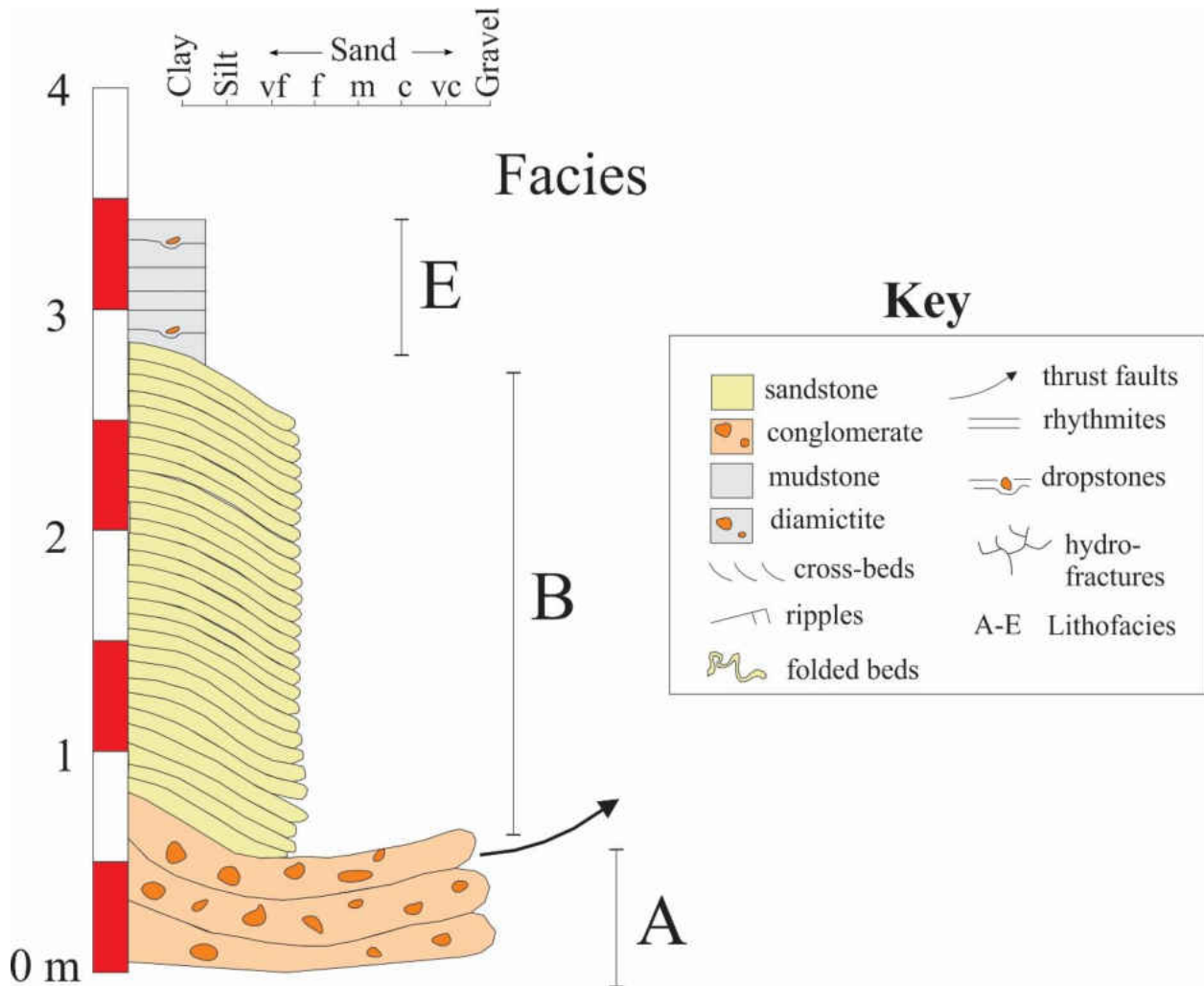
**Fig. E3. Chapter 3, Location 3 stratigraphic column**
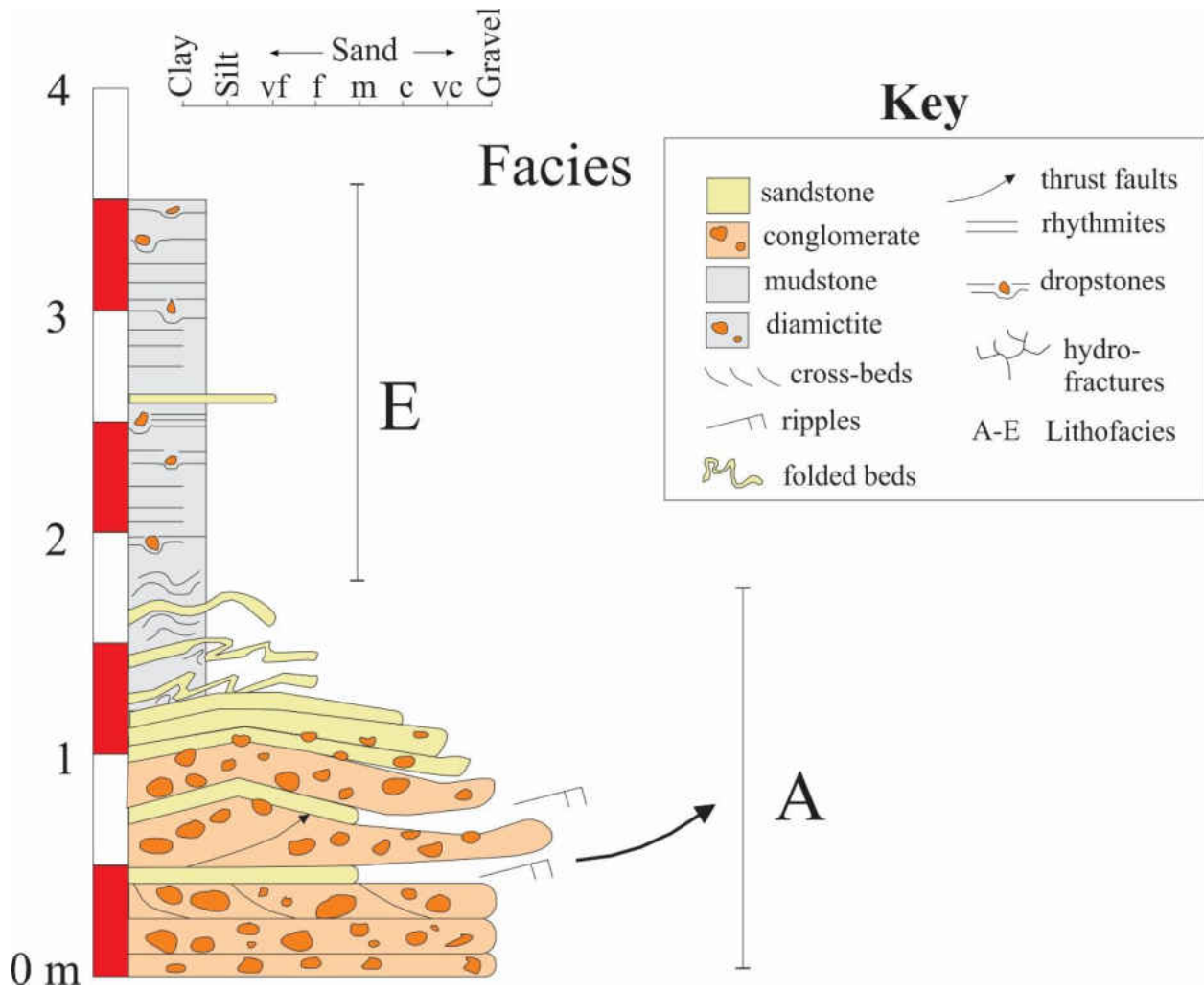
Fig. E4. Chapter 3, Location 4 stratigraphic column
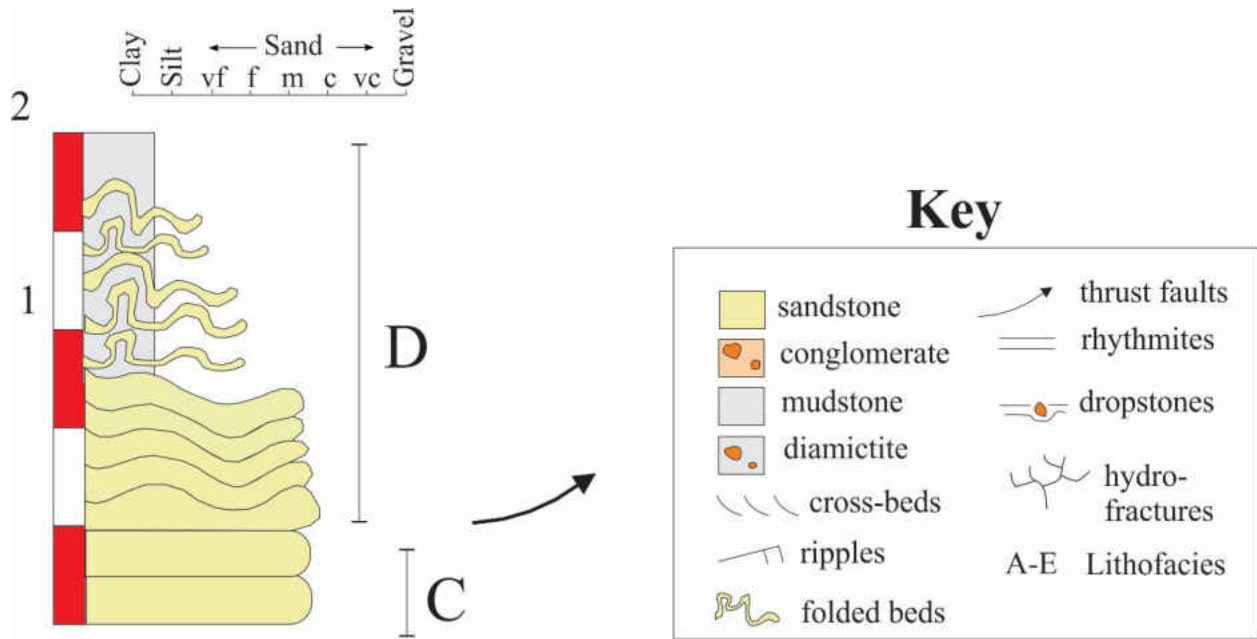
Fig. E5. Chapter 3, Location 5 stratigraphic column
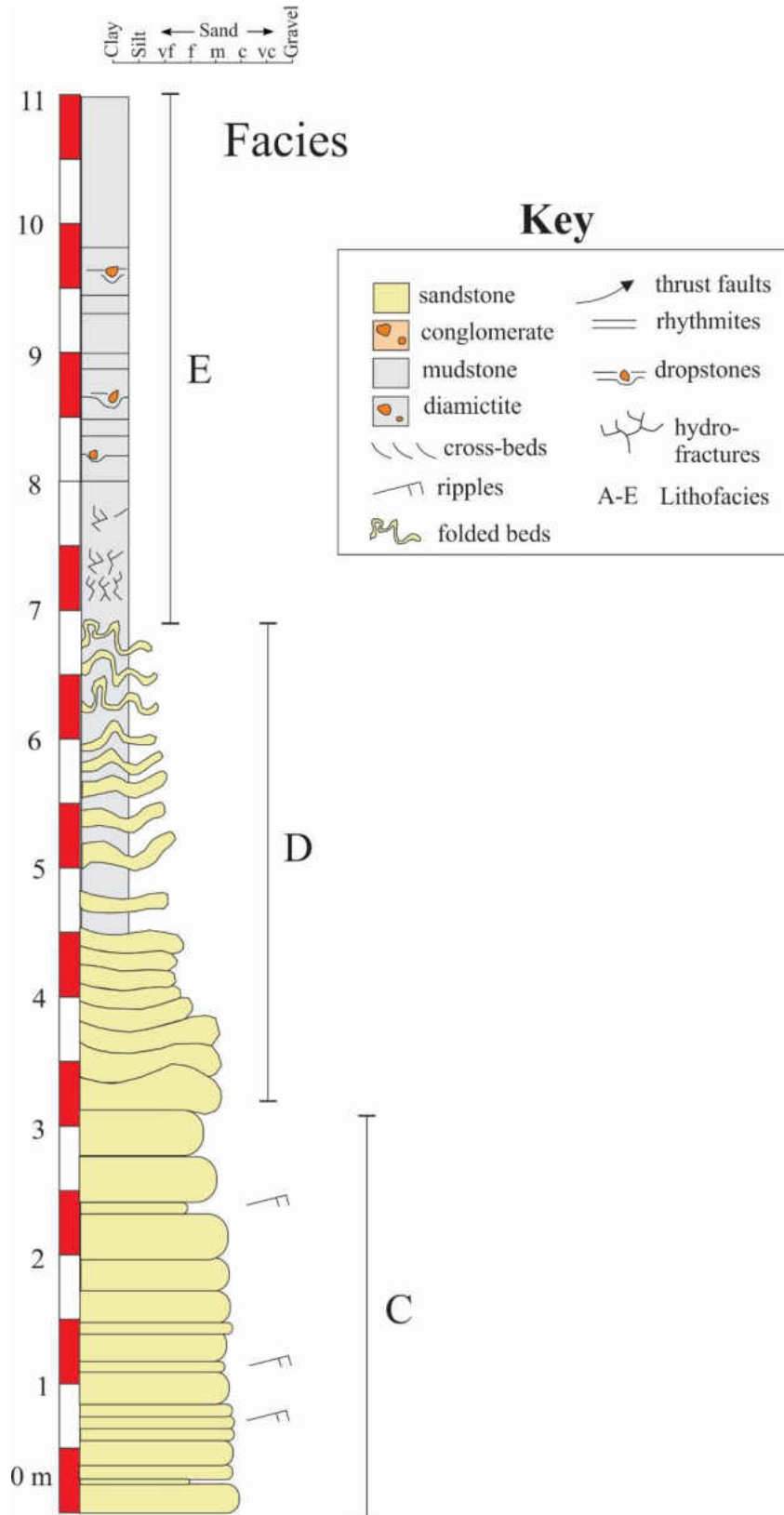
**Fig. E6. Core LA-14, 1-20 m, stratigraphic column**
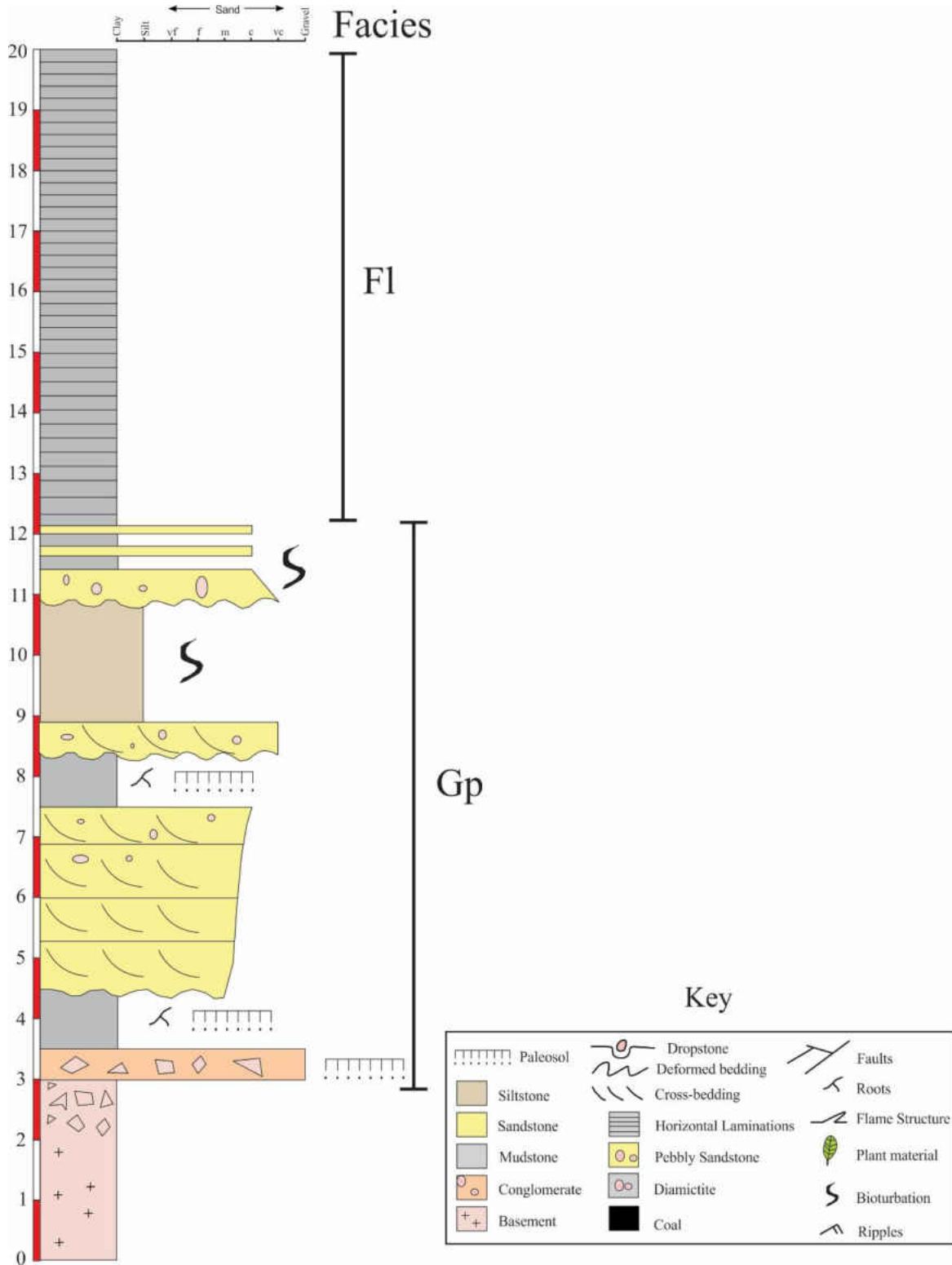
Fig. E7. Core LA-14, 20-40 m, stratigraphic column

286
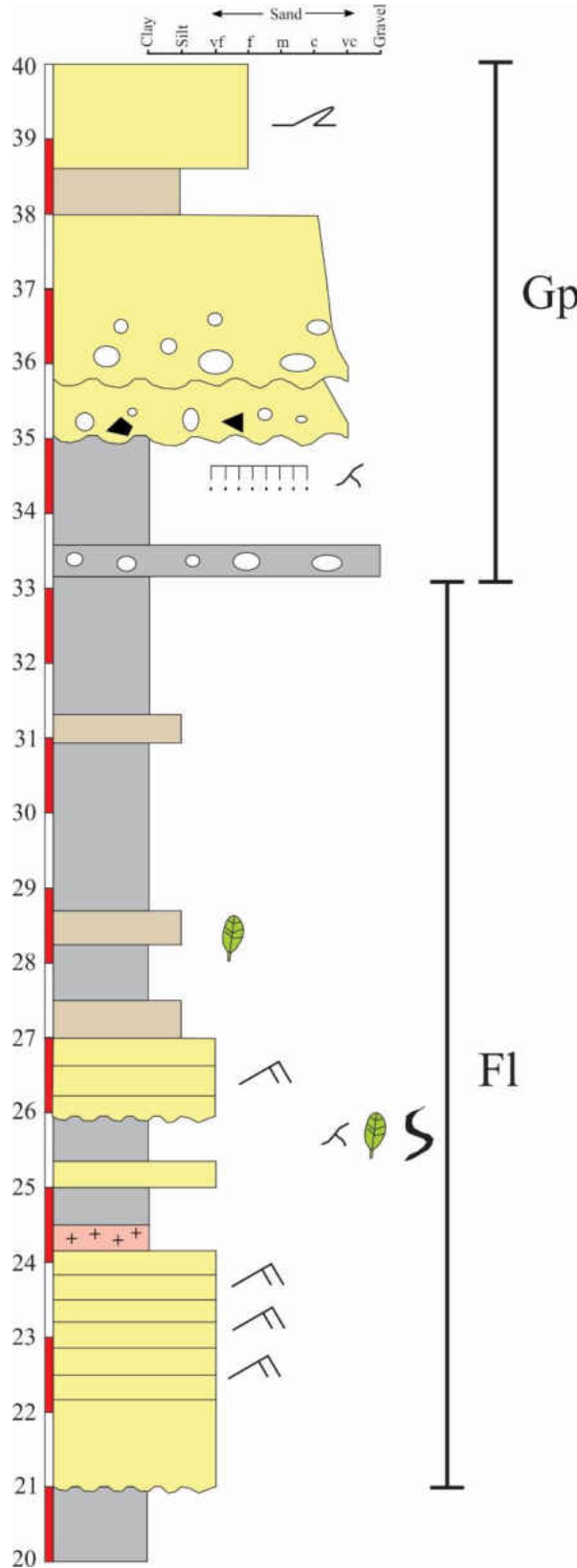
**Fig. E8. Core LA-14, 40-60 m, stratigraphic column**
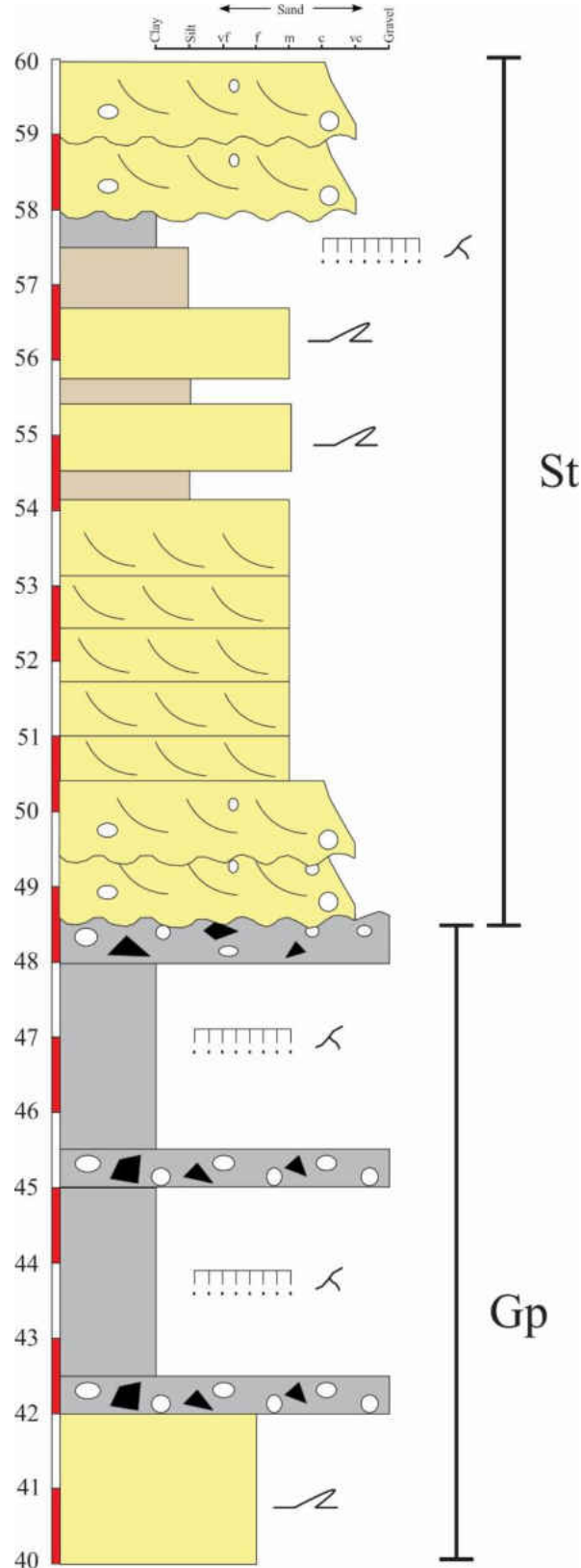
**Fig. E9. Core LA-14, 60-77 m, stratigraphic column**

288
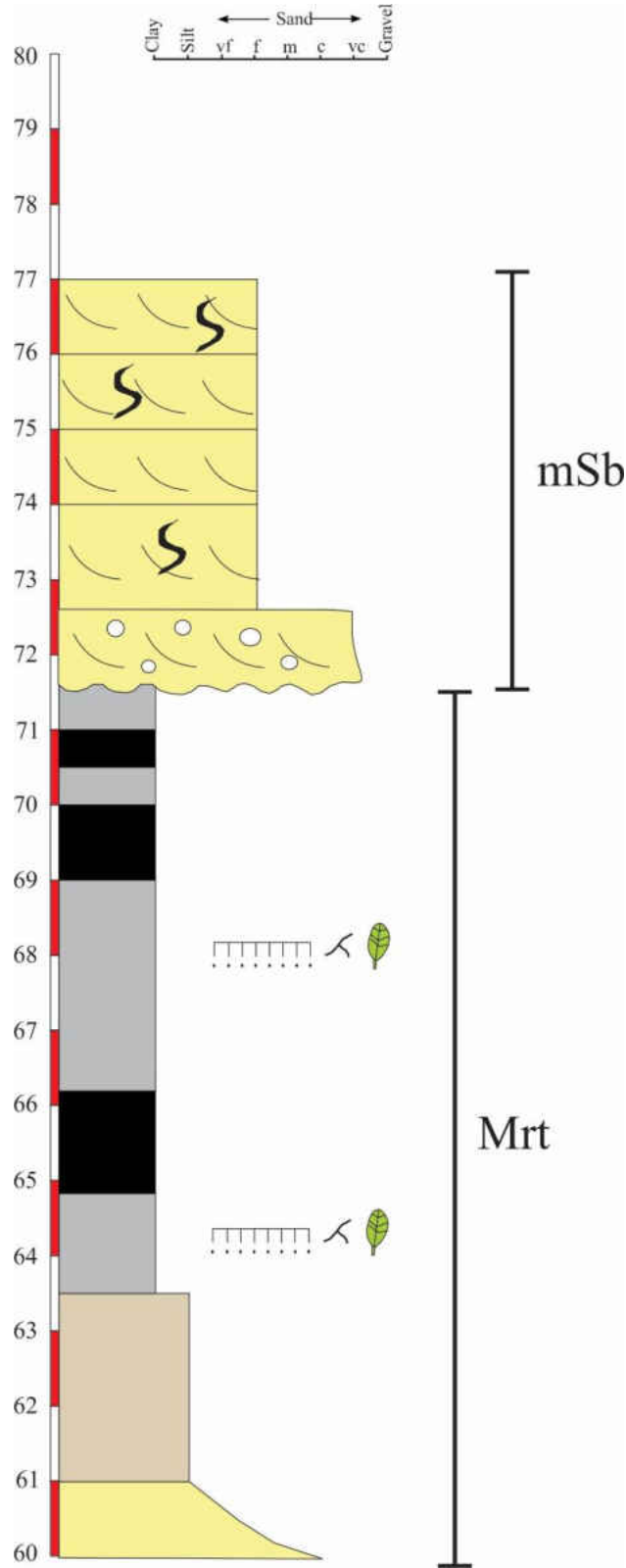
**Fig. E10. Core CA-53, 0-20 m, stratigraphic column**
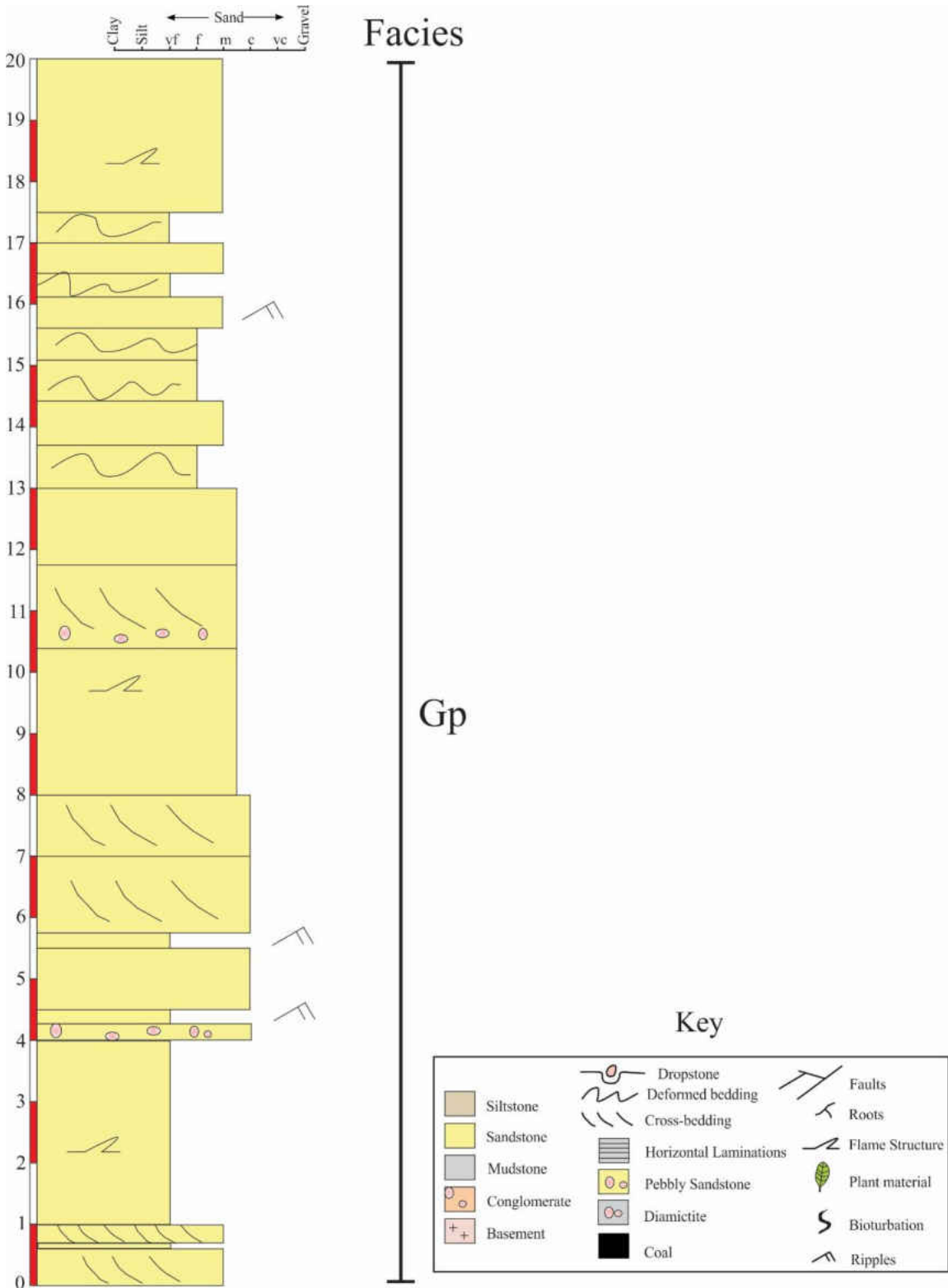
Fig. E11. Core CA-53, 20-40 m, stratigraphic column
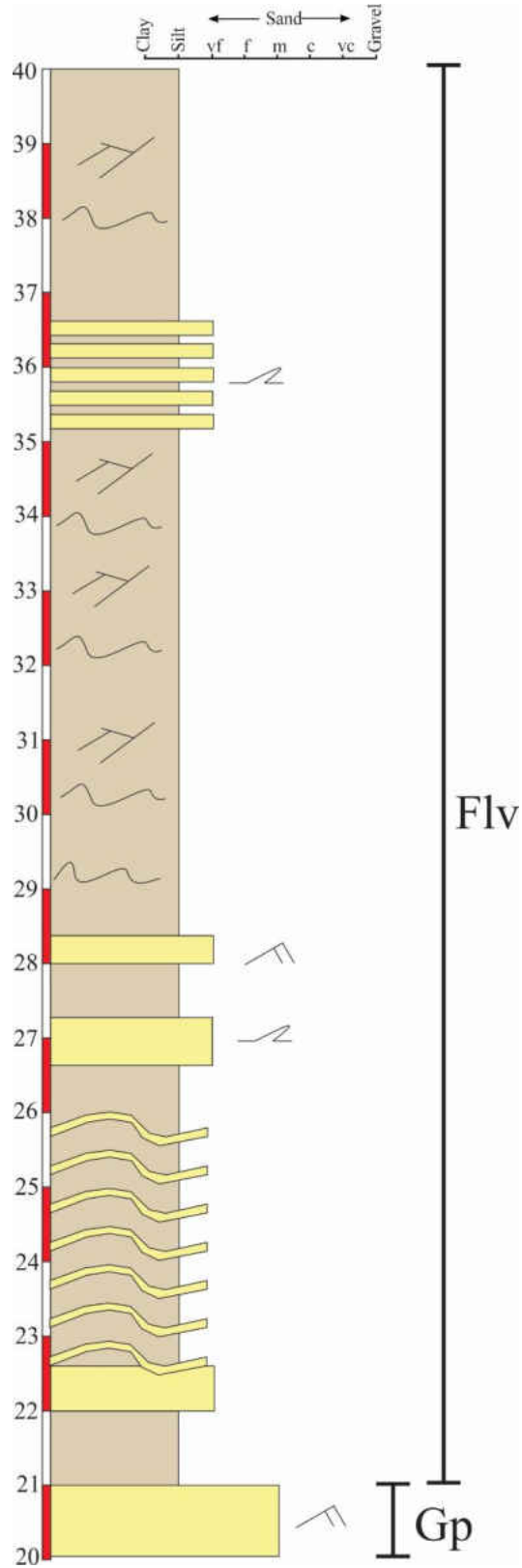
**Fig. E12. Core CA-53, 40-60 m, stratigraphic column**
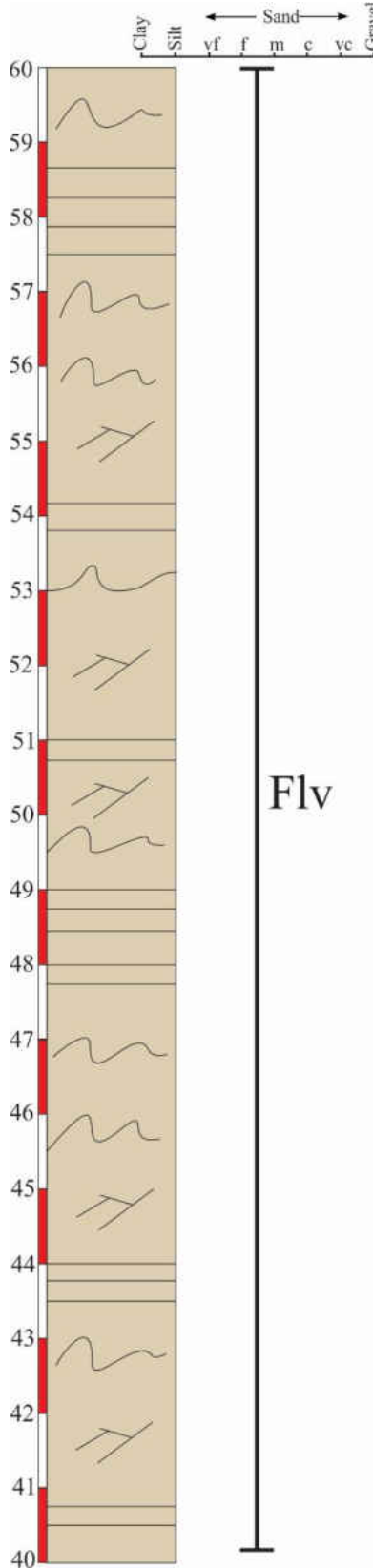
**Fig. E13. Core CA-53, 60-80 m, stratigraphic column**
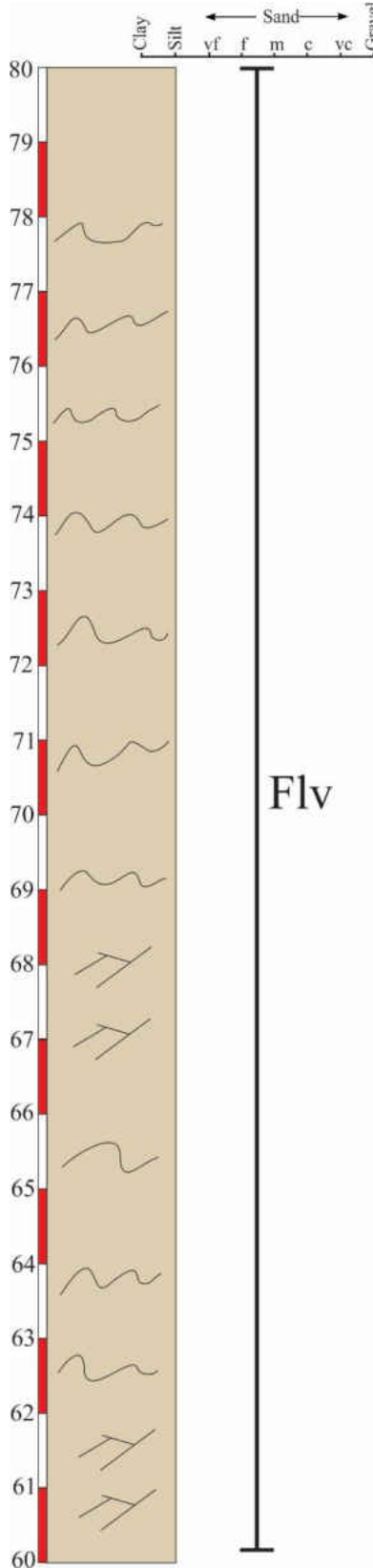
Fig. E14. Core CA-53, 80-100 m, stratigraphic column
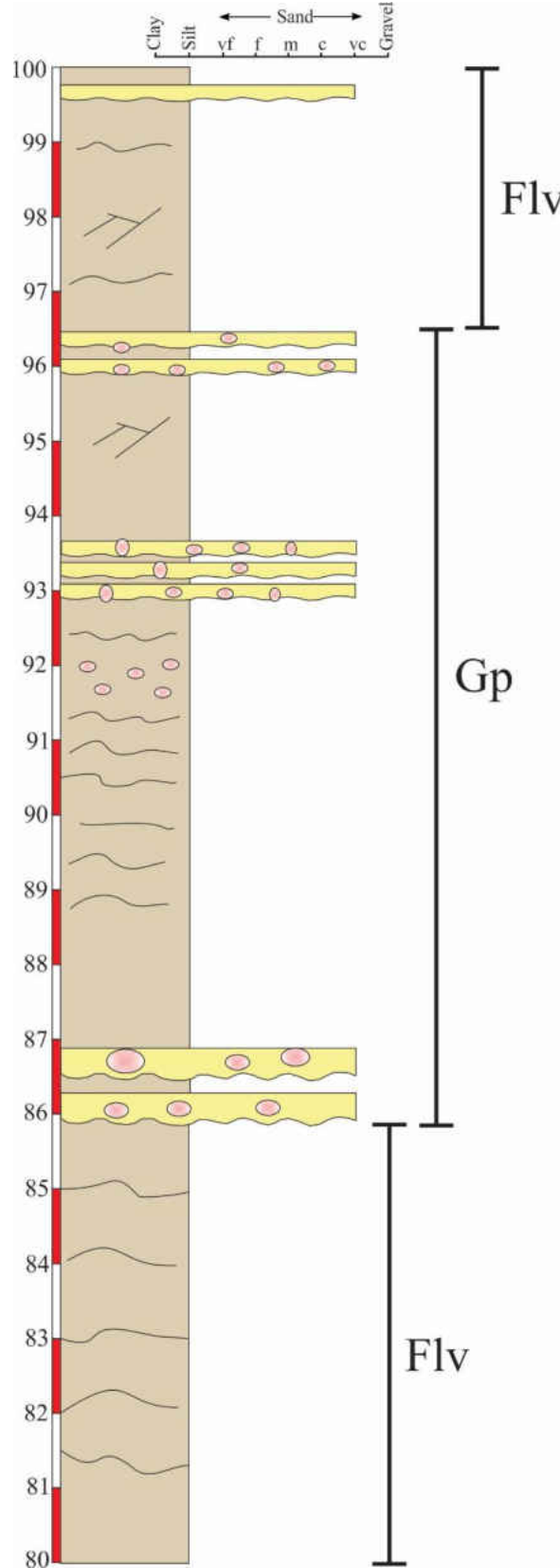
Fig. E15. Core CA-53, 100-120 m, stratigraphic column
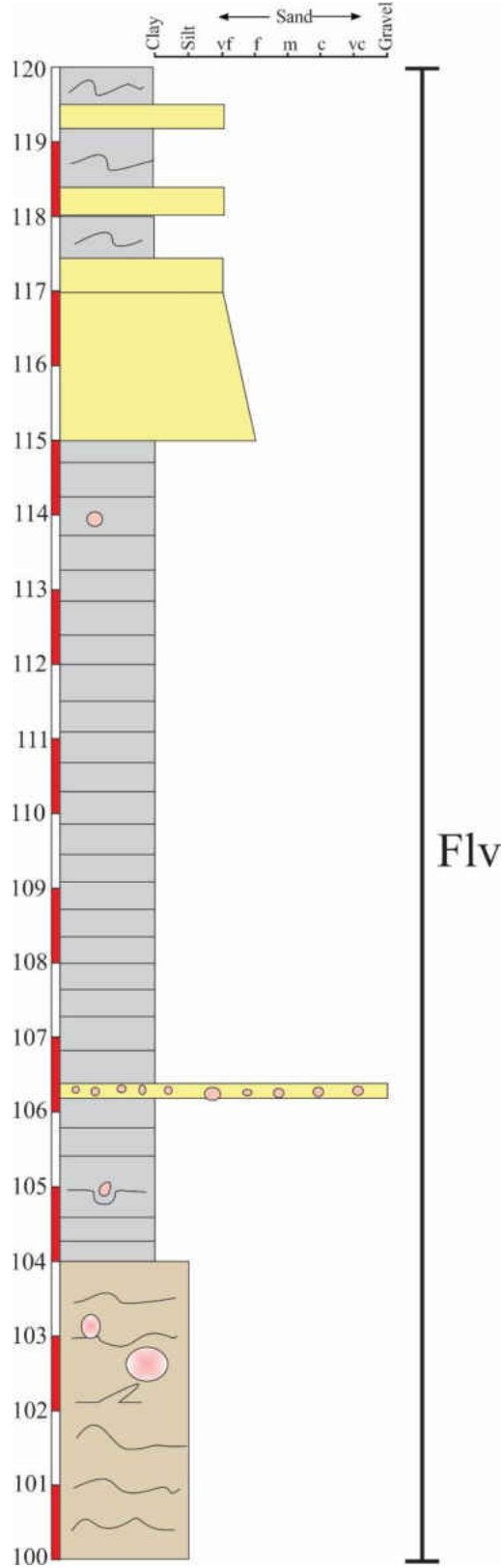
**Fig. E16. Core CA-53, 120-140 m, stratigraphic column**
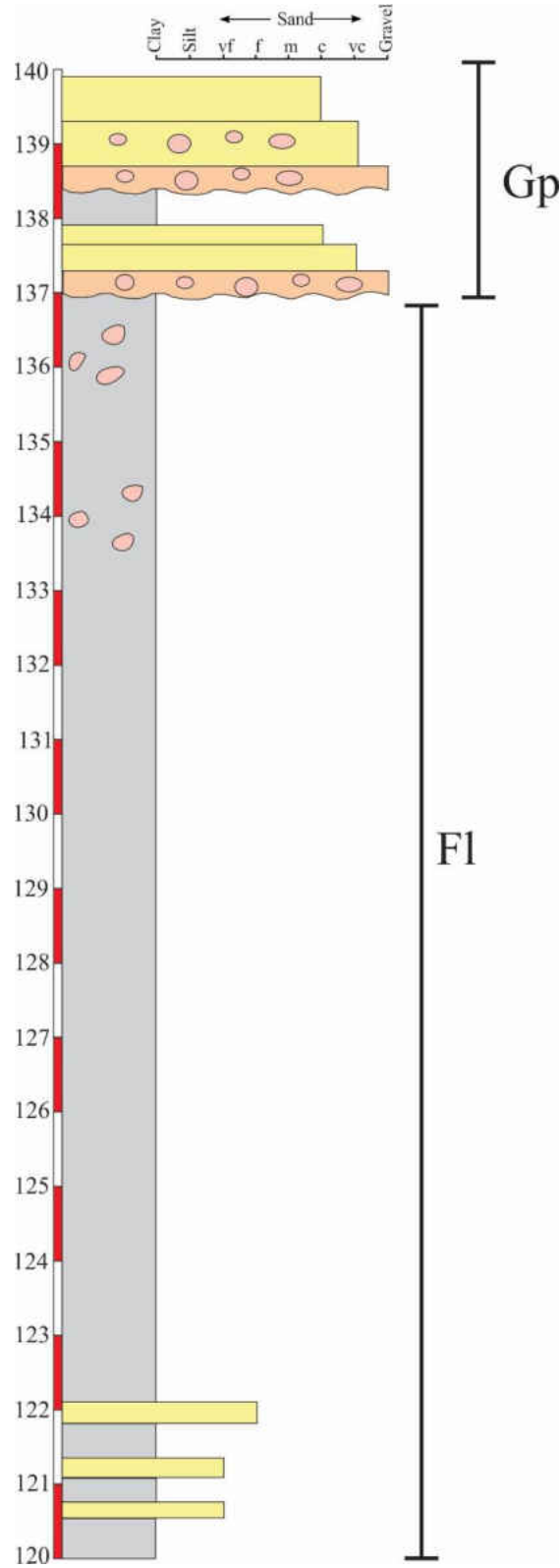
Fig. E17. Core CA-53, 140-152 m, stratigraphic column
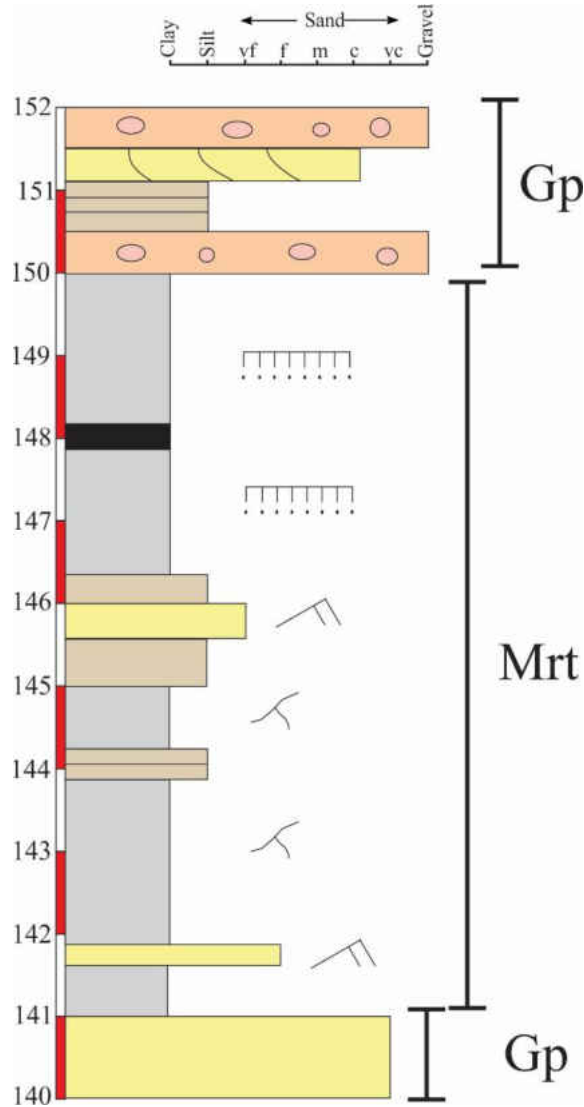
Fig. E18. Core IB-94, 0-20 m, stratigraphic column
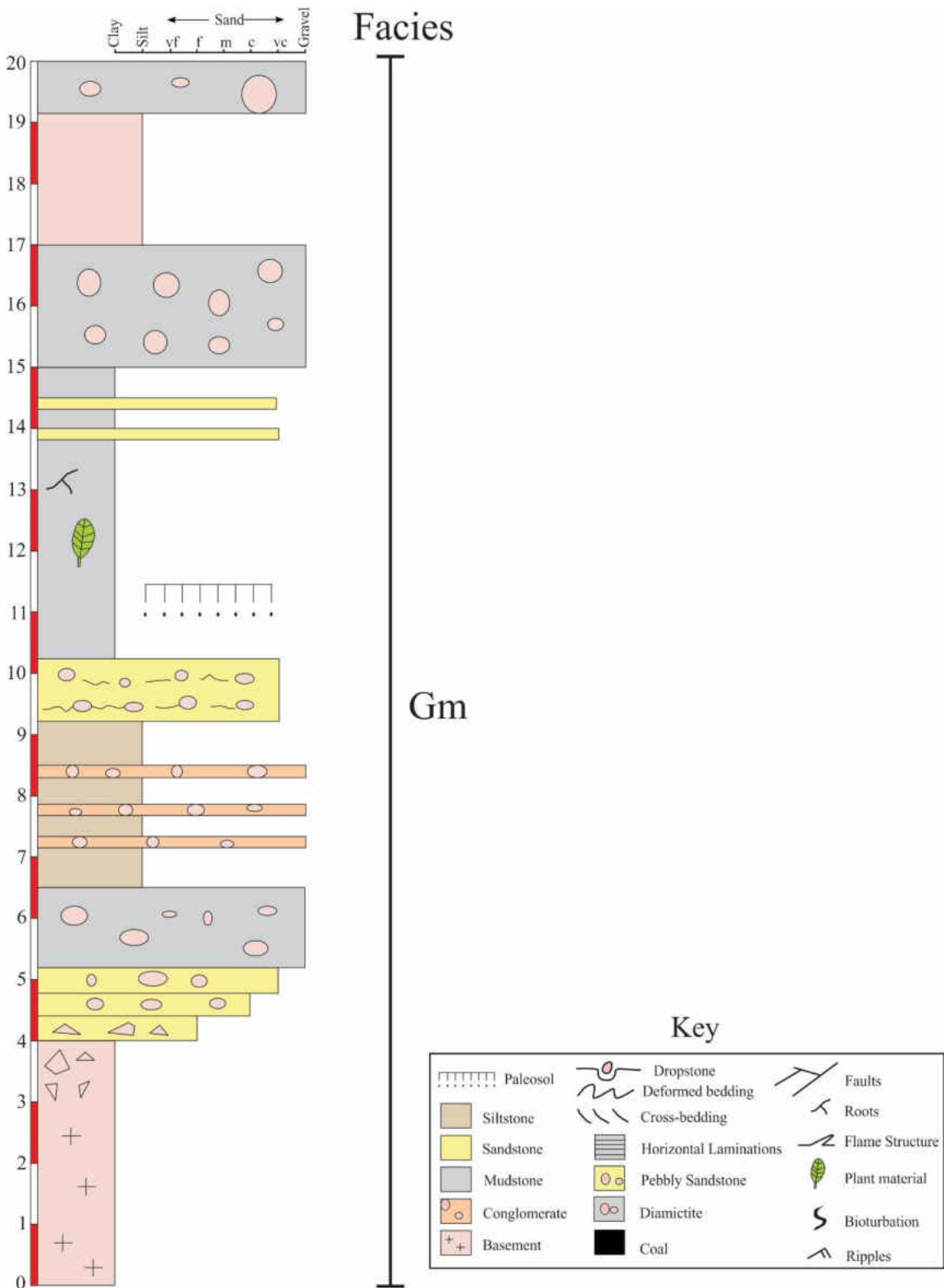
Fig. E19. Core IB-94, 20-40 m, stratigraphic column
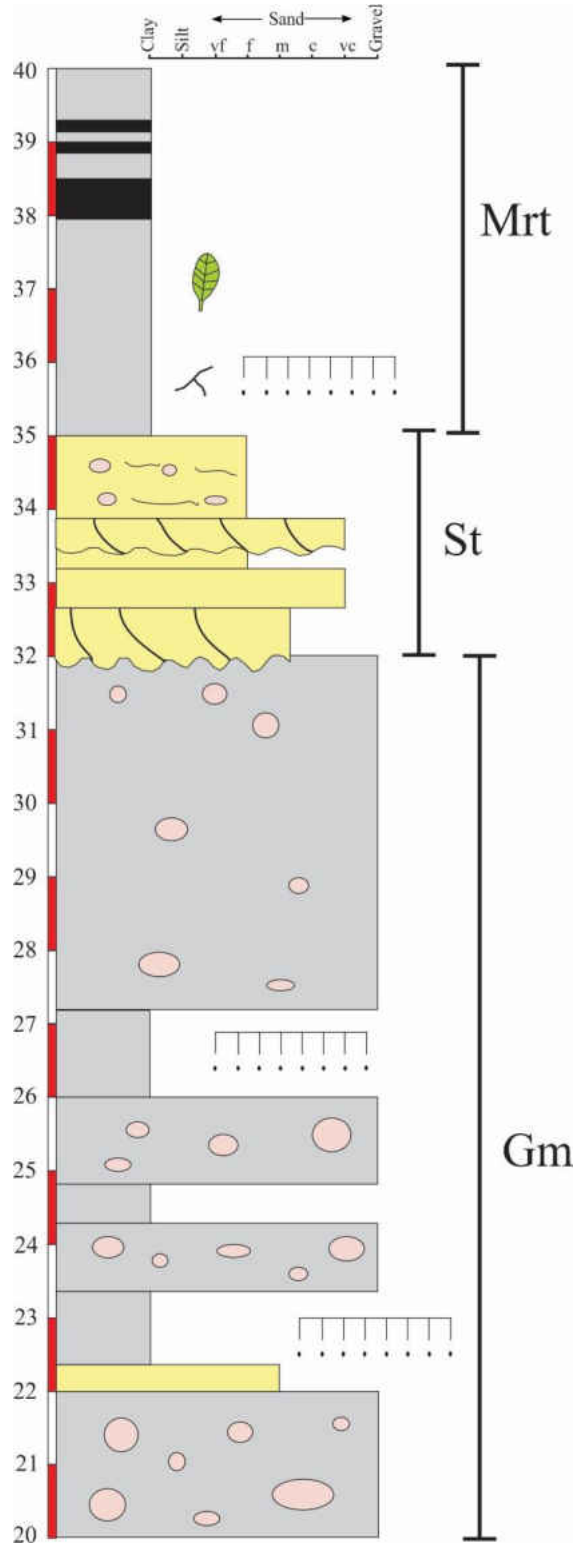
Fig. E20. Core IB-94, 40-60 m, stratigraphic column
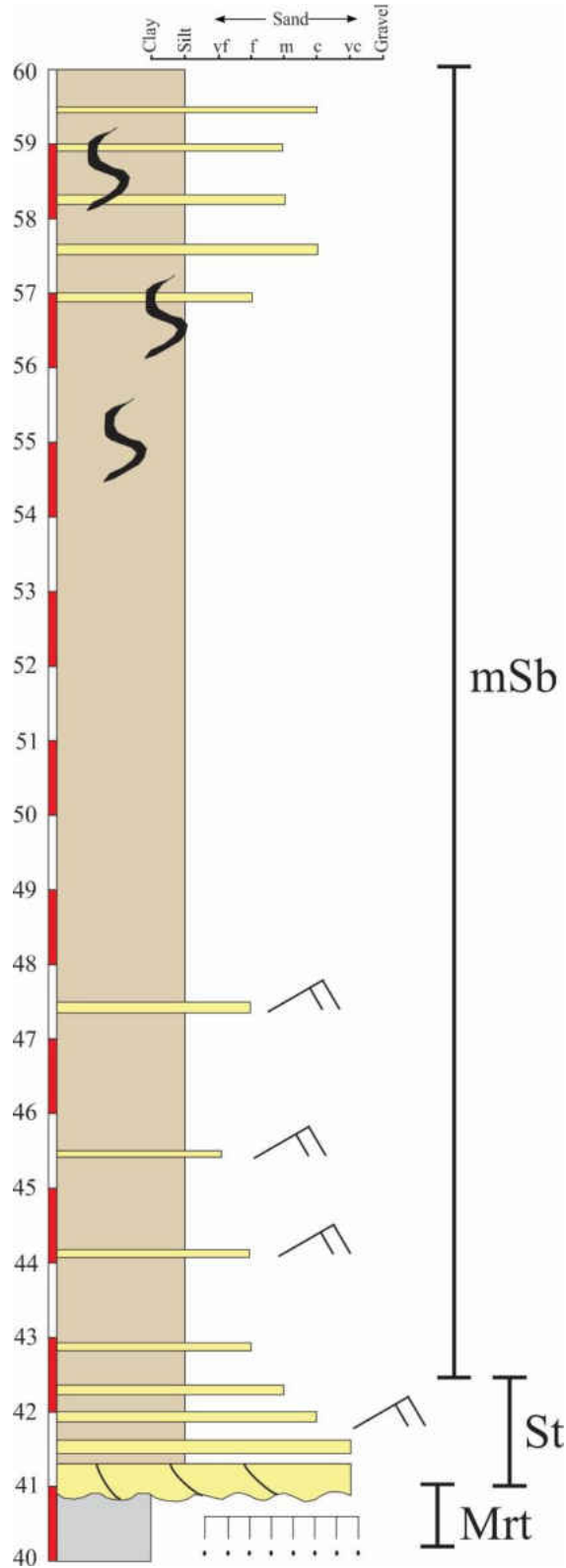
Fig. E21. Core IB-94, 60-68 m, stratigraphic column

Fig. E22. Core AB-06, 0-20 m, stratigraphic column
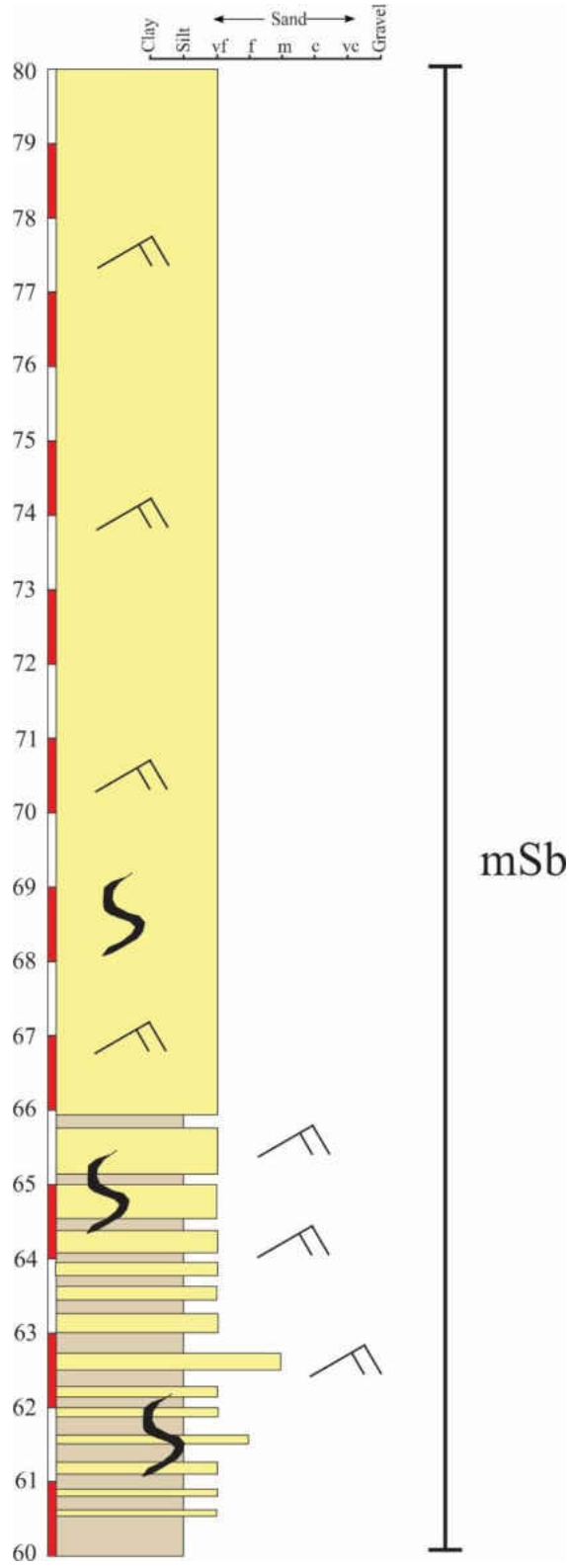
Fig. E23. Core AB-06, 20-40 m, stratigraphic column
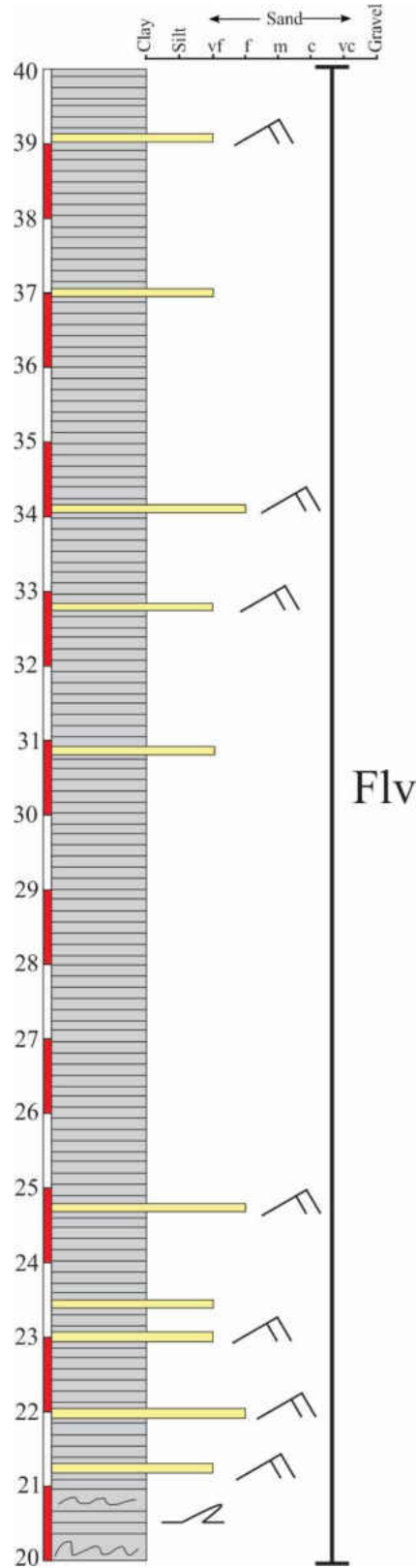
Fig. E24. Core AB-06, 40-60 m, stratigraphic column
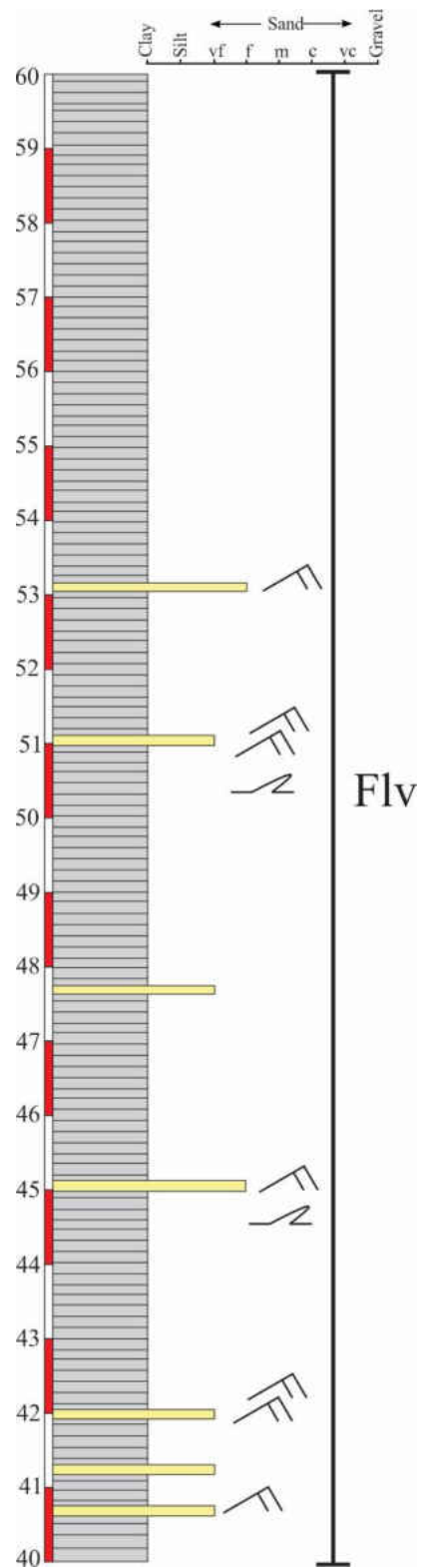
Fig. E25. Core AB-06, 60-80 m, stratigraphic column
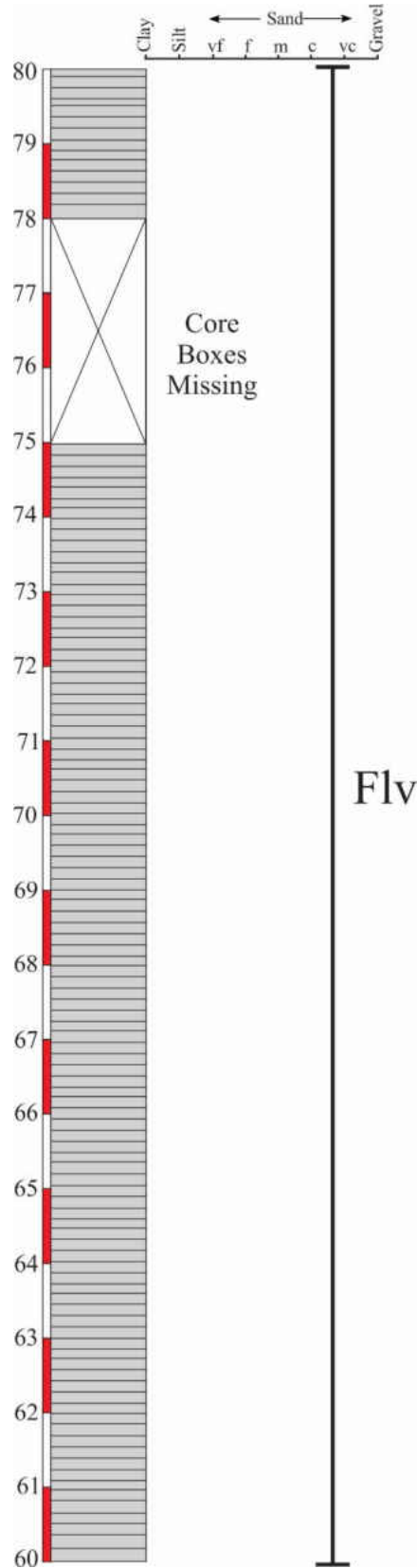
Fig. E26. Core AB-06, 80-100 m, stratigraphic column
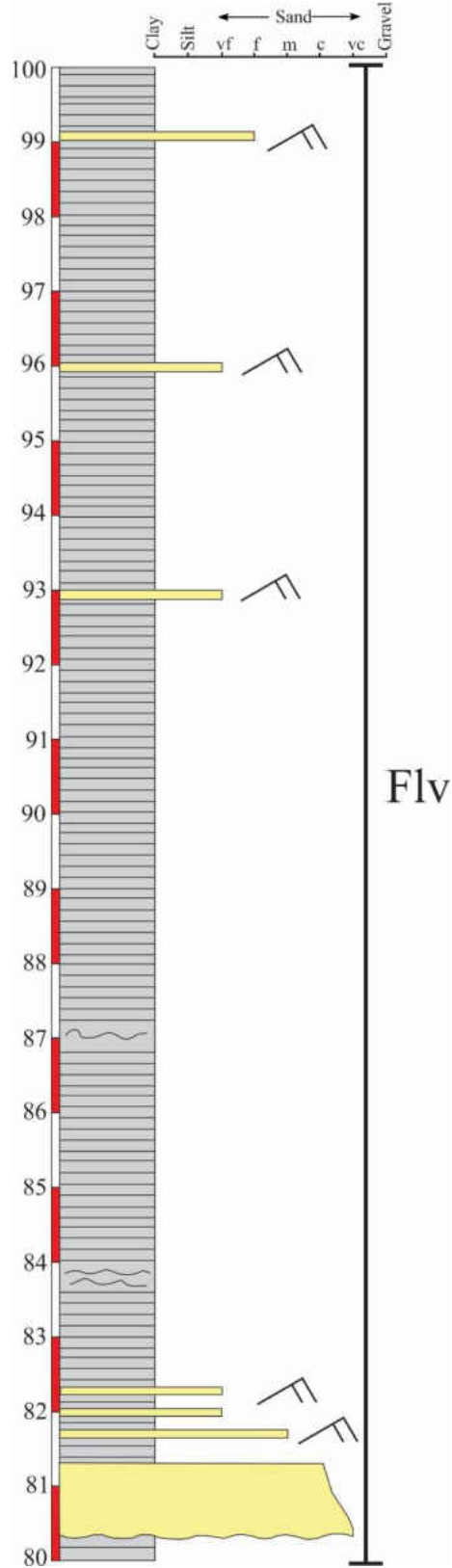
Fig. E27. Core AB-06, 100-120 m, stratigraphic column
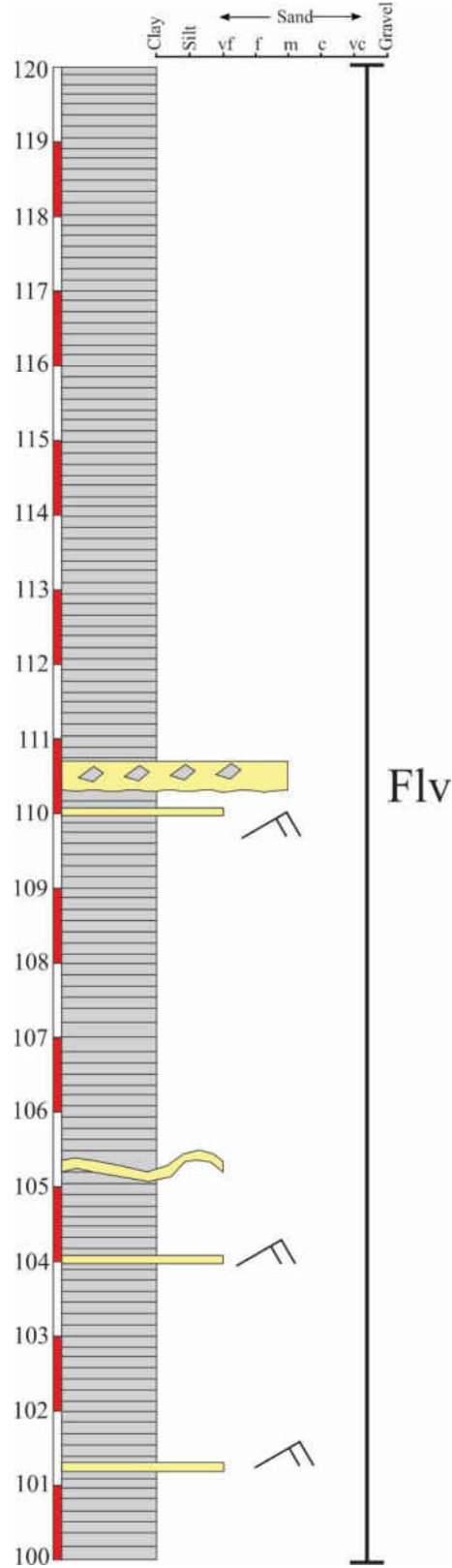
Fig. E28. Core AB-06, 120-140 m, stratigraphic column
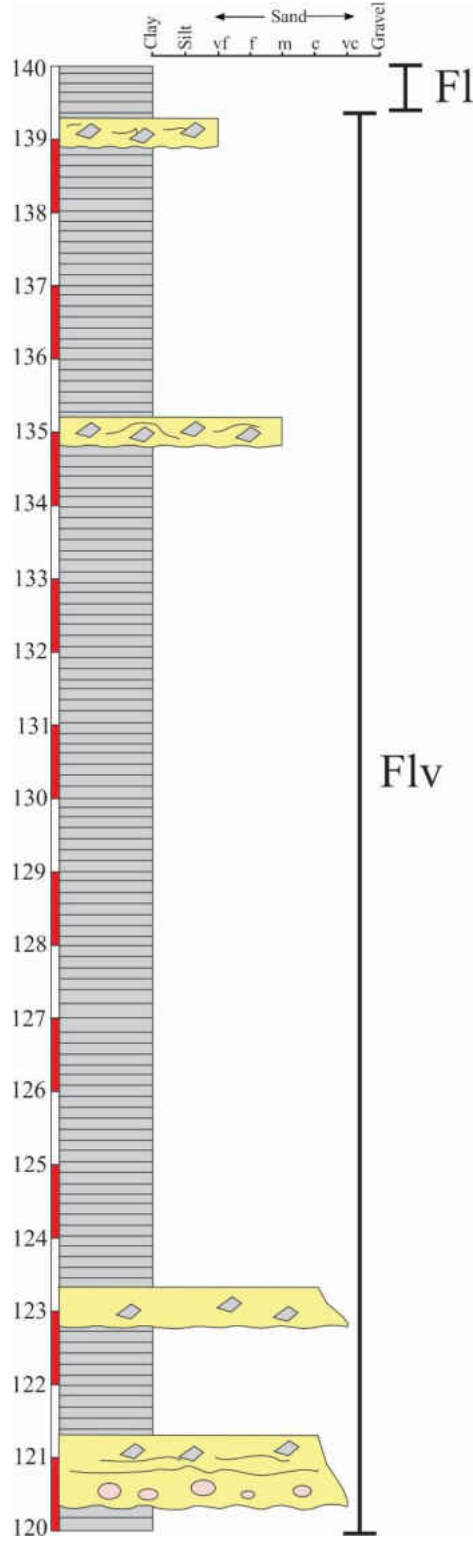
Fig. E29. Core AB-06, 140-160 m, stratigraphic column
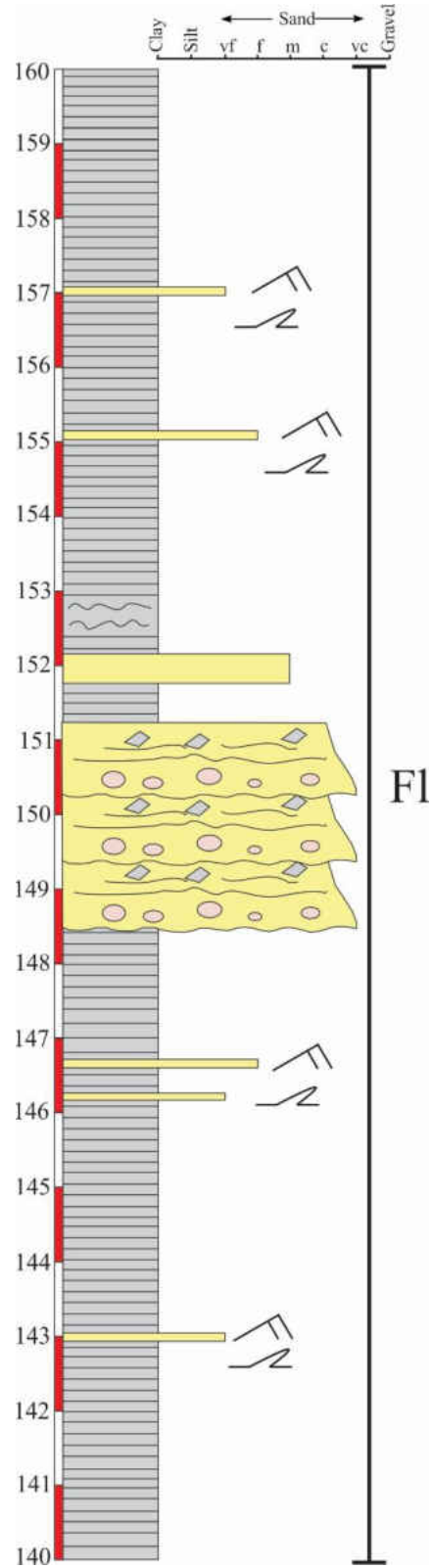
Fig. E30. Core AB-06, 160-180 m, stratigraphic column
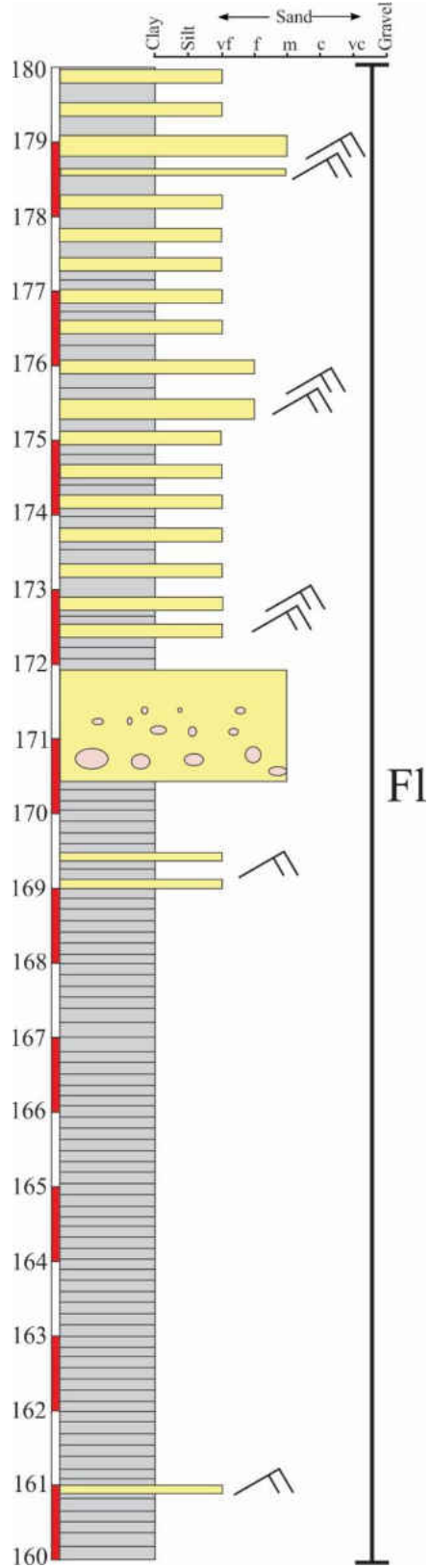
**Fig. E31. Core AB-06, 180-200 m, stratigraphic column**
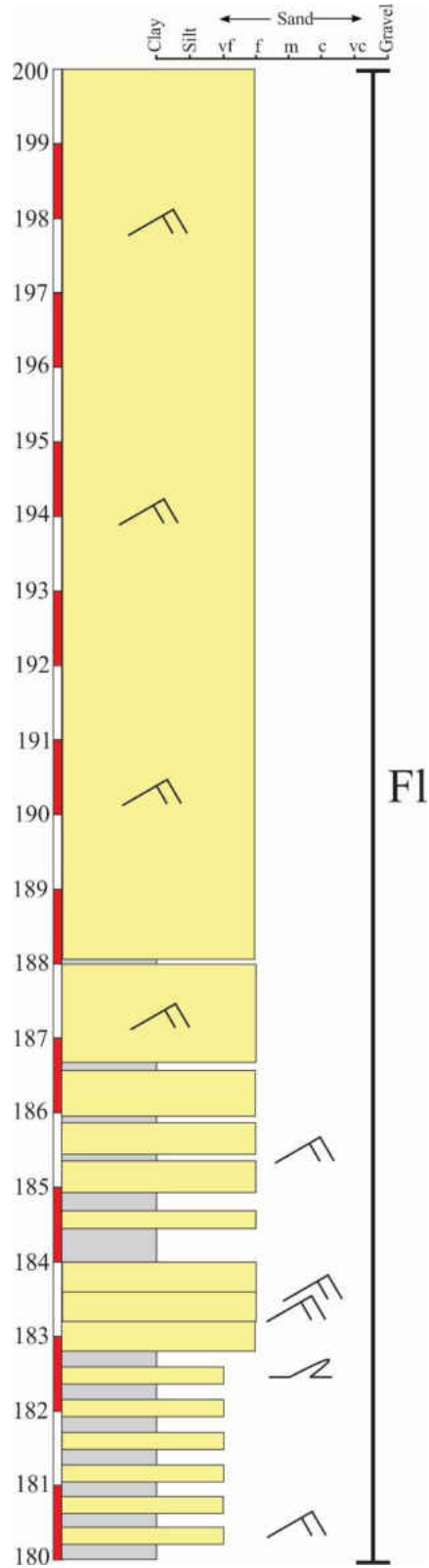
Fig. E32. Core AB-06, 200-220 m, stratigraphic column
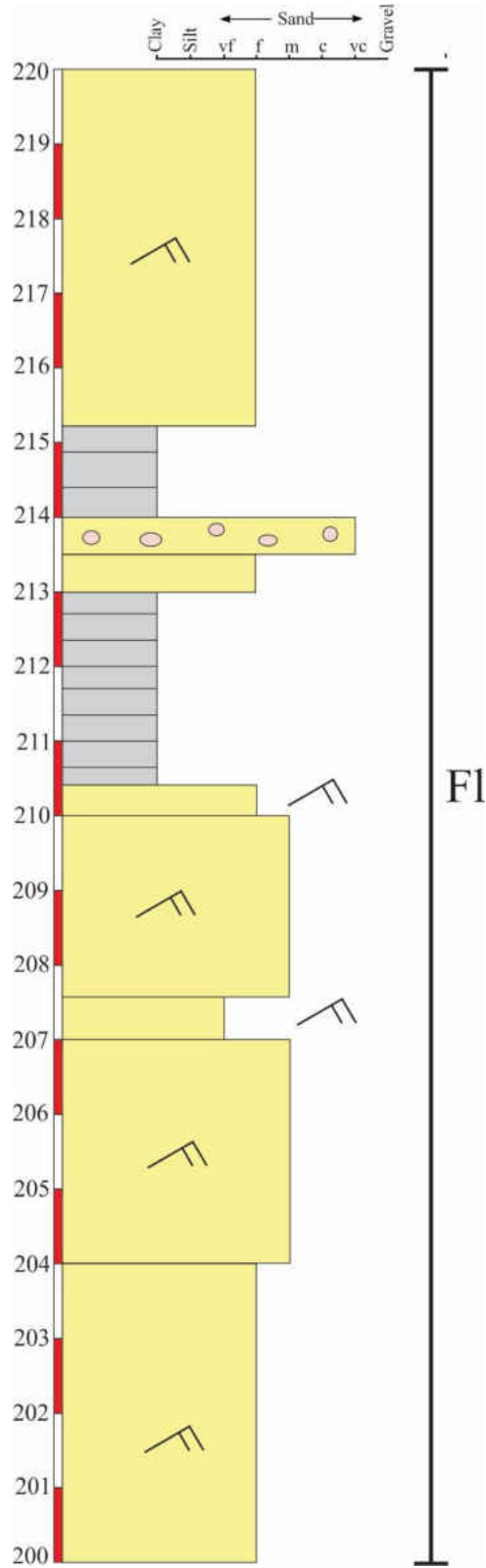
Fig. E33. Core AB-06, 220-240 m, stratigraphic column

<div align="center">
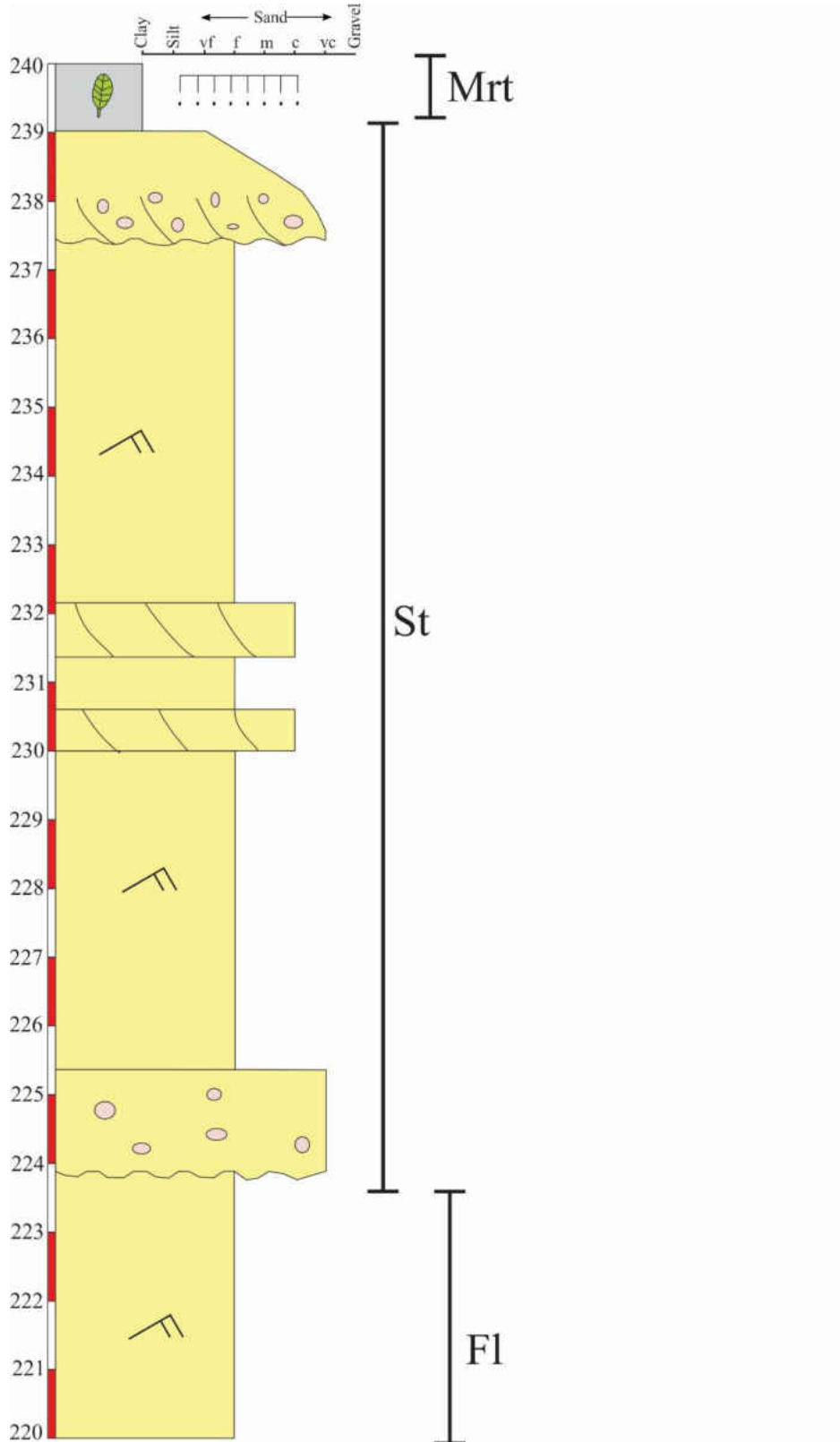
Curriculum Vitae

Nicholas David Fedorchuk

</div>

EDUCATION

May 2019, PhD, Geosciences, The University of Wisconsin-Milwaukee, Milwaukee, WI

- Dissertation: *Testing the late Paleozoic ice-volume paradox in the southernmost Paraná Basin, Brazil,* Adviser: Dr. John Isbell
- Coursework: *General Soil Science*, *Physical Sedimentology*, *Stable Isotope Geochemistry*, *Glacial and Pleistocene Geology*, *Sequence Stratigraphy and Basin Analysis*, *Advanced Topics in Clastic Sedimentology*

2014, M.S., Geosciences, The University of Wisconsin-Milwaukee, Milwaukee, WI

- Thesis: *Evaluating the biogenicity of Mesoproterozoic fluvial-lacustrine stromatolites from the Copper Harbor Conglomerate, Upper Peninsula of Michigan,* Adviser: Dr. Stephen Dornbos
- Coursework: *Carbonate Sedimentology*, *Early Animal Evolution*, *Isotope Biogeochemistry*, *Sedimentation and Stratigraphy*, *GIS Applications for Geoscience*, *Mid-Phanerozoic Climates, Environments and Life*, *History of Geologic Thought*, *X-Ray Analytical Methods*

2012, B.A. (*cum laude*), Geology (Departmental Honors, Senior Thesis Honors), History Minor, The College of Wooster, Wooster, OH

- Senior Thesis: *Stratigraphy and Paleoecology at the Wenlock/Ludlow Boundary on Saaremaa Island, Estonia,* Adviser: Dr. Mark Wilson
- Major Coursework: *Sedimentology and Stratigraphy*, *Invertebrate Paleontology*, *Structural Geology*, *Geomorphology and Hydrogeology*, *Introduction to GIS*, *Processes and Concepts in Geology, Mineralogy, Igneous and Metamorphic Petrology*, *Desert Geology*, *Oil and Gas Geology*, *History of Life*
- Related Coursework: *Chemistry 1*, *Chemistry 2*, *Calculus with Algebra A*, *Calculus with Algebra B*, *Physics 1*, *Physics 2*

ADDITIONAL EDUCATION

- 2017, Geological Society of America Short Course: *U-Pb geochronology, O and Hf isotopes, trace elements applied to detrital minerals*, Seattle, WA
- 2014, Weatherford International Short Course: *Well Log Analysis and Interpretation*, Madison, WI
- 2013, GSA/ Exxon Mobil Short Course: *Sequence Stratigraphy for Graduate Students*, Denver, CO

- 2012, Six Week Field Mapping Course: South Dakota School of Mines and Technology, Rapid City, SD
- 2011, Wooster Summer in Tuscany Study Abroad Program, Siena, Italy

TEACHING EXPERIENCE

2019 (Scheduled), Lecturer, University of Wisconsin-Milwaukee, Milwaukee, WI

- *Sedimentology and Stratigraphy* (Spring, 2019)
- Design and teach 15 week (6 hours/week) upper level geology course to majors
- Responsibilities: design course material and syllabus, give lectures and demonstrations, set up and take down demonstration materials, hold office hours, supervise teaching assistants, create and grade homework assignments, projects, in-class lab exercises, and exams

2018, Adjunct Lecturer, Upper Iowa University, Milwaukee, WI

- Course taught: *Natural Disasters* (Spring, 2018)
- Designed and taught 8 week (4.5 hours/week) introductory geology course on natural disasters
- Responsibilities: design course material and syllabus, give lecture, provide one-on-one lab instruction, set up and take down lab materials, create and grade homework assignments, projects, in-class lab exercises, and exams

2015-2017, Substitute Lecturer, University of Wisconsin-Milwaukee, Milwaukee, WI

- Courses taught: *Sedimentology and Stratigraphy* (Spring 2015, Spring 2016) and *Sequence Stratigraphy and Basin Analysis* (Spring, 2017).
- Taught upper level geology classes (4 hours/week) for adviser (Dr. John Isbell) while he was in the field (Argentina and Antarctica) for 2-3 weeks
- Responsibilities: lecture and conduct laboratory demonstrations, set up and take down demonstrations/lab activities

2012-2016, Graduate Teaching Assistant, University of Wisconsin-Milwaukee, Milwaukee, WI

- Courses taught: *Introduction to the Earth Lab* (Fall 2012, Fall 2013, Spring 2014), *History of Life Lab* (Spring 2013, Fall 2014), *Principles of Historical Geology Lab* (Fall 2015, Spring 2016)
- Each semester 2-3 laboratory sections (~4 hours each week in class) with 10-30 students in each section
- Responsibilities: setting up and taking down laboratory materials/samples, giving a 20-40 minute lecture on the course material at the start of each class, providing one-on-one assistance during lab activities, holding review sessions and office hours, administering laboratory exams, proctoring lecture exams, and grading all laboratory course materials

2010-2012, Geology Department Undergraduate Teaching Assistant, College of Wooster, Wooster, OH

- Courses: *First Year Seminar* (2010), *Processes and Concepts in Geology* (2011), *Sedimentology and Stratigraphy* (2012)
- Responsibilities: helping to set up/take down labs, provide extra assistance to students during lab sections, meet with students outside of class to provide assistance reviewing for exams and working on independent projects

RESEARCH EXPERIENCE

2014-Present, University of Wisconsin-Milwaukee, Dissertation Research, Milwaukee, WI

- Dissertation title: *Testing the late Paleozoic ice-volume paradox in the southernmost Paranà Basin, Brazil,* Adviser: Dr. John Isbell
- 4 field seasons (3-4 weeks each) to southern Brazil and Uruguay (summer 2014, 2015, 2016, 2018)
- Collaborators from UC-Davis, UC-Berkley, Federal University of Rio Grande do Sul (UFRGS), Federal University of Paraná (UFPR)
- Funded by the US National Science Foundation (NSF), UWM Research Growth Initiative, graduate student grants

2012-2014, University of Wisconsin-Milwaukee, Master's Thesis, Milwaukee, WI

- Thesis title: *Evaluating the biogenicity of Mesoproterozoic fluvial-lacustrine stromatolites from the Copper Harbor Conglomerate, Upper Peninsula of Michigan,* Adviser: Dr. Stephen Dornbos
- Field work conducted in Upper Peninsula of Michigan during 2 weeks of summer 2013
- Collaborators from the University of Southern California (USC)
- Funded by graduate student grants

2012-2014, University of Wisconsin-Milwaukee, Additional Research, Milwaukee, WI

- Title: *Permian diamictites in Northeastern Asia: their significance concerning the bipolarity of the late Paleozoic ice age,* Adviser: Dr. John Isbell
- Field work conducted in the Russian Far East (Siberia) over 2 weeks of summer 2013
- Collaborators from Boise State University and Russian Academy of Sciences, Far East Division
- Funded by UWM Research Growth Initiative

2014, University of Wisconsin-Milwaukee, Additional Research, Milwaukee, WI

- Worked over the summer of 2014 with Dr. Erik Gulbranson on dendrochronology project at Cedarburg Bog, Cedarburg, WI

- Funded by the U.S. National Science Foundation (NSF)

2010-2012, The College of Wooster, Junior/Senior Thesis, Wooster, OH

- Thesis title: *Stratigraphy and Paleoecology at the Wenlock/Ludlow Boundary on Saaremaa Island, Estonia,* Adviser: Dr. Mark Wilson
- Field work conducted in Estonia and Sweden over 2 weeks of summer 2011
- Collaborator from University of Tartu

2008-2012, Summer Intern, Kentucky Geological Survey, Lexington, KY

- Adviser: Dr. Gerald Weisenfluh (Former State Director, Kentucky Geological Survey)
- Gained experience using ArcGIS to map coal mines in eastern Kentucky
- Assisted in creating a GIS database of coal mines at risk of blowouts that is used by state mine safety officials
- Helped analyze properties for coal-mining potential by plotting and correlating well logs and creating cross sections
- Helped create a groundwater chemistry database that was used in CO_2 sequestration and hydrocarbon extraction experimentation

PUBLICATIONS

Accepted Papers

- Rosa, E.L.M., Vesely, F.F., Isbell, J.I., Kipper, F., Fedorchuk, N.D., Souza, P.A., 2019. Constraining glacier kinematics and cyclicity during the late Paleozoic Ice Age early stages (Middle Mississippian-Early Pennsylvanian) in the Paraná Basin, Brazil. *Sedimentary Geology*, v. 384, 29-49.

- Vesely, F.F., Rodrigues, M.C.N.L., Rosa, E.L.M., Amato, J.A., Trzaskos, B., Isbell, J.L., Fedorchuk, N.D., 2018. Emplacement of non-glacial mass-transport diamictite within higher frequency glacial cycles during the late Paleozoic icehouse. *Geology*, v. 46, 615-618.

- Griffis, N.P., Montañez, I.P., Fedorchuk, N.D., Isbell, J.L., Mundil, R., Vesely, F.F., Weinshultz, L., Iannuzzi, R., Yin, Q., Gulbranson, E.L., Taboada, A., Pagini, A., Sanborn, M., Huyskens, M., Wimpenny, J., and Linol, B., 2019. Isotopes to ice: Constraining provenance of glacial deposits and ice centers in west-central Gondwana. *In press:* accepted to *Palaeogeography, Palaeoclimatology, Palaeoecology* on 4/25/2018.

- Fedorchuk, N.D., Isbell, J.L., Griffis, N.P., Montañez, I.P., Mundil, R., Yin, Q., Vesely, F.F., Iannuzzi, R., Rosa, E.L.M., and Pauls, K.N., 2019. Origin of paleovalleys on the Rio Grande do Sul Shield (southernmost Brazil): Implications for the extent of late Paleozoic glaciation in west-central Gondwana. *In press:* accepted to *Palaeogeography, Palaeoclimatology, Palaeoecology* on 4/17/2018.

- Griffis, N.P, Mundil, R., Montañez, I.P., Isbell, J.L., Fedorchuk, N.D., Vesely, F.F., Iannuzzi, R., 2018. A new stratigraphic framework built on U-Pb single zircon TIMS ages with implications for the timing of the penultimate icehouse (Paraná Basin, Brazil). *Geological Society of America Bulletin*, v. 130, 848-858.

- Fedorchuk, N.D., Dornbos, S.Q., Petryshyn, V.A., Wilmeth, D.T., Corsetti, F.A., and Isbell, J.L., 2016. Evaluating the biogenicity of Mesoproterozoic fluvial-lacustrine stromatolites. *Precambrian Research*, v. 275, 105-118.

- Isbell, J.L., Biakov, A.S., Vedernikov, I.L., Davydov, V.I, Gulbranson, E.L., Fedorchuk, N.D., 2016. Permian diamictites in northeastern Asia: Their significance concerning the bipolarity of the late Paleozoic ice age. *Earth-Science Review*s, v. 154, 279-300.

Manuscripts in Review

- Fedorchuk, N.D., Isbell, J.L., Griffis, N.P., Vesely, F.F., Rosa, E.L.M., Montañez, I.P., Mundil, R., Iannuzzi, R., Roesler, G., Yin, Q., and Pauls, K.N., 2019. Carboniferous glaciotectonized sediments and their paleoclimatic significance — evidence from a terrestrial setting, southernmost Paraná Basin, Brazil. Submitted to *Sedimentary Geology* 3/21/2019.

Manuscripts in Preparation

- Fedorchuk, N.D., Isbell, J.L., Goso, C., Griffis, N.P., Rosa, E.L.M., Montañez, I.P., Yin, Q., Vesely, F.F., Mundil, R., Iannuzzi, R., 2018. Detrital zircon U-Pb geochronology of late Paleozoic glacial deposits in the Chaco-Paraná Basin, Uruguay. In preparation for *GSA Bulletin*.

- Griffis, N.P., Montañez, I.P., Mundil, R., Isbell, J.L., Fedorchuk, N.D., Iannuzzi, R., Vesely, F.F., Mottin, T., and Yin, Q., 2018. A revised stratigraphic framework for the southeast margin of the Paraná Basin – evidence for glacio-eustatic forcing across the Carboniferous through Early Permian. In preparation for *Geology*.

Abstracts

- Isbell, J.L., Fedorchuk, N.D., Pauls, K.N., Griffis, N.P., Ives, L.R.W., Moxness, L.D., Survis, S.R., Vesely, F.F., Montañez, I.P., Limarino, C.O., Iannuzzi, R., Biakov, A.S., Rosa, E.L.M., Mundil, R., Taboada, A.C., Pagani, M.A., Ciccioli, P.L., Schencman, J., Alonso-Muruaga, P.J., Davydov, V.I., Vedernikov, I.L., McNall, N.B., 2018. Glaciation during the late Paleozoic ice age. *VII Simposio Argentino del Paleozoico Superior, 5R.*

- Griffis, N.P., Mundil, R., Montañez, I.P., Keller, B., Fedorchuk, N.D., Isbell, J.L., Vesely, F., Iannuzzi, R., 2018. A new time scale constraining the timing of the Late

Paleozoic Ice Age. *European Geophysical Union Annual Meeting, Abstracts with with Programs 20, EGU2018-11303.*

- Fedorchuk, N.D., Isbell, J.L., Griffis, N.P., Montañez, I.P., Mundil, R., Yin, Q, Vesely, F.F., Iannuzzi, R., da Rosa, E.L.M., and Pauls, K.N., 2017. Origin of paleovalleys on the Rio Grande do Sul Shield (southernmost Brazil): Implications for the extent of late Paleozoic glaciation in west-central Gondwana. *Geological Society of America Annual Meeting, Abstracts with Programs* 49(6).

- Fedorchuk, N.D., Isbell, J.L., Griffis, N.P., Montañez, I.P., Mundil, R., Vesely, F.F., Iannuzzi, R., and da Rosa, E.L.M., 2017. Carboniferous glaciotectonized sediments on the western Rio Grande do Sul Shield, Paraná Basin, southernmost Brazil. *Geological Society of America Annual Meeting, Abstracts with Programs* 49(6).

- Vesely, F.F., Trzaskos, B., Mottin, T.E., Rodrigues, M.C.N.L., Schemiko, D.C.B., Rosa, E.L.M., Carvalho, A.H., Kipper, F., Souza, P.A., Iannuzzi, R., Paim, P.S.G., Isbell, J.L., Fedorchuk, N.D., Montañez, I.P., Griffis, N.P., Mundil, R., 2017. Late Paleozoic tectonics, glaciation and sedimentation in the Paraná Basin: Latest advances. *X Simpósio Sul-Brasileiro de Geologia, ST117.*

- Griffis, N., Mundil, R., Montañez, I.P., Isbell, J.L., Fedorchuk, N.D., Lopes, R., Vesely, F., Iannuzzi, R., 2016. High-Resolution Zircon U-Pb CA-TIMS Dating of the Carboniferous-Permian Successions, Paraná Basin, Brazil. *Presented at 35th International Geological Congress in Cape Town, South Africa, 27 August – 4 September 2016.*

- Griffis, N., Mundil, R., Montañez, I.P., Isbell, J.L., Fedorchuk, N.D., Lopes, R., Vesely, F., Iannuzzi, R., 2015. High-Resolution Zircon U-Pb CA-TIMS Dating of the Carboniferous-Permian Successions, Paraná Basin, Brazil. *American Geophysical Union Fall Meeting Abstracts with Programs V32B-08.*

- Fedorchuk, N.D., Isbell, J.L., Iannuzzi, R., Griffis, N., Montañez, I.P., 2015. Preliminary interpretations of glaciomarine facies, their distribution, and importance in the southern Paraná Basin, Brazil. *Geological Society of America North-Central Annual Meeting, Abstracts with Programs* 47(5).

- Fedorchuk, N.D., Dornbos, S.Q., Petryshyn, V.A., Wilmeth, D.T., Corsetti, F.A., and Isbell, J.L., 2013. Evaluating the biogenicity of Mesoproterozoic fluvial-lacustrine stromatolites in the Copper Harbor Conglomerate, Upper Peninsula of Michigan. *Institute on Lake Superior Geology Annual Meeting, Abstracts with Programs* 60.

- Fedorchuk, N.D., Dornbos, S.Q., Petryshyn, V.A., Wilmeth, D.T., Corsetti, F.A., and Isbell, J.L., 2013. Evaluating the biogenicity of Mesoproterozoic fluvial-lacustrine stromatolites in the Copper Harbor Conglomerate, Upper Peninsula of Michigan. *Geological Society of America Annual Meeting, Abstracts with Programs* 45(7).

- Isbell, J.L., Biakov, A.S.,Vedernikov, I.L., Davydov, V. I., Gulbranson, E.L., Fedorchuk,

N.D., Kolesov, E.V., and Ivanov, Y.Y, 2013. Reevaluation of Permian glaciation in Siberia during the late Paleozoic ice age: Preliminary analyses on the origin of Capitanian diamictites in the Atkan Formation, Okhotsk Region, Russia. *Geological Society of America Annual Meeting, Abstracts with Programs* 45(7).

- Fedorchuk, N.D., Wilson, M.A., Matt, R.M., and Vinn, O., 2011. Stratigraphy and paleoecology at the Wenlock/Ludlow boundary on Saarema Island, Estonia. *Geological Society of America Annual Meeting, Abstracts with Programs* 43(5): 95.

- Matt, R.M., Wilson, M.A., Fedorchuk, N.D., and Vinn, O., 2011. Paleoecology of the Hilliste Formation (Lower Silurian, Llandovery, Rhuddanian) Hiiumaa Island Estonia: an example of a shallow marine recovery fauna. *Geological Society of America Annual Meeting, Abstracts with Programs* 43(5): 82.

GRANTS RECEIVED

- UWM Center for Latin America and Caribbean Studies (CLACS) research grant (2015, 2016, 2018) -$5,000
- UWM Geosciences Graduate Research Grant (2013, 2015, 2017) - $1,500
- Wisconsin Geological Society Research Grant (2013, 2015, 2017) - $2,450
- American Association of Petroleum Geologists Student Research Grant (2016) - $1,000
- Society for Sedimentary Geology Student Research Grant (2016) - $800
- Geological Society of America Student Research Grant (2016) - $2,500
- Institute on Lake Superior Geology Student Research Grant (2013) - $500
- **Total = $13,750**

HONORS/AWARDS

University of Wisconsin-Milwaukee

- Best UWM Geosciences Symposium Poster Presentation (2018)
- UWM Distinguished Dissertator Fellowship (2018)
- Geological Society of America Annual Meeting Best Poster Award (Sedimentary Division) (2017)
- UWM Distinguished Graduate Student Fellowship (2016)
- UWM Geosciences Graduate Student Research Award (2014, 2017)
- Best UWM Geosciences Symposium Oral Presentation (2014, 2017)
- UWM Geosciences Outstanding Teaching Assistant Award (2013, 2016)
- UWM Chancellor's Graduate Student Award (2012, 2013, 2014, 2015, 2016, 2017, 2018)

The College of Wooster

- Campus Council Leadership Award (2012)
- President of Wooster Geology Club (2012)

- History Department Honor Society (2011, 2012)
- Don J. Miller Memorial Geology Scholarship (2011)
- Margaret Kate Moke Geology Scholarship (2010, 2011)
- Dean's List (Fall 2008, Spring 2010, Fall 2010, Spring 2012)

INVITED TALKS

Universidade Federal do Paraná, Curitiba, PR, Brazil, September 2018

- Oral presentation regarding dissertation research entitled: *Late Paleozoic glaciation on the Rio Grande do Sul Shield, southernmost Paraná Basin, Brazil*

Universidade do Contestado, Mafra, SC, Brazil, September 2015

- Oral presentation regarding research in the Russian Far East entitled: *Permian diamictites in Northeastern Asia: their significance concerning the bipolarity of the late Paleozoic ice age*

INVITED REVIEWER

- South African Journal of Geology, 2017, Editor: Dr. Stephen McCourt
- Palaeogeography, Palaeoclimatology, Palaeoecology, 2019, Editor: Dr. Isabel Montãnez

CONFERENCES ATTENDED

Geological Society of America Annual Meeting, Seattle, WA, September 2017

- Oral presentation regarding dissertation research in southern Brazil entitled *Origin of paleovalleys on the Rio Grande do Sul Shield (southernmost Brazil): Implications for the extent of late Paleozoic glaciation in west-central Gondwana.*
- Poster presentation regarding dissertation research in southern Brazil entitled *Carboniferous glaciotectonized sediments on the western Rio Grande do Sul Shield, Paraná Basin, southernmost Brazil.*

Geological Society of America North-Central Regional Meeting, Madison, WI, May 2015

- Poster presentation regarding dissertation research in Brazil entitled *Preliminary Interpretations of Glaciomarine Facies, their Distribution, and Importance in the Southern Paraná Basin, Brazil.*

Institute on Lake Superior Geology Annual Meeting, Hibbing, MN, May 2014

- Poster presentation regarding master's thesis research in the Upper Peninsula of Michigan entitled *Evaluating the Biogenicity of Mesoproterozoic Fluvial-Lacustrine Stromatolites in the Copper Harbor Conglomerate, Upper Peninsula of Michigan.*

Geological Society of America Annual Meeting, Denver, CO, October 2013

- Oral presentation regarding master's thesis research in the Upper Peninsula of Michigan entitled *Evaluating the Biogenicity of Mesoproterozoic Fluvial-Lacustrine Stromatolites in the Copper Harbor Conglomerate, Upper Peninsula of Michigan.*

Geological Society of America Annual Meeting, Minneapolis, MN, October 2011

- Presented a poster regarding research in Estonia entitled *Stratigraphy and Paleoecology at the Wenlock/Ludlow Boundary on Saaremaa Island, Estonia.*

Geological Society of America Annual Meeting, Denver, CO, October 2010

- Attended the Geological Society of America Meeting in Denver.

COLLABORATORS

Advisers

- PhD adviser: Dr. John Isbell, University of Wisconsin-Milwaukee
- Master's adviser: Dr. Stephen Dornbos, University of Wisconsin-Milwaukee
- Undergraduate adviser: Dr. Mark Wilson, College of Wooster

American Collaborators

- Dr. Frank Corsetti, University of Southern California
- Dr. Victoria Petryshyn, University of Southern California
- Dr. Isabel Montañez, University of California, Davis
- Dr. Roland Mundil, Berkeley Geochronology Center
- Dr. Vladimir Davydov, Boise State University
- Dr. Neil Griffis (postdoctoral researcher), Berkeley Geochronology Center
- Dr. Dylan Wilmeth (postdoctoral researcher), Institut Physique du Globe de Paris

International Collaborators

- Dr. Cesar Goso, Universidad de la República de Uruguay, Uruguay
- Dr. Roberto Iannuzzi, Universidade Federal do Rio Grande do Sul, Brazil
- Dr. William Matsumura, Universidade Federal do Piauí, Brazil
- Dr. Luiz Weinshultz, Universidade do Contestado, Brazil
- João Ricetti (PhD Student), Universidade do Contestado, Brazil
- Guilherme Arsego Roesler (PhD Student), Universidade Federal do Rio Grande do Sul, Brazil
- Eduardo Rosa (PhD Student), Universidade Federal do Paraná, Brazil
- Dr. Fernando Vesely, Universidade Federal do Paraná, Brazil

- Dr. Ricardo Lopes, Unisinos, Brazil
- Dr. Olev Vinn, University of Tartu, Estonia
- Dr. Alexander Biakov, Russian Academy of Sciences, Far East Divison, Russia
- Dr. Igor Vedernikov, Russian Academy of Sciences, Far East Division, Russia

SKILLS

- ArcGIS
- X-ray diffraction/fluorescence
- Laser ablation inductively-coupled-plasma mass spectrometry (LA-ICP-MS)
- Detrital zircon U-Pb geochronology
- Coreldraw
- Adobe Lightroom